

---

---

UNRAVELLING THE BADGRS PARADOX  
~  
PROBING THE  
BLUE AND DUSTY GAS-RICH SOURCES  
IN THE  
HERSCHEL ATLAS  
USING  
INTEGRAL FIELD SPECTROSCOPY

---

---

*by*

Zoe Ann Ballard

A THESIS SUBMITTED TO CARDIFF UNIVERSITY  
FOR THE DEGREE OF MASTER OF PHILOSOPHY

14<sup>th</sup> JUNE 2021

**Author:** Zoe Ann Ballard

**Title:** Unravelling the BADGRS Paradox

~

Probing the

Blue And Dusty Gas-Rich Sources

in the

Herschel ATLAS

using

Integral Field Spectroscopy

**Date of submission:** 14<sup>th</sup> June 2021





---

*Eragon looked back at him, confused. “I don’t understand.”*  
*“Of course you don’t,” said Brom impatiently. “That’s*  
*why I’m teaching you and not the other way around.”*

---

Eragon, Christopher Paolini



# Acknowledgements

---

*“It’s not the wolves out there,” said Eragon, hugging himself. “It’s the wolves in here.” He tapped the middle of his forehead. Arya nodded... “It is always thus. The monsters of the mind are far worse than those that actually exist.”*

---

Brisingr, Christopher Paolini

Well, this has been a *journey*. It’s been incredibly tough to get here, and at some points I didn’t think I’d get through it, but I’m finally able to say it’s done, and I’m so proud of what I’ve accomplished. However, I wouldn’t have been able to complete this journey without the help and support of the people closest to me.

Firstly, I’d like to acknowledge support from the European Research Council project CosmicDust, from which this project received funding. I would like to thank Andy Green for his virtual assistance as support astronomer during my observing run at the Anglo-Australian Telescope, and Matt Owers for extending his stay to provide support in person whilst Andy was unavailable. Also thanks again to Andy, and to Jesse Van de Sande, Chris Lidman and other members of the 2dFdr working group for their assistance at various points in the KOALA data reduction process.

A big thank you to Steve Eales and Vivienne Wild for being awesome examiners; I don’t think I was ever going to enjoy my viva, but you both made it a smooth and positive experience overall, despite my nerves. I’m incredibly grateful for your lovely comments about my project and the Thesis, and for showing me I’m not the only one who finds dust attenuation confusing at times! Thank you also to Tim Davis for chairing during the viva, and for your help and advice over the years.

I’m very grateful to my supervisory team for taking me on and letting me delve deeper into the wonderful world of the BADGRS with this project. A big thank you to Steve Maddox, your help and guidance throughout has been invaluable; I don’t

think we would have gotten through the KOALA data reduction process (which at times felt never-ending...) without your knowledge and patience. You've helped me become a careful and thorough scientist. Thank you also to Loretta Dunne, for your enthusiasm for the BADGRS, and for pulling Steve and I out of our data reduction rabbit holes! And finally thank you to Haley Gomez, who was not only a supervisor for this project, but my tutor during my undergraduate degree, and a role model throughout my time at Cardiff University. Your support and wise words have helped me through some very tough times, and I'm so thankful that I got the chance to work with you.

To those who I have had the pleasure of sharing an office with over the years, thank you for being awesome! To the office postdocs, thank you for helping with our never-ending questions and code issues. To Chris Clark, for always having an "oooooh BADGRS!" to throw at me as I worked through the project, we miss you from across the pond. To Matt Smith, for all your patience and for being 53's designated adult supervision. And to Phil Cigan, for all your spectra advice and for being my travel buddy to Australia, you made my first plane journey abroad super chill; observing at the AAT with you will be something I always remember. A big thank you also to Pieter De Vis and Kate Rowlands for your help and advice during your visits to Cardiff.

To my Ladies Wot Science, you are all wonderful. I'm so grateful to know you, and you're all going to go on to do amazing things! Thank you for always listening, and for providing a safe space with emotional support and cute pet pictures during the toughest times. To Liz, you are awesome, and I love your boundless enthusiasm; keep being your epic self. To my fellow Cosmic Dust ladies, it's been an absolute pleasure to have you by my side as we tried to understand this dusty Universe. To Rosie, thank you for always being our cheerleader, we love you. To Hannah and Jeni, you were the best desk buddies a girl could have; it's been a blast science-ing and putting the world to rights with you. Jen, I maintain you're going to be a famous science superstar (I want that autograph when it happens); you're an amazing human being and you're going to get through whatever life throws at you.

To the Tewkes of Hazzard; Jack, Becca, Ryan, Gareth, Chris, David and little Bee, you are my chosen family and I love you all. You have helped keep me (mostly) sane during both my undergraduate and postgraduate degrees, especially during the

pandemic times with our gaming and weekend chitty chats. With you I have accessed a whole new level of nerd; a world of board games and dungeons and dragons for which I shall happily continue to provide cake and cookies.

A special thank you to my therapist Maddy Dutkowski, whose guidance and advice has helped me to better understand my self and my values, and has given me the confidence to chase them. I cannot describe how important that journey of self exploration has been in getting me to this point; you helped me find myself when I felt truly lost and hopeless, and for that I will always be grateful.

Finally, to my closest family; my dad, my brother Christopher, and most importantly my mum, I love you. For encouraging a love of reading and animals and science. For making me smile and laugh when I thought it was impossible. For believing in me and being proud of me always, when I couldn't believe in myself. I wouldn't have been able to get here without you. To my partner Alex, I'm so glad I found you. You are truly my rock, my favourite person, and I wouldn't have gotten through this whole journey without your support. You're the best. A final mention to our lovely kitty, Pepper, for all the snuggles and biscuits and zoomies in the last year; floof cuddles really are the best medicine.

---

*"I am not who I was, but I know who I am."*

---

Inheritance, Christopher Paolini



# Contents

Acknowledgements	vii
List of Figures	xv
List of Tables	xix
Abstract	xxi
<b>1 Introduction</b>	<b>1</b>
1.1 Cosmic Dust . . . . .	1
1.2 A selection of surveys of Local Galaxies with <i>Herschel</i> . . . . .	2
1.2.1 The <i>Herschel</i> ATLAS . . . . .	2
1.2.2 The HAPLESS sample and the discovery of BADGRS . . . . .	4
1.2.3 Recent Molecular Gas Observations of a sample of BADGRS . . . . .	6
1.2.4 The Paradoxical Properties of BADGRS . . . . .	7
1.3 Dust Attenuation in Galaxies . . . . .	8
1.3.1 The anatomy of an Attenuation Curve . . . . .	9
1.3.2 What processes can influence the slope of the attenuation curve? . . . . .	11
1.3.3 Observations of Extinction and Attenuation in the local Universe . . . . .	12
1.4 Integral Field Spectroscopy . . . . .	15
1.4.1 KOALA . . . . .	21
1.5 What can we do with KOALA data? . . . . .	21
1.6 Thesis Outline . . . . .	24
<b>2 The Sample and Data</b>	<b>27</b>
2.1 Introduction . . . . .	27
2.2 Obtaining the KOALA data . . . . .	27

2.3	Individual Galaxies . . . . .	30
2.3.1	NGC 5584 . . . . .	30
2.3.2	NGC 5496 . . . . .	31
2.3.3	UGC 9299 . . . . .	31
2.3.4	UGC 9215 . . . . .	32
2.4	Extra Targets . . . . .	32
2.4.1	NGC 4030 . . . . .	32
2.4.2	NGC 7361 . . . . .	33
2.4.3	NGC 0007 . . . . .	33
2.5	Conclusions . . . . .	33
<b>3</b>	<b>Data Reduction and Calibration</b>	<b>37</b>
3.1	Introduction . . . . .	37
3.2	Cosmic ray removal with PyCosmic . . . . .	38
3.3	Scattered light subtraction . . . . .	40
3.4	The 2dFdr software package . . . . .	42
3.4.1	Choosing which extraction method to use . . . . .	43
3.5	Throughput calibration . . . . .	47
3.6	Sky subtraction . . . . .	53
3.6.1	Moonlit skies . . . . .	55
3.7	Masking of sky line remnants, defects and leftover cosmics . . . . .	57
3.7.1	Sky line remnants . . . . .	57
3.7.2	Defects in the blue CCD . . . . .	58
3.7.3	Leftover cosmic rays . . . . .	58
3.8	Flux calibration . . . . .	60
3.9	Creating the final product: Data Cubes . . . . .	65
3.10	Example results from the final Data Cubes . . . . .	69
3.11	Conclusions . . . . .	72
<b>4</b>	<b>Investigating the properties of BADGRS</b>	<b>75</b>
4.1	Extracting galaxy properties from IFU data cubes . . . . .	75
4.1.1	Voronoi Binning . . . . .	76
4.1.2	pPXF . . . . .	78
4.2	Investigating the dust law of UGC 9215 . . . . .	81

4.2.1	Modelling the Reddening Law . . . . .	81
4.2.2	Fitting F, E and $\delta$ . . . . .	85
4.2.3	Fitting F and E, and keeping $\delta$ fixed . . . . .	85
4.2.4	What does the attenuation curve of UGC 9215 tell us? . . . . .	87
4.2.5	Obtaining a dust mass from attenuation . . . . .	90
4.3	Investigating the stellar populations of UGC 9215 . . . . .	96
4.4	Investigating the excitation and metallicity of UGC 9215 . . . . .	102
4.5	Conclusions . . . . .	104
<b>5</b>	<b>Conclusions</b>	<b>105</b>
	<b>Appendix A Additional Observing Information</b>	<b>109</b>
	<b>Appendix B More details on Data Reduction changes</b>	<b>113</b>
B.1	Investigating the upturn in the blue end of the spectra . . . . .	113
B.1.1	Biases in flux calibration curves . . . . .	113
B.1.2	Characterising the scattered light . . . . .	114
B.2	2dFdr Settings . . . . .	121
B.3	Gauss versus OPTEX Extraction Methods . . . . .	121
B.4	Throughput Calibration using Quartz Flats . . . . .	123
B.5	Sky Subtraction . . . . .	123
B.5.1	Sky subtraction on moonlit nights . . . . .	125
B.6	Flux Calibration . . . . .	126



# List of Figures

1.1	The positions of the <i>Herschel</i> ATLAS fields on the galactic plane. . . . .	3
1.2	Images of a subset of BADGRS from Clark et al. (2015). . . . .	5
1.3	Schematic showing the difference between extinction and attenuation. . . . .	8
1.4	Schematic showing the different parts of an extinction/attenuation curve. . . . .	10
1.5	Extinction curves for the Milky Way, Large Magellanic Cloud, Small Magellanic Cloud, and the starburst attenuation curve of Calzetti et al. (2000). . . . .	14
1.6	Attenuation curves created using the modified Calzetti law of Salim et al. (2018). . . . .	16
1.7	Diagram of the workings of an integral field spectrograph. . . . .	17
1.8	The lenslets of the KOALA IFU. . . . .	22
1.9	Diagram of the AAOmega spectrograph set-up. . . . .	23
2.1	SDSS <i>g</i> -band images of our pilot BADGRS sample. . . . .	28
2.2	Optical images of our three extra targets. . . . .	29
3.1	An example of the workings of PyCosmic. . . . .	39
3.2	Example of the effect of cosmic ray removal. . . . .	41
3.3	Intensity map of the flux standard LTT3128. . . . .	44
3.4	Fibre number map for the observation of LTT3218. . . . .	45
3.5	$\Delta_{Flux}/\sigma_{\Delta}$ map for the flux standard LTT3218. . . . .	46
3.6	Examples of throughput calibrators for the KOALA IFU. . . . .	48
3.7	Fibre throughputs for the observing runs with KOALA. . . . .	49
3.8	Example of the effect of throughput calibration. . . . .	50
3.9	Example of the effect of checking for TLM creep. . . . .	52
3.10	Example of the effect of improper sky subtraction. . . . .	54

3.11	Test results for a bootstrap to obtain errors. . . . .	55
3.12	Example of the effect of moonrise on KOALA observations. . . . .	56
3.13	Example of the effect of interpolated sky subtraction. . . . .	57
3.14	Example of the effect of sky line masking. . . . .	59
3.15	Examples of the effect of defect masking in the blue CCD. . . . .	60
3.16	Example of a leftover cosmic ray. . . . .	60
3.17	Spectrum of the standard star LTT3218. . . . .	61
3.18	Smoothed calibration curves for the KOALA IFU. . . . .	63
3.19	Example position match between an SDSS fibre and a KOALA data cube. . . . .	65
3.20	Example of the effect of zero point and first order calibration corrections.	66
3.21	Comparison between the original and IVW cubing techniques. . . . .	70
3.22	Example of the effect of the IVW cubing technique. . . . .	71
3.23	Example flux maps of the galaxy UGC 9215. . . . .	73
3.24	Example spectra from two regions within the galaxy UGC 9215. . . . .	74
4.1	Result of Voronoi pixelation for UGC 9215. . . . .	77
4.2	Comparison of original pixels and Voronoi spatial bins for UGC 9215.	78
4.3	Example full spectrum pPXF fit for a spatial bin of UGC 9215. . . . .	80
4.4	Example emission line fits for a spatial bin of UGC 9215. . . . .	82
4.5	Example template weights for a spatial bin of UGC 9215. . . . .	83
4.6	Fitted line flux maps for UGC 9215. . . . .	84
4.7	Results from a three parameter model of the reddening law of UGC 9215. . . . .	86
4.8	Distribution of total $\chi^2$ with $\delta$ for the two parameter reddening law fit.	87
4.9	Results from a two parameter model of the reddening law of UGC 9215.	88
4.10	Comparison of the derived UGC 9215 attenuation law with other sources.	91
4.11	Mie theory calculations for spherical dust grains. . . . .	92
4.12	<i>Herschel</i> SPIRE 250 $\mu\text{m}$ image of UGC 9215. . . . .	94
4.13	Regions of interest within UGC 9215. . . . .	98
4.14	Average spectra from regions of interest within UGC 9215. . . . .	99
4.15	Template weight maps for the upper and lower bulge. . . . .	100
4.16	Template weight maps for a HII region. . . . .	101
4.17	Maps of metallicity and excitation indicators for UGC 9215. . . . .	103

B.1	Example spectra from KOALA observations of LTT3218. . . . .	114
B.2	Comparisons of different methods of scattered light subtraction. . . .	117
B.3	Example of the effect of 2D scattered light subtraction on a quartz flat.	118
B.4	Example of the effect of 2D scattered light subtraction in different regions of a quartz flat. . . . .	120
B.5	Example of the behaviour of PyCosmic with different extraction meth- ods in 2dFdr. . . . .	122
B.6	Results of different model fits to the profile of LTT3218. . . . .	127
B.7	Comparison of residuals from a model fit with differing extraction methods. . . . .	128
B.8	Example of scattered light in a quartz flat. . . . .	128
B.9	Example of incorrect sky subtraction. . . . .	129
B.10	Example of the effect of wavelength calibration. . . . .	130
B.11	Effect of moonrise on KOALA observations for all observing nights. .	131
B.12	Effect of moonrise on KOALA observations for 28 <sup>th</sup> April 2016. . . .	132
B.13	Example of an interpolated sky spectrum. . . . .	133
B.14	Intensity map of flux standard LTT3218. . . . .	134
B.15	An example smoothed and unsmoothed calibration curve. . . . .	135



# List of Tables

1.1	Spatial and spectral properties of various integral field spectrographs.	20
1.2	Spatial and spectral properties of the KOALA IFU. . . . .	22
2.1	Summary of the observing time spent on each target field. . . . .	31
2.2	Properties of our pilot sample of BADGRS. . . . .	34
2.3	Properties of our three extra targets. . . . .	35
3.1	Final PyCosmic parameter values. . . . .	40
3.2	FWHM measurements of KOALA 'MFARC' lines. . . . .	67
4.1	Mean line fluxes for the UGC 9215 data cube. . . . .	79
4.2	Constants encoding standard Balmer line ratios for $H\alpha$ , $H\beta$ , $H\gamma$ and $H\delta$ .	85
4.3	Parameters and results for the calculation of dust mass for UGC 9215.	96
4.4	Mean properties of regions of interest within UGC 9215. . . . .	101
A.1	Full observing log for both observing runs with the KOALA IFU. . .	109



# Abstract

We present integral field spectroscopy of a pilot sample of Blue And Dusty Gas-Rich Sources, or BADGRS, discovered in the first dust-selected survey from the *Herschel* ATLAS. These BADGRS make up over 50% of the local volume of H-ATLAS and have puzzlingly paradoxical properties; they are *blue but dusty*, with bright UV emission despite high dust masses; they are *hot but cold*, with lower than average dust temperatures despite bright UV emission; they are *young but old*, with blue colours and high gas fractions, indicating a young population, whilst having high dust masses and being metal rich, indicating an older population; and they are *metal rich but CO poor*, they have low ratios of H<sub>2</sub> mass over dust mass, despite being metal rich in their central regions. We observe this pilot sample of BADGRS with the KOALA integral field unit, and describe in detail the data reduction and calibration process carried out; custom scripts were created and parts of the existing AAO pipeline adapted to carry out the data reduction for KOALA and solve issues found with the data, and create the highest quality data cubes possible.

We investigate the dust attenuation law of one of the pilot BADGRS, UGC 9215, with the *blue but dusty* paradox in mind. We fit the spectra in each spacial bin to extract emission line fluxes. We apply a model using the Balmer emission lines H $\alpha$ , H $\beta$ , H $\gamma$  and H $\delta$ , and their intrinsic line ratios, to constrain the slope,  $\delta$ , of the Salim et al. (2018) modified reddening law. We find a  $\delta$  of -0.25 for UGC 9215, steeper than the starburst attenuation curve of Calzetti et al. (2000), but shallower than similar galaxies in the Salim et al. (2018) sample. A shallow attenuation curve can indicate a more complex, clumpy dust geometry, as well as, in galaxies that are dusty and star forming, the presence of a high fraction of unobscured OB stars and regions where the galaxy has become transparent to UV radiation. These findings may indicate that the *blue but dusty* BADGRS are not paradoxical at all, but have merely been caught in a stage of their evolution where they have clumpy dust, and regions that are transparent to the UV radiation of the young OB stars present.

# CHAPTER 1

## INTRODUCTION

---

---

### 1.1 COSMIC DUST

Approximately half the light emitted by objects in the Universe has been absorbed by cosmic dust, found in galaxies and the interstellar medium (ISM), and re-emitted at far-infrared (FIR) and submillimetre (submm) wavelengths (Dole et al., 2006). Therefore, by studying the Universe in the FIR and submm, we can directly probe the dust content of the objects within it. However, for a long time we were unable to study a large portion of this wavelength range.

On the 26<sup>th</sup> January 1983, the Infrared Astronomical Satellite (IRAS) was launched, and subsequently carried out an unbiased all sky survey at 12, 25, 60 and 100  $\mu\text{m}$  (Neugebauer et al., 1984). The survey covered more than 96% of the sky and led to great advances in the study of extragalactic sources; the survey took the number of sources detected at these wavelengths from a few dozen to 20,000 (Soifer et al., 1987). The launch of both the Infrared Space Observatory (ISO) and the Spitzer Space Telescope followed IRAS; the telescopes operated along similar wavelength ranges to IRAS (2.5 to 240  $\mu\text{m}$  for ISO (Kessler et al., 1996) and 3.6 to 160  $\mu\text{m}$  for Spitzer (Werner et al., 2004)) but boasted larger mirrors and greater resolution and sensitivity.

Surveys have been carried out at the other end of the FIR and submm wavelength range using the Submillimetre Common-User Bolometer Array (SCUBA) camera, which was mounted on the ground-based James Clerk Maxwell Telescope (JCMT). The camera was capable of observing at wavelengths ranging from 350  $\mu\text{m}$  to 2 mm, and was able to observe using two filters simultaneously (Holland et al., 1999). This ability was exploited by both the Canada-UK Deep Submillimetre Survey (Stephen Eales et al., 1999) and the SCUBA Half-Degree Extragalactic Survey

(SHADES) (Mortier et al., 2005) to make observations at 450  $\mu\text{m}$  and 850  $\mu\text{m}$ . However, these surveys only covered very small areas of sky, unlike the all sky survey carried out by IRAS.

The wavelength region between 250  $\mu\text{m}$  and 450  $\mu\text{m}$  remained rather unexplored, with very few observations being made at these wavelengths. This hindered the study of the extragalactic sky. Full wavelength coverage across the electromagnetic spectrum is necessary to accurately determine the properties of the objects in the Universe; with this gap in the spectrum, cold dust properties such as dust temperature and dust mass could not be accurately determined due to a lack of data points in the far infrared Spectral Energy Distribution (SED).

However, with the launch of the *Herschel Space Observatory* (hereafter *Herschel*) on 14<sup>th</sup> May 2009, this gap between surveys in the FIR and submm has begun to be bridged. *Herschel* consisted of a cooled telescope, 3.5 m in diameter, with the ability to observe from 55 to 671  $\mu\text{m}$  (Pilbratt et al., 2010). The telescope had two main cameras on board; the Photodetector Array Camera and Spectrometer (PACS) and the Spectral and Photometric Imaging REceiver (SPIRE). Each instrument was capable of observing across three bands; PACS had bands with central wavelengths of 70, 100 and 160  $\mu\text{m}$ , whilst SPIRE had bands with central wavelengths of 250, 350 and 500  $\mu\text{m}$  (Poglitsch et al., 2010; Griffin et al., 2010). *Herschel* had a better angular resolution than any FIR telescope before it (approximately 18'' at 250  $\mu\text{m}$ , S. Eales et al., 2010), and allowed observations of objects in the Universe to be made at previously unexplored wavelengths.

## 1.2 A SELECTION OF SURVEYS OF LOCAL GALAXIES WITH *Herschel*

### 1.2.1 THE *Herschel* ATLAS

Several surveys were carried out during *Herschel*'s open observing time; one of the largest of these was the *Herschel* Astrophysical Terahertz Large Area Survey (*Herschel* ATLAS or H-ATLAS). The survey was allocated 600 hours of time and covered 510  $\text{deg}^2$  of the sky in 5 photometric bands; PACS 100 and 160  $\mu\text{m}$  and SPIRE 250, 350 and 500  $\mu\text{m}$  (S. Eales et al., 2010). The main goal of the survey was to cover the largest area of the sky possible, so the maximum scan rate of the telescope, 60''  $\text{s}^{-1}$ , was used. Observations were carried out in parallel mode, which allowed observations to be made simultaneously with PACS and SPIRE.

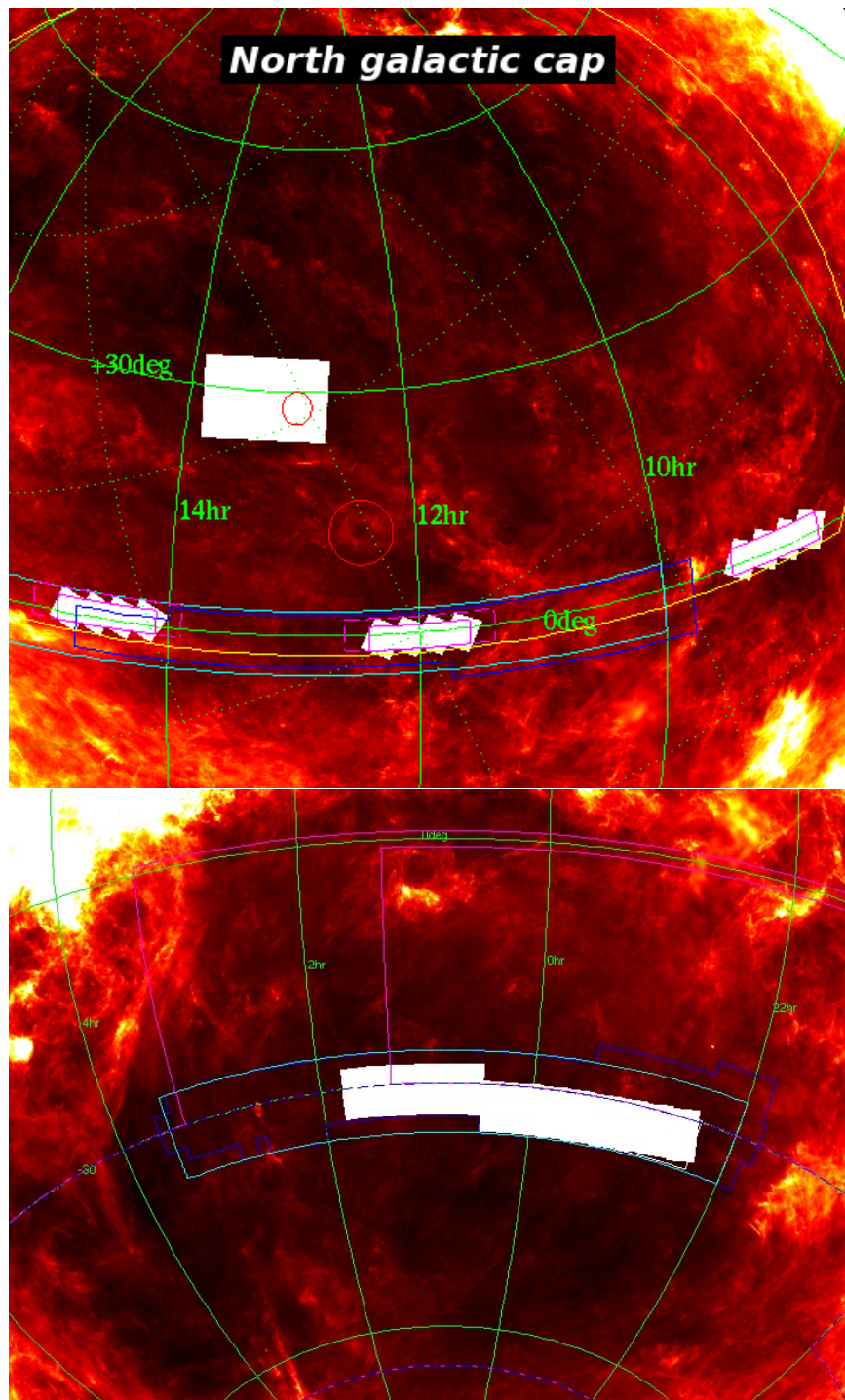


**Figure 1.1.** The positions of the *Herschel* ATLAS fields on the galactic plane in white, shown over the IRAS 100  $\mu\text{m}$  map. These fields include (top) the NGP field and the GAMA fields with the SGP fields shown on the bottom. The green lines show the RA and Dec on the IRAS map, and the other coloured lines show the observing areas of other surveys, the colour codes of which are as follows: cyan — KIDS/VIKING, yellow — SDSS, blue — 2dFGRS, magenta — Dark Energy Survey, magenta/blue dashed — South Pole Telescope. Images obtained from the *Herschel* ATLAS website (<http://www.h-atlas.org/survey/fields>).

The survey was spread across several fields placed near the northern and southern galactic poles (NGP and SGP with areas of 150 and 250 deg<sup>2</sup> respectively) and along the celestial equator (the GAMA fields - named after the fields of the Galaxy and Mass Assembly redshift survey (Driver et al., 2009), each with an area of 36 deg<sup>2</sup>). The positions of these fields, shown in white in Figure 1.1, were chosen to maximise the complementary data available to the survey and minimise the effect of galactic cirrus emission, the infrared emission from dust grains in our own galaxy, highlighted in colour in Figure 1.1.

There is a range of complementary data, as discussed fully in S. Eales et al. (2010), available to support the H-ATLAS observations. This includes: spectroscopic redshift measurements from the GAMA survey, the Sloan Digital Sky Survey (SDSS, Stoughton et al., 2002) and the 2dF Galaxy Redshift Survey (2dFGRS, Colless et al., 2001), optical from the SDSS and the Kilo-Degree Survey (KIDS) with the VLT Survey Telescope (VST), ultraviolet from the Galaxy Evolution Explorer (GALEX, Tuffs, 2008), near infrared from the VISTA Kilo-Degree Infrared Galaxy Survey (VIKING, Edge et al., 2013) and the Large Area Survey (LAS) as part of the UKIRT Infrared Deep Sky Survey (UKIDSS, Lawrence et al., 2007), and radio from a 325 MHz survey with the Giant Metrewave Radio Telescope (GMRT, Mauch et al., 2013).

### 1.2.2 THE HAPLESS SAMPLE AND THE DISCOVERY OF BADGRS

Clark et al. (2015) presented the properties of the first dust-selected sample of nearby galaxies, at distances between 15 and 46 Mpc, using the H-ATLAS Phase-1 data, which covers the area of the three H-ATLAS GAMA fields (GAMA-09, GAMA-12 and GAMA-15). These 42 sources form the H-ATLAS Phase-1 Limited Extent Spatial Survey, or the HAPLESS sample. Photometry in 20 bands was obtained for the sources; these bands are: GALEX FUV and NUV, SDSS *ugri*, VIKING *ZYJHK<sub>S</sub>*, Wide-field Infrared Survey Explorer (WISE) 3.4, 4.6, 12 and 22  $\mu\text{m}$ , PACS 100 and 160  $\mu\text{m}$  and SPIRE 250, 350 and 500  $\mu\text{m}$ . This wide range of photometric data was used to obtain the properties of these galaxies, such as cold dust temperature, dust mass, colour and star formation rate (Clark et al., 2015; De Vis et al., 2017a).

The median cold dust temperature for the HAPLESS sample was found to be 14.6 K, several K colder than galaxies found in other submillimetre surveys (a median  $T_c$  of 18.5 K for the *Herschel* Reference Survey (HRS), and 17.7 K for the *Planck* Early Release Compact Source Catalogue (ERCSC) (Clark et al., 2015)).

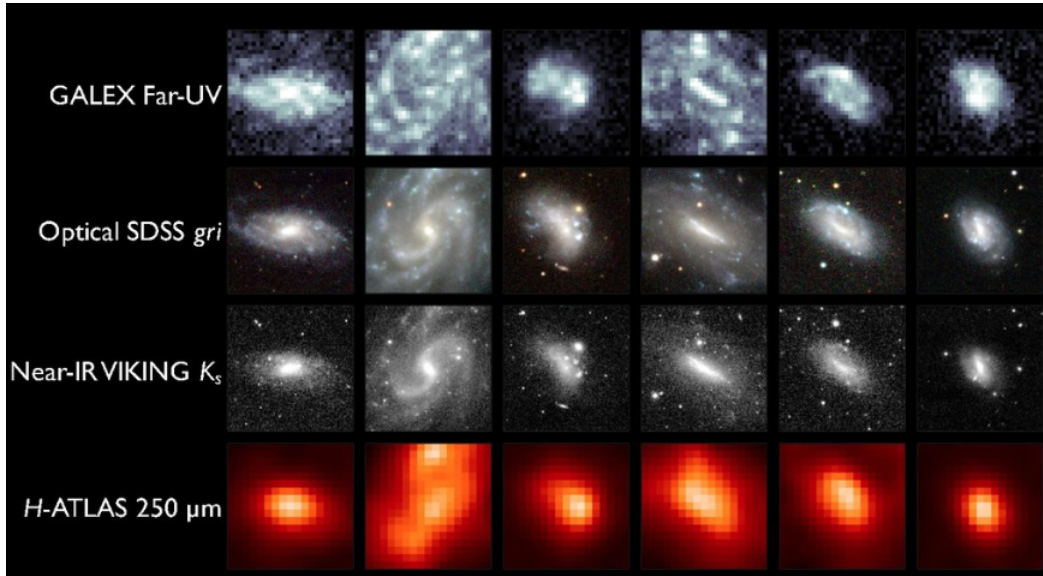


**Figure 1.2.** A subset of BADGRS from Clark et al. (2015) showing the UV, optical, Near-IR and *Herschel* 250  $\mu\text{m}$ . Notice their very blue colours and flocculent nature. Image credit: H-ATLAS/C. Clark.

They were also found to have higher ratios of dust mass to stellar mass; on average the HAPLESS have ratios of dust mass to stellar mass greater by factors of 2-4 compared to the same surveys. They were also found to be very gas rich; this was found to be particularly true for a curious subset of the HAPLESS sample. These galaxies were identified by very blue  $FUV - K_S$  colours of less than 3.5. They were found to be irregular and flocculent in morphology, with a median gas fraction of 66%. Some galaxies in the subset were found to have gas fractions as high as 96%, and at least 74% of the subset are found to have HI masses greater than their stellar mass (Clark et al., 2015; De Vis et al., 2017a). These galaxies are also dust rich whilst having low stellar masses; they account for only 6% of the stellar mass in the local volume, but contain 35% of the dust mass (Clark et al., 2015).

As well as very blue  $FUV - K_S$ , the distribution of  $NUV - r$  colour for the HAPLESS are also bluer than the HRS on average (De Vis et al., 2017a). This quantity is closely related to specific star formation rate (sSFR) and shows that HAPLESS sources are more actively star forming than those in the HRS. To summarize, the HAPLESS sample therefore contains some very blue, gas rich, low surface brightness sources, which are irregular or flocculent and have high sSFRs. These Blue And Dusty Gas-Rich Sources, or BADGRS as they have been nicknamed (Clark et al., 2015), make up more than 50% of the population in the local volume of the H-ATLAS. A visual example of a subset of BADGRs from Clark et al. (2015) is shown in Figure 1.2. We will explore their unusual properties in later sections.

### 1.2.3 RECENT MOLECULAR GAS OBSERVATIONS OF A SAMPLE OF BADGRS

As mentioned in Section 1.2.2, Clark et al. (2015) discovered a sample of galaxies, dubbed BADGRS, using a blind dust selected survey with very curious properties compared to other galaxies in the local Universe. Dunne et al. (2018) carried out the first in-depth study of a pilot sample of these BADGRS. This pilot sample contained four galaxies chosen from the HAPLESS sample of Clark et al. (2015) which were classified as BADGRS: NGC 5584, NGC 5496, UGC 9215 and UGC 9299. Due to the fact that the HAPLESS was made up of local galaxies, these sources often have large angular sizes, making a survey of a larger sample of BADGRS costly to carry out in terms of observing time. These sources were chosen for the pilot sample because, between them, the four sources provide a representative sample of galaxies from the original sample of BADGRS; their properties span the full range of stellar mass, gas fraction, morphology and  $FUV - K_S$  colour. Also, they are bright and well-resolved examples from the parent sample, so made excellent targets for follow up and therefore perfect for an in depth study of these sources.

Dunne et al. (2018) make use of the wide range of photometric data available for these sources, as described in Clark et al. (2015) and De Vis et al. (2017a). They also use optical spectra from the literature of the central regions of the galaxies (from GAMA and SDSS) to derive rough estimates of the metallicities for those regions. The four sample BADGRS were then observed using the IRAM 30-m telescope, to obtain the  $^{12}\text{CO}(1-0)$  and  $^{12}\text{CO}(2-1)$  lines, and the Atacama Pathfinder Experiment (APEX) 12-m telescope to obtain the  $^{12}\text{CO}(3-2)$  line.

For all four of the BADGRS that were observed, the CO luminosities were found to be very low. The average molecular gas density implied by these CO observations over the 2–3 kpc physical scale that these observations probe is found to be 6–10 times lower than the inter-arm regions of M51, a local ‘typical’ galaxy, averaged over a similar sized region. Dunne et al. (2018) also compared the dust content of the BADGRS with the measured CO luminosities, as dust is often used as a tracer of molecular gas content (Scoville et al., 2016; Tacconi et al., 2018; Millard et al., 2021). The mean ratio of  $M_{\text{H}_2}/M_d$  for CO pointing regions is  $\sim 10$  times lower than values seen in local spiral galaxies. *For a given metallicity, the BADGRS show a much lower  $M_{\text{H}_2}/M_d$ .*

### 1.2.4 THE PARADOXICAL PROPERTIES OF BADGRS

In the previous Sections, we saw that these Blue And Dusty Gas-Rich Sources (BADGRS) make up more than 50% of the population in the local volume of the H-ATLAS, with lower average dust temperatures and  $M_{H_2}/M_d$  ratios, and higher dust-to-stellar mass ratios compared to other local galaxies with similar metallicities. This raises a few questions, indeed their properties are puzzlingly paradoxical:

- Blue but dusty: These galaxies were selected for their dust content, but are found to be very blue, with a lot of bright emission in the ultraviolet (UV). Dust plays an important role in the regulation of gas chemistry by shielding molecules from harsh UV radiation that would destroy them. The abundance of UV radiation here suggests the dust may be behaving differently; could this be due to geometry or a different attenuation law?
- Hot but cold: As mentioned before, these galaxies have bright UV radiation, but the majority of their dust is at very cold temperatures of 12 to 16 K. This is unusual not only due to their UV emission, but also because these temperatures are far lower than those usually seen in massive spiral galaxies and low metallicity dwarf galaxies (approximately 23 to 32 K) (Dale et al., 2012; Rémy-Ruyer et al., 2013).
- Young but old: These galaxies are very blue and have very high gas fractions, which implies that they are relatively young. However, they are also reasonably metal rich in their central regions, and also have high amounts of dust emission, suggesting that they have cycled through several generations of stars.
- Metal rich but CO poor: Recent observations of the  $^{12}\text{CO}(1-0)$  transition in these galaxies reveal that they have very little  $\text{H}_2$  with respect to their dust content (Dunne et al., 2018). This is surprising as they do not have low metallicities; the central metallicities from the SDSS indicate metallicities of  $Z \sim 0.8 Z_\odot$  (De Vis et al., 2017b). This could suggest that there is dissociation of CO occurring in these galaxies, and therefore dark molecular gas present that is not being traced by the CO (Wolfire et al., 2010). Another possibility is that these galaxies are in fact deficient of molecular gas, despite having plenty of dust and metals. High radiation fields, metallicity gradients or extreme turbulence could all be possibilities for this lack of CO, or we could just be seeing these galaxies in a state where they lack  $\text{H}_2$  whilst being at the peak of dust production.

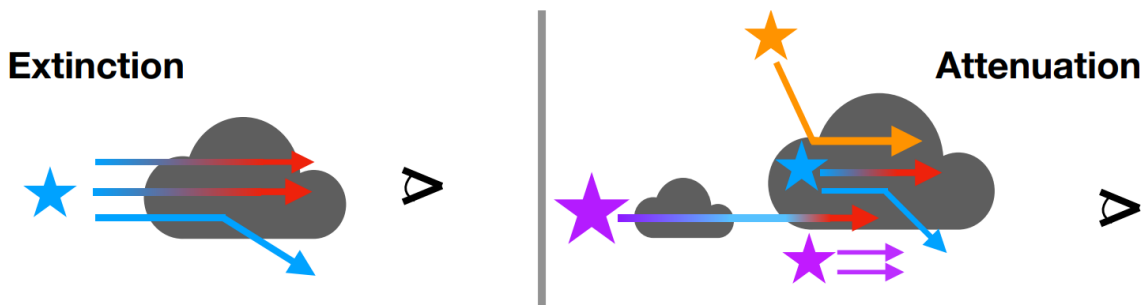


**Figure 1.3.** Schematic showing the difference between extinction and attenuation, created by and obtained from Salim et al. (2020). Extinction describes the simple case where light from a source is interacting with a single dust screen, and absorbing and scattering that light out of the line of sight. Attenuation encapsulates the more complex situation where there may be multiple dust screens, differences in source-dust geometry, scattering of light back into the line of sight, and light from unobscured sources.

In this Thesis, we will investigate these paradoxes, with emphasis on the first item on the list above: is the difference in the BADGRS dust and UV radiation properties due a different attenuation law?

### 1.3 DUST ATTENUATION IN GALAXIES

As mentioned in the previous sections, dust grains, which typically range in size between approximately  $0.01\ \mu\text{m}$  and  $10\ \mu\text{m}$  (Kim et al., 1994b; Kim et al., 1994a), scatter and absorb light, and re-emit it in the IR and sub-mm. This process can be known as both extinction and attenuation, however there are differences between these two definitions. These differences are shown schematically in Figure 1.3, created by Salim et al. (2020). Extinction, shown in the left panel of Figure 1.3, is defined as the case where the light from a single source is interacting with a dust screen, and the light is absorbed and scattered out of the line of sight. Extinction must be measured observationally over a smaller angular scale than that of a galaxy, as a single bright background source is required, for example, stars or quasars (Salim et al., 2020). Attenuation, shown in the right panel of Figure 1.3, adds more complex mechanisms to the definition of extinction. This situation can include multiple dust screens, differences in source-dust geometry, scattering of light back into the line of sight, and light from unobscured sources. This is the situation more likely seen in a galaxy on a wider scale.

### 1.3.1 THE ANATOMY OF AN ATTENUATION CURVE

When we observe a source that has been affected by dust, we can relate the observed and intrinsic flux with the following equation:

$$F_{\text{obs}}(\lambda) = F_{\text{int}}(\lambda)10^{-0.4A(\lambda)}, \quad (1.1)$$

where  $F_{\text{obs}}$  is the observed flux of the source,  $F_{\text{int}}$  is the intrinsic flux of the source, and  $A(\lambda)$  describes the extinction or attenuation caused by the dust between the observer and the source. The components of  $A(\lambda)$  are further given by:

$$A(\lambda) = k(\lambda) \times E(B - V), \quad (1.2)$$

where  $E(B - V)$  is the colour excess, which is a measure of the degree of reddening, and  $k(\lambda)$  is the extinction or attenuation law for the system. Shorter wavelengths of light are extinguished or attenuated more strongly than longer wavelengths of light; this wavelength dependence, and therefore the shape of the curve, is encoded within  $k(\lambda)$ .

The shape of an extinction/attenuation curve can be broken down into five different parts (Salim et al., 2020):

- The overall UV-optical slope,  $S$ , which is defined as the ratio of the extinction at 1500 Å,  $A_{1500}$ , to the extinction in the V-band,  $A_V$ .
- The strength of the UV bump feature,  $B$ , which is defined as the ratio of extra extinction due to the bump,  $A_{\text{bump}}$ , to the baseline extinction at 2175 Å,  $A_{2175}$ .
- The UV slope, which is defined as the ratio of the extinction at 1500 Å,  $A_{1500}$ , to the extinction at 3000 Å,  $A_{3000}$ .
- The optical slope, which is defined as the ratio of the extinction in the B-band,  $A_B$ , to the extinction in the V-band,  $A_V$ .
- The near-IR slope, which is a power-law of  $\lambda^{-\beta_{\text{NIR}}}$ , where  $\beta_{\text{NIR}}$  is the slope that best describes the curve between approximately 0.9 μm and 2 to 5 μm.

This is shown graphically in Figure 1.4. In general, an extinction/attenuation curve will have a steeper slope in the UV-optical, which will then flatten out towards the red end of the optical and the near-IR, however, how steep or shallow the slope is will vary depending on the source.

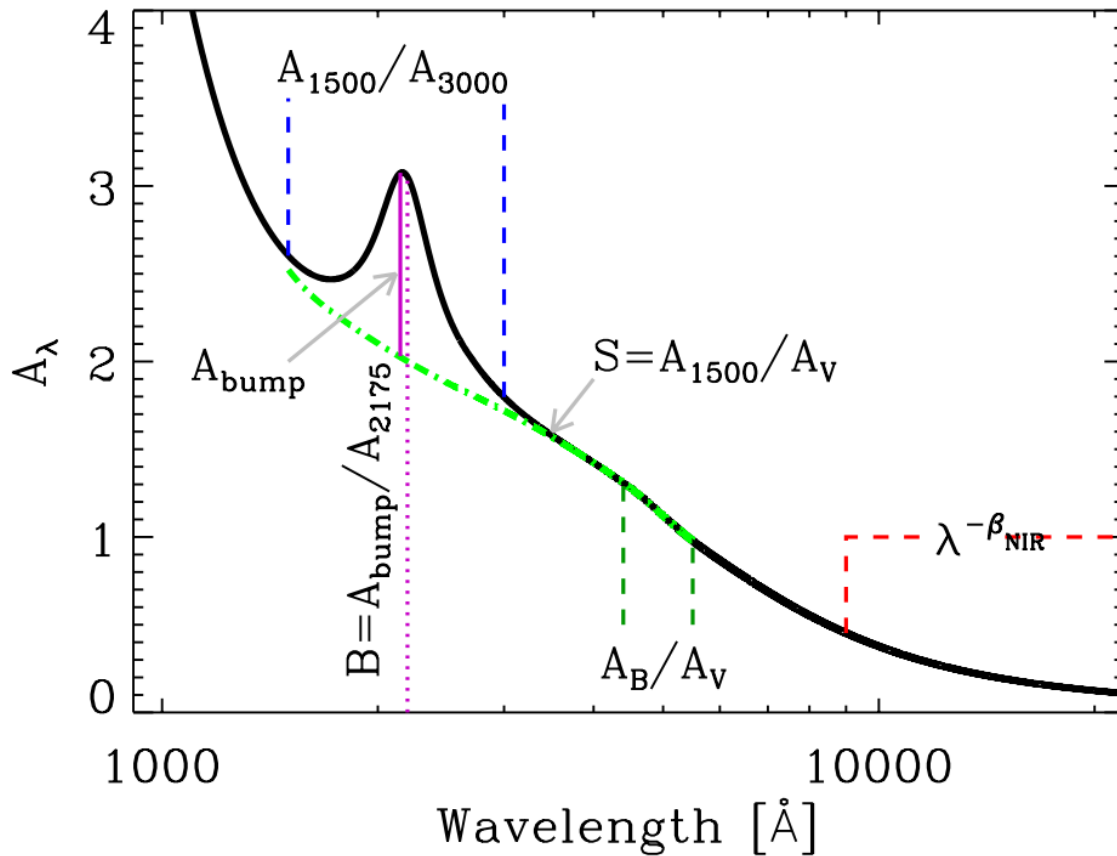


**Figure 1.4.** A schematic showing the different parts of an extinction/attenuation curve, created by and obtained from Salim et al. (2020). The overall curve is shown in the solid black line, the region where the UV slope is measured is shown by the vertical dashed blue lines, the region where the optical slope is measured is shown by the vertical dashed green lines, the overall UV-optical slope is shown in the dot-dashed green line, the UV bump strength is shown by the vertical solid purple line, and the near-IR slope is shown by the region enclosed with the red dashed line.

### 1.3.2 WHAT PROCESSES CAN INFLUENCE THE SLOPE OF THE ATTENUATION CURVE?

The general shape of an extinction or attenuation curve is well defined, but how do the physical processes happening in galaxies affect this shape? Theoretical modelling has been employed, along with observations, to try and explain the physical mechanisms at play, and how they can change the slope of the attenuation curves of galaxies. A few of these mechanisms are discussed below.

#### Birthclouds

Charlot et al. (2000) introduced a two component dust model that considered both a diffuse dust component, which the light from all stars is subject to attenuation from, and an additional component coming from dust within stellar birthclouds, which only stars below a certain age threshold are affected by. This was motivated by the discovery that attenuation towards nebular lines in galaxies was higher than that of the stellar continuum (Fanelli et al., 1988). This model was able to replicate the constraints set by the observed nebular line strengths. The Charlot et al. (2000) model produces an attenuation curve that evolves over time and steepens when there has been a large burst of star formation activity; *the presence of young luminous stars in birthclouds will result in more attenuation overall, and steepen the attenuation curve.*

#### Geometry

Many theoretical models agree on the effect geometry has on dust attenuation curves (Salim et al., 2020): *simple geometries result in steeper attenuation curves, whereas more complex, clumpy dust geometries result in shallower attenuation curves.* The effect of geometry on the attenuation curve was first demonstrated by Witt et al. (1996), Gordon et al. (1997), and Witt et al. (2000), using analytic model geometries. Further evidence of this effect has been found using analytic models, for example, those of Ferrara et al. (1999), Inoue (2005), and Wild et al. (2011), and hydrodynamic and semi-hydrodynamic simulations, such as those of Natale et al. (2015), Seon et al. (2016), and Trayford et al. (2020). Physically, this means that more complex star-dust geometries, such as clumpy dust, within galaxies allow UV photons from massive stars more opportunity to escape, as there is a lack of homogeneous dust screen for the photons to interact with. As a result, the optical depths at shorter wavelengths is smaller, and the attenuation curve is flattened.

## Dust Content

The total dust column density is known to have an important contribution to the attenuation curve of a galaxy. Observations by Salim et al. (2018) found that larger optical depths  $A_V$  result in shallower attenuation curves. Theoretical studies by Witt et al. (2000) and Inoue (2005) have predicted the same result. A large study into several different works on theoretical attenuation laws was performed by Chevallard et al. (2013), who found that all four of the works studied predicted the same result; *a relationship between the optical depth  $A_V$  and attenuation law slope*. More recent work by Narayanan et al. (2018) derived the same relationship using hydrodynamic cosmological zoom simulations. Chevallard et al. (2013) and Narayanan et al. (2018) suggested a physical reason for the observed and theorised relation between optical depth and attenuation curve slope:

- In the high optical depth limit, this corresponds to high amounts of dust on the galactic scale. This means that there is more star formation, and therefore a large amount of both obscured and unobscured OB stars. There is a high fraction of unobscured young stars compared to unobscured evolved stars, and therefore a lot of UV light is escaping from transparent regions. This leads to a flattening of the attenuation curve.
- In the low optical depth limit, this corresponds to lower amounts of dust on the galactic scale. This means there is less star formation, and the fraction of unobscured evolved stars is now higher than unobscured young stars, because a lot of those young stars have now evolved and died. Therefore, there is less unobscured UV light to flatten the attenuation curve, as with the high optical depth limit. This leads to a steeper attenuation curve.

### 1.3.3 OBSERVATIONS OF EXTINCTION AND ATTENUATION IN THE LOCAL UNIVERSE

The Milky Way (MW), the Large Magellanic Cloud (LMC) and the Small Magellanic Cloud (SMC) are the only galaxies to have extensively studied extinction curves (Pei, 1992). The extinction curves have been measured, and have been found to vary, along many lines of sight within these galaxies (E. L. Fitzpatrick et al., 1988; E. Fitzpatrick, 1989); a good example of this is the notable difference between the average LMC extinction curve, and the extinction curve of the 30 Doradus star-forming region within the LMC, which has a steeper UV-optical slope and a less

prominent UV bump (E. Fitzpatrick, 1989). These extinction curves have also been found to vary drastically between the galaxies; the functional forms of the MW, LMC and SMC extinction curves from Cardelli et al. (1989) and Pei (1992) were parameterised by E. L. Fitzpatrick (1999) and are shown in Figure 1.5 in light blue, pink and red respectively. The UV-optical slope of these curves varies between each galaxy, and only the MW and LMC possess the UV bump feature seen at  $2175 \text{ \AA}$ , with differing strengths. Due to these differences, these curves cannot be extended to extinction and attenuation curves in general (Salim et al., 2020).

For attenuation laws of galaxies outside of the local group, one of the most commonly used is that of Calzetti et al. (2000). A relative attenuation law was empirically derived from a sample of starbursting and blue compact dwarf galaxies at  $z \lesssim 0.05$  by Calzetti et al. (1994), using UV and optical spectra. This law was then anchored using IR measurements and energy balance to create the Calzetti et al. (2000) attenuation law. The functional form of the Calzetti attenuation law,  $k_{\text{Cal}}(\lambda)$ , is given by the following equation:

$$\begin{aligned} k_{\text{Cal}}(\lambda) &= 2.659(-1.857 + 1.040/\lambda) + R_{V,\text{Cal}} & 0.63 \mu\text{m} \leq \lambda \leq 2.20 \mu\text{m} \\ &= 2.659(-2.156 + 1.509/\lambda - 0.198/\lambda^2 + 0.011/\lambda^3 + R_{V,\text{Cal}} & (1.3) \\ & & 0.12 \mu\text{m} \leq \lambda < 0.63 \mu\text{m} \end{aligned}$$

where  $\lambda$  is the wavelength and  $R_{V,\text{Cal}}$  is the effective obscuration at V, which was measured to be  $R_{V,\text{Cal}} = 4.05 \pm 0.80$  by Calzetti et al. (2000). This curve is shown alongside the MW, LMC and SMC extinction curves in Figure 1.5 in dark blue. Like the SMC curve, there is no sign of a UV bump at  $2175 \text{ \AA}$ , however the UV-optical slope is quite shallow in comparison.

Whilst the Calzetti et al. (2000) attenuation curve is commonly used as an option to model the dust attenuation within spectral and SED fitting methods, Noll et al. (2009) developed a parameterisation of the Calzetti et al. (2000) curve which gave it a variable slope,  $\delta$ , and a UV bump using a Drude profile. The parameterisation is fully described in Salim et al. (2018), and the functional form of this parameterised attenuation law is shown below:

$$k_{\text{mod}}(\lambda) = k_{\text{Cal}}(\lambda) \frac{R_{V,\text{mod}}}{R_{V,\text{Cal}}} \left( \frac{\lambda}{5500 \text{ \AA}} \right)^\delta + D_B(\lambda), \quad (1.4)$$

where  $\delta$  is the modified slope of the Calzetti reddening law,  $k_{\text{Cal}}(\lambda)$  is the Calzetti reddening law, as shown in Equation 1.3,  $D_B(\lambda)$  is the Drude profile describing the UV bump, and  $R_{V,\text{mod}}$  and  $R_{V,\text{Cal}}$  are the ratios of total to selective extinction for the

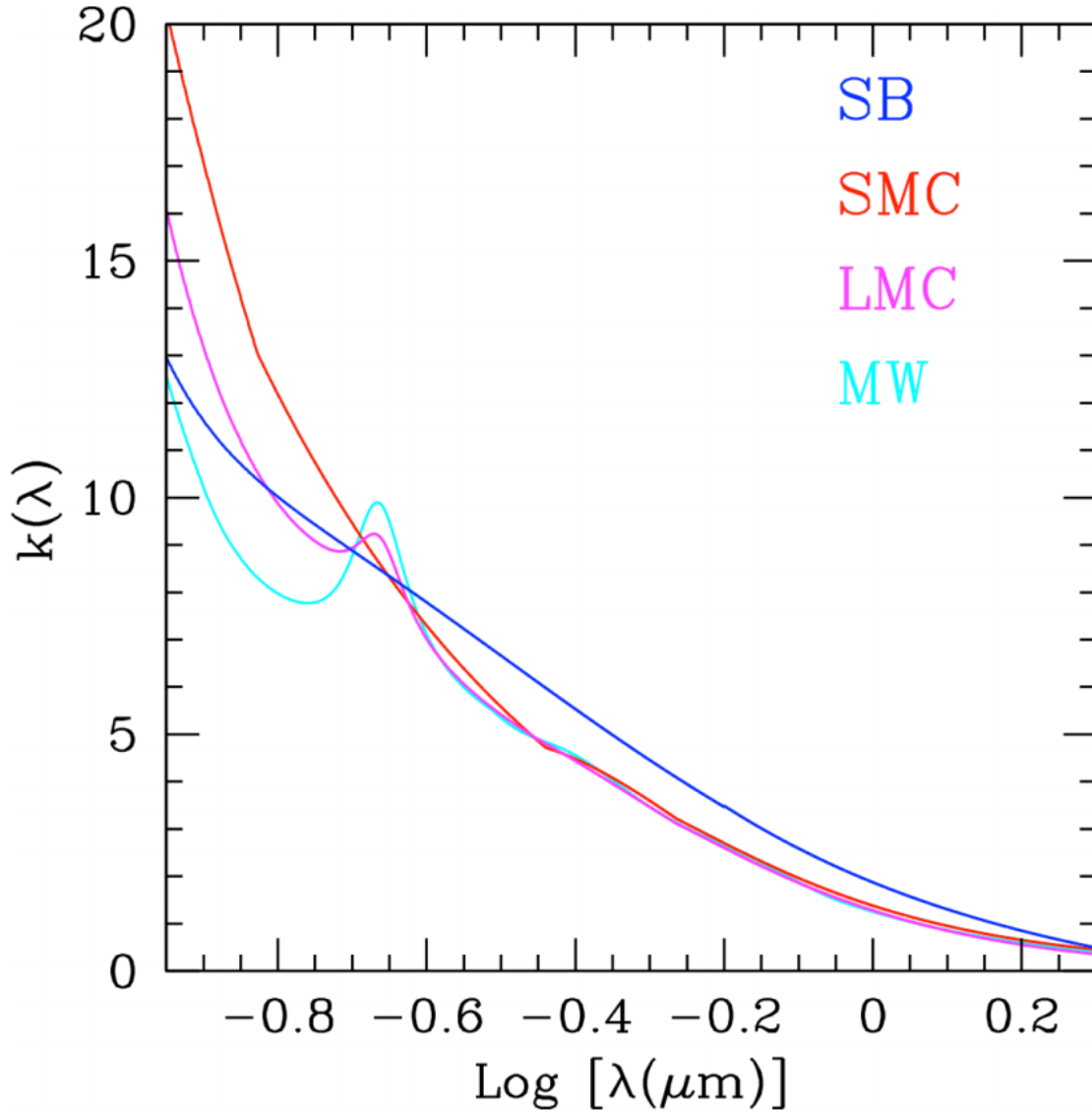


**Figure 1.5.** Extinction curves for the Milky Way (MW, light blue curve), Large Magellanic Cloud (LMC, pink curve), Small Magellanic Cloud (SMC, red curve), and the starburst attenuation curve of Calzetti et al. (2000) (SB, dark blue curve), shown over the wavelength range of approximately  $1000 \text{ \AA}$  to  $20\,000 \text{ \AA}$ . The functional forms of the curves for the MW, LMC and SMC are from Cardelli et al. (1989) and Pei (1992), and were parameterised by E. L. Fitzpatrick (1999). The UV bump feature at  $2175 \text{ \AA}$  is visible in the curves of the MW and LMC. This figure was created by and obtained from Calzetti et al. (2021).

Salim and Calzetti laws respectively. The quantity  $R_{V,\text{mod}}$  is dependent on  $\delta$  and is given by:

$$R_{V,\text{mod}} = \frac{R_{V,\text{Cal}}}{(R_{V,\text{Cal}} + 1)(4400/5500)^\delta - R_{V,\text{Cal}}}. \quad (1.5)$$

The functional form of the Drude profile used for the UV bump is given by:

$$D_B(\lambda) = \frac{B\lambda^2W^2}{[\lambda^2 - \lambda_0^2]^2 + \lambda^2W^2}, \quad (1.6)$$

where  $B$  is the amplitude of the bump,  $\lambda_0$  is the central wavelength of the bump (which would be fixed to  $2175 \text{ \AA}$ ), and  $W^2$  is the width of the bump. An example of how this modified attenuation curve changes for different values of  $\delta$  is shown in Figure 1.6 (for simplicity, we set the Drude profile to zero so as not to include a UV bump here). A  $\delta$  value of 0 means the modified law is equivalent to the Calzetti law, a negative value of  $\delta$  leads to a steeper UV-optical slope, and a positive value of  $\delta$  leads to a shallower UV-optical slope. The maximum  $\delta$  can reach whilst still making physical sense is approximately 0.7, as for values above this the attenuation curve turns over at small wavelengths, and will cause the light to become more blue, rather than becoming reddened.

Salim et al. (2018) determine the slope  $\delta$  for a sample of over 200,000 galaxies with an average redshift of 0.1 using the SED fitting code CIGALE (Noll et al., 2009). They find for this sample that  $\delta$  varies between approximately -0.9 and 0. The most massive star-forming galaxies in the sample tend to have values of  $\delta$  close to 0, whilst less massive star-forming galaxies and quiescent galaxies tend to have significantly steeper attenuation curves, up to values of  $\delta$  of -0.9. Salim et al. (2018) find that two main trends for attenuation curve slope arise from this work; one is that higher mass tends to lead to a shallower curve slope. The other is that galaxies which deviate from the galaxy main sequence tend to have steeper attenuation curve slopes; for example, a galaxy with a higher star formation rate for its mass (i.e. a starburst galaxy) will have a steeper slope than a galaxy that sits more in line with the galaxy main sequence. We will apply this parameterised attenuation law later in this Thesis, in Chapter 4, to investigate the value of  $\delta$  for galaxies classified as BADGRS, using data obtained for them through integral field spectroscopy.

## 1.4 INTEGRAL FIELD SPECTROSCOPY

Currently, there is a wealth of spectroscopic data available for galaxies at varying distances and redshifts. Initially, however, large surveys of galaxies were

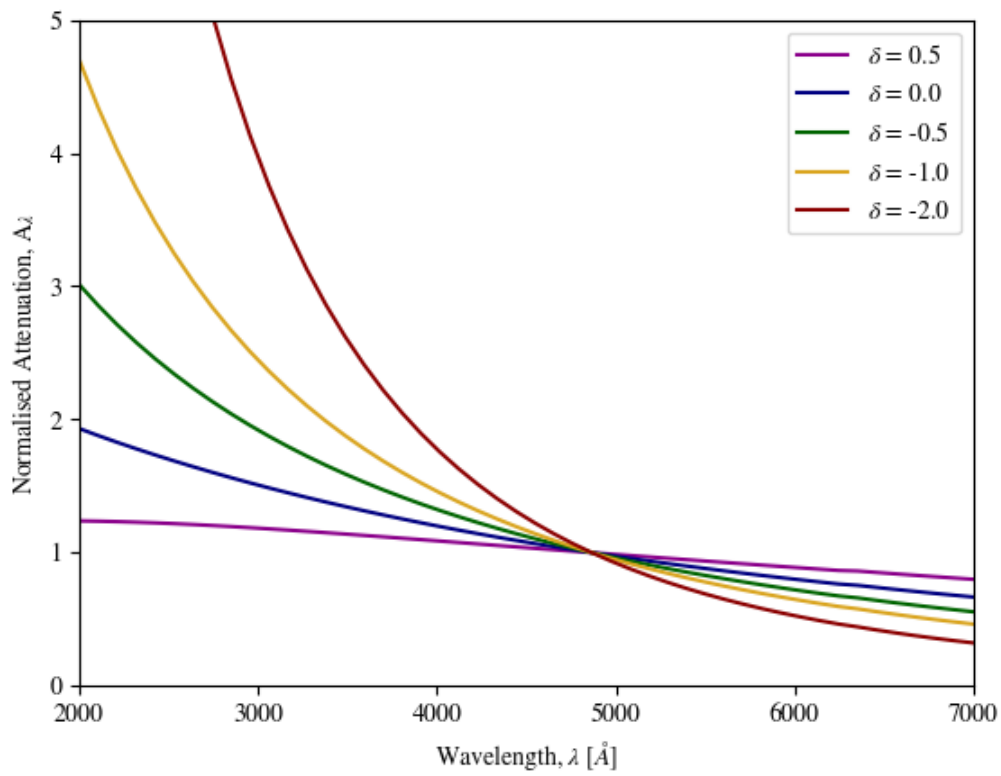


**Figure 1.6.** Attenuation curves created using the modified Calzetti law of Salim et al. (2018). The different curves show how the slope changes for different values of  $\delta$ , varying between -2.0 and 0.5.

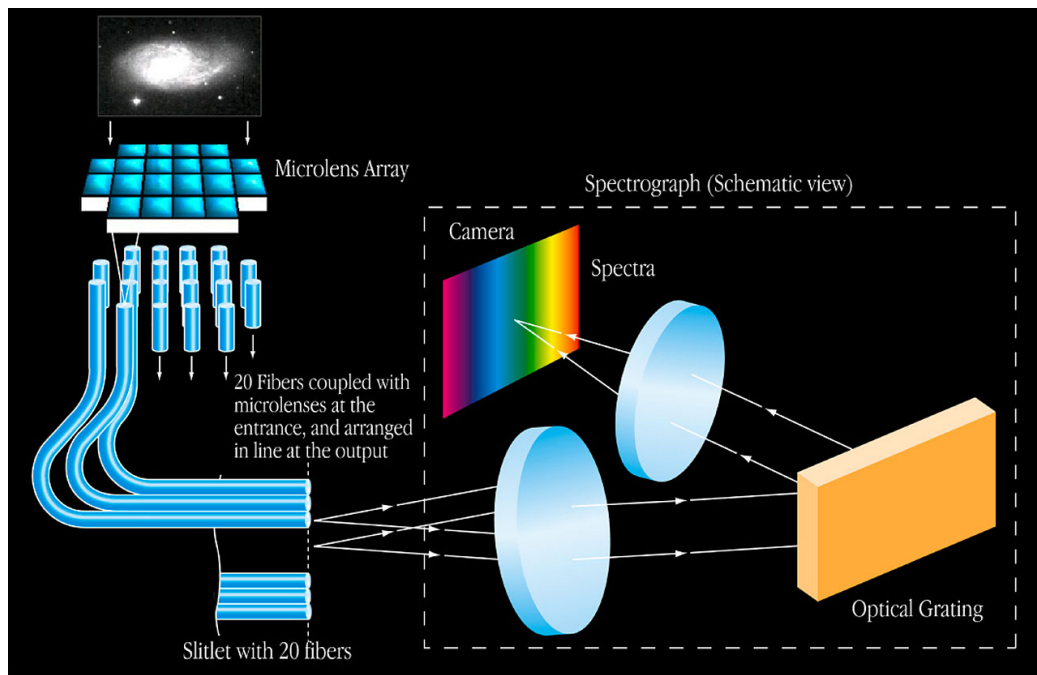


**Figure 1.7.** Diagram of the workings of an integral field spectrograph that consists of a fibre-lenslet IFU and spectrograph. Image created by the ESO and obtained from <https://www.eso.org/public/unitedkingdom/teles-instr/technology/ifu/>.

not possible due to being limited to observing the spectrum of one galaxy at a time using a single slit spectrograph. With the development of fibre-optic spectrographs and multi-slit spectrographs, large surveys of galaxy spectra became possible, resulting in redshift surveys such as the 2dF Galaxy Redshift Survey (Colless et al., 2001), the Sloan Digital Sky Survey (Stoughton et al., 2002) and the Galaxy And Mass Assembly survey (Driver et al., 2009). The 2dF Galaxy Redshift Survey (2dFGRS) alone measured reliable spectra for over 221,000 galaxies by the time the project had ended (Colless et al., 2003). The Sloan Digital Sky Survey (SDSS) has since overtaken that value, with over 4 million galactic and extragalactic spectra having been observed as of SDSS Data Release 15 (*Optical Spectra Overview — SDSS 2020*). Whilst this represents a huge resource of data for galaxies, these spectra are usually taken in the central regions of the galaxy. Therefore, they can be used to gain an idea of the overall properties of the galaxy in question, but cannot be used to study the galaxy in detail, or any changes in these properties outside of these central regions unless multiple pointings were completed on the galaxy. A solution where spatially resolved information was required came about in the form of integral field spectroscopy.

An integral field spectrograph, or IFS, allows you to obtain spectra for a two-dimensional area of sky. The main components required for an IFS are a spectrograph and an integral field unit, or IFU. There are several different forms of

IFU that can be used in conjunction with a spectrograph, however for the purposes of this Thesis, we will focus on fibre-lenslet IFUs. A diagram of the workings of a fibre-lenslet IFU is shown in Figure 1.7. In this set-up, a microlens array collects light from the object of interest being observed. Each microlens is coupled with a fibre; these fibres are lined up at the entrance to the spectrograph so that the light from the object can be passed into it. The light is then passed through a collimator before it reaches the grating, which splits it into a spectrum. This spectrum is then refocused onto a camera. Once the raw data obtained from this process is reduced and calibrated, the final output is a data cube, with the  $x$  and  $y$  axes showing the position on the sky, and the  $z$  axis showing wavelength.

In the last decade, many integral field spectrographs have been commissioned to obtain spatially resolved spectra of galaxies, and to begin building up the number statistics for this type of data. One of the largest IFS surveys using a single IFU was the Calar Alto Legacy Integral Field Area, or CALIFA, survey, which used the PMAS and PPAk instruments on the 3.5 m Calar Alto Observatory (CAHA) telescope (Sánchez et al., 2012). This legacy survey observed approximately 600 galaxies of varying types within the local universe ( $0.005 < z < 0.03$ ), which were chosen such that their full spatial extent was covered by the  $>1$  arcmin<sup>2</sup> field of view of the PPAk IFU. CALIFA was designed to begin bridging the gap between large surveys like the SDSS, and detailed studies of individual sources.

Larger IFS surveys include the Sydney-AAO Multi-object Integral field spectrograph (SAMi) galaxy survey and the Mapping Nearby Galaxies at Apache Point Observatory (MaNGA) survey. The SAMi galaxy survey observed approximately 3400 galaxies at  $z < 0.12$  using 13 IFUs, which could be used simultaneously, on the 3.9 m Anglo-Australian Telescope (AAT) (Allen et al., 2015). These IFUs had an approximately 15'' diameter, and, like CALIFA, were used to observe the entire extent of the galaxies that were surveyed; mass and redshift limits were imposed during target selection such that galaxies were small enough to fit within the FOV of the IFUs, and large enough to be resolved by several fibres. The MaNGA survey was a far larger undertaking, observing a sample of 10000 galaxies over a 6 year period (Law et al., 2015). MaNGA had a collection of 17 hexagonal IFUs in a range of sizes, from 12.5'' to 32.5'' in diameter. The galaxies observed were selected to have a stellar mass  $> 10^9 M_{\odot}$ , and covered a range in redshifts from 0.01 to 0.15, with the average redshift of the primary sample being 0.03 (Bundy et al., 2015).

An instrument tailored more for deep imaging and detailed observations of specific targets is the Multi Unit Spectroscopic Explorer, or MUSE (Roland Bacon et al., 2006). With a 1 arcmin<sup>2</sup> field of view, like that of CALIFA, what really sets

this instrument apart is its high spatial resolution of  $0.65''$ , which can be improved even further to  $0.46''$  through the use of adaptive optics. The potential for observing a wide variety of source types was explored during the commissioning of MUSE, with observations of planets and star clusters (R. Bacon et al., 2014), to an observation of a region in the Hubble Deep Field South (Roland Bacon et al., 2017).

The main spatial and spectral properties of the above mentioned integral field spectrographs are summarised in Table 1.1. The CALIFA, MaNGA and SAMI surveys all possess similar wavelength coverage, though MaNGA extends further into the near-IR than CALIFA and SAMI. This allows them to observe important spectral lines for low redshift objects, from the OII doublet at  $3727 \text{ \AA}$  down to the SII doublet at  $6717 \text{ \AA}$  and  $6731 \text{ \AA}$ . Of the three surveys, SAMI possesses the best spatial and spectral resolution, but also has the smallest field of view, and therefore would not be able to efficiently observe large nearby sources. MUSE has an excellent field of view and high spatial resolution, which make it well equipped to observe objects with high angular size. However, the wavelength coverage does not extend as far into the blue end of the optical as CALIFA, MaNGA and SAMI, and would therefore miss some spectral lines for very local sources; a galaxy would need to be at  $z > 0.22$  for MUSE to observe the OII doublet. For observations of extended very local sources, an instrument with a larger field of view and good spatial resolution, such as that of MUSE, which also possesses similar wavelength coverage to CALIFA and SAMI, is required. The KOALA IFU fills this gap.

**Table 1.1.** Spatial and spectral properties of various integral field spectrographs. The information quoted below for the MUSE instrument was obtained from Roland Bacon et al. (2006). The spatial resolution and FOV correspond to the wide field of view. The values of spatial resolution are achieved when the instrument is used with and without adaptive optics, respectively. The MUSE instrument is an image slicer IFU, and therefore has image slicer modules instead of fibres and lenslets. The information quoted for the CALIFA survey, which uses the PMAS/PPak instruments, was obtained from Kelz et al. (2006) and Sánchez et al. (2012). The information for the MaNGA survey was obtained from Law et al. (2015). The FOV and number of elements are quoted for the largest IFU available. The information below for the SAMI galaxy survey was obtained from Croom et al. (2012) and Allen et al. (2015). The information for the KOALA IFU was obtained from the KOALA-AAOmega Manual, by Andy Green and Ángel López-Sánchez, [https://aat.anu.edu.au/files/KOALA-AAOmega-obs-manual\\_1.pdf](https://aat.anu.edu.au/files/KOALA-AAOmega-obs-manual_1.pdf). The spatial resolution and FOV quoted are for the wide field mode of KOALA. The wavelength coverage and spectral resolution correspond to a set-up using the 580V and 1000R gratings within the AAOmega spectrograph.

	<b>MUSE</b>	<b>CALIFA</b>	<b>MaNGA</b>	<b>SAMI</b>	<b>KOALA</b>
<b>Spatial resolution</b>	0.46 to 0.65''	2.68''	2.0''	1.6''	1.25''
<b>Field of view (FOV)</b>	60'' × 60''	74'' × 64''	32.5'' diameter	14.9'' diameter	27.4'' × 50.6''
<b>Number of elements</b>	24 modules	331 fibres	127 fibres	61 fibres	1000 fibres
<b>FOV arrangement</b>	Square	Hexagonal	Hexagonal	Circular	Rectangular
<b>Wavelength coverage</b>	4560 to 9300 Å	3700 to 7000 Å	3600 to 10 300 Å	3700 to 7000 Å	3700 to 8000 Å
<b>Spectral resolution</b>	2000 to 4000	850 to 1650	1400 to 2200	1700 to 4500	1300 to 3400

### 1.4.1 KOALA

The Kilofibre Optical AAT Lenslet Array, or KOALA instrument, is a fibre-lenslet IFU. It is designed for use alongside the AAOmega spectrograph, mounted on the Anglo-Australian Telescope (AAT) operated by the Australian Astronomical Observatory (AAO), and located at Siding Springs Observatory, Australia<sup>1</sup>. KOALA has 1000 hexagonal lenslets, arranged in a  $40 \times 25$  array. It has two possible fields of view; a narrow field of view of  $15.3'' \times 28.3''$  with  $0.7''$  sampling, and a wide field of view of  $27.4'' \times 50.6''$  with  $1.25''$  sampling. The array set-up is shown in Figure 1.8. AAOmega is a dual beam spectrograph. The fibres from KOALA are fed into a pseudo-slit, and the light from the fibres is then collimated and split along the blue and red arms of the spectrograph, where the data is read out by the blue and red CCDs. The setup is shown in Figure 1.9. The wavelength coverage and resolution of KOALA is selectable, thanks to it being used alongside AAOmega, with a number of gratings available at low, medium and high resolutions, across a wavelength range covering 3300 to 10 000 Å. The properties of the KOALA IFU are summarised in Table 1.2.

When using its wide field mode, the KOALA instrument is well equipped to observe highly resolved nearby galaxies. The field of view in this mode is approximately half the size of that of the MUSE instrument, with superior spatial resolution than CALIFA, MaNGA and SAMI (see Table 1.1). Using the adaptable gratings of the AAOmega spectrograph, the wavelength coverage of CALIFA and SAMI can be mimicked, with similar spectral resolution. In this Thesis, we will use KOALA to observe a sample of local galaxies, and show what can be achieved with the data from this instrument.

## 1.5 WHAT CAN WE DO WITH KOALA DATA?

With optical IFS data, we can obtain information that will help shed some light on the unusual properties of the BADGRS, such as:

- Resolved gas phase metallicities: this is a very important measurement required to understand why there is so little CO in these galaxies with respect to their dust content (Dunne et al., 2018). The central metallicities of these galaxies are not low (Table 2.2), but previous metallicity values only sampled the central regions of the galaxy, not taking into account what is happening in the outer disk regions. With KOALA, spatially resolved metallicity measurements will

---

<sup>1</sup>[https://aat.anu.edu.au/files/KOALA-AAOmega-obs-manual\\_1.pdf](https://aat.anu.edu.au/files/KOALA-AAOmega-obs-manual_1.pdf)

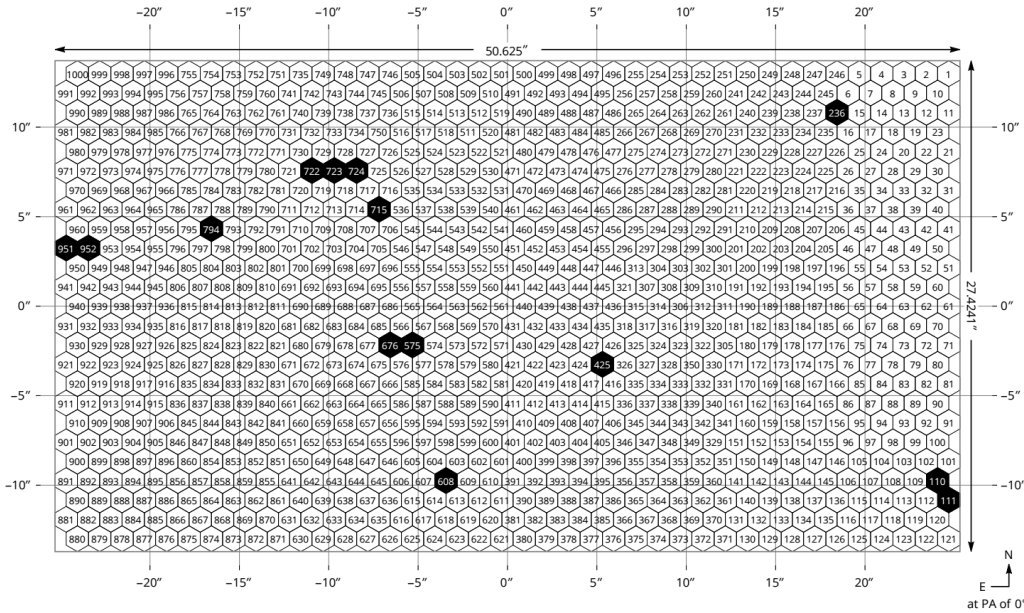


**Figure 1.8.** The lenslets of KOALA are arranged in a  $40 \times 25$  fibre field of view. The dimensions shown here correspond to the wide field of view, with  $1.25''$  sampling. The black lenslets correspond to the positions of dead fibres. (Figure obtained from KOALA-AAOmega Manual, by Andy Green and Ángel López-Sánchez, [https://aat.anu.edu.au/files/KOALA-AAOmega-obs-manual\\_1.pdf](https://aat.anu.edu.au/files/KOALA-AAOmega-obs-manual_1.pdf).)

**Table 1.2.** Spatial and spectral properties of the KOALA IFU when used with the AAOmega spectrograph. The values quoted below were obtained from the KOALA-AAOmega Manual, by Andy Green and Ángel López-Sánchez, [https://aat.anu.edu.au/files/KOALA-AAOmega-obs-manual\\_1.pdf](https://aat.anu.edu.au/files/KOALA-AAOmega-obs-manual_1.pdf). The spatial resolution and FOV are quoted for both the narrow and wide field modes of KOALA, respectively. The total wavelength coverage and spectral resolutions quoted are the full range possible with the variety of different gratings available for AAOmega.

<b>KOALA</b>	
<b>Spatial resolution</b>	$0.7''$ or $1.25''$
<b>Field of view (FOV)</b>	$15.3'' \times 28.3''$ (433 sq. arcsec) or $27.4'' \times 50.6''$ (1386 sq. arcsec)
<b>Number of elements</b>	1000 fibres
<b>FOV arrangement</b>	Rectangular, $40 \times 25$ fibres
<b>AAOmega</b>	
<b>Total wavelength coverage</b>	3300 to 10 000 Å
<b>Spectral resolution</b>	1000 to 10 000

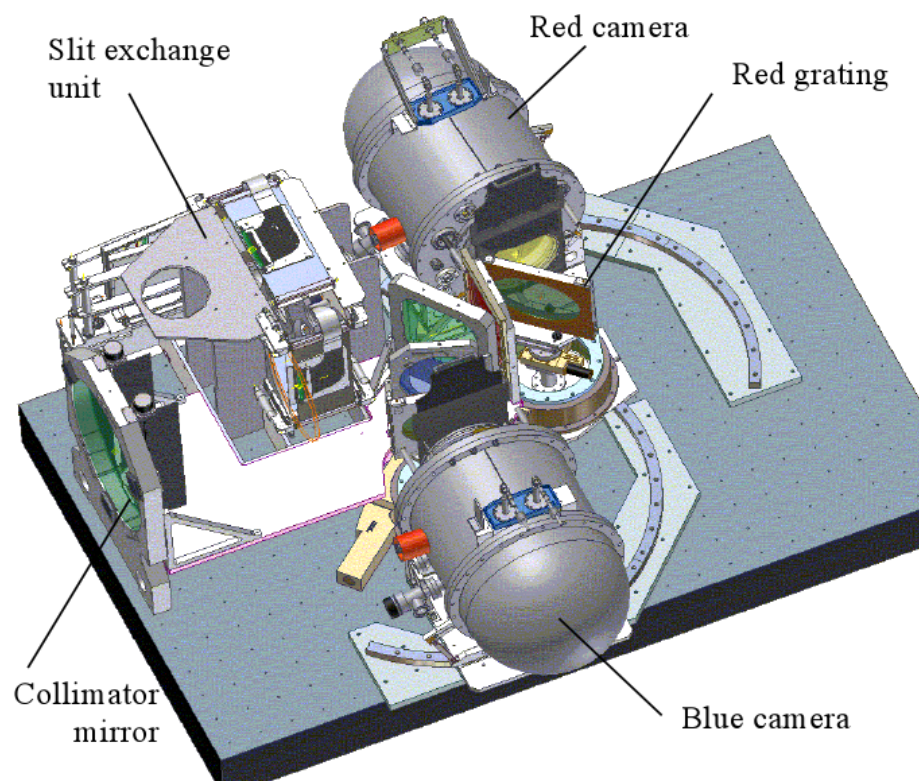


**Figure 1.9.** Diagram of the AAOmega spectrograph set-up. The light from the fibres, which are fed into a pseudo-slit, is passed through the collimator mirror, and then split and sent into both the red and blue cameras of the spectrograph. (Figure obtained from KOALA-AAOmega Manual, by Andy Green and Ángel López-Sánchez, [https://aat.anu.edu.au/files/KOALA-AAOmega-obs-manual\\_1.pdf](https://aat.anu.edu.au/files/KOALA-AAOmega-obs-manual_1.pdf).)

be possible for the disk regions. With these resolved metallicity measurements, one could refine the  $X_{CO}$  (Wolfire et al., 2010) factor used to relate the CO emission to the amount of  $H_2$  in these galaxies, as it is dependent on metallicity (Leroy et al., 2011; Bolatto et al., 2013; Papadopoulos et al., 2012; Glover et al., 2011).

- Spatially resolved dust attenuation: Using the Balmer emission lines and the shape of the continuum, one can gain valuable information about the attenuation in these galaxies. Having spatially resolved dust attenuation will allow us to learn more about the grain properties and relative geometry of the dust in these galaxies.
- Properties of the ionised gas phase: By studying the strong emission lines in these galaxies, we can discover the properties of the gas (Ho et al., 2014; Kewley et al., 2013), such as the excitation mechanism and the electron temperature. From this, we can gain information about the local radiation fields in these galaxies; these fields determine the dust temperature and photo-dissociation conditions in the molecular gas. We can use the information gained on these localised radiation fields to compare with the dust and cold gas measurements that we already have, and help shed light on the lack of CO emission in these galaxies.
- Spatially resolved star formation histories: We can obtain information about the age of the young stellar population using the region around the 4000 Å break and the  $H\delta$  line. This will allow us to age different regions of the stellar disk and correlate this with localised conditions in the ISM. We can also use measurements of the  $H\alpha$  line, corrected for dust attenuation using the Balmer decrement, along with stellar mass maps to get an accurate picture of the specific star formation rate in the different regions of these galaxies. This information can be used alongside dust and chemical evolution modelling (Clark et al., 2015; Rys' et al., 2013; De Vis et al., 2017a; De Vis et al., 2017b) to investigate how these galaxies have created so much dust so quickly.

## 1.6 THESIS OUTLINE

This Thesis will focus on the development of a data reduction ‘pipeline’ for the KOALA IFU data of a pilot sample of BADGRS. We will also investigate the attenuation curve properties of one of the sources.

- 
- In Chapter 2, we will introduce the sample of galaxies used in this Thesis.
  - In Chapter 3, we will outline the core basic reduction techniques and the more advanced techniques we needed to create in order to obtain the highest quality data from the KOALA IFU raw data. We also discuss our flux calibration methods.
  - In Chapter 4, we will investigate the KOALA IFU results from UGC 9215 and discuss its dust attenuation properties.
  - Chapter 5 lists our conclusions for this work.



# CHAPTER 2

## THE SAMPLE AND DATA

---

---

### 2.1 INTRODUCTION

In this Chapter, we outline the properties of the sample of pilot sources studied in this Thesis, and the integral field unit data obtained to study their emission line properties.

### 2.2 OBTAINING THE KOALA DATA

An initial proposal for four nights of time to observe the four BADGRS from the Dunne et al. (2018) pilot sample (NGC 5584, NGC 5496, UGC 9215 and UGC 9299) with the KOALA IFU was granted, and was scheduled for and completed over the 28<sup>th</sup> April – 1<sup>st</sup> May 2016. The four pilot BADGRS in our sample are shown in Figure 2.1. These sources were not visible for the entirety of the night during the observing run. Therefore another target from the HAPLESS sample of Clark et al. (2015), NGC 4030, was added to the list of targets so that it could be observed at the beginning of the night, before the BADGRS had risen above the horizon. This source is shown in the top left panel of Figure 2.2. The target fields, shown in orange, were observed using the wide configuration of KOALA, with  $27.4'' \times 50.6''$  field of view and  $1.25''$  sampling. The 580V and 1000R gratings were used in the blue and red CCDs respectively, with the central wavelengths set to  $4700 \text{ \AA}$  and  $6750 \text{ \AA}$  respectively.

The observing strategy for each target field was to complete five exposures of 2400s. This meant that each field would need a total time of 3.5h, if observed in good conditions. However, the weather was not ideal during the observing time, and due to the adverse conditions, only around half of the planned observations were completed. This included the full 3.5h of time on target field 1 of NGC 5584 (the lower left target field in the panel for NGC 5584 in Figure 2.1),

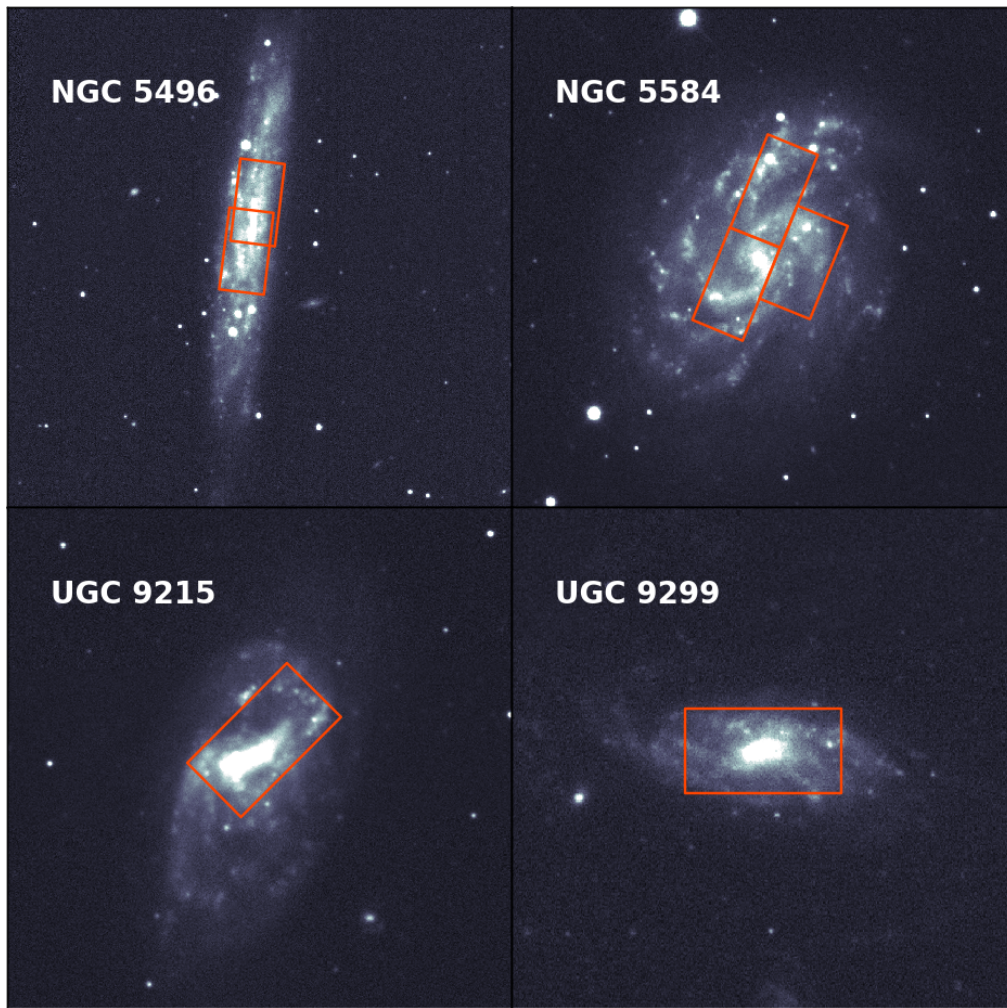


**Figure 2.1.** SDSS  $g$ -band images of NGC 5496, NGC 5584, UGC 9215 and UGC 9299, our pilot BADGRS sample. The orange outline shows the position of the KOALA IFU target fields chosen for each galaxy.

completed in favourable conditions. Three out of the five planned exposures of UGC 9215 were also completed in favourable conditions. Target field 2 of NGC 5584 (the right target field in the panel for NGC 5584 in Figure 2.1) was given eleven exposures of 1800s, with the exposure times being altered to try and make the best of the poor conditions, as there was intermittent cloud during observations. The target field of UGC 9299 was observed for five exposures of 2400s and two exposures of 1800s, again in conditions that were not ideal, so the observations were not of the quality necessary. No observations were carried out on the final target field of NGC 5584, or the two fields of NGC 5496.

Due to these poor weather conditions, a second observing proposal was put in to complete the time initially requested; this was granted and carried out over

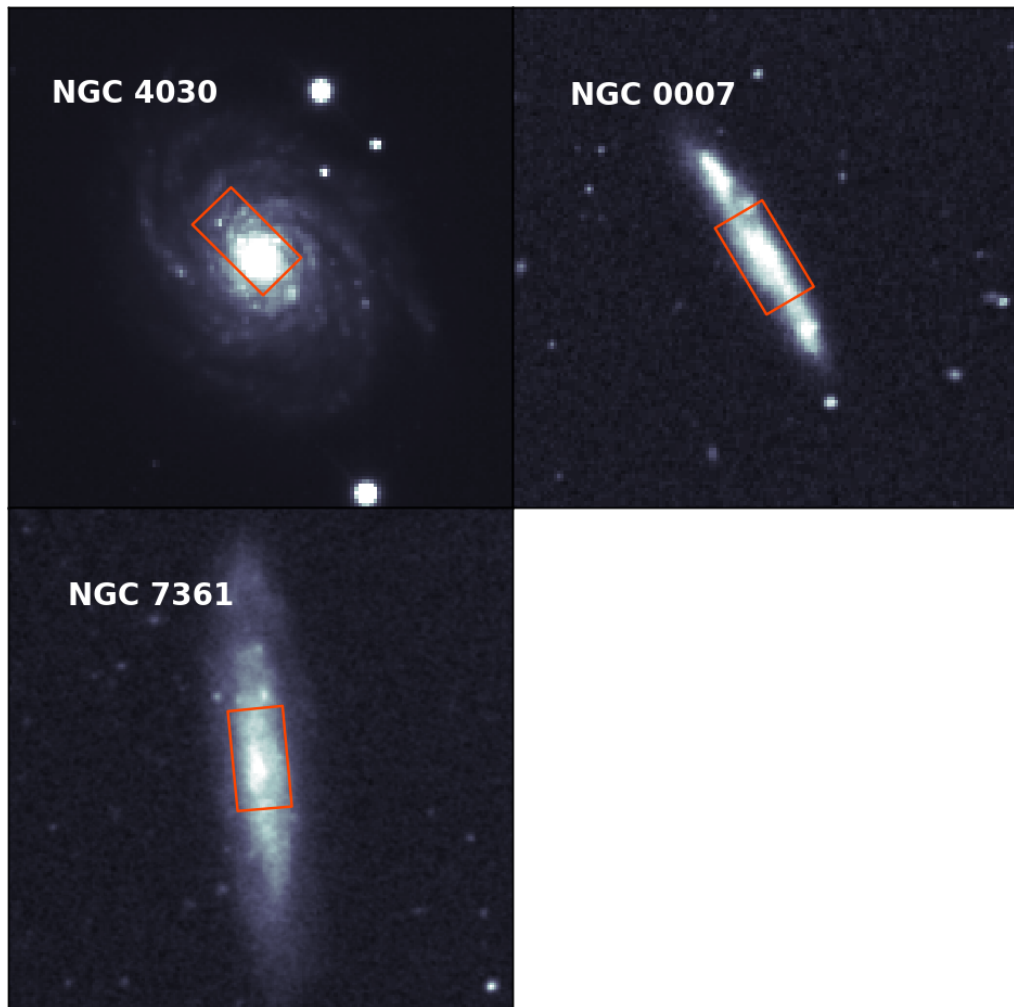


**Figure 2.2.** Optical images of our three extra sources, NGC 4030, NGC 0007 and NGC 7361, added so that they could be observed when our main pilot sources were not visible. The orange outline again shows the position of the KOALA IFU target fields chosen for each source.

the 21<sup>st</sup> – 23<sup>rd</sup> May 2017. During observations, the gratings and central wavelengths were set up to match that of the initial observing run. The main target for the second run was NGC 5496, as it was the only galaxy that was not observed at all in the first observing run. The next target was UGC 9299, as this was one of the galaxies for which the weather conditions were poorest during the initial observations. Next was the third target field of NGC 5584 (the upper left target field in the panel for NGC 5584 in Figure 2.1), as that field had also yet to be observed. Finally, UGC 9215 needed to be completed, as only three of the five exposures were obtained during the previous run.

An extra target was again included, as the BADGRS were only visible until 2am on the available observing days. NGC 7361 was chosen as the extra target for this observing run before it began (see the lower left panel of Figure 2.2). This is a large galaxy found in the SGP fields of the *Herschel* ATLAS. A second end of night target was added during the run, as the observations of NGC 7361 were completed. The galaxy NGC 0007 was chosen (see the upper right panel of Figure 2.2), as its  $FUV - K_S$  colour classifies it as one of the BADGRS, but it comes from the Southern Galactic Plane (SGP) field of the H-ATLAS (Figure 1.1), and was therefore observable at different times of the night to those from the original HAPLESS sample.

All of the observations were achieved during the two observing runs, although the quality of the data varies. A log of all of the observations carried out is shown in Table A.1, and a summary of the total exposure time spent on each galaxy target field is shown in Table 2.1. The final data used to create our KOALA data cubes will be discussed further in Chapter 3.

## 2.3 INDIVIDUAL GALAXIES

Each of the sources in the sub-sample of BADGRS are described briefly below. Their main properties are summarized in Table 2.2; each of these sources have been studied extensively using the large range of photometric data available.

### 2.3.1 NGC 5584

NGC 5584 is a face-on spiral galaxy at a distance of 30.2 Mpc and a redshift of 0.00548. It has a morphology of Scd, or 6 in the EFIGI catalogue of Baillard et al. (2011); the galaxy has a relatively weak bulge, very loosely bound spiral arms and displays highly flocculent features, with Clark et al. (2015) classifying it as possessing a flocculence of 1.00, again using the prescription of Baillard et al. (2011).

**Table 2.1.** Summary table of the total amount of observing time spent on each target field. The number of exposures per target field, and their individual exposure times are listed and used to calculate the total exposure time per target field. The total exposure time includes all data taken, regardless of quality. A standard total exposure is 3.33h, or  $5 \times 2400$ s exposures; variations in total exposure time above and below this number are due to poor weather conditions or lack of observing time to focus on that source.

Target Field	$N_{\text{EXPOSURE}}$	Exposure [s]	Total Exposure [h]
NGC 5584 (TF1)	5	2400	3.33
NGC 5584 (TF2)	11	1800	5.5
NGC 5584 (TF3)	5	2400	3.33
UGC 9299	7 (6)	2400 (1800)	7.67
UGC 9215	6	2400	4.0
NGC 5496 (TF1)	5	2400	3.33
NGC 5496 (TF2)	3	2400	2.0
NGC 0007	2	2400	1.33
NGC 4030	3	2400	2.0
NGC 7361	6	2400	4.0

An SDSS  $g$ -band image of NGC 5584 is shown in the upper right panel of Figure 2.1, overlaid with the KOALA pointings used to obtain the IFU data for this source.

### 2.3.2 NGC 5496

NGC 5496 is an edge-on spiral galaxy located at a distance of 27.4 Mpc and a redshift of 0.00488. It is classed as a morphological type of Scd, or 6 in the EFIGI catalogue of Baillard et al. (2011); loose and weak spiral arms can be just about made out in the edge-on orientation of this galaxy, and the bulge is weak. An SDSS  $g$ -band image of NGC 5496 is shown in the upper left panel of Figure 2.1, overlaid with the KOALA pointings used to obtain the IFU data for this source.

### 2.3.3 UGC 9299

UGC 9299 is a face-on spiral galaxy located at a distance of 28.3 Mpc and a redshift of 0.00516. It is classed as a morphological type of Sm, or 9 in the EFIGI catalogue of Baillard et al. (2011); the galaxy only has the faintest hint of spiral arms and a very weak bulge. An SDSS  $g$ -band image of UGC 9299 is shown in the lower right panel of Figure 2.1, overlaid with the KOALA pointing used to obtain the IFU data for this source.

### 2.3.4 UGC 9215

UGC 9215 is a face-on spiral galaxy located at a distance of 25.6 Mpc and a redshift of 0.00457. It is classed as a morphological type of Scd, or 6 in the EFIGI catalogue of Baillard et al. (2011); the galaxy has two main loosely bound spiral arms around a weak bulge. An SDSS  $g$ -band image of UGC 9215 is shown in the lower left panel of Figure 2.1, overlaid with the KOALA pointing used to obtain the IFU data for this source.

## 2.4 EXTRA TARGETS

As outlined previously in Section 2.2, along with the main pilot sample of BADGRS, observations of three extra targets were obtained. These galaxies were observed when the main targets were not visible in the sky, so as to make the most of the observing time obtained from the proposals. These extra targets were NGC 4030 in the first observing run, and NGC 7361 and NGC 0007 in the second observing run. The main properties of these galaxies are shown in Table 2.3, and a brief outline of each source is given below.

### 2.4.1 NGC 4030

This is a face-on spiral galaxy located in the Virgo Cluster, at a distance of 29.4 Mpc and redshift of 0.00477. Its morphology is classed as Sb, or 3 in the EFIGI catalogue of Baillard et al. (2011), meaning it has a prominent galactic bulge, with tightly wound arms and prominent dust lanes. An optical image of NGC 4030 is shown in upper left panel of Figure 2.2, overlaid with the KOALA pointing that was used to obtain IFU data for this source.

NGC 4030 was studied extensively as part of the HAPLESS sample of Clark et al. (2015), as one of the 42 brightest local infrared sources in the GAMA fields of the H-ATLAS. It was chosen as one of the extra targets during our KOALA observing runs due to it being visible when the main pilot sample were not, and because it does not possess the same unusual properties as the BADGRS. Observations of this galaxy could be compared to the BADGRS as a sort of control source, a representative of more 'normal' galaxies. The properties of this galaxy are what is typically seen for a more evolved spiral, with high stellar mass and dust mass, but low HI mass as a fraction of total mass. It also possesses a high metal content; all of these properties indicate an older, more evolved galaxy.

### 2.4.2 NGC 7361

This is a nearly edge-on spiral galaxy located at a distance of 16.07 Mpc and a redshift of 0.004166. It is classed as a morphological type of SAB(s)dm sp in the system of Buta et al. (2015); the sp in the classification means the galaxy is highly inclined, but not so much that you are unable to distinguish features within the disk. The rest of the classification indicates that the galaxy is a barred spiral, with spiral arms that originate from the bar, and a disk that possess irregularities, such as asymmetry and considerable star formation. An optical image of NGC 7361 is shown in the lower right panel of Figure 2.2, overlaid with the KOALA pointing that was used to obtain the IFU data for this source.

### 2.4.3 NGC 0007

This is a nearly edge-on spiral galaxy located at a distance of 19.14 Mpc and a redshift of 0.004987. The morphological classification for this source in the system of Buta et al. (2015) is Sd/Im sp, indicating that it is an almost edge-on, extremely late type spiral that shows irregularity and regions of considerable star formation. An optical image of NGC 0007 is shown in the upper right panel of Figure 2.2, overlaid with the KOALA pointing that was used to obtain the IFU data for this source.

## 2.5 CONCLUSIONS

Here we have described the sample of galaxies and the data sets obtained to study their properties. In the next Chapter, we will outline our data reduction procedure and the customised pipeline we built to produce high quality resolved IFU data.

**Table 2.2.** Properties of the sub-sample of BADGRS chosen for further study in Dunne et al. (2018). Morphological types follow the EFIGI catalogue of Baillard et al. (2011). Spiral galaxies have morphological types ranging from 0 to 9. The Milky Way (usually classified as Sb or Sbc) would sit at 3 or 4 in the EFIGI catalogue; higher numbers indicate less prominent bulges and weaker spiral arms. Distance is obtained from De Vis et al. (2017a), and is local flow corrected using the prescription of Baldry et al. (2012). HI masses ( $M(\text{HI})$ ) are obtained from Clark et al. (2015). Stellar mass ( $M_*$ ), dust mass ( $M_{\text{dust}}$ ), cold dust temperature ( $T_c$ ), star formation rate (SFR), and specific star formation rate (sSFR) are listed for the works of both Clark et al. (2015) and De Vis et al. (2017a). Gas fractions,  $f_g$ , are obtained from Dunne et al. (2018), using the prescription outlined in Clark et al. (2015) and including a factor to account for helium mass. Central metallicity values for the sources are obtained from De Vis et al. (2017b) and are listed as  $12 + \log(\text{O}/\text{H})$ .

Parameter	NGC 5584	NGC 5496	UGC 9299	UGC 9215
HAPLESS No. <sup>a</sup>	14	7	9	3
Morphological Type <sup>a</sup>	6/Scd	6/Scd	9/Sm	6/Scd
RA <sup>b</sup> [J2000 deg]	215.599	212.908	217.394	215.863
Dec <sup>b</sup> [J2000 deg]	-0.387	-1.1591	-0.0191	1.724
Redshift <sup>a</sup>	0.0055	0.0049	0.0052	0.0046
Distance <sup>b</sup> [Mpc]	30.2	27.4	28.3	25.6
$M(\text{HI})^a$ [ $\log_{10} M_{\odot}$ ]	9.76	10.03	9.94	9.56
Clark et al. (2015)				
$M_*$ [ $\log_{10} M_{\odot}$ ]	9.5	9.5	8.6	9.2
$M_{\text{dust}}$ [ $\log_{10} M_{\odot}$ ]	7.4	7.4	6.7	7.2
$T_c$ [K]	14.6	12.2	15.0	13.5
SFR [ $\log_{10} M_{\odot} \text{ yr}^{-1}$ ]	-0.1	-0.3	-0.6	-0.2
sSFR [ $\log_{10} \text{ yr}^{-1}$ ]	-9.6	-9.9	-9.3	-9.5
De Vis et al. (2017a)				
$M_*$ [ $\log_{10} M_{\odot}$ ]	9.97	9.46	8.61	9.31
$M_{\text{dust}}$ [ $\log_{10} M_{\odot}$ ]	7.51	7.12	6.39	6.95
$T_c$ [K]	17.0	16.9	17.3	17.4
SFR [ $\log_{10} M_{\odot} \text{ yr}^{-1}$ ]	0.26	-0.23	-0.55	-0.24
sSFR [ $\log_{10} \text{ yr}^{-1}$ ]	-9.71	-9.69	-9.16	-9.55
$f_g^c$	0.44	0.83	0.97	0.70
Metallicity <sup>d</sup> (PG16S)	8.36	8.19	8.25	8.29

<sup>a</sup>Clark et al. (2015). <sup>b</sup>De Vis et al. (2017a). <sup>c</sup>Dunne et al. (2018). <sup>d</sup>De Vis et al. (2017b).

**Table 2.3.** Properties of the extra targets chosen for observation when the BADGRS in the main pilot sample were not visible. Morphological classification follows the EFIGI catalogue of Baillard et al. (2011) for NGC 4030, and the analysis of Buta et al. (2015) for NGC 7361 and NGC 0007. The HI masses for NGC 7361 and NGC 0007 are calculated following the standard prescription outlined in Clark et al. (2015), using their corresponding distance values and the integrated 21cm line flux obtained from Meyer et al. (2004).

Parameter	NGC 4030	NGC 7361	NGC 0007
Other Names	HAPLESS 6 <sup>a</sup>	IC 5237, UGCA 434 <sup>d</sup>	PGC 000627 <sup>d</sup>
Morphological Type	3/Sb <sup>a</sup>	SAB(s)dm sp <sup>e</sup>	Sd/Im sp <sup>e</sup>
RA [J2000 deg]	180.09841 <sup>b</sup>	340.574623 <sup>d</sup>	2.087333 <sup>d</sup>
Dec [J2000 deg]	-1.10033 <sup>b</sup>	-30.057655 <sup>d</sup>	-29.915000 <sup>d</sup>
Redshift	0.00477 <sup>a</sup>	0.004166 <sup>f</sup>	0.004987 <sup>i</sup>
Distance [Mpc]	29.4 <sup>b</sup>	16.07 <sup>g</sup>	19.14 <sup>g</sup>
M(HI) [ $\log_{10} M_{\odot}$ ]	10.16 <sup>a</sup>	9.43 <sup>h</sup>	9.11 <sup>h</sup>
$M_{*}$ [ $\log_{10} M_{\odot}$ ]	10.88 <sup>b</sup>	-	-
$M_{\text{dust}}$ [ $\log_{10} M_{\odot}$ ]	7.96 <sup>b</sup>	-	-
$T_c$ [K]	20.9 <sup>b</sup>	-	-
SFR [ $\log_{10} M_{\odot} \text{ yr}^{-1}$ ]	0.78 <sup>b</sup>	-	-
$f_g$	0.16 <sup>b</sup>	-	-
Metallicity (PG16S)	8.54 <sup>c</sup>	-	-

<sup>a</sup>Clark et al. (2015). <sup>b</sup>De Vis et al. (2017a). <sup>c</sup>De Vis et al. (2017b). <sup>d</sup>NASA/IPAC Extragalactic Database (<https://ned.ipac.caltech.edu/>). <sup>e</sup>Buta et al. (2015). <sup>f</sup>Koribalski et al. (2004). <sup>g</sup>Tully et al. (2016). <sup>h</sup>Calculated using the standard prescription outlined in Clark et al. (2015). <sup>i</sup>Theureau et al. (1998).



# CHAPTER 3

## DATA REDUCTION AND CALIBRATION

---

---

### 3.1 INTRODUCTION

In this Chapter we outline the methods used to reduce the KOALA data, including our own scripts written to resolve data quality issues produced by the AAO pipeline.

The data that is initially produced from the KOALA IFU is the raw output from the CCDs. These data files require many steps of reduction and calibration to get to the final science quality data products, which are the data cubes for each galaxy. The general steps that are required are as follows:

1. Cosmic ray removal with PyCosmic.
2. Scattered light subtraction.
3. Data reduction (bias-subtraction, location and extraction of fibre spectra, wavelength calibration) using the AAO software 2dFdr.
4. Throughput calibration.
5. Sky subtraction.
6. Masking of sky lines, defects and leftover cosmics.
7. Flux calibration using standard stars.
8. Scaling, rebinning and convolution of observations.
9. Production of data cubes.
10. Combining the blue and red data cubes.

Some of these steps are completed using a pipeline provided by the AAO KOALA team<sup>1</sup> whereas other steps and techniques were designed and produced as part of this Thesis. Additional pipeline steps, tests and parameter settings we carried out to obtain the highest quality data from the raw telescope data include:

- Switching to an external cosmic ray removal method, rather than the default 2dFdr method.
- Choice of extraction method: Gauss or OPTEX?
- Wavelength calibration from sky lines.
- Sky subtraction for moonlit nights.
- Using the twilight flats for throughput calibration, rather than the default 2dFdr method.
- Scattered light subtraction.
- Data cube issues, dead fibre flags, lack of weighting for exposure time or variance.
- Dealing with tramline map creep.

In the next Sections, we will discuss each of the steps and changes we needed to make in turn.

## 3.2 COSMIC RAY REMOVAL WITH PYCOSMIC

The first step that is carried out on the raw output from the KOALA IFU is the removal of cosmic rays. Cosmic rays are single high-energy particles, which cause showers of particles when entering the Earth's atmosphere. Due to their high energies, they leave bright tracks on the CCDs at the telescope if they hit it, and the number that are incident upon the CCD increases with the length any exposure that is taken. Therefore, our object and offset sky observations will have contamination from cosmic rays. It is important to remove this cosmic ray contamination from the spectra because they are similar in appearance to bright emission lines, and can be mistaken for these features. One of the main methods to remove cosmic rays from

---

<sup>1</sup>Example KOALA cubing scripts are available at <https://aat.anu.edu.au/science/instruments/current/koala/reduction>. Assistance with the reduction process can be obtained by getting in touch with Ángel López-Sánchez at [angel.lopez-sanchez@mq.edu.au](mailto:angel.lopez-sanchez@mq.edu.au).

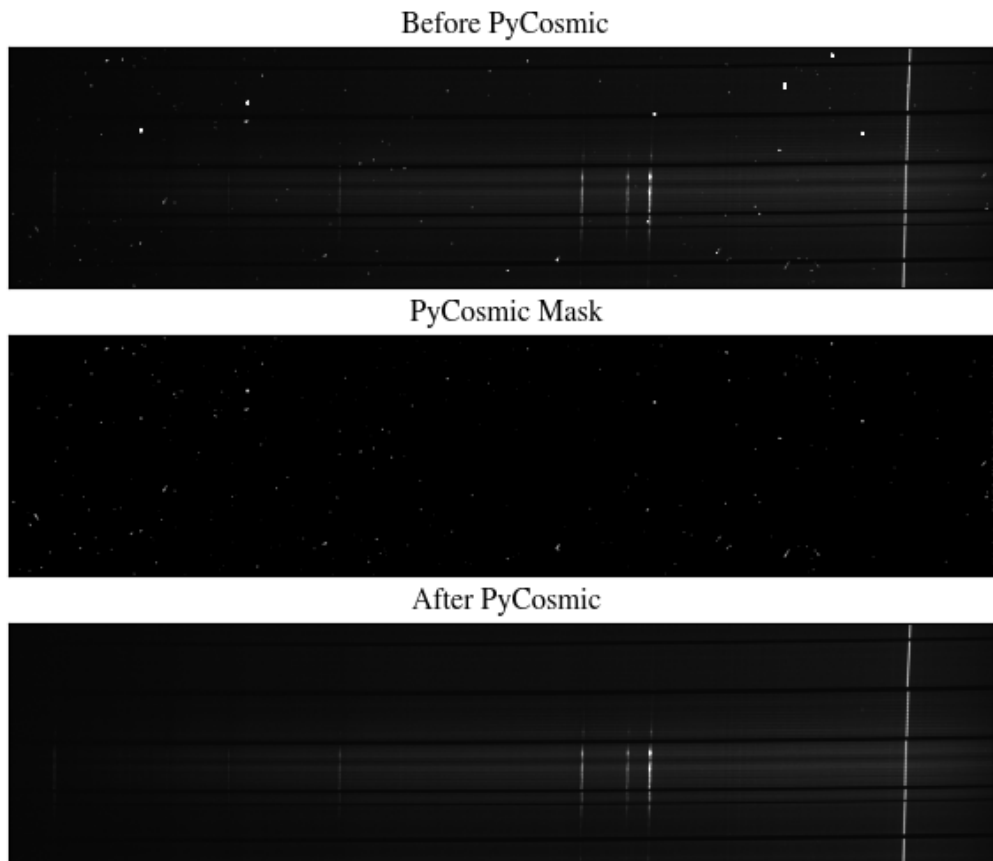


**Figure 3.1.** An example of how PyCosmic works when applied to a frame of raw KOALA data; a 500 pixel horizontal strip of a raw frame is shown here. Top panel: The raw frame as it comes from the telescope. You can see there are small, bright spots of light at random all over the frame; these are the cosmic rays. Middle panel: The mask PyCosmic applies after it has identified the positions of the cosmic rays. Bottom panel: The data after the mask has been applied and the cosemics have been removed from the data.

IFU data is to use PyCosmic (Husemann et al., 2012), which was designed specifically to be used on fibre-fed IFS data. PyCosmic identifies the cosmic rays according to a variety of parameters set by the user, and then masks them before interpolating using the surrounding data to fill the gaps left by the mask. Removing cosmic rays without also removing emission line flux from our sources required some investigation of different parameter combinations.

There are a couple of different ways we can apply the PyCosmic algorithm to our data: (i) within 2dFdr as part of the data reduction process<sup>2</sup>, or (ii)

<sup>2</sup>During our initial investigations of the data reduction process using version 6.28 of 2dFdr (the recommended release version at the time), we tried using the internal version of PyCosmic with a couple of the different extraction methods available in 2dFdr. We encountered an issue where using one method of reduction (so-called OPTEx) gave poor results, regardless of the parameters being

running PyCosmic outside of 2dFdr.

We tested both ways (see Appendix B.2 for more details) and found that the best results came from running PyCosmic outside of 2dFdr; the final parameter values used here are listed in Table 3.1. Figure 3.1 demonstrates that this approach successfully removes the contamination of most of the cosmic rays in our observations. Once the cosmic rays had been removed satisfactorily the data was then put through 2dFdr as normal, with the internal 2dFdr version of PyCosmic turned off. Figure 3.2 shows the importance of removing cosmic ray contamination from KOALA data.

**Table 3.1.** Final parameter values used with PyCosmic to remove cosmic rays from the data from the blue and red CCDs of KOALA. Different values of the fwhm parameter were chosen for the two CCDs to find the best balance between removing as many cosmics as possible whilst leaving important emission lines intact.

Parameter	CCD 1	CCD 2
siglim	5.0	5.0
iter	5	5
fwhm	2.0	3.0
rlim	1.0	1.0
gain	2.0	2.0

### 3.3 SCATTERED LIGHT SUBTRACTION

Scattered light can be an issue for instruments that use the AAOmega spectrograph; it was found to be an issue for the SAMI instrument (Green et al., 2018), and we have found that this is also the case for the KOALA instrument. This scattered light is caused by light at all wavelengths entering the spectrograph and being reflected and bounced around in the setup of AAOmega. This is particularly a problem at the very blue end of the blue CCD; due to the low counts of our sources in this region, the scattered light has a larger percentage contribution to the total counts. Without accounting for and subtracting this light, we end up with our final spectra displaying an upturn in flux at the very blue end of our wavelength coverage. This causes issues when trying to fit the spectrum, so the scattered light needs to be removed from our final data.

To characterise the scattered light, we have to partially reduce the data first using the reduction software 2dFdr. The scattered light analysis is done using an output file known as an im.fits file. These files have had the bias subtracted from the  


---

 used in PyCosmic.

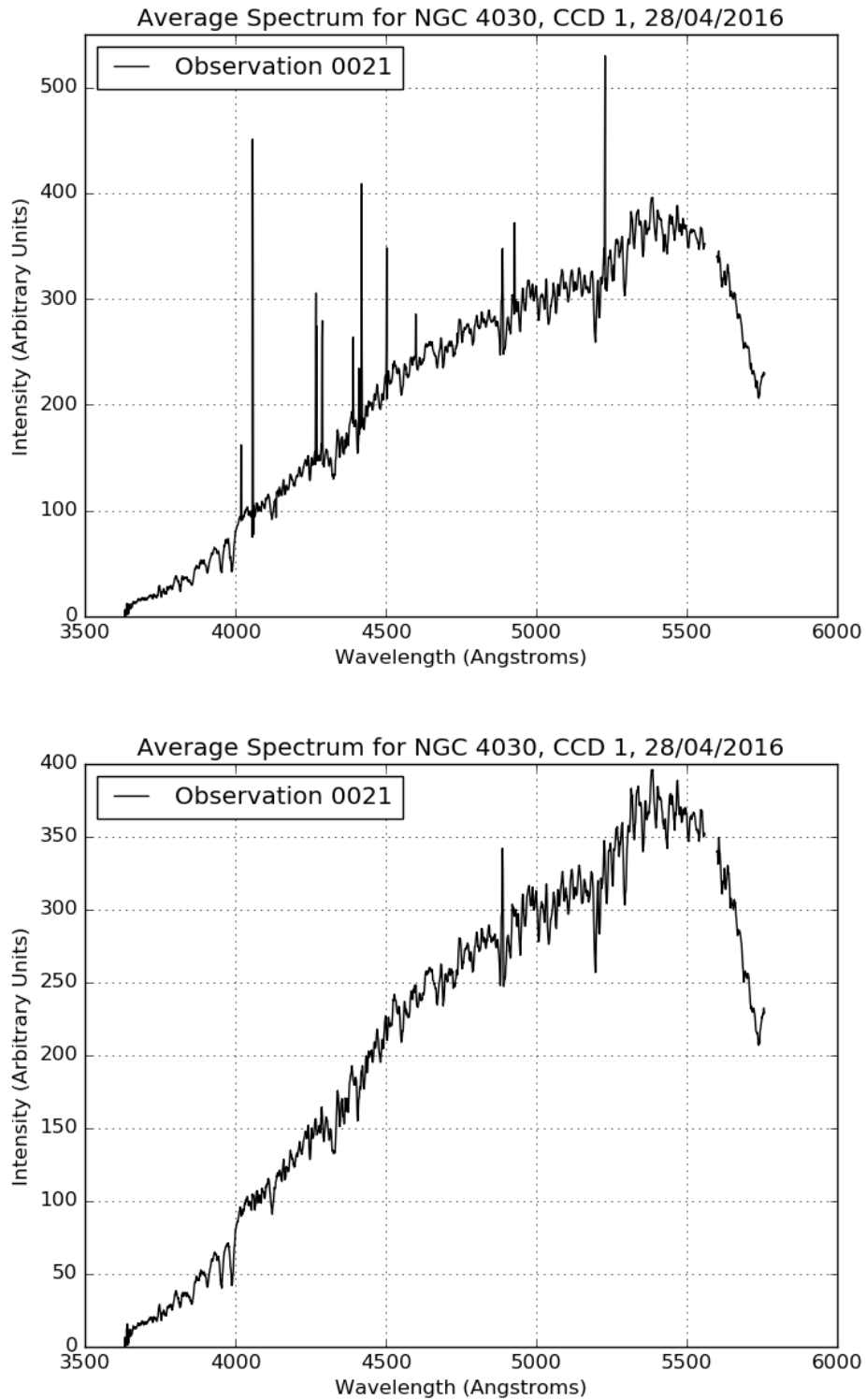


**Figure 3.2.** The average spectrum of NGC 4030 before and after cosmic ray removal with PyCosmic. The top panel shows the average spectrum from the blue CCD (CCD 1) without cosmic ray removal. The bottom panel shows the same observational data, but this time with cosmic ray removal using the final chosen PyCosmic parameters.

frame using the overscan region but have not yet had the extraction process carried out, so there are still gaps between fibres. The scattered light is present throughout the data frames, so we use these gaps between fibres to obtain the profile of the scattered light.

We exclude all of the pixels that have data from the fibres present within them, which leaves behind only the data within the gaps. We obtain the data from all the empty regions, and for each wavelength we calculate the average across the perpendicular axis, covering all the gaps between fibres. This becomes the 1D scattered light profile (other options were explored, and are explained in more detail in Appendix B.1). We then subtract this final profile from the raw frames; this data can then be reduced as normal within the data reduction package 2dFdr.

### 3.4 THE 2DFDR SOFTWARE PACKAGE

2dFdr (AAO Software Team, 2015) is the software package used to reduce data that has come from the AAOmega spectrograph on the AAT. 2dFdr takes in the raw data files from KOALA (and other instruments) and AAOmega, and returns an extracted spectrum with a wavelength solution.

To reduce the data, two types of calibration observations are necessary from KOALA: fibre flat fields and ARC fields. The fibre flat fields are obtained from lamps in the AAOmega spectrograph which have a very consistent flux response with wavelength, and have no large spectral features. These are used to find and trace each fibre across the detector. When the path of each fibre has been found and a tramline map has been made, the flux values of the spectrum at each wavelength pixel can be found. This is done by fitting a gaussian to the profile of the fibre at each wavelength pixel and integrating the light under the resulting curve. This allows a single flux value to be found for each wavelength pixel. The ARC fields are then used to characterise the wavelength solution of the data. They are also obtained from lamps within the spectrograph, but these have many well-known spectral features in the output, which helps to pin down the wavelength solution for the spectra we obtained from our sources.

We use version 6.88 of the software to reduce our data<sup>3</sup>. The parameters used during the reduction are chosen in the tabs at the top of the page. We changed several of the default parameters to customise the reduction process for our data. For

---

<sup>3</sup>The current release version of 2dFdr can be obtained from [https://www.aao.gov.au/science/software/2dfdr?\\_ga=2.73303571.1408321010.1608138046-116206076.1608138046](https://www.aao.gov.au/science/software/2dfdr?_ga=2.73303571.1408321010.1608138046-116206076.1608138046). Older versions can be found at <https://www.aao.gov.au/science/software/2dfdr/other-versions>.

example, we choose to remove some of the options found in the default configuration of 2dFdr, and add an extra calibration option (discussed further in the following Sections).

### 3.4.1 CHOOSING WHICH EXTRACTION METHOD TO USE

One of the first things we focused on during the reduction process was which extraction method to use within 2dFdr: Gaussian (Gauss) or optimal (OPTEX) extraction. Gaussian extraction is the most simple form of extraction that can be used for the data. It fits a Gaussian profile to the fibre spread function, and then uses this to calculate the flux for each pixel along the fibre. The optimal method is similar; it fits a Gaussian profile to the fibre spread function, but also assumes there is some overlap, known as cross-talk, between the profiles of each fibre, and tries to deal with any erroneous flux that results from these overlapping profiles. This may become an issue if there is a very bright fibre next to a much fainter fibre, as the bright fibre profile will overlap with the fainter fibre next to it and could cause it to seem brighter than it actually is.

Cross-talk is expected to be an issue with KOALA, as the fibres are all packed very close together. To assess whether cross-talk was an issue for our data, and whether the optimal extraction was doing a good job of solving it, we compared the Gaussian and optimal extraction methods. The optimal extraction process is more computationally expensive than the Gaussian extraction, so a check would enable us to determine if OPTEX made a noticeable difference to the quality of the data to justify the extra time taken during the reduction process. To carry out this comparison, we focused on a simple case: observations taken of the standard star LTT3218 as part of our observing programme (known as the flux standard). The standard star provides a small, bright area of flux for us to study the effects of cross-talk, since the star behaves effectively as a point source, most of the flux will pass down only a few of the KOALA fibres.

To prepare the data for these tests, the flux standard observations are first put through the external version of PyCosmic to remove any cosmic rays that hit the detector during the observing time of the frames. Two copies of the resulting files are then passed through 2dFdr. Both reductions have the exact same settings except for the extraction method. Finally, the observations are sky subtracted. For the purpose of this test, we are only interested in the average flux passing through each fibre, so we collapse the wavelength axis of the observations. After we have done this, we remove any fibres containing flux from the star and calculate the average

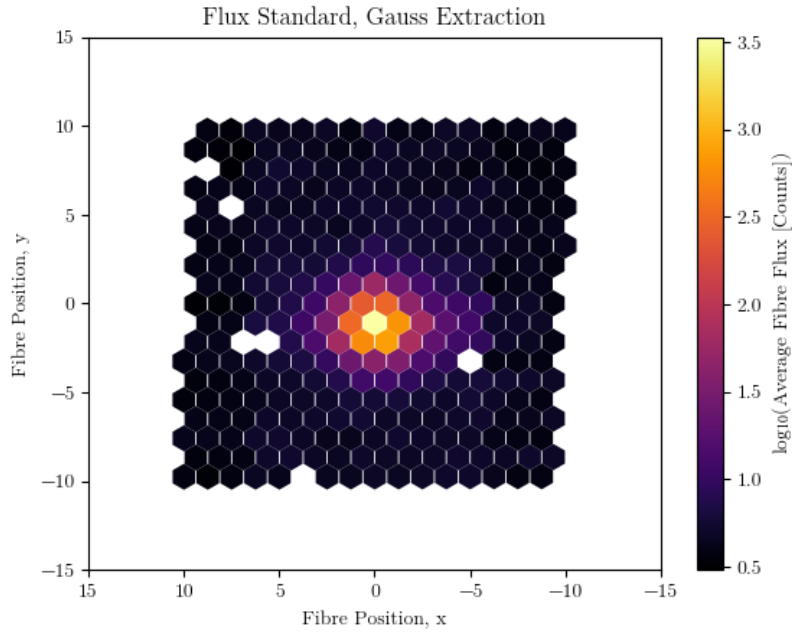


**Figure 3.3.** Cutout flux intensity map for an observation of the flux standard LTT3218 from the 28<sup>th</sup> April 2016, reduced using the Gauss extraction method.

value of flux in the remaining fibres to get an idea of the background flux. This is then subtracted from the average flux in all fibres.

We want to assess how much flux is coming through each fibre in the vicinity of the star. Figure 3.3 shows a fibre intensity map for one of our flux standard observations taken on the 28<sup>th</sup> April 2016 and reduced using the Gauss extraction method (zoomed in on the central area).

To get an idea of where cross-talk might have the biggest effect, we need to identify the brightest fibre, which contains the majority of the flux from the star, and its neighbours, both on the sky and on the CCD. To do this, we also plotted a map of the fibre numbers (Figure 3.4) which correspond to the cutout region containing our star. The brightest fibre in the field of view is number 431. This fibre has neighbours on the sky and CCD, fibres 430 and 432, which will be prime candidates to check for cross-talk. However, the flux from the star is not limited to just fibre 431, as Figure 3.3 shows, so there are other fibres around the star which may have neighbours showing cross-talk. Therefore, we will focus on the group of fibres around the star as well during this investigation.

Firstly, we compare the observations of the standard star output for both GAUSS and OPTEX extraction methods, and compare with an analytical model

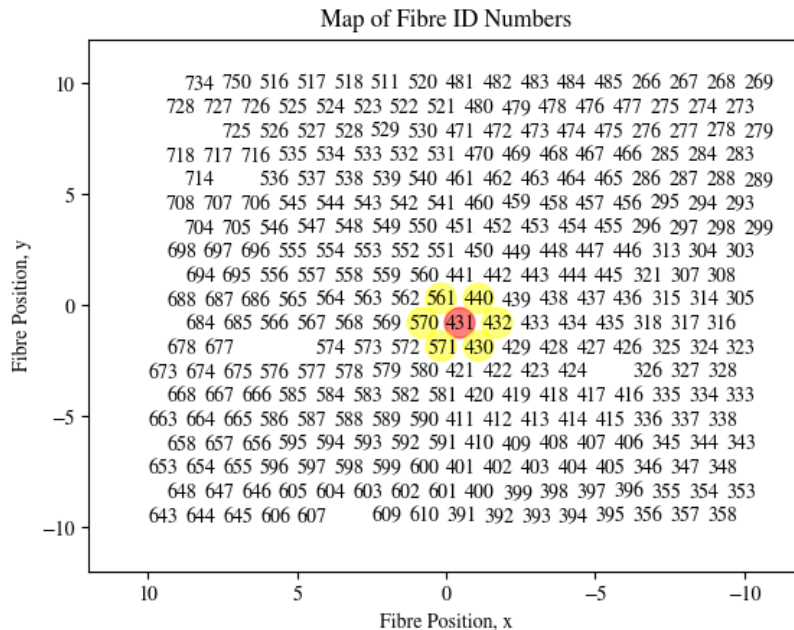


**Figure 3.4.** Map of fibre numbers corresponding to the cutout area around the star LTT3218, shown in Figure 3.3. Fibre 431 is the brightest fibre in the field of view, and is highlighted in red. The neighbouring fibres of interest are highlighted in yellow.

of the stellar profile. For the GAUSS data, we might expect the stellar flux to have evidence of cross-talk in the fibres (particularly fibres 430 and 422) in the form of seeing additional flux than predicted from the model. If OPTEX is working well, we would expect to see a stellar flux close to the analytical model since it should have corrected for any cross-talk. More details on this method are provided in Appendix B.3.

We used a stellar model described by a double two dimensional Gaussian function, of the form:

$$f(x, y) = a \exp\left(-\left[\frac{(x - x_o)^2}{2\sigma_1^2} + \frac{(y - y_o)^2}{2\sigma_1^2}\right]\right) + b \exp\left(-\left[\frac{(x - x_o)^2}{2\sigma_2^2} + \frac{(y - y_o)^2}{2\sigma_2^2}\right]\right) + c, \quad (3.1)$$

where  $x_o$  and  $y_o$  are the central positions of the Gaussian function,  $\sigma_1$  and  $\sigma_2$  are the standard deviations of the first and second Gaussian functions respectively, and  $a$ ,  $b$  and  $c$  are constants. The best fitting parameters of the functions were found by minimising the sum of the squared residuals between the data and the model. (The model fits and their residuals for GAUSS and OPTEX data reduction are shown in Figure B.6.) We find very little difference in the comparison of the GAUSS and OPTEX stellar profiles with the final fit model.

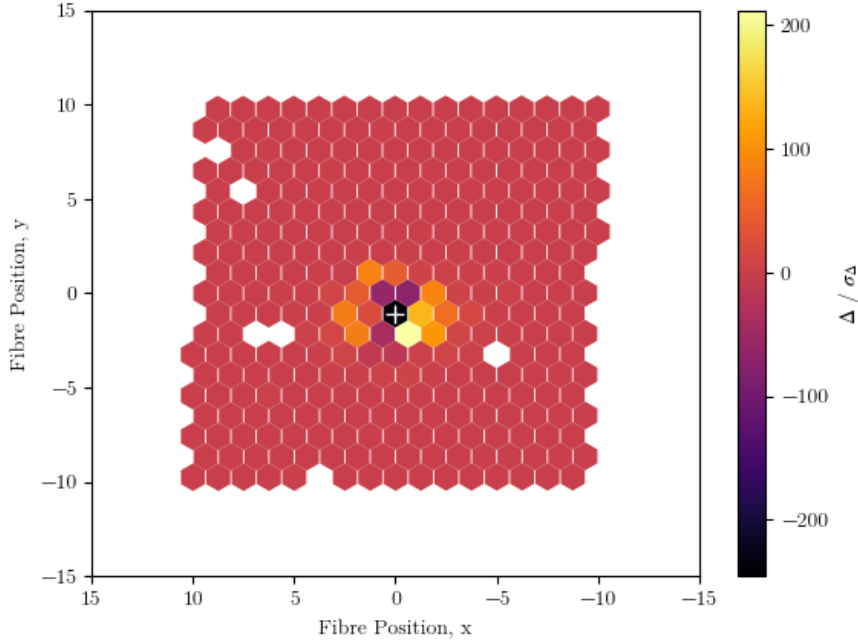


**Figure 3.5.** Ratio of the quantities in Equation 3.2 and Equation 3.3 shown with fibre position for the flux standard LTT3218. The white cross indicates the position of fibre 431, the brightest fibre in the field of view of the flux standard.

Next we directly compare the standard star output by the GAUSS and OPTEX methods. Since the latter method will have had any flux due to cross talk removed, we first needed to make sure the fluxes were scaled to match one another. Any variations we then see in the fibres that we predict cross talk might be a problem are definitely due to cross-talk. We estimate the difference between the total (scaled) fluxes  $\Delta_{\text{Flux}}$  for both methods using:

$$\Delta_{\text{Flux}} = F_{\text{Gauss}} - F_{\text{OPTEX,scaled}}, \quad (3.2)$$

and compare with the error in  $\Delta_{\text{Flux}}$  to see if any differences are significant:

$$\sigma_{\Delta} = (\sigma_{\text{Gauss}}^2 + \sigma_{\text{OPTEX}}^2)^{\frac{1}{2}}. \quad (3.3)$$

Figure 3.5 shows fibre position in  $x$  and  $y$ , with the colourbar indicating the ratio of the quantities calculated in Equation 3.2 and Equation 3.3. Higher values of  $\Delta_{\text{Flux}}/\sigma_{\Delta}$  indicate that the flux in the Gauss extracted standard is higher than in the OPTEX extracted standard, and that this is a statistically significant difference. In fibres 430 and 432, the neighbours on the CCD of the brightest fibre 431, are

brighter than average. In fibre 571 (not a neighbour of fibre 431 on the CCD, but it is a neighbour on the sky) we would not expect that fibre to have a high ratio of  $\Delta_{\text{Flux}}/\sigma_{\Delta}$  since cross-talk would not be seen here. For fibres 570 and 572, we would expect that the ratio is higher since these are close neighbours on the CCD. Comparing with Figure 3.5, we see that this is indeed the case, suggesting that OPTEX does indeed seem to be removing flux where we expect there to be cross-talk and working well where we do not expect cross talk.

To summarise, we choose the optimal flux extraction method, OPTEX, over the default GAUSS routine despite its more expensive computational needs. Full details of this justification are provided in Appendix B.3.

### 3.5 THROUGHPUT CALIBRATION

Throughput calibration is applied to our data to make sure there is effectively a consistent amount of light being let through each fibre in the KOALA instrument. If the instrument was perfect, each fibre would let through 100% of the light that is incident upon it, but in reality this is not the case. No fibre will be completely efficient, and some fibres will have throughputs that are far lower than others. The process of throughput calibration will scale up the flux coming through a less efficient fibre to make sure it matches the throughput of the more efficient fibres and give a consistent output from the instrument.

There are a few ways that we can do this calibration, and all involve using an observation we assume to be flat. For example, twilight flat observations (exposures taken of the sky during twilight), quartz flat observations (exposures taken of a quartz lamp with the dome shut) and offset sky observations (exposures taken of a blank area of dark sky, between object exposures) should have a very similar and repeatable spectrum for every fibre in the field of view of KOALA, providing there are no stars in the field at the time of exposure for the twilight flats and offset skies. These can therefore be used to extract the throughputs of the fibres so that they can be re-applied to our observations to make sure we are not losing flux due to a poor fibre throughput. We investigated two different methods for calculating the throughput: (i) using 2dFdr's inbuilt throughput calibration method which uses offset skies, and (ii) a method we carried out using the quartz or twilight flats.

For method (i), we found persistent problems with the offset skies that may have affected their ability to accurately characterise the fibre throughput. An example of this is shown in the top panel of Figure 3.6. The observation shown is an offset sky, observed in the red CCD. As mentioned before, we expect the offset skies

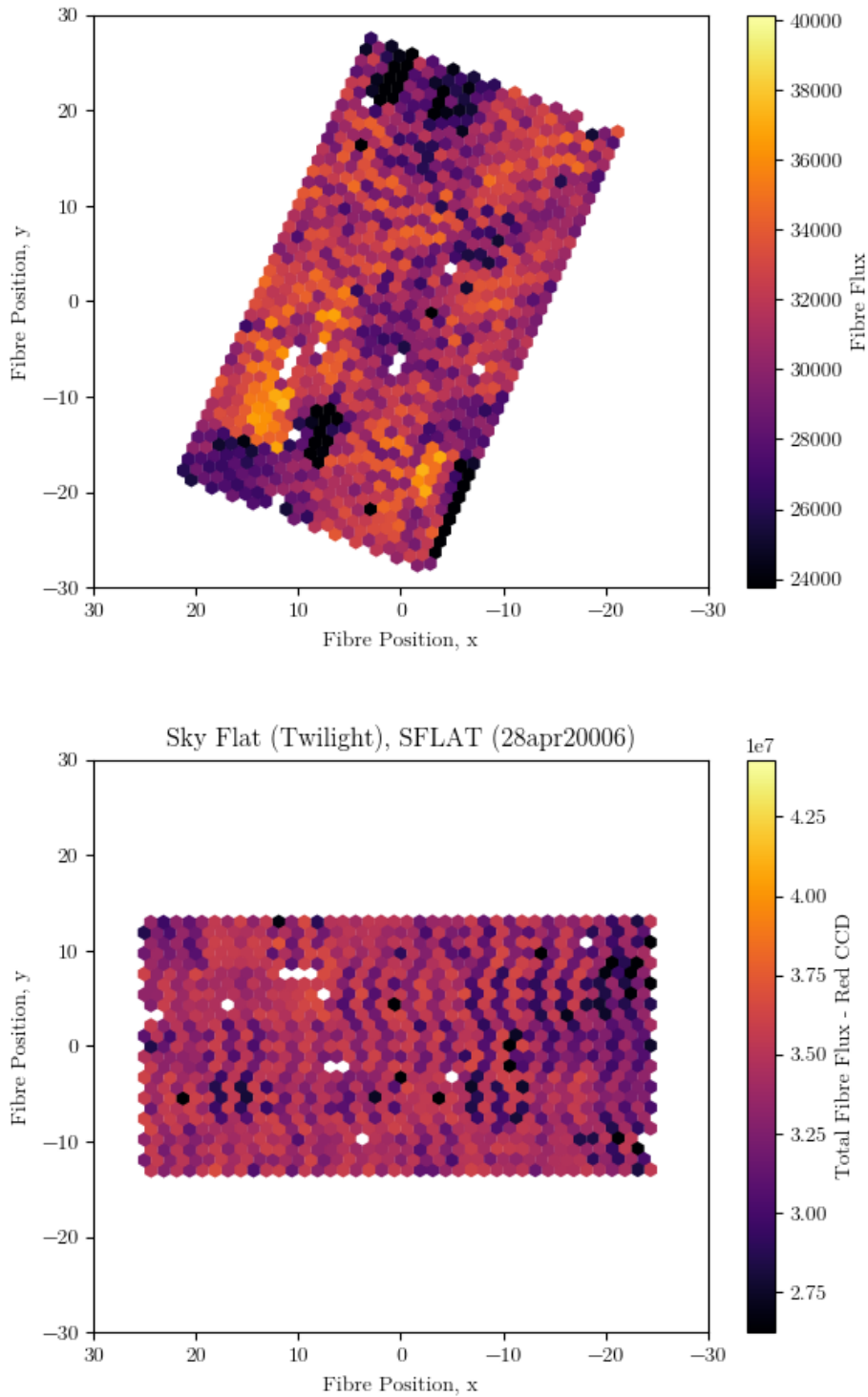


**Figure 3.6.** Examples of two observations that can be used to throughput calibrate KOALA IFU data. The top panel shows a fibre flux map of an offset sky in the red CCD as would be used in the 2dFdr pipeline. This shows variations in bias and throughput across the field of view. The bottom panel shows a fibre flux map of a twilight flat. Here, we can clearly see the throughput variations.

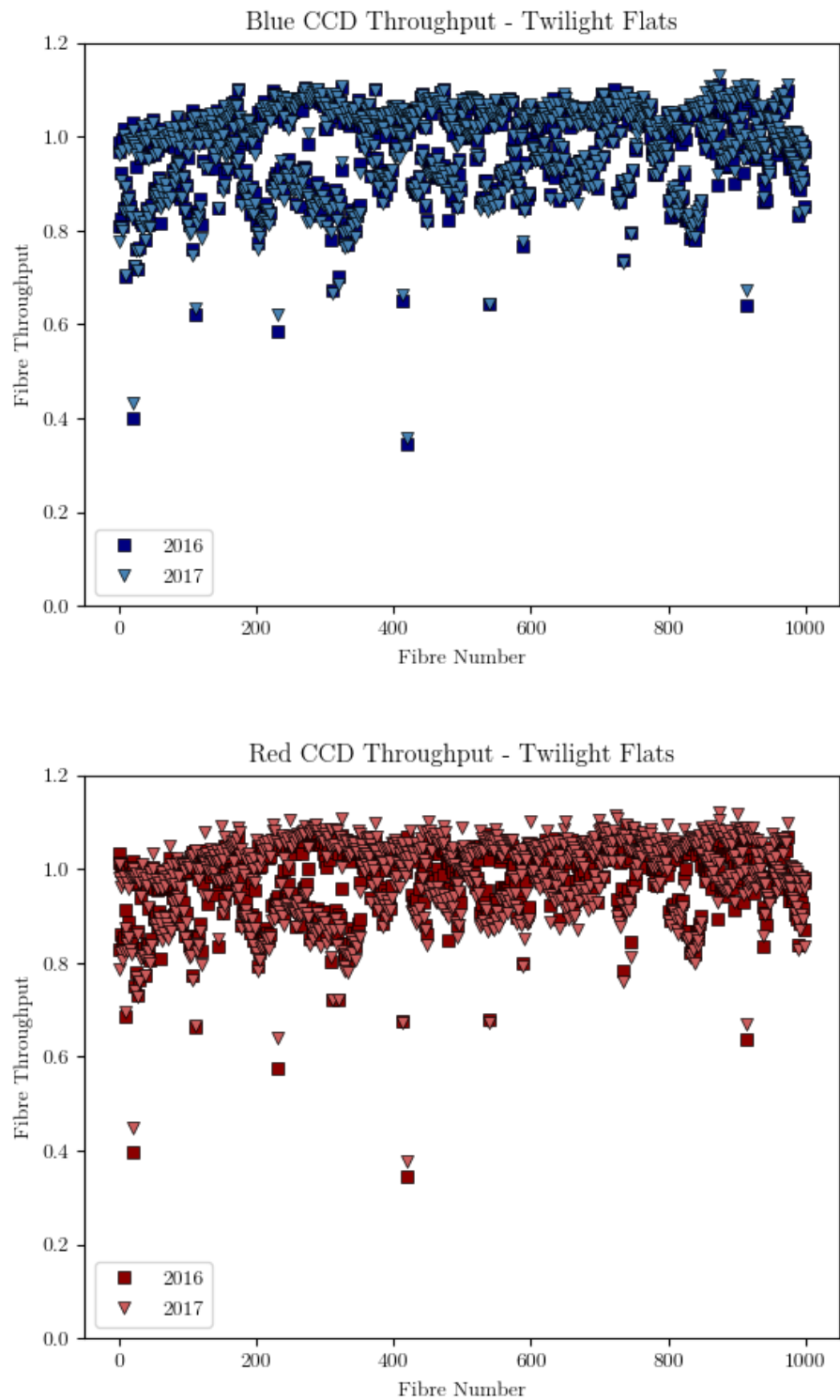


**Figure 3.7.** Fibre throughputs for the blue and red CCDs for the 2016 and 2017 observing runs. The top panel shows the fibre throughputs for the blue CCD, with the 2016 and 2017 throughputs indicated by squares and triangles respectively. The bottom panel shows the fibre throughputs for the red CCD, with the 2016 and 2017 throughputs again represented with squares and triangles respectively. You can see that the throughputs in the blue and red CCDs for each fibre are similar.

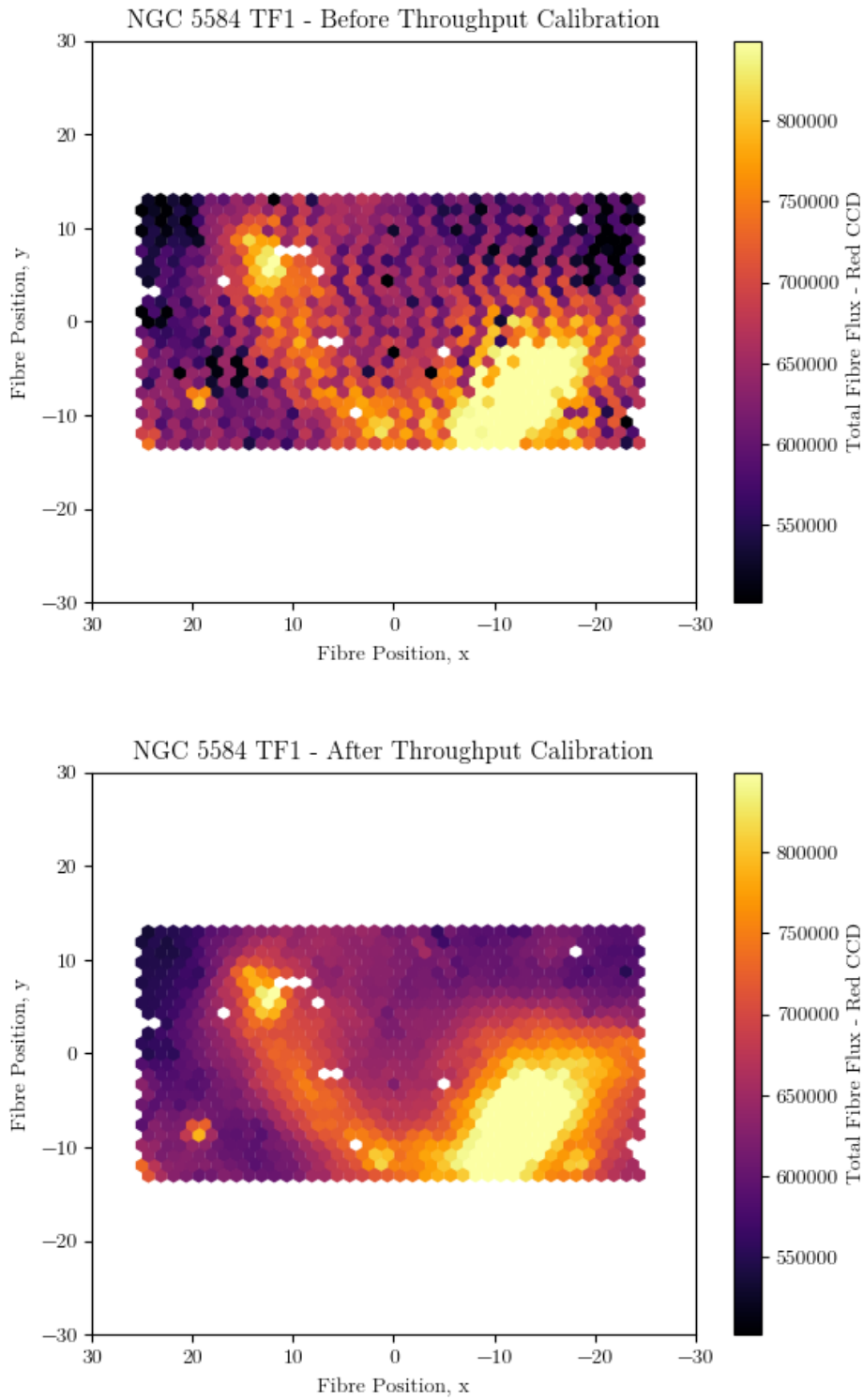


**Figure 3.8.** Fibre maps showing the total flux in each fibre for an observation of NGC 5584, target field 1. The top panel shows the total flux in each fibre before throughput calibration has been applied to the data, and the bottom panel shows the same data after the throughputs derived from the twilight flats have been applied.

to be relatively flat apart from the variations in throughput; this is not the case for the offset skies observed in the red CCD. We find variations in the bias level in the red CCD, which cause bright and dark patches across the field of view dominating over any variations in throughput, making the offset skies unreliable as a measure of throughput. These bias level variations are significant because the sky photon count is small. Longer sky exposures, matching the length of the target observations, would have solved this, but would have meant less time spent on targets, and therefore less signal in the data overall.

For method (ii), we inspected the quality of the quartz and twilight flats from our observing runs. We determined the former to be unsuitable for this purpose; low signal from the quartz lamp in the blue CCD means that the contribution from scattered light in these fields is a major issue (Appendix B.4). An example of the fibre flux map of a twilight flat from our observing run is shown in the bottom panel of Figure 3.6. We see less scattered light in this flat, though we note this becomes a bigger problem in the very blue end of our data where the flux from our object is lowest, and when the scattered light therefore makes up a higher percentage of the total flux present. It seems that the twilight flats in these edge regions are bright enough that the contribution of flux from scattered light is less of an issue. In comparison to the quartz flats, the twilight flats on average have approximately 10 times more flux in the blue end. We therefore use the twilight flat observations to obtain the throughputs. These throughput values are shown in Figure 3.7, for each CCD and each observing run. A data frame is shown in Figure 3.8 both before and after throughput calibration to demonstrate the importance of this process.

Whilst checking the quality of our throughput calibration, we encountered an interesting problem. This issue is illustrated in Figure 3.9 (top). Whilst we had removed most of the fibre-to-fibre variations present in the data via our throughput calibration, when we created fibre maps showing the total flux in each fibre, there were many groups of fibres that appeared across the field of view, that possessed two brighter than average fibres and two fainter than average fibres. We dubbed these ‘bees’, due to their physical appearance in the data frames.

We thought that this issue might be due to tramline map (TLM) creep, where the positions of the tramlines of the fibres change over time during an observing night. When we discovered this issue, we were using version 6.28 of 2dFdr. A later version of 2dFdr, version 6.88, had a new data reduction option available: ‘check for TLM creep’. After selecting this option in the new version of 2dFdr we see that the bees are almost completely removed (Figure 3.9 (bottom)). This issue led us to decide to reduce our data using version 6.88 of 2dFdr.

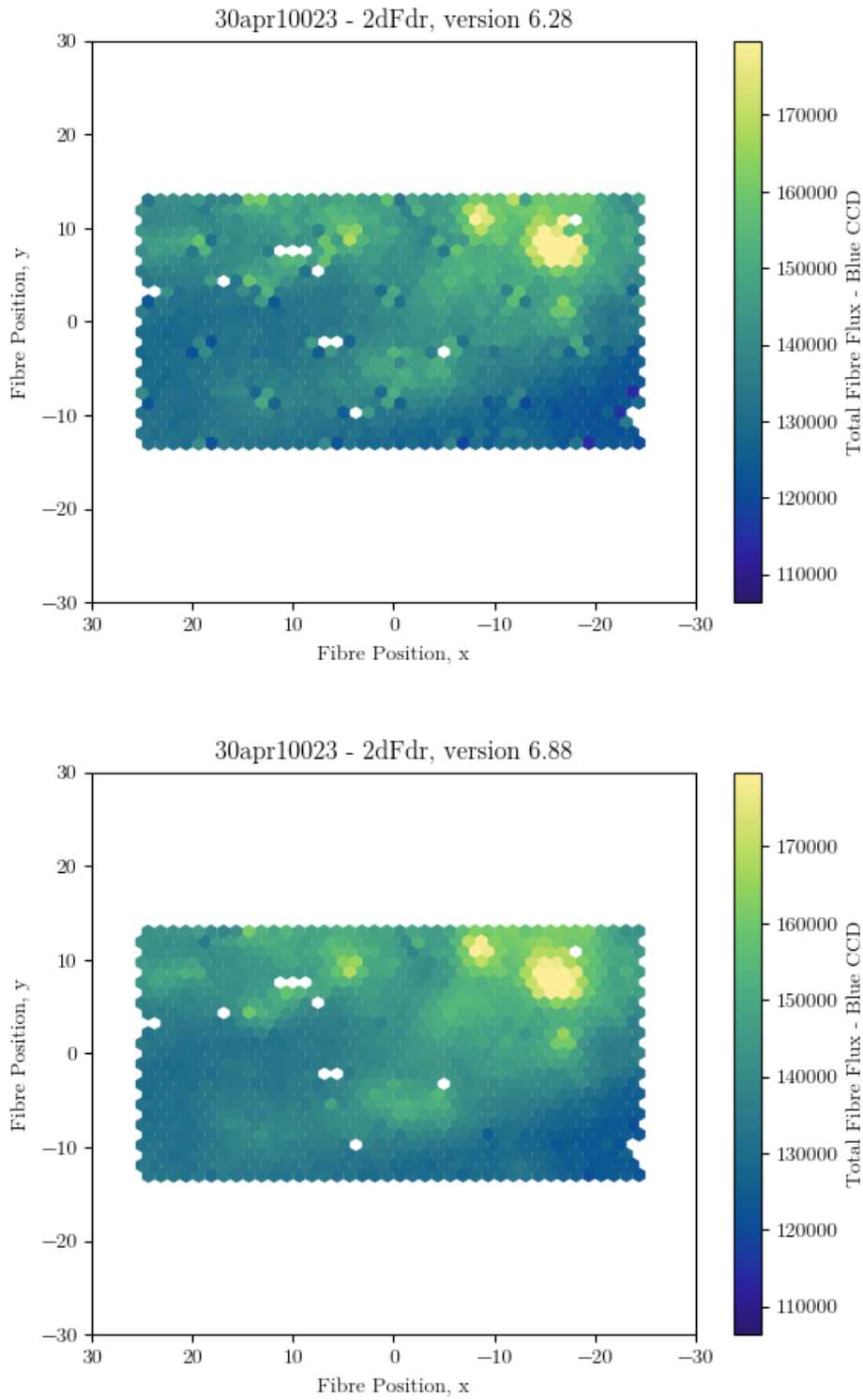


**Figure 3.9.** Total fibre flux maps of object 23 from 30<sup>th</sup> April 2016. Top: the data after being reduced using 2dFdr version 6.28. Bottom: using 2dFdr version 6.88, with the ‘check from TLM creep’ option selected. Both data sets have been throughput calibrated.

## 3.6 SKY SUBTRACTION

During an observing run, along with the calibration and object fields, offset sky fields are also obtained, where the entire KOALA field of view is pointed at a blank area of sky. This is so that the flux from the sky can be measured and then removed from our observations, so that it does not contaminate the emission from our sources. Offset sky observations are required for our sources because they fill the whole of the KOALA field of view, so no fibres in the field of view can be designated as ‘sky fibres’ for the purpose of the sky subtraction. The sky spectra also contains very prominent emission lines which need to be removed from our object spectra. An example of the effect of incorrectly accounting for the sky emission lines is shown in the Figure 3.10. Originally we were using 2dFdr version 6.28 to reduce our data. The top panel shows the object spectrum with prominent sky lines, and the lower panel shows an initial attempt at removing the sky using this version. Remnants of the sky emission lines are present in both the blue and red CCD data. These features remain because the sky emission lines of the object spectrum are offset in wavelength from those in the sky spectrum obtained by 2dFdr from the offset skies.

Unfortunately we discovered that 2dFdr does not deal with this type of sky subtraction using its default method of offset sky fields (Appendix B.5), so we had to create our own process to solve this issue. To do this we use the following steps:

1. The offset sky frames are combined to make a ‘master’ sky for each observing night by finding the median flux of all of the offset sky frames at each wavelength pixel in each fibre.
2. The ‘master’ sky field can then be used to remove the sky contamination from the observations. This is done by scaling the exposure time of the sky frame to match those of the observations, and then subtracting the median sky spectrum from each fibre in each of the object frames.
3. Before the median sky spectrum is subtracted from the spectrum in the fibres of the object frames, a cross-correlation is carried out between the sky and object spectra to estimate any wavelength offset between the sky and object. Then the sky spectrum is shifted to make sure the sky emission lines in the spectrum line up with one another and are therefore removed correctly.

Since we take the median value of flux to create the offset skies, we perform a bootstrap to obtain the error for each pixel. The errors are assumed to

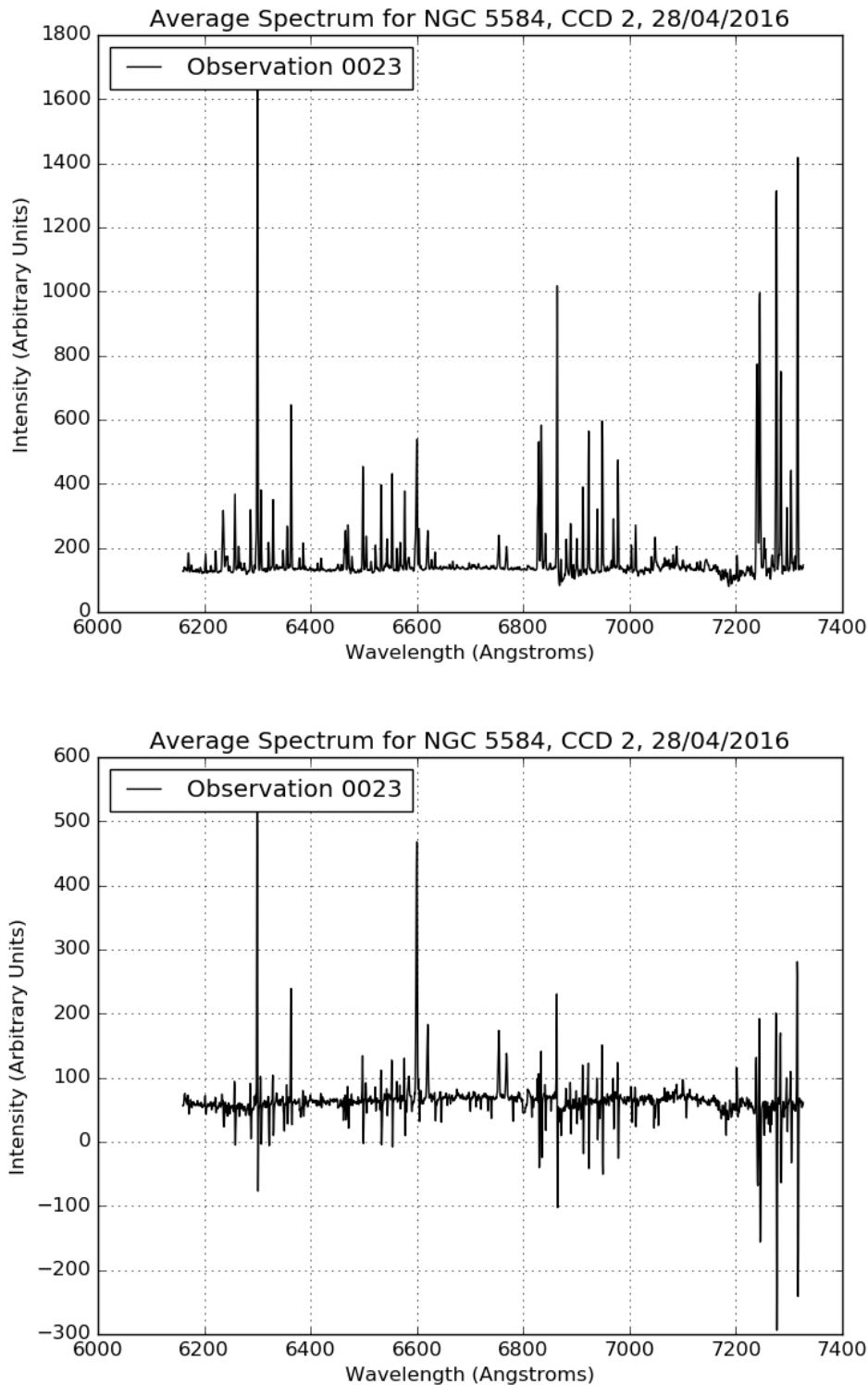


**Figure 3.10.** Example of the average spectrum of an observation of NGC 5584, taken on the 28<sup>th</sup> April 2016. Top: the spectrum of the red CCD after being reduced using 2dFdr version 6.28. The dominating features are the sky emission lines. Bottom: the object observation after sky subtraction. We can see that prominent sky emission lines have not been removed correctly.

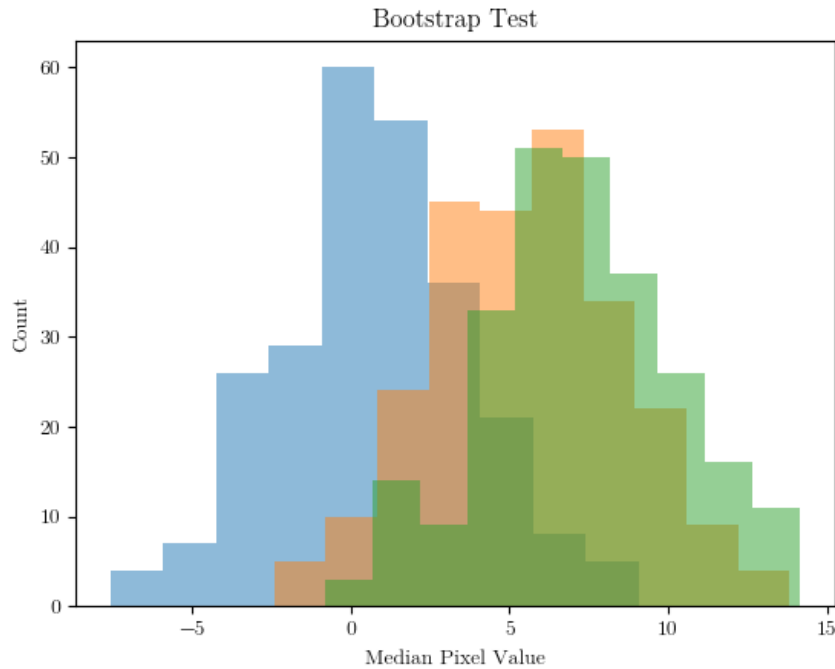


**Figure 3.11.** Test pixel distributions resulting from a bootstrap to obtain errors for the master sky files. Each colour is a distribution that was formed from a different initial test pixel.

be Gaussian, and each pixel value is perturbed by a random number pulled from a normal distribution, with a mean of 0 and a standard deviation of 1. This is done 250 times, and the standard deviation of the resulting distribution of pixel values is taken as the error on the pixel value. An example of the distributions of pixel values obtained from the bootstrapping process is shown in Figure 3.11. This process is carried out for each observing night, with a couple of exceptions (see the following Section).

### 3.6.1 MOONLIT SKIES

During observations on the 28<sup>th</sup> April 2016, the moon rose half way through the night and caused a change in the resulting sky spectra in both the offset sky and object frames; a similar issue occurred on the 21<sup>st</sup> May 2017 for the latter part of the night. An example of this is shown in Figure 3.12 for the 21<sup>st</sup> May 2017. The presence of the moonlight required a slightly different technique for finding and subtracting the sky spectrum from the effected observations as simply using the sky observations led to over subtraction of flux, and object spectra with negative values.

On nights where the moon rose during observations, the brightness

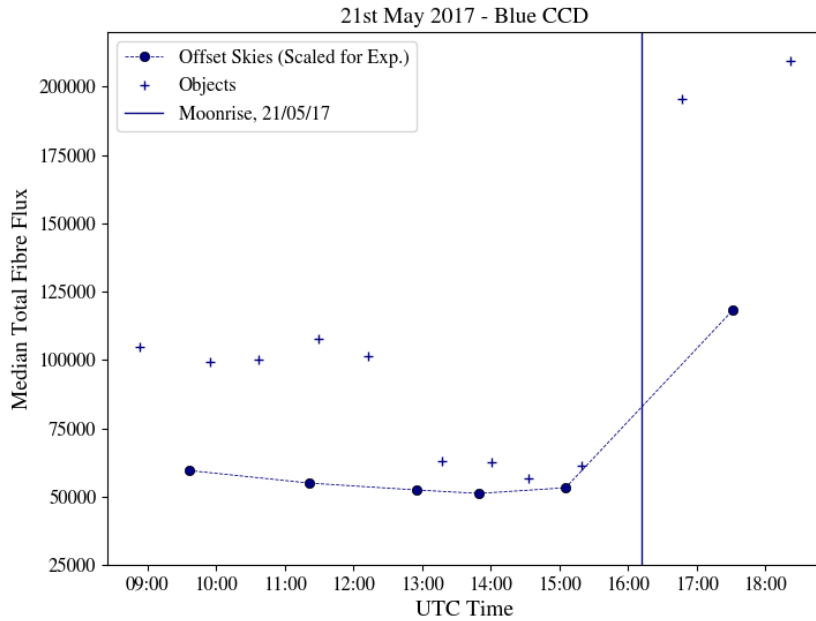


**Figure 3.12.** Plot of median fibre flux with time for the object and offset sky observations taken on the 21<sup>st</sup> May 2017. The object observations are plotted as crosses, and the offset sky observations are plotted as circles, connected by the dashed line. The time of moonrise on that night is indicated by the solid vertical line.

of the sky spectrum in each of the offset skies and object frames increases roughly linearly with time. Using this, we use the closest offset sky observations to each object frame, and interpolate or extrapolate to obtain the expected sky spectrum for that object frame given the linear increase in brightness observed (Appendix B.5.1). We can derive the sky flux at time of the source observation if we interpolate between sky observations before and after our source observation using:

$$S(t_{\text{Obs}}) = \frac{S(t_1)(t_2 - t_{\text{Obs}}) + S(t_2)(t_{\text{Obs}} - t_1)}{(t_2 - t_1)}, \quad (3.4)$$

where  $S(t_{\text{Obs}})$  is the sky flux at the time a particular object observation was taken,  $S(t_1)$  and  $S(t_2)$  are the fluxes of offset skies taken before and after the object observation respectively, and  $t_{\text{Obs}}$ ,  $t_1$  and  $t_2$  are the times the object observation, sky before the object observation and sky after the object observation were taken respectively. An example of this process is shown in Figure 3.13; the resulting sky subtracted object spectrum no longer has negative features.

We then follow a similar procedure as before to carry out the sky subtraction: we subtract the median sky spectrum from each fibre in the object frame,

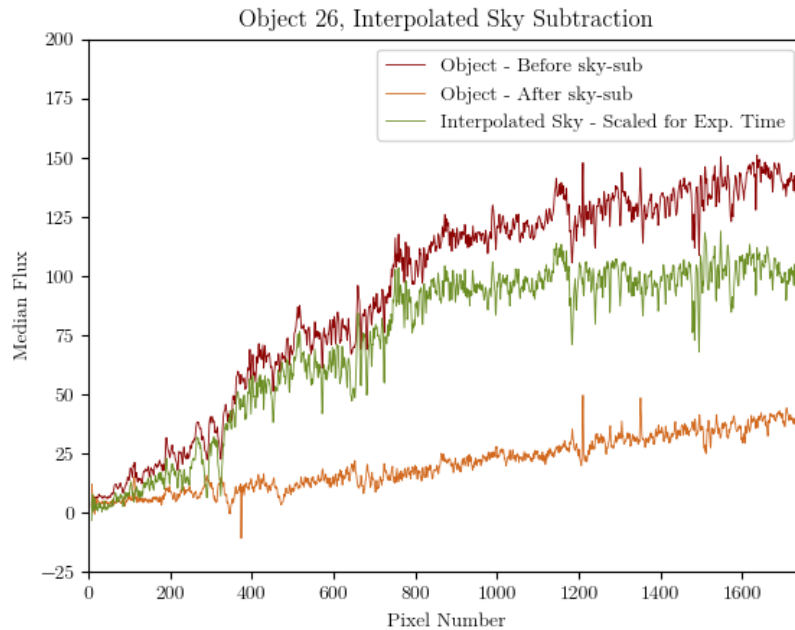


**Figure 3.13.** Example spectra of NGC 5584 taken on the 28<sup>th</sup> April 2016. The median spectrum is compared before sky subtraction (red) and after subtraction (orange). The interpolated sky spectrum for the time of the object observation is shown in green (see Appendix B.5.1 for more details).

after performing a cross-correlation to match up sky emission lines, but instead of using the master skies we use the interpolated or extrapolated skies created for each object frame affected by moonlight.

## 3.7 MASKING OF SKY LINE REMNANTS, DEFECTS AND LEFTOVER COSMICS

After the sky subtraction has been carried out, we perform an inspection of the data frames to check for any issues that require masking. We find three issues that need to be sorted out before we move on.

### 3.7.1 SKY LINE REMNANTS

Due to our method of creating a master sky file for each observing night, sky emission lines (which can change in brightness as the night progresses) are not always completely removed. By making sure we are removing them at the correct wavelength through cross-correlation, the remaining features are not huge, but still

appear similar to object emission lines, and therefore could confuse an algorithm during a spectrum fitting process. To avoid this being an issue, we go through the sky subtracted frames and mask any remnants of the sky subtraction process. An example of this is shown in Figure 3.14 for both the blue and red CCDs.

To choose which wavelengths to mask, we use the OH emission line catalogue of Rousselot et al. (2000). We check each sky emission line within our wavelength range in turn. If the line is close to a galaxy emission line of interest, then no remnant masking is performed so that no galaxy flux is erroneously removed; in those instances we trust the sky subtraction to have done as good a job as it can, because we don't want to risk removing parts of our galaxy emission line profiles. For example, in the blue end of the spectrum, there are only four sky emission lines within our wavelength range. Two of those four sky emission lines are close to galaxy Balmer emission lines, so no masking is performed in those cases to avoid removing useful flux. The red end of the spectrum has far more sky emission lines. In this case, we also use a flux cut to choose which lines to mask, since the catalogue of Rousselot et al. (2000) also contains the relative flux of these sky emission lines. Only the brighter sky emission lines are masked, as the fainter lines do not show up in our spectrum. The brighter lines are again assessed for their position relative to important galaxy emission lines, and if they are too close, they are not masked.

### 3.7.2 DEFECTS IN THE BLUE CCD

The blue CCD of the AAOmega spectrograph has two defects which cause features to appear consistently in the data. These defects mainly consist of NaNs in the final data, but some hot pixels slip through and can cause issues in the final data cubes. These features can be seen as the diagonal lines in the top panel of Figure 3.14. To sort these issues, we make sure the hot pixels are masked by performing a binary dilation of the NaNs in these defects by 1 pixel. The effect of this dilation is to essentially enlarge the mask by one pixel in each direction, as shown in Figure 3.15. This solves the problem and makes sure that no erroneous flux is included in the final data cubes.

### 3.7.3 LEFTOVER COSMIC RAYS

As discussed in Section 3.2, trial and error was required to find the balance between removing the contamination of as many cosmic rays as possible, whilst leaving the emission lines of our objects intact. Due to this cautious approach,

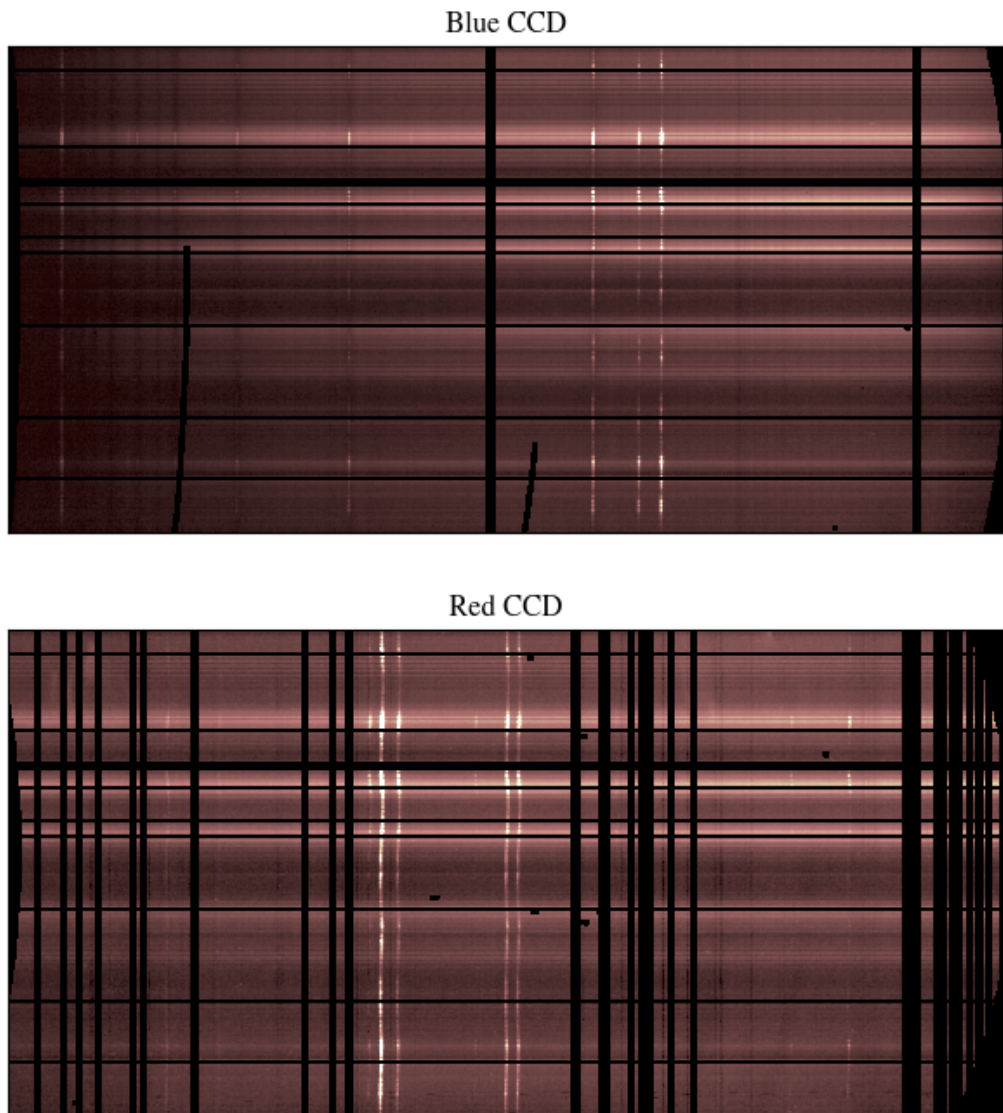


**Figure 3.14.** Examples of a blue (top) and red (bottom) CCD data frame after having the sky line remnants masked. Any place that has been masked with a NaN value is shown in black; the sky line masks are vertical black lines in both frames. The defects in the blue CCD can also be seen in the top panel as the jagged features in black rising from the bottom of the frame.

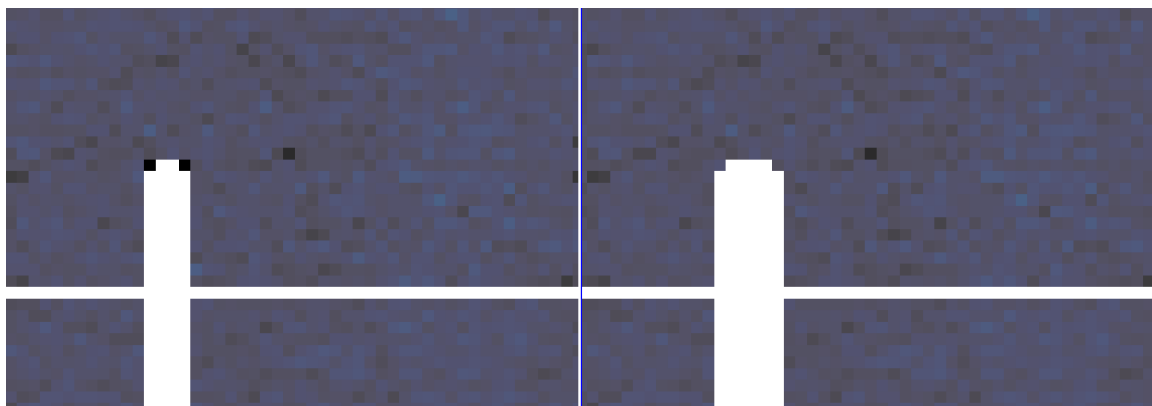


**Figure 3.15.** An example of how the issues caused by the defect in the blue CCD are removed. Left: Defect in the blue CCD before masking. Right: Defect after masking has been carried out using binary dilation.

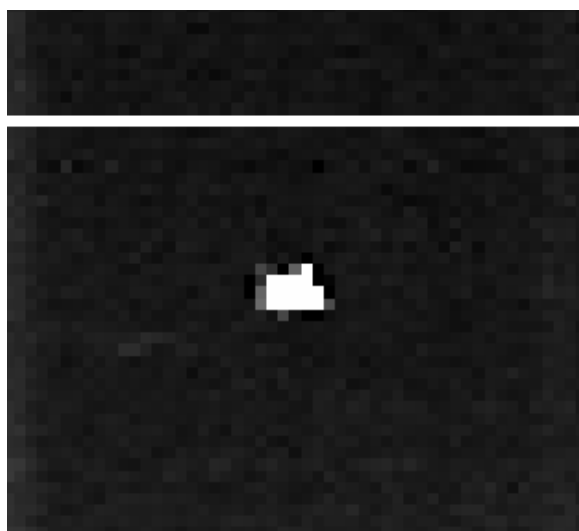


**Figure 3.16.** An example of a cosmic ray left in the data frames post running PyCosmic.

some cosmics slipped through the initial removal. We perform a by eye inspection of the data frames to search for any bright cosmics that may have slipped through PyCosmic, and mask them before moving on. Some of the leftover cosmics are large and exceptionally bright (see Figure 3.16 for an example), and therefore it is important that they are removed. NaN masks are manually applied to any cosmics spotted in each frame, using apertures in Starlink-GAIA.

### 3.8 FLUX CALIBRATION

After the sky subtraction has been completed, the next step in the reduction and calibration process is flux calibration. Flux calibration allows us to tie

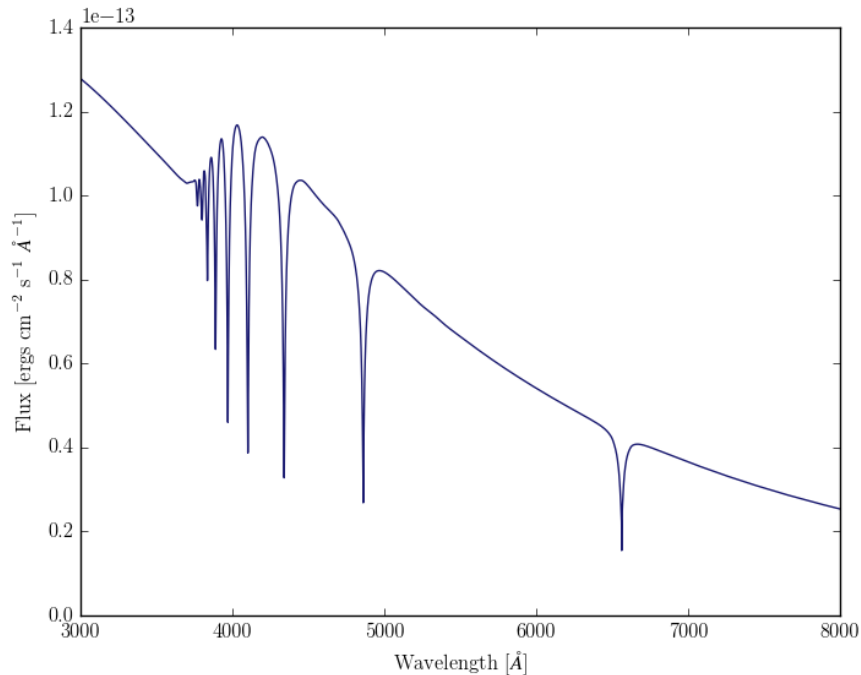


**Figure 3.17.** Spectrum for the standard star LTT3218, shown over the same wavelength range covered by our KOALA data, obtained by Moehler et al. (2014) using X-SHOOTER on the VLT.

the observations of our sources (in units of counts) to a physical unit system, and enables us to compare our spectra to those from other telescopes. This is done using flux standards: observations of standard stars that have accurate and well sampled spectra available.

During our two observing runs with KOALA, we observed the standard star LTT3218 on several nights. We found previous observations of LTT3218 from X-SHOOTER on the VLT (Moehler et al., 2014)<sup>4</sup>. The data spans a wavelength range from 3000 to 25 000 Å with 0.05 to 0.2 Å wavelength spacing, and is shown in Figure 3.17 over the range of 3000 to 8000 Å. We use this data to calibrate both the red and blue arms of our KOALA spectra.

To perform the flux calibration, we first need to extract the spectrum of the standard star from our KOALA observations (see Appendix B.6). The sky is subtracted using a blank area of sky within the flux standard observations to obtain a median sky spectrum, which is then subtracted from each fibre in the flux standard observations. The flux in the fibres containing the star are summed. Calibration curves are created by regridding the X-SHOOTER standard data for LTT3218 to

<sup>4</sup><https://www.eso.org/sci/observing/tools/standards/spectra/ltt3218.html>

match the wavelength resolution of our KOALA observations of the star, and then taking the ratio of the X-SHOOTER standard spectra to the KOALA spectra. The final calibration curves obtained from each flux standard observation are shown in Figure 3.18 for both the blue and red CCDs. The curves labelled 16, 17, 27 and 28 are from the first observing run, and those labelled 44 and 45 are from the second observing run. The shapes of the curves are slightly different between the two observing runs, and even between different days. However, we do not have a standard star observation for every observing night. Therefore, we choose the best curves from each observing run to apply to the data: the final chosen curves, 28 and 45, have the highest throughput of all the flux standard observations. In practice, using one calibration curve for all of the data from one observing run is not ideal, but we can attempt to deal with any resulting variations in flux level due to the difference in the calibration curves by further scaling the flux after this step. These final calibration curves are also multiplied by a factor of 120 before being applied to the data; this is to account for the exposure time of the flux standards (see Table A.1), which is included in the data cubing code. Without this factor being accounted for prior to the data cubing step, the final cube flux values end up lower than they should be.

Once we have our chosen flux calibration curves for each run and for each CCD, these are then applied to the data. Each pixel in the calibration curve is applied to each pixel in the data for each fibre. Since we saw above that the flux calibration curves are slightly different in flux and shape between the two observing runs, we apply a further flux scaling to each one, according to:

$$F'_i = \frac{F_i}{\langle F_i \rangle} \times \langle F_{\max} \rangle, \quad (3.5)$$

where  $F_i$  is the flux in a wavelength pixel in observation  $i$  of any galaxy field,  $\langle F_i \rangle$  is the average flux over all wavelength pixels in observation  $i$  of any galaxy field,  $\langle F_{\max} \rangle$  is the average flux over all wavelength pixels in the brightest observation of any galaxy field and  $F'_i$  is the scaled flux in a wavelength pixel in observation  $i$  of any galaxy field.

The units of the calibration curve are  $\text{ergs cm}^{-2} \text{s}^{-1} \text{ \AA}^{-1} \text{ count}^{-1}$ , so when each pixel in each fibre of our object spectra or standard star is multiplied by the corresponding pixel in the calibration curve, the data has physical flux units of  $\text{ergs cm}^{-2} \text{s}^{-1} \text{ \AA}^{-1}$ , and can now be compared to spectra from other telescopes.

Despite the efforts described here to make sure the flux calibration of the red and blue arms is as good as it can be, we find an offset in the calibration between the red and blue arms, due to the use of the two different CCDs to obtain the

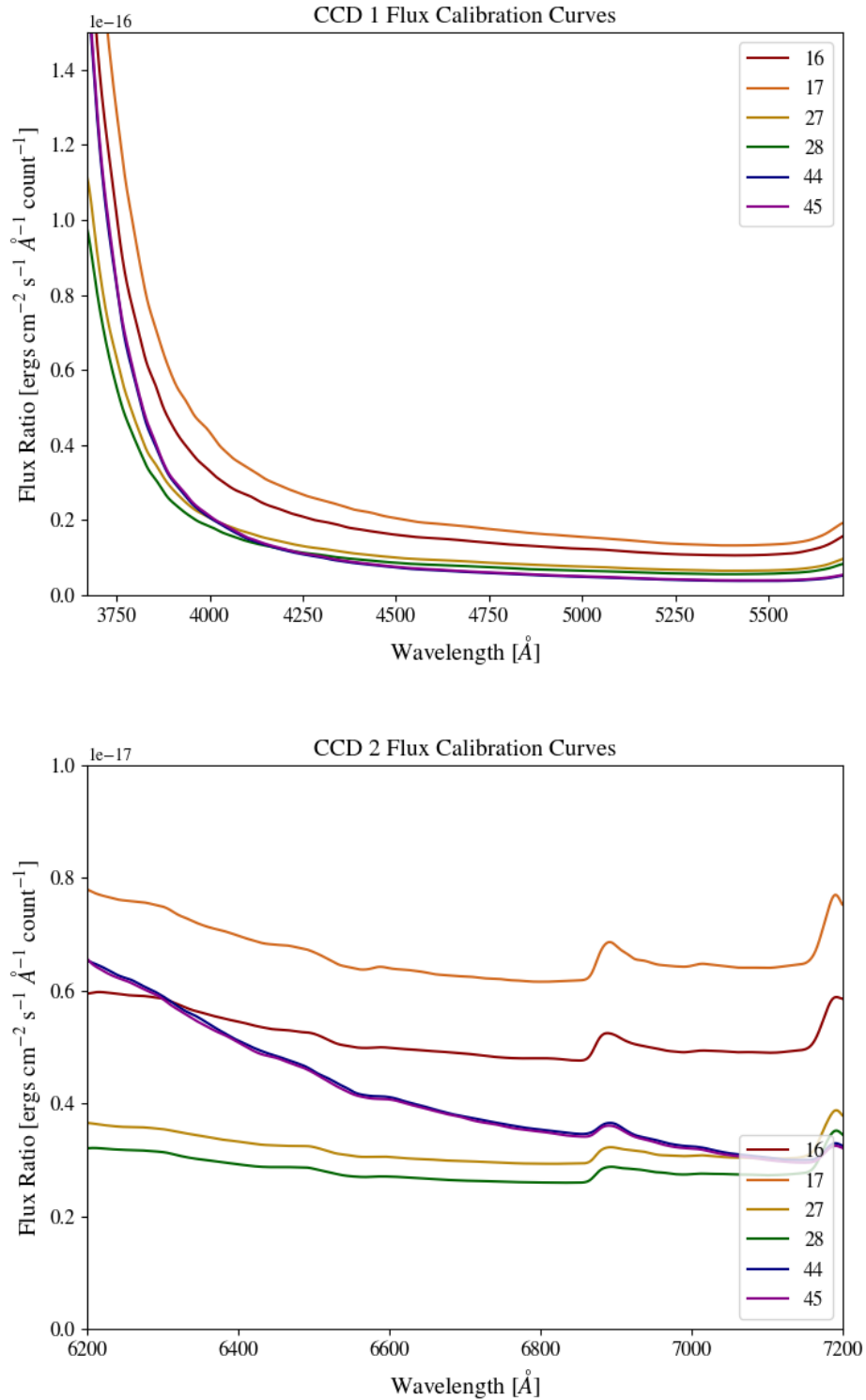


**Figure 3.18.** Smoothed calibration curves for each of the flux standard observations for the blue CCD (top) and the red CCD (bottom) taken during the two observing runs. The bumps and wiggles in the red calibration curves are due to atmospheric absorption features.

data. To address this offset, we look at the SDSS spectra that are available for our sources. The wavelength coverage of the SDSS overlaps our data and covers the gap between the CCDs, so we use this data to calibrate the blue end of our KOALA data to match the red. The SDSS spectra available for our primary sources are single fibre spectra, observed mostly within the central bulges of these galaxies. To compare the SDSS spectra with our KOALA data, we need to obtain a spectrum from our KOALA data using the same position on the sky and aperture size as the SDSS spectrum. However, we cannot simply use the RA and Dec of the SDSS spectrum to find the correct position in the KOALA cube, as there is a difference in the positional calibration between the SDSS and KOALA. Therefore, we need to find the correct position to place the aperture in the KOALA cube by eye. This was done using the following method:

- Obtain the SDSS g-band image of the source in question.
- Find the RA and Dec and fibre size from the headers of the SDSS fibre spectra for that source. Create and place an aperture the size of the fibre at the RA and Dec of the SDSS spectrum on the SDSS g-band image.
- Sum the KOALA data cube over the SDSS g-band wavelength range to obtain a KOALA g-band image.
- Use the aperture position on the SDSS g-band image and the features in the two images to place an aperture of the same size in the correct position on the KOALA g-band image.
- Use the aperture to extract a spectrum from the KOALA data cube at the chosen position in the KOALA g-band image.

Figure 3.19 shows an example of the match between the SDSS fibre spectrum position (left panel) and the placement of the KOALA aperture (right panel) for UGC 9215.

We tested a couple of ways to match the calibration of the blue and red arms using the SDSS fibre spectra; using a zero point correction, and using a first order fit. We first take the ratio of each arm of our extracted KOALA cube spectrum with the SDSS fibre spectrum. To get the zero point correction, we take the median of these ratios for each arm. To get the first order correction, we perform a straight line fit to the ratio for each arm. An example of the effect of each correction is shown in Figure 3.20. Both of these methods give much the same result, so we choose to apply the zero point correction to the final data to account for the difference between the red and blue arms.

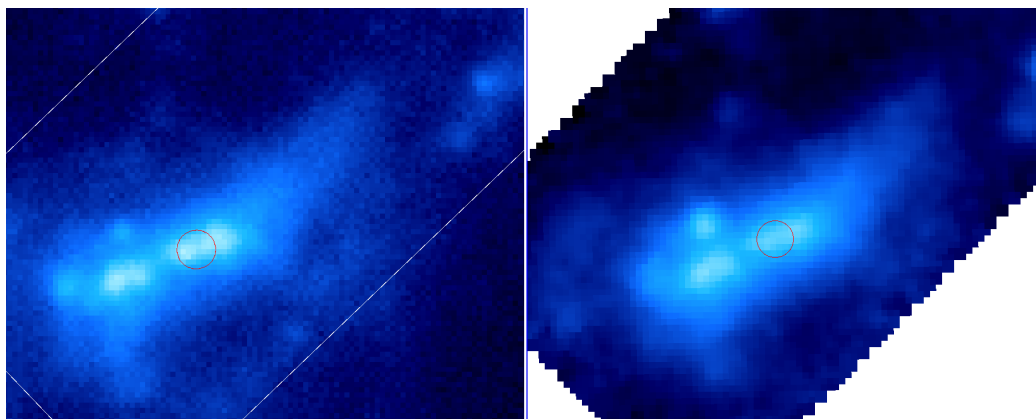


**Figure 3.19.** An example of the position match between the SDSS fibre spectrum and the aperture placed on the KOALA cube. The left panel shows the SDSS g-band image of UGC 9215, and the right panel shows the KOALA cube of the same source, summed over the wavelength range of the SDSS g-band. The red circle shows the position of the SDSS fibre spectrum in the left panel, and the matched KOALA spectrum in the right panel.

### 3.9 CREATING THE FINAL PRODUCT: DATA CUBES

The penultimate step in the process is to combine all of the individual data frames for each galaxy field into a data cube. The script used to do this was originally designed for SAMI (see Sharp et al. (2015) for full details), but has been adapted for use with the KOALA instrument, and was provided by the KOALA team.

To make the data cubes, the object frames need to be grouped together according to galaxy field. Each observation of a particular galaxy field needs to be entered into the cubing script with an offset value, which corresponds to how far it was dithered with respect to the previous observation. This is so that the fibres in each individual observation can be assigned to the correct position in the output pixel grid that the cube is built into. The first observation listed in the cubing script will be assigned to sit at the centre of the final pixel grid, with the subsequent observations dithered with respect to that central position. The flux in the fibres of each observation will be split up over the pixels in the output grid that the fibre area covers; this is done in turn for each observation and each wavelength slice until each wavelength slice is full and the final data cube has been created. Cubes are created for the blue and red CCDs individually, as the two wavelength ranges cannot be combined within the script. Therefore, the output from the script will be two data cubes for each galaxy field.

Prior to running the cubing script, we must convolve the red and blue frames to a common spectral resolution. The blue and red arms of the spectrograph

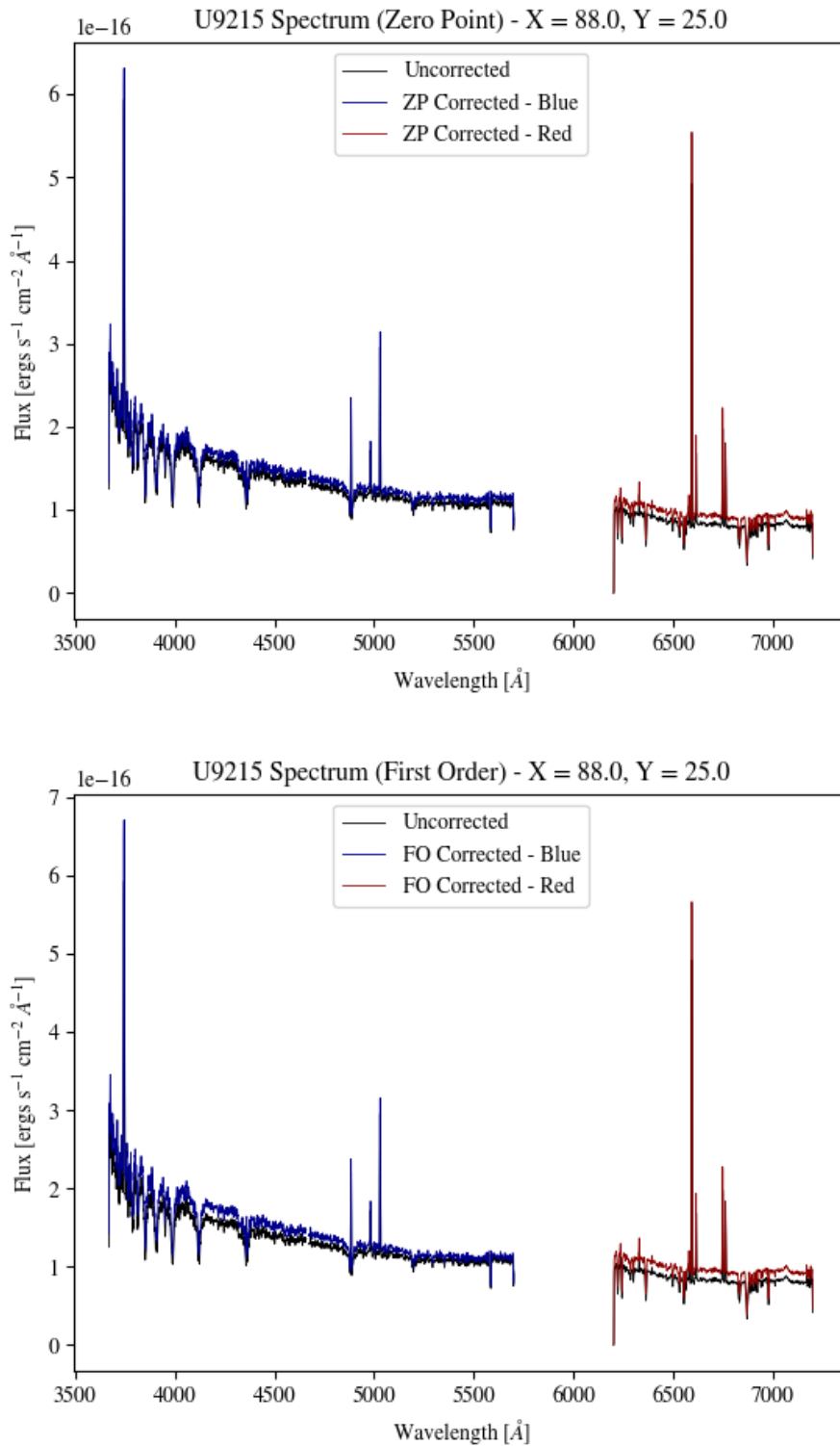


**Figure 3.20.** Examples of the spectrum of UGC 9215 with the zero point correction (top panel) and the first order correction (bottom panel) applied.

have different spectral resolutions, quoted as 2.181 Å and 1.208 Å respectively from the AAT<sup>5</sup>. However, these values have been shown to be inaccurate (van de Sande et al., 2017), so we calculate the actual resolutions for our data for each observing night. We do this using the ‘MFARC’ fields: we find the brightest, unblended emission lines in these frames and fit these lines with a Gaussian after removing the background flux level. The full-width half-maximum (FWHM) of the Gaussian gives the spectral resolution for that night. (These measurements were repeated at various positions across the CCD and at various wavelengths to make sure there was no large variation in the resolution.) The resolutions are provided in Table 3.2. The poorest resolution is for the blue frames from the 22<sup>nd</sup> May 2017 (FWHM of 2.93 Å). To ensure our data is consistent, all of the data obtained from the other nights in the blue CCD, and all of the data from the red CCD were convolved to a common resolution of 2.93 Å.

**Table 3.2.** Measurements of the FWHM of ‘MFARC’ lines for each observing night. With the AAOmega spectrograph set up to have central wavelengths of 4700 Å in the blue and 6750 Å in the red, the spectral resolution should be 2.181 Å and 1.208 Å respectively.

Observing Night	Measured FWHM [Å]	
	CCD 1	CCD 2
28/04/2016	2.59	2.02
29/04/2016	2.59	1.11
30/04/2016	2.54	1.61
01/05/2016	2.52	1.63
21/05/2017	2.91	1.68
22/05/2017	2.93	1.74
23/05/2017	2.92	1.73

The next step is to use the cubing script to create data cubes from the fibre spectra. This involves calculating the contribution that each fibre makes to each spaxel, and then summing over fibres and observations. In the standard approach, for each observation  $o$ , the contribution that fibre  $f$  makes to the spaxel at position  $(x, y)$  is determined by the geometrical overlap of the circular fibre profile with the square spaxel boundaries. The overlap area as a fraction of the total fibre area is denoted by  $F_o(x, y, f, \lambda)$ , so the total flux in the spaxel is given by:

$$g(x, y, \lambda) = \sum_{o,f} F_o(x, y, f, \lambda) g_o(f, \lambda), \quad (3.6)$$

<sup>5</sup>[https://www.aao.gov.au/cgi-bin/aaomega\\_calc.cgi](https://www.aao.gov.au/cgi-bin/aaomega_calc.cgi)

where  $g(x, y, \lambda)$  is the flux in the pixel at position  $x, y$  and wavelength  $\lambda$ , and  $g_o(f, \lambda)$  is the flux in fibre  $f$  at wavelength  $\lambda$  for observation  $o$ . The sum extends over all fibres and all observations.

One of the big changes we have made is to add an inverse variance weighting (IVW) technique when combining the data files to make the final cube for each galaxy. This is important because a significant fraction of our observations were made through thin cloud. These observations have reduced signal to noise ratio, but still contain useful signal. If we simply excluded all the poorer observations, we would be rejecting a lot of useful data; if we include all data, the total is down-graded by the lower signal to noise observations. The optimal approach is to use a weighted mean so that the poorer data is down-weighted, but not simply discarded.

Before we can use a weighted mean, the observations must be scaled so that they have the same expected value. Also, we want to form an optimal estimate of the data as it would have been with no cloud. So we use the average data in each observation to estimate the atmospheric transmission for that observation, and divide by this factor to match the observation that has maximum transmission. On the assumption that each observation is of the same patch of sky, the true total count in each observation should be the same. So the transmission factor for observation  $o$  is given by:

$$k_o = \frac{\sum_{f,\lambda} g_o(f, \lambda)}{\max_o \left( \sum_{f,\lambda} g_o(f, \lambda) \right)}, \quad (3.7)$$

where the sums extend over all fibres  $f$  and wavelengths  $\lambda$ , and the maximum is over the different observations,  $o$ . The scaled fluxes and variances for observation  $o$  are then given by:

$$\hat{g}_o(f, \lambda) = g_o(f, \lambda)/k_o \quad (3.8)$$

and

$$\hat{\sigma}_o^2(f, \lambda) = \sigma_o^2(f, \lambda)/k_o^2. \quad (3.9)$$

Now we can form the weighted mean to provide the minimum variance estimate of the total data cube:

$$\hat{g}(x, y, \lambda) = \frac{\sum_{o,f} F_o(x, y, f) w_o(f, \lambda) \hat{g}_o(f, \lambda)}{\sum_{o,f} w_o(f, \lambda)}, \quad (3.10)$$

where  $w_o(f, \lambda)$  is the weight for each fibre, wavelength and observation. We then

sum the variances over each fibre and wavelength, and set a single weight for each observation:

$$w_o = \frac{1}{\sum_{f,\lambda} \hat{\sigma}_o^2(f, \lambda)}. \quad (3.11)$$

The addition of this IVW technique to the cubing code gives us two potential settings to use when creating our data cubes:

- When  $IVW = 0$ , the original cubing code (provided by the KOALA team and adapted from the code used for SAMI) is enabled.
- When  $IVW = 1$ , the IVW version of the code (which introduces a per observation weighting, as described by Equation 3.11) is enabled.

Using data cubes of UGC 9215 created using both the original and IVW methods, we check to make sure flux is being conserved correctly with the new method. The results of this are shown for a small wavelength section in the red and blue ends in Figure 3.21. When compared, both methods seem consistent in conserving flux. We then tested this new cubing method on target field 2 of NGC 5584, a galaxy field that was affected by bad weather. Figure 3.22 compares a slice of the data cube for this source, with and without using the IVW technique. When directly compared, the cube created using the IVW method has less noise overall in the image than the cube created with the original cubing method, showing that the noisy data is indeed being down-weighted by the new IVW technique.

Once the cubes have been created for both the blue and red arms, we combine the two arms together ourselves to make one complete data cube for each galaxy field. We regrid the blue and red on the same wavelength scale. The red arm has a finer wavelength scale (0.57 Å) than the blue, so we use the blue wavelength scale (1.04 Å) for the whole cube i.e. we degrade the red arm. Since the data was convolved to a common resolution of 2.93 Å at an earlier stage in the reduction process, the final data products are finally complete and ready to be analysed.

## 3.10 EXAMPLE RESULTS FROM THE FINAL DATA CUBES

Now that we have the final data cubes reduced and calibrated, we can take a look at the information that they can provide. We take the data cube of one of our sources, UGC 9215, as an example to show what we can see within this data.

Figure 3.23 shows flux maps of UGC 9215, from left to right focusing on the OII line, a section of the continuum, and the H $\alpha$  and NII lines. The maps

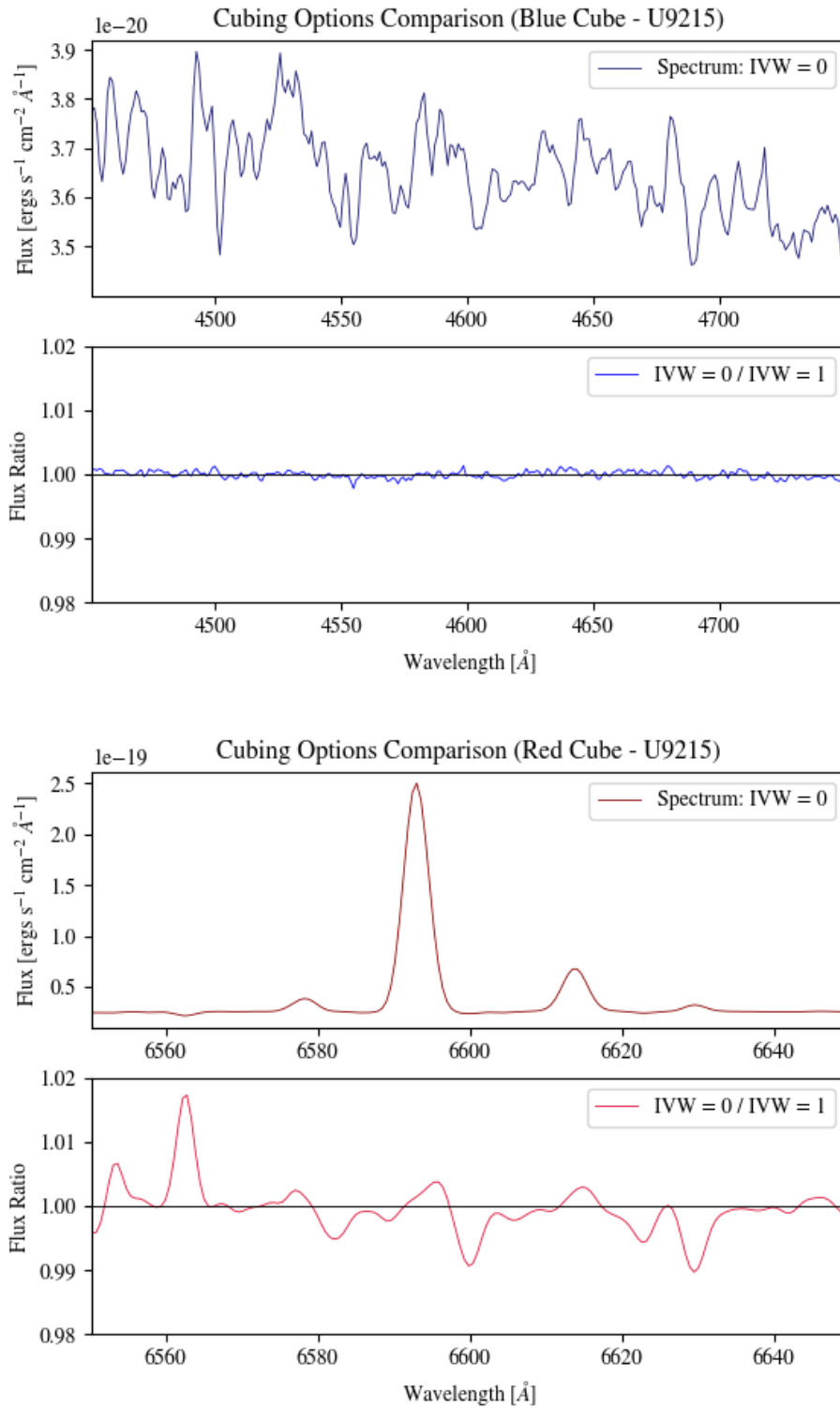


**Figure 3.21.** Comparisons between the original and IVW cubing techniques for galaxy UGC 9215. The upper two panels show a section of the blue wavelength range, and the bottom two panels show a section of the red wavelength range. Ratios of the spectra for the original and IVW cubing methods are shown in the second and fourth panels, and are shown to be near a 1:1 ratio, shown as the black horizontal line.

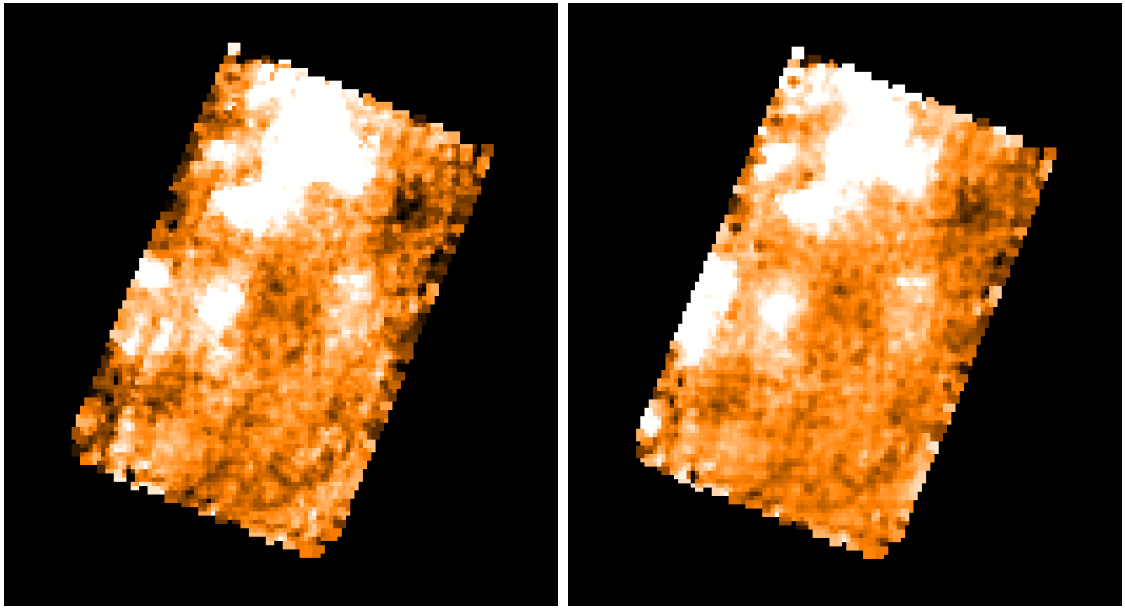


**Figure 3.22.** The cube of target field 2 of NGC 5584 sliced at  $4861 \text{ \AA}$  ( $H\beta$  emission). Left and right panels show without and with combining the data using the inverse variance weighting technique.

showing OII and  $H\alpha + \text{NII}$  were created by performing a simple sum of the spectrum in each spaxel. This sum extended approximately  $30 \text{ \AA}$  on either side of the OII and  $H\alpha$  lines. The continuum map was also created using a simple sum of the spectrum in each spaxel, but shows an approximately  $100 \text{ \AA}$  range of the continuum in the blue end of the cube, centred on  $4480 \text{ \AA}$ .

The continuum map in Figure 3.23 shows light being emitted from both the stars and gas in the galaxy. The emission from the bulge and spiral arms can be seen as the bright emission in orange and yellow. The maps of OII and  $H\alpha + \text{NII}$  show the emission from the gas in this source. The two maps, especially the  $H\alpha + \text{NII}$  map, show smaller areas of intense emission within the spiral arm and bulge of the galaxy. These are HII regions, areas of ionised gas due to intense star formation. These regions possess very strong emission lines from the ionised gas.

Figure 3.24 shows example spectra from two regions of the data cube for UGC 9215; the bulge (top panel) and an HII region within the spiral arm (bottom panel). These spectra were obtained by summing a square of 9 pixels in each of these regions. Emission lines of interest are labelled in black on both spectra. There are clear differences to be seen between these two regions. The spectrum from the bulge possesses features from the stars in the galaxy, which can be seen as the absorption features appearing from the beginning of the spectrum to approximately  $4400 \text{ \AA}$ . These features appear as the stars in the galaxy age. By contrast, the spectrum for

the HII region has a very flat continuum with very few features from the stars, due to the content of these regions being very young, hot stars. Some of the emission lines are far brighter in the HII region than in the bulge. The Balmer series in the HII region is brighter than in the bulge, with the series detectable down to  $H\eta$ . The OIII doublet is also far brighter than in the bulge.

The large variety of emission lines present in these spectra can be used to examine a number of properties of the source in question. The Balmer emission lines can be used to probe the dust attenuation law of the source by investigating their deviation from their intrinsic ratios. Oxygen, hydrogen, nitrogen and sulfur lines can be used with various calibrators to investigate the metallicity of the source. These emission lines can also be used to probe the excitation of the source. We will use these emission lines to investigate these properties in Chapter 4.

### 3.11 CONCLUSIONS

In this chapter, we have described in detail the data reduction and calibration process for data taken with the KOALA IFU. We adapted some scripts from the KOALA team to better suit our needs, and created other scripts from scratch to perform parts of the process. Problems encountered during the process, and the methods used to solve them are also described. We show the quality of the final output of the data reduction and calibration process, and briefly describe what can be achieved using that final product.

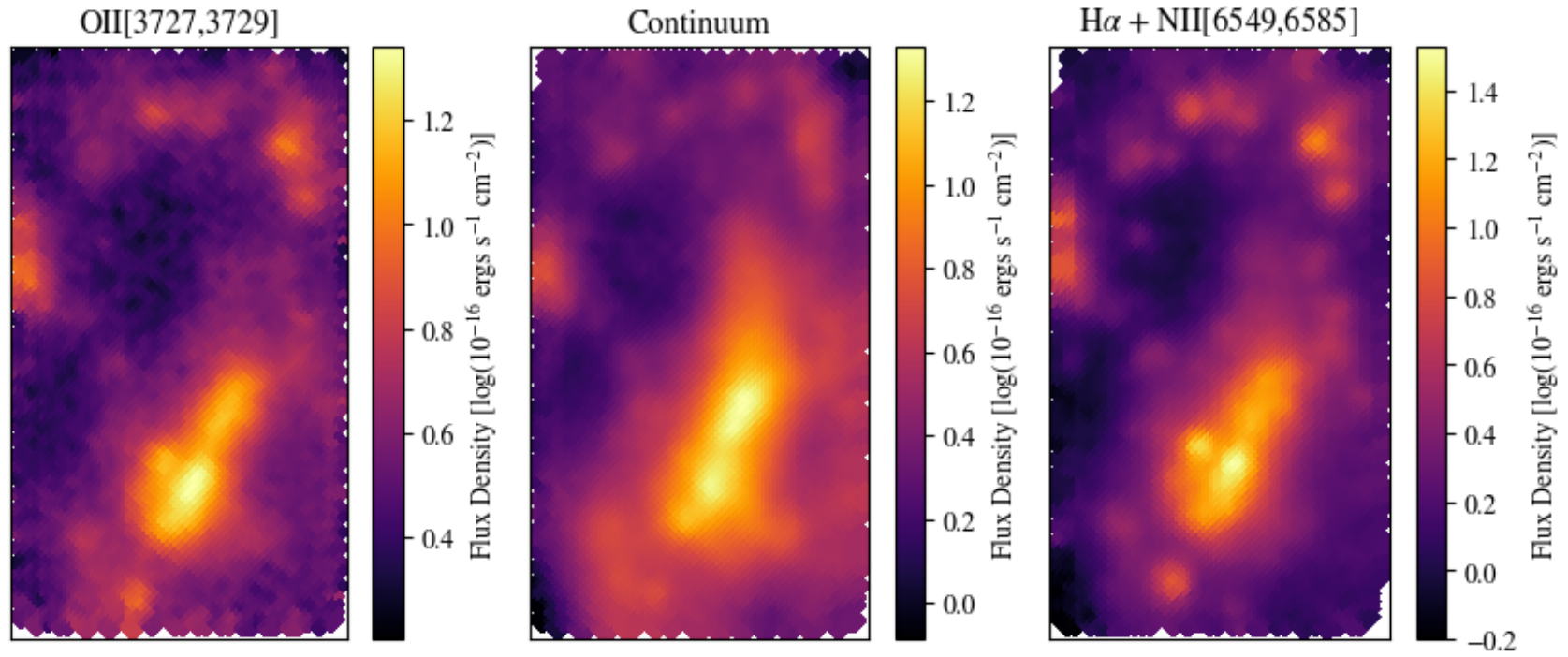


**Figure 3.23.** Example flux maps of the galaxy UGC 9215. The left panel shows a map of the OII emission line, the middle panel shows a map of the section of the continuum, and the right panel shows a map of the H $\alpha$  and NII lines.

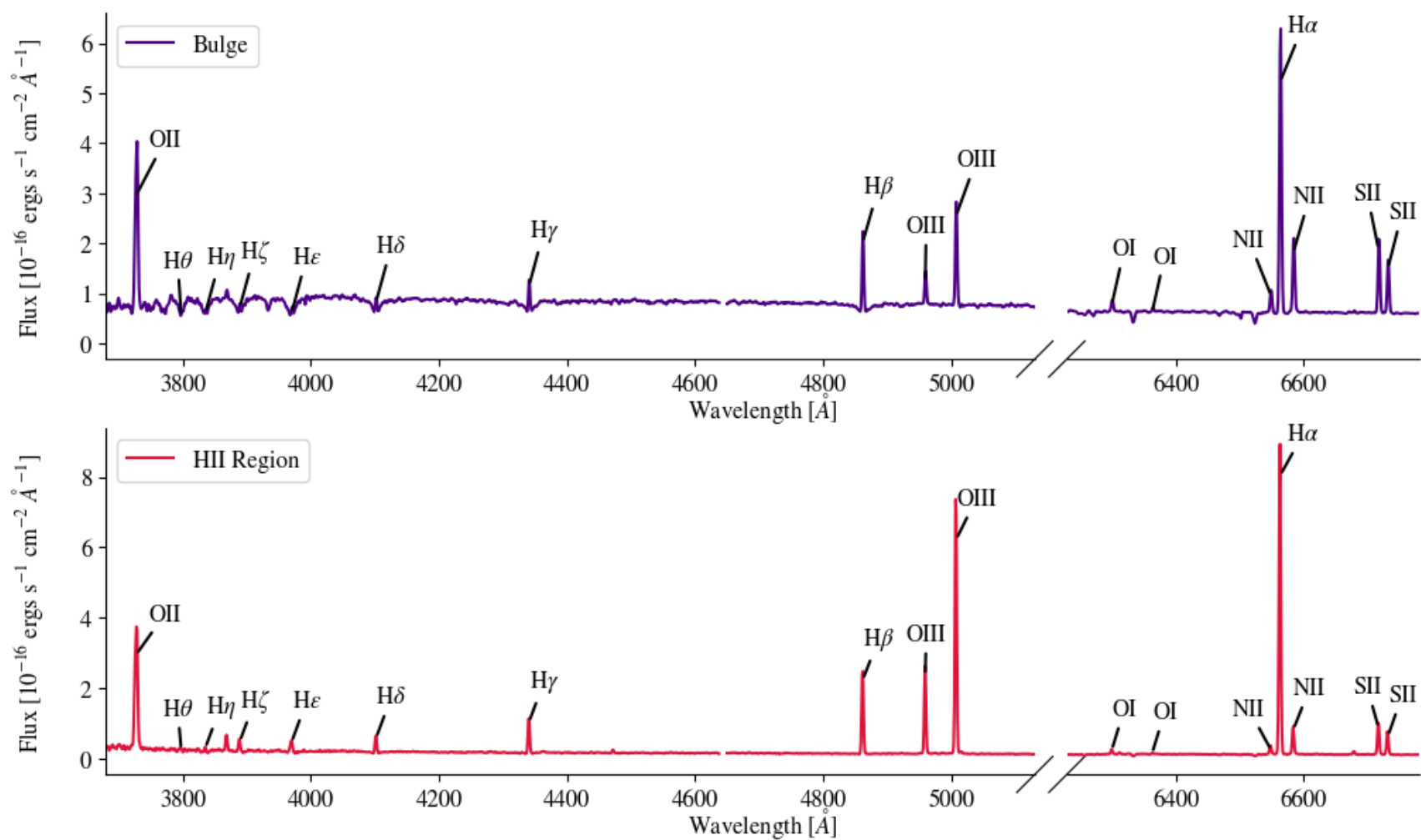


**Figure 3.24.** Example spectra from two regions within the galaxy UGC 9215. The top panel shows a spectrum obtained from the bulge of the galaxy, and the bottom panel shows a spectrum obtained from a HII region within the spiral arm of the galaxy. The names and positions of emission lines of interest are shown in black on both panels.

## CHAPTER 4

# INVESTIGATING THE PROPERTIES OF BADGRS USING IFU DATA

---

---

In this chapter we will use the reduced and calibrated IFU data cube of UGC 9215, one of the main sample of BADGRS outlined in Chapter 2, to demonstrate what kinds of properties we can investigate with this sort of data.

### 4.1 EXTRACTING GALAXY PROPERTIES FROM IFU DATA CUBES

There is a wealth of information that can be obtained from a galaxy spectrum, using both the continuum, which allows you to probe the stellar population and dust in a galaxy, and the emission and absorption lines, which allows you to probe the gas and stars in a galaxy, depending on the source of the line. To access this information, we need to fit the continuum and lines of the spectra in each pixel of the data cube. This can be done in a simplistic fashion with a subtraction of the continuum in the immediate area around the emission lines. However, this can be inadequate if there are prominent spectral features coming from the stellar component in the vicinity of the lines you are interested in. To deal with this, a more common approach is to fit the continuum using stellar population and dust modelling, to try and more accurately reproduce the features seen in the spectrum. This can then be subtracted from the spectrum, allowing the emission line features to be fit, often with a Gaussian profile, without interference from the continuum. This has the added bonus of allowing the fit to access information about the stellar continuum, such as stellar age, dust properties and velocity of the stars. We use this approach with the data cube for UGC 9215.

### 4.1.1 VORONOI BINNING

We could apply a fitting routine to all of the pixels in the data cube of UGC 9215. However, some of these pixels have far less signal than others, so it would be difficult to obtain meaningful information from those lower signal pixels. This would also be very computationally expensive to fit all pixels in the cubes which have a signal; the data cube for UGC 9215 is 140 by 140 pixels, and whilst not all of these have signal because of the inclination of the KOALA field, this would still mean fitting thousands of spectra, some of which might not even have reliable signal. To reduce the computational load, and try to ensure the best results are obtained from the fitting routines, we use Voronoi binning on the data cube.

Voronoi binning is a technique used to spatially bin two-dimensional data, and higher dimensions of data, such that there is a consistent signal to noise ratio in all spatial bins (Cappellari et al., 2003). We apply this technique to our data cube using the Python version of the VORBIN package<sup>1</sup>. To define the signal to noise of our Voronoi bins, we use a region of the spectrum around the H $\beta$  and OIII[ $\lambda$ 5007] lines. The target signal to noise, TargetSN, is defined as:

$$\text{TargetSN} = \text{SN} \times \sqrt{N_{\text{slices}}}, \quad (4.1)$$

where SN is the signal to noise ratio we desire and  $N_{\text{slices}}$  is the number of wavelength slices of the spectrum used to define the signal to noise of the bins. The result of the Voronoi pixelation is shown in Figure 4.1 for UGC 9215 for an SN of 6 and an  $N_{\text{slices}}$  of 240. This figure shows the positions and sizes of the new spatial bins and compares the original signal to noise of each pixel to the new signal to noise of the Voronoi bins. The signal to noise of the individual pixels achieved a maximum signal to noise of approximately 70 before Voronoi binning; after this, the new spatial bins at minimum possess a signal to noise of approximately 70, with the TargetSN, being 92.95. This process turns several thousand pixels into 304 spatial bins. Figure 4.2 shows a comparison of the original 0.5'' pixels of the UGC 9215 data cube compared to the new Voronoi bins. An example of the effect the new spatial bins have on the signal to noise can be seen in the top right corner of the cube; a number of low signal to noise pixels are amalgamated into a higher signal to noise bin.

Now that we have our new spatial bins defined for the UGC 9215 data cube with a consistent signal to noise ratio, we can fit the spectrum in each bin and derive properties from those fits.

---

<sup>1</sup>Available for download at <https://www-astro.physics.ox.ac.uk/~mxc/software/#binning>.

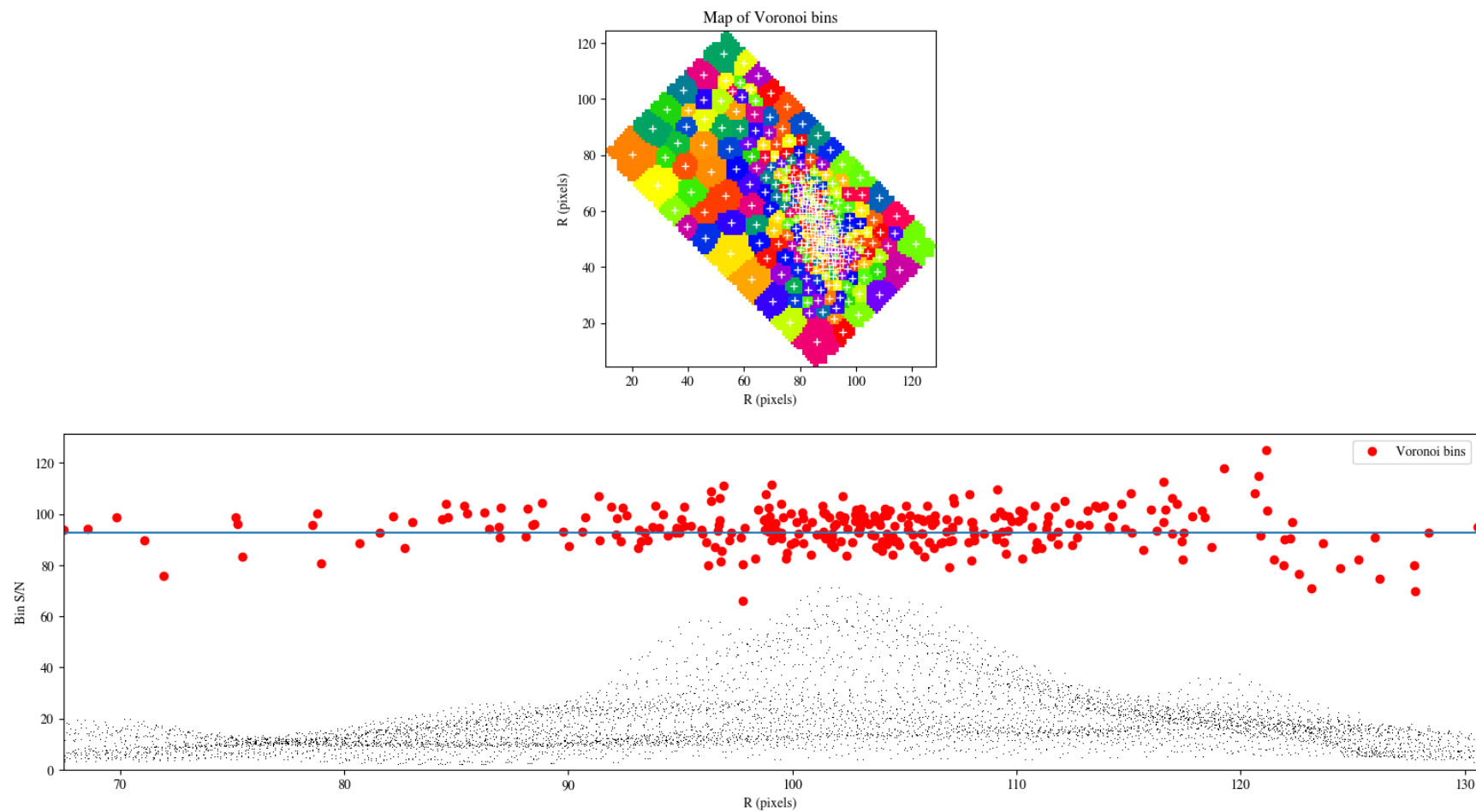


**Figure 4.1.** Result of Voronoi pixelation using the VorBin package on the UGC 9215 data cube, for an SN value of 6. The top panel shows the positions and size of the new spatial bins. The bottom panel shows the signal to noise of the individual pixels in black, and the signal to noise of the new spatial bins in red, with the TargetSN indicated with the blue horizontal line.

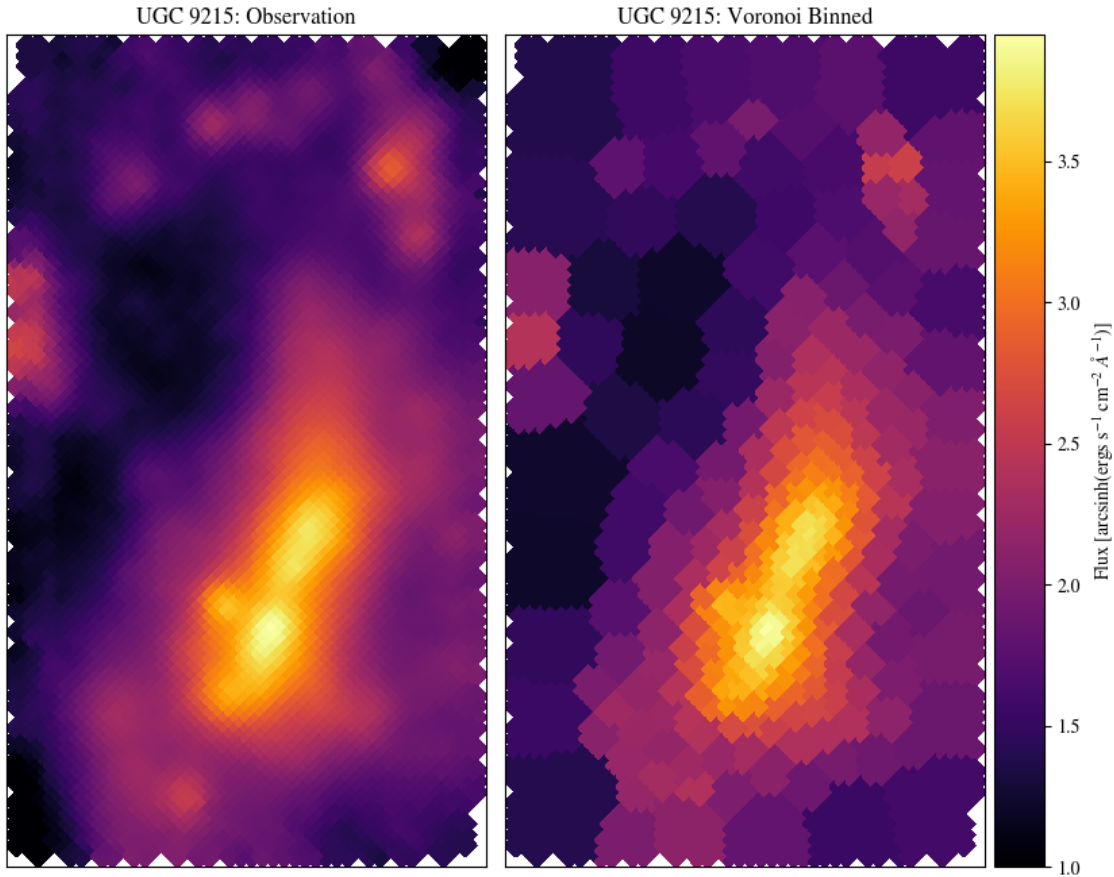


**Figure 4.2.** A comparison between the original spatial pixels of UGC 9215 (left panel) and the new Voronoi bins (right panel). Here we set  $\text{SN} = 6$ .

### 4.1.2 pPXF

To fit the spectra of UGC 9215, we use the Python implementation of pPXF<sup>2</sup> (Cappellari et al., 2004; Cappellari, 2017). We adapt an example pPXF script for use with spectra from the KOALA instrument. We fit the spectra in each spatial bin of our data cube using the MILES library of stellar population models (Vazdekis et al., 2010). The models we use range in age from 0.063 Gyr to 12.59 Gyr (we exclude templates that have ages older than the Universe) and metallicity  $[\text{M}/\text{H}]$  (which is a measure of the total abundance of metals to hydrogen) from -1.71 to 0.22. An  $[\text{M}/\text{H}]$  of 0 is equivalent to solar metallicity, -1.71  $[\text{M}/\text{H}]$  is  $0.02 Z_{\odot}$  and 0.22  $[\text{M}/\text{H}]$  is  $1.58 Z_{\odot}$ . Errors could be introduced by the stellar library if there are imperfections in the stellar templates, or if the ages and metallicities of the templates are not sampled well enough for our sources.

<sup>2</sup>Available for download at <https://www-astro.physics.ox.ac.uk/~mxc/software/#ppxf>.

**Table 4.1.** Mean line fluxes for the UGC 9215 data cube. The errors were calculated by adding the line errors on each spatial bin in quadrature and dividing by the square root of the number of spatial bins to get an approximate error on the mean for each line.

<b>Line</b>	<b>Flux</b>	<b>Error</b>	<b>Line</b>	<b>Flux</b>	<b>Error</b>
	[ $10^{-18}$ ergs s $^{-1}$ cm $^{-2}$ ]			[ $10^{-18}$ ergs s $^{-1}$ cm $^{-2}$ ]	
<b>OII</b>	254.1	7.27	<b>OIII</b>	252.27	1.90
<b>H<math>\epsilon</math></b>	15.6	1.30	<b>OI</b>	14.67	0.96
<b>H<math>\delta</math></b>	23.04	1.18	<b>NII</b>	92.45	1.13
<b>H<math>\gamma</math></b>	44.67	1.13	<b>H<math>\alpha</math></b>	370.86	1.76
<b>H<math>\beta</math></b>	103.98	1.25	<b>SII</b>	109.59	1.15

We allow the Balmer emission lines and emission line doublets to be free parameters. By default, only the Balmer lines down to H $\delta$  are fit, but we find that this causes the H $\beta$ , H $\gamma$  and H $\delta$  lines and the continuum around the higher order Balmer lines to be fit poorly. Therefore, to prevent the higher order Balmer lines from causing a bias in the continuum fit, we allow pPXF to fit Balmer lines down to H $\theta$ . The reddening for the stars and gas are applied separately within pPXF; we allow the stellar reddening to be fit with the Calzetti attenuation law, and do not assume any reddening law for the gas component, as we want to probe this law with the Balmer decrement. Additive polynomials of degree 10 are allowed to fix any issues with calibration; this will help with any lingering problems caused by scattered light at the very blue end of our wavelength range.

pPXF outputs the velocity and velocity dispersion of the stellar component of the spectrum, the weighted age of the stellar population and weighted metallicity of the templates that make up the best fitting spectrum, and the flux, flux error, velocity and velocity dispersion of each fitted emission line in the spectrum. Visual outputs are also produced for each bin; examples of these are shown in Figures 4.3-4.5 for bin 0. Figure 4.3 shows the full spectrum fit output from pPXF, Figure 4.4 shows zoomed in panels of the fits to key emission lines, and Figure 4.5 shows the metallicity and stellar age of the most highly weighted templates pPXF used to fit the stellar component of the galaxy.

Mean line fluxes and their errors for UGC 9215 are shown in Table 4.1. Emission line fluxes for the emission lines of interest are shown in Figure 4.6 for all Voronoi bins. Blank bins show undetected lines. Line doublets are summed together. These line fluxes will be used in subsequent sections to investigate the properties of the galaxy.

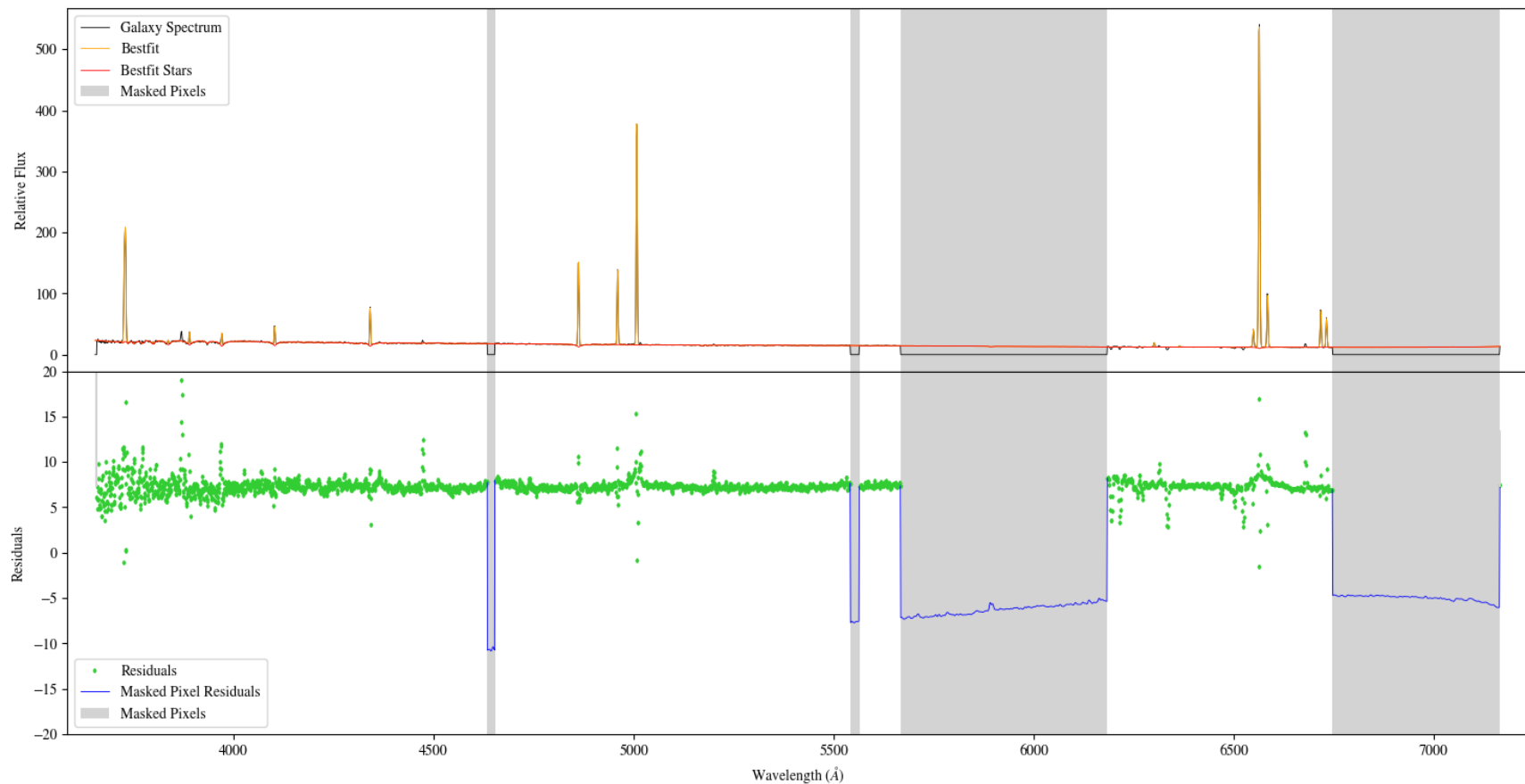


**Figure 4.3.** Output full spectrum fit from pPXF for spatial bin 0 of UGC 9215. The top panel shows the galaxy spectrum in black, the best fit to the stars and gas in yellow, and the best fit to the stars in red. The bottom panel shows the residuals between the best fitting model and the galaxy spectrum in green, with the masked residuals in blue. The masked regions are shown in grey shading in both panels.

## 4.2 INVESTIGATING THE DUST LAW OF UGC 9215

As mentioned in Section 4.1.2, we chose not to assume a reddening law for the gas component when fitting the spectra of UGC 9215, as we wish to probe this using the Balmer lines and their ratios. We will compare with a model based on the modified reddening law of Salim et al. (2018), which is a parameterisation of Calzetti et al. (2000). We will investigate the *blue but dusty* paradox and determine if this galaxy deviates from the Calzetti et al. (2000) law.

### 4.2.1 MODELLING THE REDDENING LAW

Our model is as follows. For each spatial bin in our Voronoi binned data cube, we have measurements of the first four Balmer emission lines: H $\alpha$ , H $\beta$ , H $\gamma$  and H $\delta$ . These emission line measurements will include some unknown amount of reddening; we designate these observed fluxes  $F_{\text{obs},i}$ , where  $i = 1, 2, 3, 4$  and H $\alpha$  is  $F_{\text{obs},1}$ , H $\beta$  is  $F_{\text{obs},2}$ , H $\gamma$  is  $F_{\text{obs},3}$  and H $\delta$  is  $F_{\text{obs},4}$ .

The intrinsic non-reddened line strengths of each Balmer emission line, are linked by standard ratios (Storey et al., 1995). We relate these standard ratios to the pre-reddened fluxes,  $F_i$ , using an unknown normalising flux,  $F$ , and four constants,  $a_i$ , with the following equation:

$$a_i = \frac{F_i}{F}. \quad (4.2)$$

For convenience we set one of these ratios to be 1, and set the other three constants using the values for an electron density of  $10^2 \text{ cm}^{-3}$  and a temperature of 10,000 K from Groves et al. (2012). These constants are shown in Table 4.2. The attenuation,  $A_i$ , of each line is given by:

$$A_i = k(\lambda_i) \times E, \quad (4.3)$$

where  $E$  is the unknown  $E(B - V)$  reddening, in magnitudes, of the spatial bin being modelled, and  $k(\lambda_i)$  is the modified Salim et al. (2018) reddening law, evaluated at the wavelength  $\lambda_i$ . This is given by:

$$k(\lambda_i) = k_{\text{Cal}}(\lambda_i) \frac{R_V}{R_{V,\text{Cal}}} \left( \frac{\lambda_i}{5500 \text{ \AA}} \right)^\delta, \quad (4.4)$$

where  $\delta$  is the modified slope of the Calzetti reddening law,  $k_{\text{Cal}}(\lambda_i)$  is the Calzetti reddening law and  $R_V$  and  $R_{V,\text{Cal}}$  are the ratios of total to selective extinction for the Salim and Calzetti laws respectively. The equation used to derive  $R_V$  is given in Section 1.3. We use the Salim et al. (2018) value of 4.05 for  $R_{V,\text{Cal}}$ . We do not include

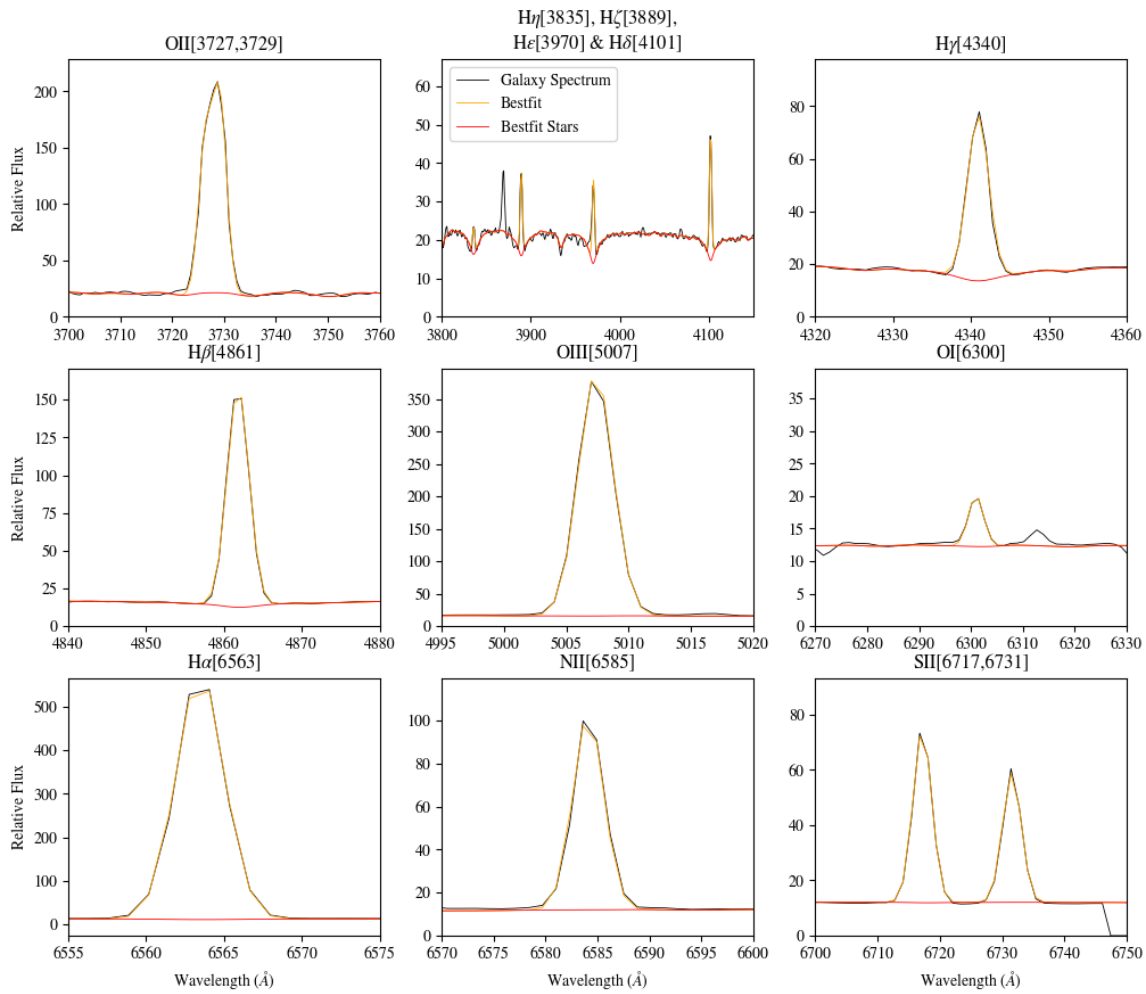


**Figure 4.4.** Examples of emission line fits from pPXF for spatial bin 0 of UGC 9215. The black line shows the galaxy spectrum, the yellow line shows the best fit to the gas and stars, and the red line shows the best fit to the stars.

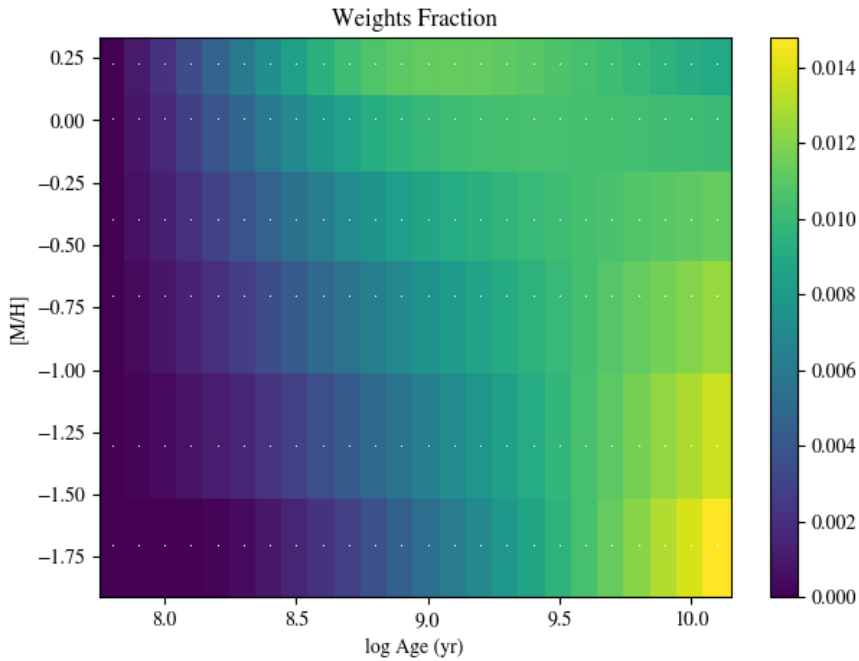


**Figure 4.5.** Output template weights from pPXF for spatial bin 0 of UGC 9215, indicating the combination of Vazdekis et al. (2010) templates which best represent the KOALA spectrum for this spatial bin.

a term for the strength of the UV bump in Equation 4.4 as our wavelength range does not extend far enough into the UV to constrain a UV bump with our model.

This model gives us three unknowns: the normalising flux  $F$ , the reddening  $E$ , and the modified slope  $\delta$ . We then have our four measurements; the observed fluxes for each spatial bin,  $F_{\text{obs},1}$ ,  $F_{\text{obs},2}$ ,  $F_{\text{obs},3}$  and  $F_{\text{obs},4}$ . To solve for the unknowns, we need to calculate the reddened fluxes within our model,  $F_{\text{red},i}$ :

$$F_{\text{red},i} = F_i \times 10^{-0.4A_i} = F a_i \times 10^{-0.4Ek(\lambda_i, \delta)}. \quad (4.5)$$

We then vary  $F$ ,  $E$  and  $\delta$ , performing a  $\chi^2$  minimisation, where the  $\chi^2$  is given by:

$$\chi^2 = \sum_i \frac{(F_{\text{obs},i} - F_{\text{red},i})^2}{\sigma_i^2}, \quad (4.6)$$

where  $\sigma_i$  is the error on the observed flux,  $F_{\text{obs},i}$ . This process is performed for every spatial bin in the data cube of UGC 9215, such that we obtain the best fitting values of  $F$ ,  $E$  and  $\delta$  for all bins.

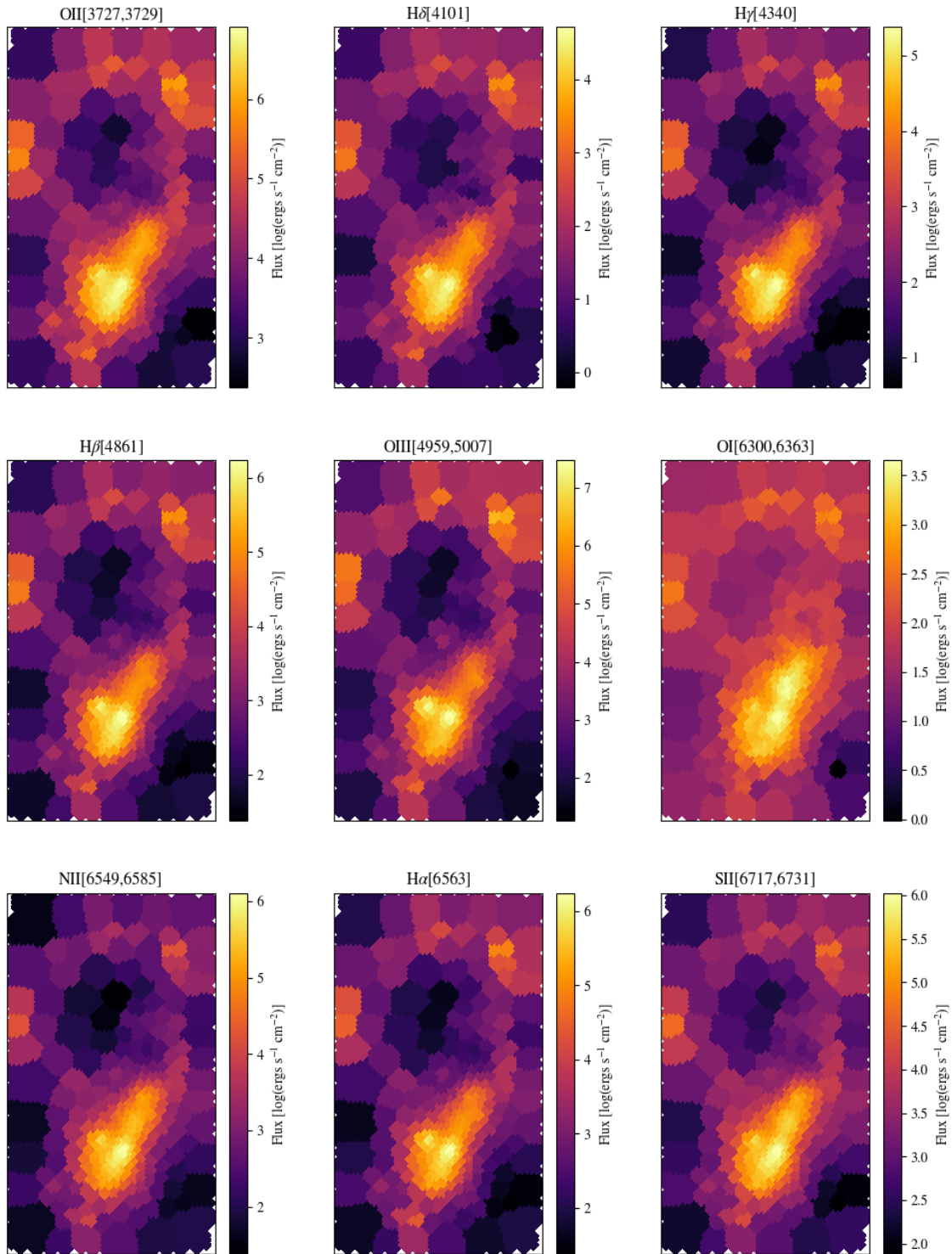


**Figure 4.6.** Fitted line flux values from pPXF for all spatial bins of UGC 9215. Each panel shows an emission line of interest from our galaxy spectrum.

**Table 4.2.** Constants  $a_i$  which encode the standard Balmer line ratios for  $H\alpha$ ,  $H\beta$ ,  $H\gamma$  and  $H\delta$  in order from  $a_1$  to  $a_4$ . The values shown relate to an electron density of  $10^2 \text{ cm}^{-3}$  and a temperature of 10,000 K (Groves et al., 2012).

Constant $a_i$	Value
$a_1$	1.000
$a_2$	0.350
$a_3$	0.164
$a_4$	0.091

#### 4.2.2 FITTING $F$ , $E$ AND $\delta$

We apply the model described above within Python, using the LMFIT package to perform the minimisation process. We apply some constraints to the values of  $F$ ,  $E$  and  $\delta$  to make sure the values produced make physical sense. For  $F$ , we set the minimum value allowed to be zero, such that we do not produce negative fluxes. We set the same constraint for  $E$ , as a negative value of reddening is similarly unphysical. Finally, for  $\delta$ , we set a minimum value of -5.0, to prevent anything more extreme being fit. We also set a maximum value of 0.7, which is the point at which the reddening curve begins to turn over and produce bluer fluxes (as discussed in Section 1.3.3), which is again unphysical. We use the confidence interval functionality in LMFIT to avoid dealing with edge effects caused by the constraints on the parameters.

The best fitting parameters for each bin are shown in Figure 4.7. The gray bins show where the model fit was unconstrained. Most bins are constrained in  $F$  and  $E$ , however, the constraint on  $\delta$  is poor. The bulge region seems to be where the model has the most success with constraining a value of  $\delta$ ; it mainly varies between approximately -1 and 0.7 in this region. The lack of constraint on  $\delta$  is not surprising; we have three variables, and only 4 data points per bin, so there is only one degree of freedom in the model fit.

#### 4.2.3 FITTING $F$ AND $E$ , AND KEEPING $\delta$ FIXED

To try and obtain a more accurate constraint on the value of  $\delta$  for this galaxy, we reduce the number of free parameters from 3 to 2, and keep  $\delta$  fixed in each fit. We then perform the fit many times, varying the set value of  $\delta$ , and summing the  $\chi^2$  over all bins. We then find the value of  $\delta$  which minimises the total  $\chi^2$ . We vary  $\delta$  between -5.0 and 0.7. We keep the same constraints on  $F$  and  $E$  as we had for the three parameter fit. The resulting distribution of total  $\chi^2$  values for various values of  $\delta$  is shown in Figure 4.8; the value of  $\delta$  that minimises the total  $\chi^2$  of all of the

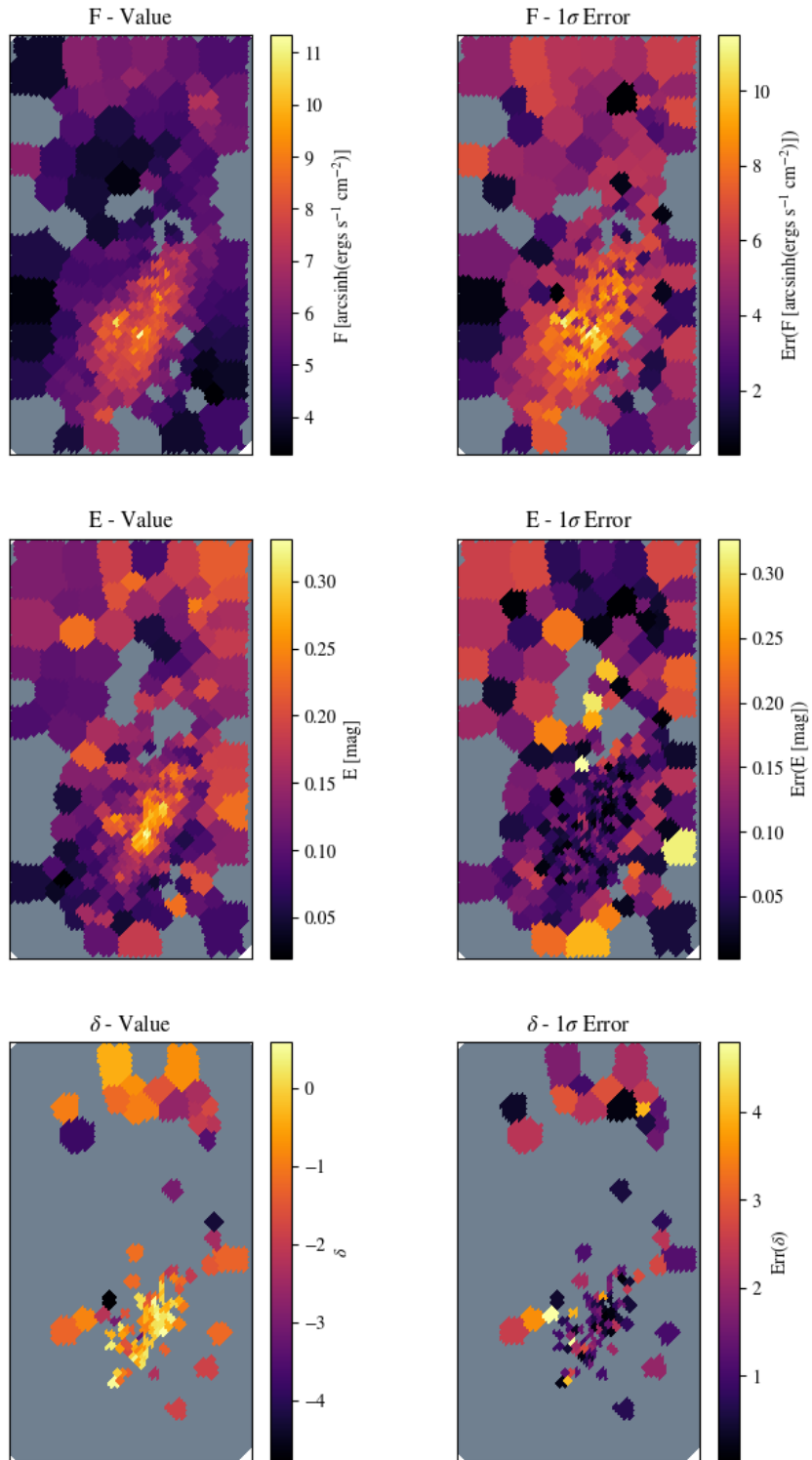


**Figure 4.7.** Results for each spatial bin from modelling the reddening law of UGC 9215 with three parameters:  $F$ ,  $E$  and  $\delta$ . The best fitting value for each parameter is shown in the left panels, and the  $1\sigma$  error is shown in the right panels. Gray spatial bins show where the model fit was poorly constrained for the parameter in question.

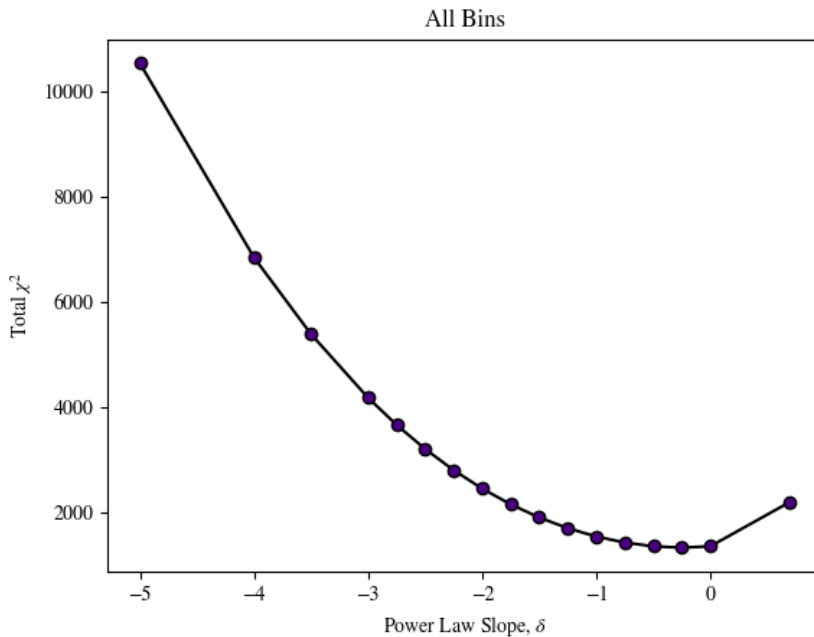


**Figure 4.8.** Distribution of total  $\chi^2$  with  $\delta$  for the two parameter fit with our reddening law model. The value of  $\delta$  that minimises the total  $\chi^2$  here is -0.25.

spatial bins is -0.25. The fitted values of  $F$  and  $E$  for this best value of  $\delta$  are shown in Figure 4.9;  $F$  and  $E$  are constrained more successfully now that the model is only having to fit 2 parameters instead of 3.

#### 4.2.4 WHAT DOES THE ATTENUATION CURVE OF UGC 9215 TELL US?

We look back at the paradoxical properties that define the BADGRS to try and understand what these results might be telling us about UGC 9215. Two of the defining features of the BADGRS are their high dust masses, and their bright UV emission; they are *blue but dusty*. They are also found to have low dust temperatures, despite this bright UV emission; they are *hot but cold*. Where there are large amounts of dust, we expect to see UV emission being attenuated strongly, however, this is not the case for the BADGRS. Looking at Figure 4.9, UGC 9215 has very low values of reddening,  $E$ , for the majority of the KOALA field of view, with values ranging between 0 and 0.15 mag. Only in the central bulge does the value of  $E$  reach higher values of 0.2 to 0.25 mag. This seems to correlate well with the fact that there is a large amount of UV emission coming from this galaxy.

The best value of  $\delta$  for UGC 9215 was found to be -0.25; an example of

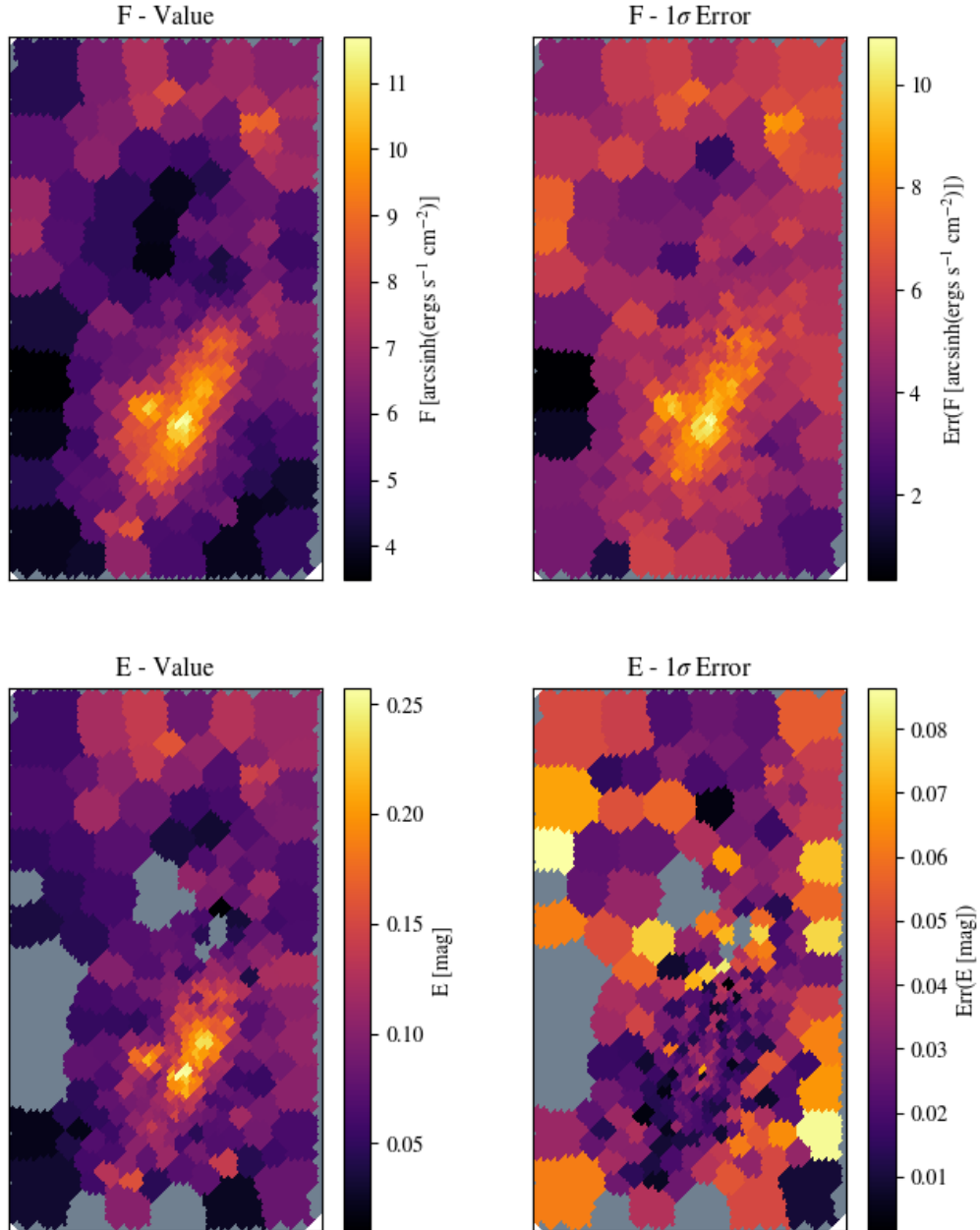


**Figure 4.9.** Results for parameters  $F$  and  $E$  from our reddening law model for each spatial bin when we set  $\delta = -0.25$ . The values of  $F$  and  $E$  are shown in the left panels, and the  $1\sigma$  errors are shown in the right panels. Gray bins show areas where the fit was unconstrained.

what this attenuation curve looks like is shown in Figure 4.10 as the black solid line. This value of  $\delta$  is in line with the range of  $\delta$  values found by Salim et al. (2018) for their sample of over 200,000 local galaxies; they find that  $\delta$  varies between -0.9 (the blue dotted line in Figure 4.10) and 0 (the red dot-dashed line in Figure 4.10). With a stellar mass of  $9.31_{-0.04}^{+0.14} \log_{10} M_{\odot}$  and a specific star formation rate of  $-9.55_{-0.15}^{+0.04} \log_{10} \text{yr}^{-1}$  (De Vis et al., 2017a), UGC 9215 has a higher value of  $\delta$ , and therefore a shallower attenuation curve, than galaxies with similar properties found in the Salim et al. (2018) sample, which are expected to have a  $\delta$  between -0.6 and -0.5 (see the top left panel of Figure 3 in Salim et al., 2018). The attenuation curve for a galaxy with the same properties as UGC 9215 from the Salim et al. (2018) sample is shown in the yellow shaded region of Figure 4.10. This yellow shaded region also encompasses the range in errors of the stellar mass and sSFR. The attenuation curve derived for UGC 9215 is therefore steeper than that of Calzetti et al. (2000), but is still relatively shallow when compared with the SMC and the results of Salim et al. (2018). This shallow attenuation curve again seems to correlate well with the low reddening and high amounts of UV emission of this galaxy.

As discussed in Section 1.3.2, there are several mechanisms that are thought to affect the slope of the attenuation curve in a galaxy. Of particular interest to the paradoxical nature of the BADGRS is the role of dust content and geometry in shaping the attenuation curve. A shallow attenuation curve can be an indication of a more complex, clumpy dust geometry in galaxies. A shallow attenuation curve can also indicate a galaxy which is in the high optical depth limit in terms of dust content, with the UV dominated by radiation from unobscured OB stars outside of regions where  $\tau \geq 1$ . Either of these mechanisms could be the cause of the shallow attenuation curve that we find for UGC 9215, or it could be caused by a combination of both of these mechanisms. For example, a galaxy could be both in the high  $A_V$  limit, and possess a clumpy dust geometry, resulting in clumpy high  $A_V$  regions which obscure the stars within them, whilst also resulting in transparent regions, allowing light from exposed OB stars to easily escape.

We know that the BADGRS are star-forming. They possess high gas fractions ( $f_g = 0.7$  for UGC 9215, Dunne et al., 2018), indicating that they have plenty of fuel for star formation. They are also very blue, with high amounts of UV emission, which would not be possible without a current or recent burst of star formation. The stellar mass and sSFR of UGC 9215 also place it approximately on the galaxy main sequence according to Figure 3 of Salim et al. (2018). The BADGRS also have high dust masses. Considering these properties, and the derived shallow attenuation curve of UGC 9215, it seems likely that the dust in UGC 9215 is existing

in a clumpy geometry, given the lack of attenuation that is seen despite the high dust mass. These clumpy regions could also exist in the high  $A_V$  limit, however, we are not able to disentangle this information by using the derived attenuation curve alone.

These findings therefore go some way to explaining the two paradoxes: *blue but dusty* and *hot but cold*. The shallow attenuation curve of UGC 9215, along with its high dust mass and large amount of UV radiation, indicates we may be catching this galaxy at a stage where it has regions which are transparent to UV radiation, with a high fraction of unobscured OB stars and a clumpy dust geometry. In this scenario, these properties are not paradoxical at all, and are just a natural consequence for a galaxy that is dusty and actively forming stars. Similarly, with the dust in a clumpy geometry, light will only interact with the surface of these clumps, resulting in colder average dust temperatures. These seemingly paradoxical properties of the BADGRS may simply be a consequence of the stage of evolution these galaxies are currently in. Clark et al. (2015) used a chemical and dust evolution model to show that the HAPLESS, especially those that were classified as BADGRS, seemed to be in an earlier stage of converting their gas into stars. With a gas fraction of 0.7, UGC 9215 is placed close to the peak of its dust mass within the Clark et al. (2015) model, and is at an earlier stage of evolution compared to the Milky Way. Perhaps a shallow attenuation curve is another common property of galaxies in this stage of their evolution; repeating this study with the other BADGRS in the pilot sample of Dunne et al. (2018) would help in understanding this further, as the range in gas fractions (0.44 to 0.97, Dunne et al., 2018) place them at different points on the evolutionary track of Clark et al. (2015).

#### 4.2.5 OBTAINING A DUST MASS FROM ATTENUATION

We now describe how we obtain an approximate dust mass from the attenuation in UGC 9215, which we will compare to the value of dust mass obtained from photometry. We will obtain our dust mass through the calculation of optical depth from the Balmer emission lines, which we used above to obtain our attenuation curve.

Our method is as follows. We use Equation 2 of Calzetti et al. (1994), to calculate the difference in optical depth,  $\tau_{\alpha i}$ , between the  $H\alpha$  line, and another Balmer line,  $H_i$ , where  $i = (\beta, \gamma, \delta)$ :

$$\tau_{\alpha i} = \tau_i - \tau_{\alpha} = \ln \left( \frac{H\alpha/H_i}{r_{\alpha i}} \right), \quad (4.7)$$

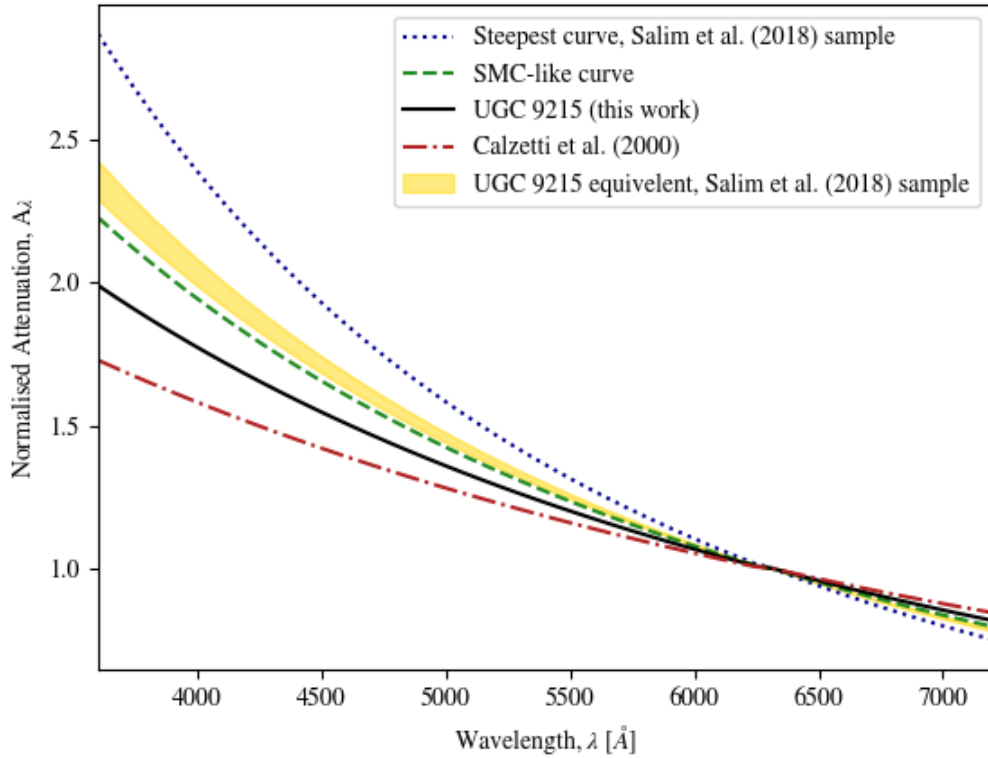


**Figure 4.10.** Example attenuation curves created using the modified Calzetti law of Salim et al. (2018). The starburst attenuation law of Calzetti et al. (2000) is shown in the red dot-dashed line, with a  $\delta$  of 0. The best fitting attenuation law for UGC 9215 is shown in the solid black line, with a  $\delta$  of -0.25. An SMC-like attenuation curve is shown in the green dashed line, which has a  $\delta$  of -0.45 (Salim et al., 2018). The steepest curve found for the Salim et al. (2018) sample is shown in the blue dotted line, with a  $\delta$  of -0.9. The shaded yellow region shows the attenuation curve that a galaxy with the same stellar mass and specific star formation rate as UGC 9215 would have in the Salim et al. (2018) sample, including the range in error on the stellar mass and sSFR.

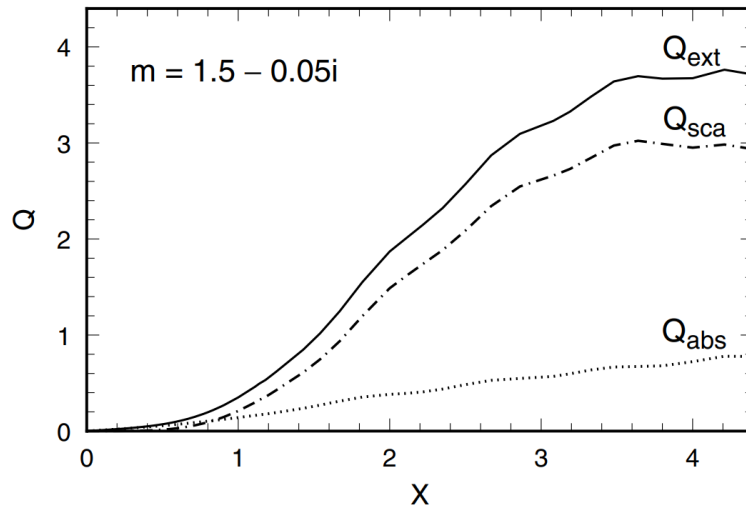


**Figure 4.11.** Figure 3.2 from Whittet (2002), which shows results from Mie theory calculations for spherical dust grains. The dimensionless size parameter,  $X$ , is plotted against the extinction efficiency factor,  $Q_{\text{ext}}$ .

where  $H\alpha/Hi$  is the observed ratio of  $H\alpha$  flux to the flux of Balmer line  $Hi$ , and  $r_{\alpha i}$  is the intrinsic flux ratio of  $H\alpha$  flux to the flux of Balmer line  $Hi$ . We will then use the following equation from Salim et al. (2020) to obtain a column density of dust,  $N_d$ :

$$N_d = \frac{\tau_{\alpha i}}{Q_{\text{ext}}(\lambda_i)\pi a^2}, \quad (4.8)$$

where  $a$  is the size of a dust grain, and  $Q_{\text{ext}}(\lambda_i)$  is the extinction efficiency factor, or the ratio of the extinction cross section to the geometric cross section, at the wavelength  $\lambda_i$ . To obtain  $Q_{\text{ext}}$  at the wavelengths of  $H\beta$ ,  $H\gamma$  and  $H\delta$ , we first calculate the size parameter,  $X$ , given by:

$$X(\lambda_i) = \frac{2\pi a}{\lambda_i}. \quad (4.9)$$

We then use Figure 4.11 from Whittet (2002) and our values of  $X$  to find the appropriate values of  $Q_{\text{ext}}$ . These values are listed in Table 4.3.

To convert our column density into a dust mass, we obtain the dust mass surface density,  $\Sigma$ :

$$\begin{aligned} \Sigma &= N_d V \rho \\ &= N_d \frac{3}{4} \pi a^3 \rho, \end{aligned} \quad (4.10)$$

where  $V$  is the volume of a dust grain, which we assume are spherical, and  $\rho$  is the density of a dust grain. We choose a value of  $0.1 \mu\text{m}$  for the dust grain size,  $a$ , as

scattering in the visible wavelength range indicates that grains vary in size between  $0.1\ \mu\text{m}$  and  $0.3\ \mu\text{m}$  (Whittet, 2002). We use a value of  $3\ \text{g cm}^{-3}$  for the dust grain density, as this is an approximate mean density between that of amorphous silicates and carbonaceous grains (Draine et al., 2007). Finally, we obtain the dust mass using the following equation:

$$\begin{aligned} M_{\text{dust}} &= \Sigma A \\ &= \frac{\frac{3}{4} a \rho \tau_{\alpha i} A}{Q_{\text{ext}}(\lambda_i)}, \end{aligned} \quad (4.11)$$

where  $A$  is the physical area of the galaxy observed by the KOALA field, which we calculate by multiplying the angular size of the KOALA field by the distance to the galaxy squared. As discussed in Section 1.4.1, the KOALA field of view for wide field mode is  $27.4'' \times 50.6''$ . However, due to the dither pattern used when observing UGC 9215, this field of view expands by approximately  $2''$  in each direction. Therefore, we round up the dimensions of the original field of view, and add  $4''$  to each side, making the final field of view  $32'' \times 55''$ , with an angular size of 1760 square arcseconds. The calculated values for  $\bar{\tau}$  and  $M_{\text{dust}}$  are shown in the final two columns of Table 4.3. To obtain  $\bar{\tau}$ , we calculate the difference in optical depth for each spatial bin using Equation 4.7, and then take the mean of these values to obtain an average optical depth for the KOALA field of view. The resulting dust masses are almost identical, which suggests small random errors.

We want to compare our calculated dust masses from the attenuation in UGC 9215 with the dust mass obtained in De Vis et al. (2017a), estimated by fitting the SED to the panchromatic photometry using the MAGPHYS algorithm (da Cunha et al., 2008). This was found to be  $6.95^{+0.09}_{-0.10} \log_{10} M_{\odot}$  for the whole galaxy. However, to compare our attenuation dust mass for the KOALA field with the photometric dust mass like for like, we need to know what portion of the dust mass measured by De Vis et al. (2017a) sits within the KOALA field of view. To get an approximation of this, we use the  $250\ \mu\text{m}$  SPIRE image, which we obtain using the H-ATLAS cutout server (*Herschel Astrophysical Terahertz Large Area Survey Cutouts* 2021); the KOALA field of view is plotted over the top of the  $250\ \mu\text{m}$  SPIRE image in Figure 4.12. We calculate the amount of  $250\ \mu\text{m}$  flux in the KOALA field of view, and then take the ratio of this to the total amount of  $250\ \mu\text{m}$  flux in the cutout shown in Figure 4.12; we can do this as we use the background subtracted and filtered  $250\ \mu\text{m}$  SPIRE image, so all significant flux in the image will be coming from the galaxy. The ratio of  $250\ \mu\text{m}$  flux in the KOALA field compared to total  $250\ \mu\text{m}$  flux for the galaxy is 0.4. The dust mass estimated from the IR in the KOALA field is therefore  $6.55 \log_{10} M_{\odot}$ .

UGC 9215  
(Herschel SPIRE, 250  $\mu\text{m}$ )

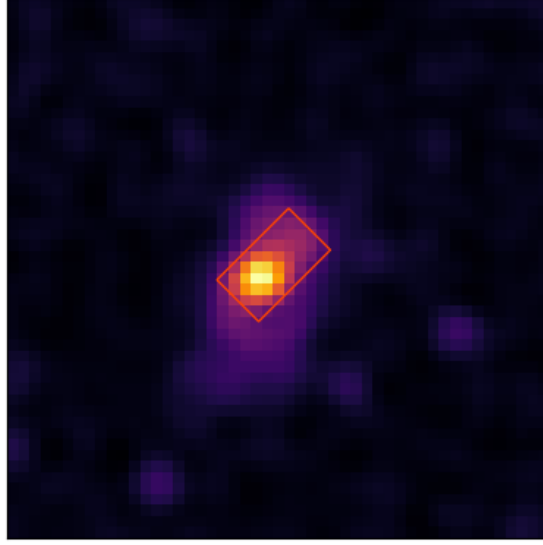


**Figure 4.12.** *Herschel* SPIRE 250  $\mu\text{m}$  image of UGC 9215, obtained from the H-ATLAS cutout server (*Herschel Astrophysical Terahertz Large Area Survey Cutouts 2021*). The orange box shows the position of the KOALA field of view, of size  $32'' \times 55''$ , used to calculate the proportion of the dust mass that resides within it.

We calculate three values of dust mass from the attenuation, using the different Balmer line ratios:  $H\alpha/H\beta$ ,  $H\alpha/H\gamma$  and  $H\alpha/H\delta$ . These are 5.8, 5.9 and 5.9  $\log_{10} M_{\odot}$  respectively, roughly in agreement with one another, indicating that the dust mass from attenuation is approximately  $5.9 \log_{10} M_{\odot}$ . This is more than 4 times lower than the value found from the photometry. This correlates well with the hypothesis that UGC 9215 has dust existing in a clumpy geometry. When observed with IR bands, all of the dust, regardless of geometry will be detected, therefore the dust mass obtained from photometry will give a more complete picture of the dust mass in UGC 9215. The dust mass measurement from attenuation will only be complete if all of the dust within the KOALA field of view is interacting with the light being emitted from stars in some capacity. The attenuation curve and UV photometry of UGC 9215 indicates the presence of unobscured OB stars, which have cleared their surroundings and created an inhomogeneous dust geometry, making the light from them less likely to interact with the dust. Therefore, a clumpy dust geometry would lead to a lower dust mass from attenuation.

However, we treat this with caution. Assumptions were made in the calculation of the dust mass from the attenuation in UGC 9215, and could be responsible for the disparity between that value and that derived from photometry. We only consider a single grain size of  $0.1 \mu\text{m}$ , when it is known that grain size varies

(Kim et al., 1994b; Kim et al., 1994a). If the grain size is larger, or the efficiency factor smaller, then the dust mass from attenuation would increase. Certain sizes of grain are more efficient at attenuating certain wavelengths of light; by considering the attenuation in the visible spectrum only, we may miss a portion of the dust mass which is more efficient at attenuating UV light, for example, grains that are less than  $0.04\ \mu\text{m}$  in size (Whittet, 2002). The equation we use to calculate our optical depth, from Calzetti et al. (1994), assumes a uniform screen of dust between the source and observer, which may not be the case within the spatial bins of UGC 9215, especially if our hypothesis of a clumpy dust geometry is correct.

We also note that using the  $250\ \mu\text{m}$  SPIRE image to calculate the ratio of the dust mass within the KOALA field of view to the total galaxy will not give an accurate result if the average temperature in the KOALA field of view differs compared to the entire galaxy; a higher average temperature in the KOALA field of view will lead to a lower value of dust mass. Dust mass,  $M_{\text{dust}}$ , is related to the blackbody function,  $B(\lambda, T_{\text{dust}})$ , which is a function of the dust temperature,  $T_{\text{dust}}$ , and emitting wavelength,  $\lambda$ :

$$\begin{aligned} M_{\text{dust}} &\propto \frac{1}{B(\lambda, T_{\text{dust}})} \\ &\propto \frac{\lambda^5}{2hc^2} \left( \exp\left(\frac{hc}{\lambda k_B T_{\text{dust}}}\right) - 1 \right), \end{aligned} \quad (4.12)$$

where  $h$  is the Planck constant,  $c$  is the speed of light and  $k_B$  is the Boltzmann constant. We use this relation, and the ratio of the dust mass from the IR to the dust mass obtained from attenuation for the KOALA field to see what change in temperature within the KOALA field at  $250\ \mu\text{m}$  is necessary to account for the difference in dust mass. We find that the average cold dust temperature in the KOALA field of view would need to be  $29.9_{-4.0}^{+2.3}$  K to produce a dust mass of  $5.9 \log_{10} M_{\odot}$ , compared to an average of  $17.4_{-1.5}^{+0.9}$  K for the whole galaxy. For the HIGH, HAPLESS and HRS samples, De Vis et al. (2017a) find that cold dust temperature varies between 12 K and 26 K. Our estimated temperature lies within this range (within error), and therefore the difference in temperature between our estimate for the KOALA field compared with the whole galaxy could account for our observed difference in dust mass. However, this temperature does lie at the upper end of this range.

**Table 4.3.** Parameters and results from the calculation of a dust mass for the UGC 9215 KOALA field using the Balmer emission lines. The values for  $r_{\alpha i}$  correspond to an electron density of  $10^2 \text{ cm}^{-3}$  and a temperature of 10,000 K (Groves et al., 2012). The values of  $Q_{\text{ext}}$  were obtained using the values of  $X$ , calculated using Equation 4.9, and Figure 4.11. The values of  $\bar{\tau}$  were obtained by taking the mean value of the optical depth for all spatial bins in the KOALA data cube. The values of  $M_{\text{dust}}$  were calculated using Equation 4.11, assuming spherical dust grains with size  $0.1 \mu\text{m}$  and density  $3 \text{ g cm}^{-3}$ .

Balmer Line, $H_i$	$\lambda$ [ $\text{\AA}$ ]	$r_{\alpha i}$	$X$	$Q_{\text{ext}}$	$\bar{\tau}$	$M_{\text{dust}}$ [ $\log_{10} M_{\odot}$ ]
H $\beta$	4861	2.86	1.29	0.7	0.16	5.8
H $\gamma$	4340	6.12	1.45	0.85	0.22	5.9
H $\delta$	4101	11.08	1.53	1.0	0.27	5.9

### 4.3 INVESTIGATING THE STELLAR POPULATIONS OF UGC 9215

We now move on to take a brief look at some of the features in the very blue end of the spectra in UGC 9215, to investigate what they indicate about the stellar population of several regions within the galaxy. The strength of the Balmer absorption lines and the strength of the 4000  $\text{\AA}$  break are strong indicators of the age of the population (Wild et al., 2007), therefore we shall focus on the wavelength range from 3700  $\text{\AA}$  to 4150  $\text{\AA}$ .

We have chosen three areas within UGC 9215 to focus on, these are indicated in the map in Figure 4.13. We study two areas within the bulge, which we dub the upper and lower bulge, and a large HII region within the spiral arm. We choose several bins in each of these regions, and obtain an average spectrum from each of them; these are shown in Figure 4.14. The average properties of these regions are shown in Table 4.4. We choose to examine these regions because they each exhibit different spectral shapes, and are also high signal regions. We will compare our spectra with the study of Rowlands et al. (2018), who performed principal component analysis using the strength of the 4000  $\text{\AA}$  break and Balmer absorption lines, on a sample of 2404 MaNGA galaxies to assess their star formation histories.

The top panel of Figure 4.14 shows the average spectrum from the lower bulge. This spectrum displays strong emission lines, with clear emission in the Balmer series down to H10 at approximately 3800  $\text{\AA}$ . There is also clear Balmer absorption features around the emission lines. This spectrum is most reminiscent of the example starburst spectrum in Figure 3 of Rowlands et al. (2018). The middle panel of Figure 4.14 shows the average spectrum from the upper bulge. This spectrum has

far less emission in the Balmer series than that of the lower bulge spectrum; only the emission in  $H\delta$  rises above the depth of the absorption feature it sits within, however, it does present similar absorption lines. This spectrum seems to be somewhere between the starburst spectra of Rowlands et al. (2018) and the post-starburst and star-forming spectra. The emission lines are weaker than a starburst, but the spectrum shows very little evidence of a 4000 Å break; perhaps a region which is in the process of transitioning out of a starburst? The final panel of Figure 4.14 shows the average spectrum from the HII region in the spiral arm of UGC 9215. This spectrum displays far fewer features; there is some evidence of absorption features around the Balmer emission lines, but the emission lines are the dominating component. The lack of strong absorption features suggests a stellar component dominated by young OB stars, which have narrow and weak absorption features (Walborn et al., 1990).

We also examine the weighting of the Vazdekis et al. (2010) stellar templates for a spatial bin in each region we identify in Figure 4.13. Spatial bin 3, which in the lower bulge region, is shown in the top panel of Figure 4.15, spatial bin 135, which is from the upper bulge region, is shown in the bottom panel of Figure 4.15, and bin 280, from the HII region, is shown in Figure 4.16. The weight map for the lower bulge region shows that the best fitting model for the stars in this bin has contribution from a wide range of templates, with particularly highly weighted templates in two regions; templates with ages of approximately  $8.7 \log(\text{yr})$  and  $0.22 [M/H]$  ( $1.58 Z_{\odot}$ ), and templates with ages of approximately  $10.1 \log(\text{yr})$  and  $-1.71 [M/H]$  ( $0.02 Z_{\odot}$ ). The weight map for the upper bulge region shows a similar wide range of templates contributing to the best fitting stellar spectrum, but shows only one region with particularly high weights, where templates have an age of approximately  $10.1 \log(\text{yr})$  and  $0.22 [M/H]$  ( $1.58 Z_{\odot}$ ). The weight map for the HII region, by contrast, shows a far clearer separation of the most highly weighted templates into two populations; templates with ages of approximately  $8.5 \log(\text{yr})$  and high  $[M/H]$ , and templates with ages of approximately  $10.1 \log(\text{yr})$  and high  $[M/H]$ .

In summary, the upper bulge has an old, high metallicity population; the lower bulge has an old, low metallicity population and a young, high metallicity population; and the HII region has young and old high metallicity populations. It is surprising to see such a high weighting to older stellar templates in the HII region, considering the appearance of the spectrum and its lack of absorption features, however the strength of the gas emission lines may be dominating the spectrum's appearance. It is also surprising that the lower bulge does not have a similar old, high metallicity population that the upper bulge has, considering that they are both bulge regions. We could be seeing indications of real differences in the stellar populations,

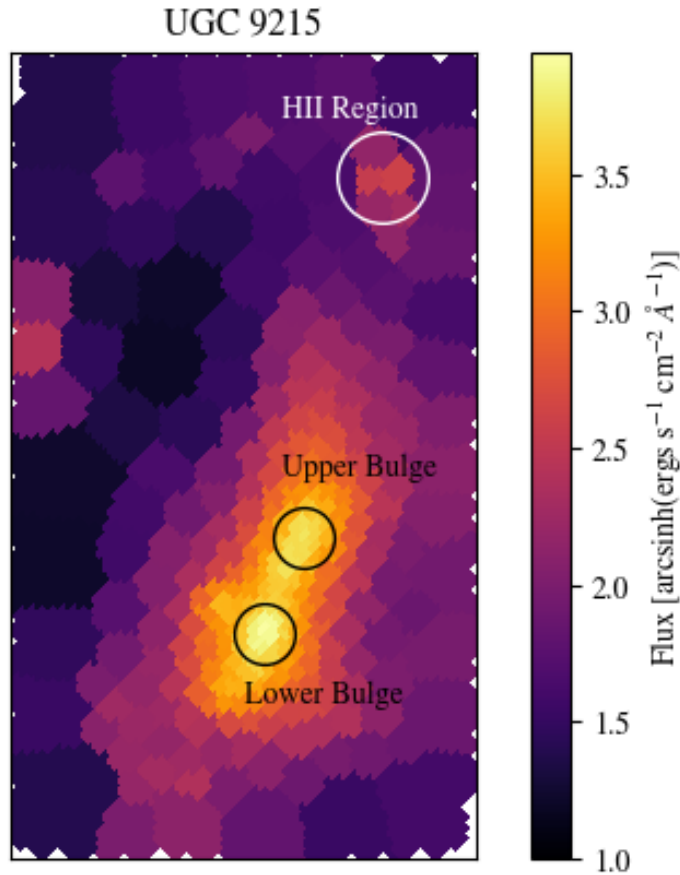


**Figure 4.13.** Voronoi binned map of UGC 9215. Regions of interest are indicated with the black and white circles. The two black circles indicate two regions within the bulge, dubbed upper and lower bulge. The white circle indicates a HII region within the spiral arm of the galaxy.

but there could also be some degeneracy between the age and metallicities within the weight maps.

We can again look back here at the paradoxes that define the BADGRS. One of these paradoxes is that these galaxies appear *young but old*, with their blue colours and high gas fractions, whilst also having reasonably metal rich central regions and high dust masses. Looking at the spectra from UGC 9215 in Figure 4.14, there are clearly regions of intense star formation within the galaxy, whilst there is also evidence of regions where there are populations of older stars. Perhaps UGC 9215 is going through a current starburst period, but has had previous bouts of star formation which have built up the metals in the centre of the galaxy. A more in depth study of the stellar populations for UGC 9215 and the rest of the pilot BADGRS sample would be necessary to fully understand this paradox.

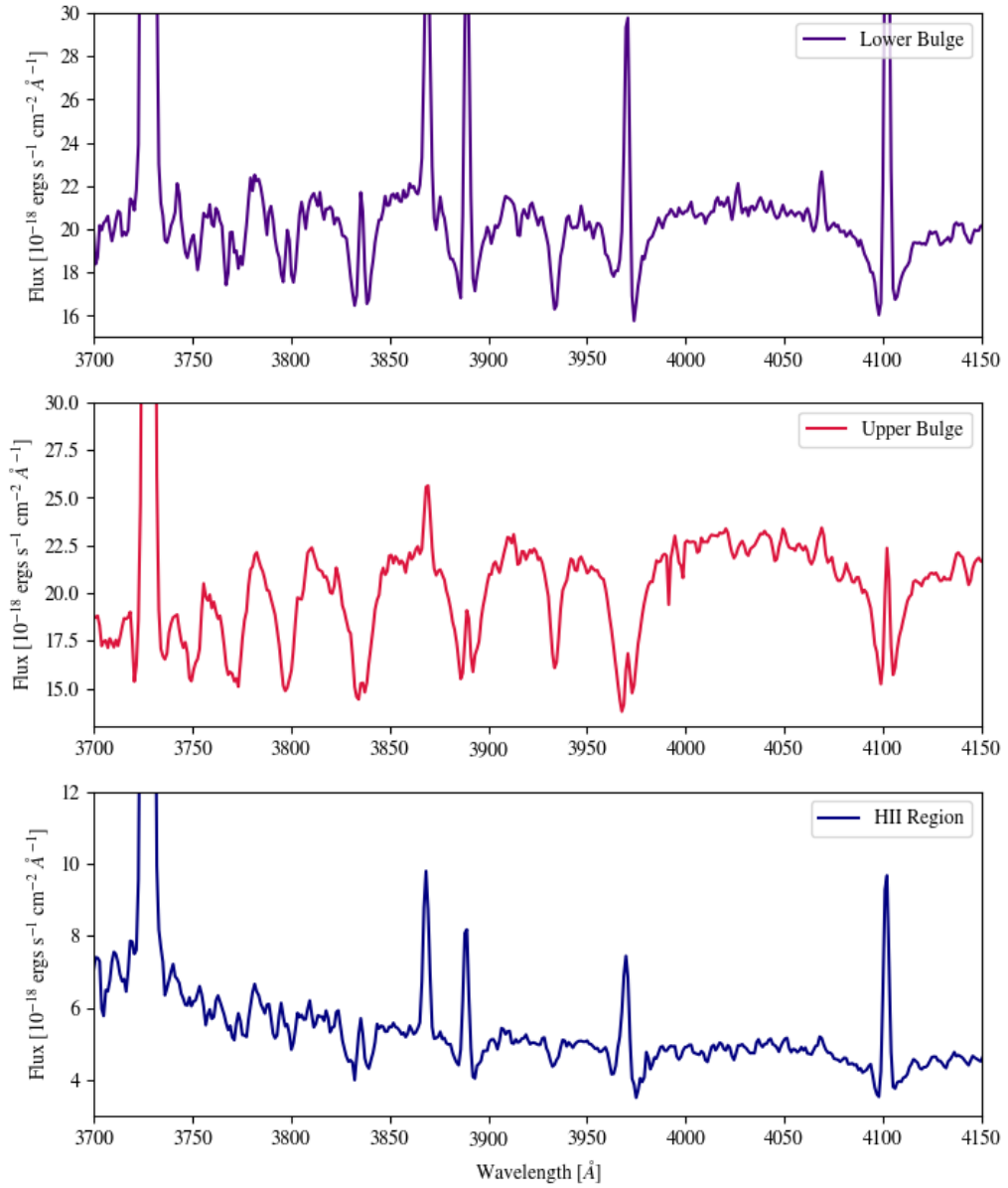


**Figure 4.14.** Average spectra for bins from the UGC 9215 data cube in the three regions indicated in Figure 4.13. The top panel shows the spectrum from the lower bulge region, the middle panel shows the upper bulge region, and the bottom panel shows a HII region. We focus on the spectrum between 3700 Å and 4150 Å to clearly show any features from the stellar population in these regions.

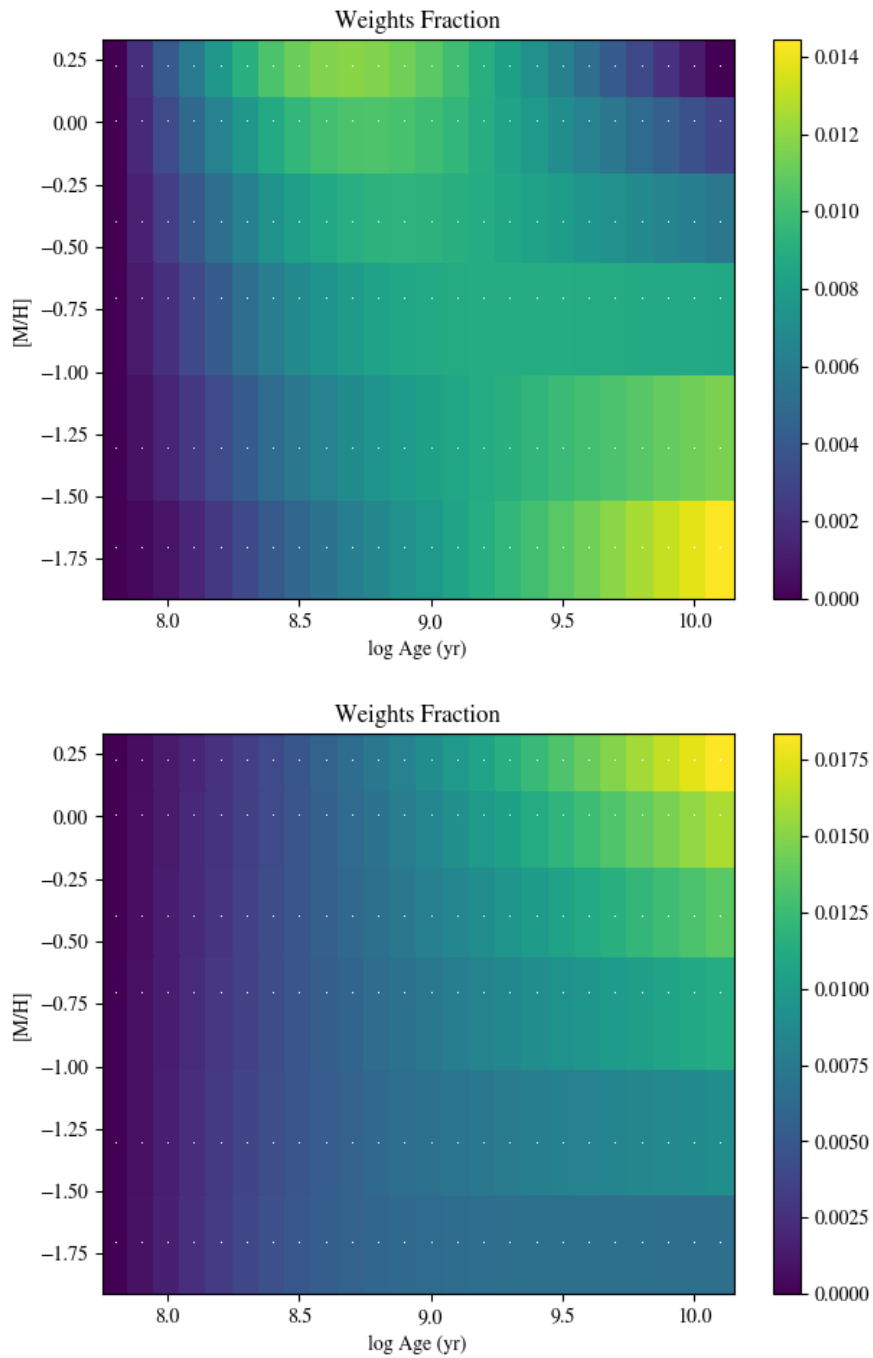


**Figure 4.15.** Output template weights from pPXF for spatial bin 3 (from the lower bulge, top panel) and spatial bin 135 (from the upper bulge, bottom panel), indicating the best combination of Vazdekis et al. (2010) templates to fit the spectra in these bins.

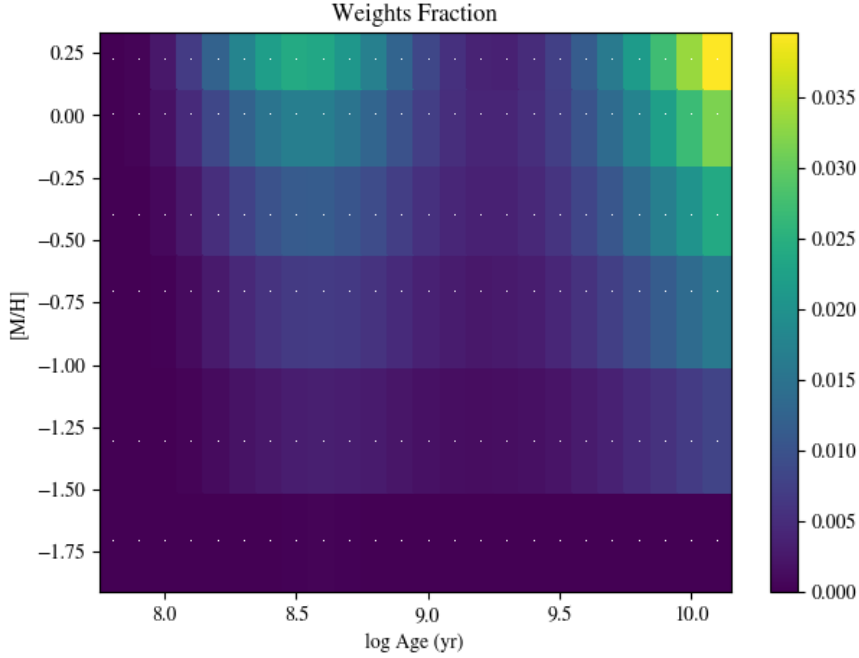


**Figure 4.16.** Output template weights from pPXF for spatial bin 280 (from the HII region), indicating the best combination of Vazdekis et al. (2010) templates to fit the spectrum in this bin.

**Table 4.4.** Mean properties for the lower bulge, upper bulge and HII region. The age and metallicity [M/H] are the weighted values from the Vazdekis et al. (2010) templates, averaged over the bins considered in these regions. The line strengths are obtained from the pPXF fits to each bin, and again are averaged over the bins considered in the three regions listed.

	Age [log(yr)]	[M/H]	H $\beta$	H $\delta$	OII	OIII
			[ $10^{-18}$ ergs s $^{-1}$ cm $^{-2}$ ]			
Lower Bulge	9.29	-0.59	441.89	91.23	875.90	1314.85
Upper Bulge	9.34	-0.43	147.06	33.42	402.44	265.75
HII Region	9.42	-0.29	101.97	21.80	264.63	360.66

## 4.4 INVESTIGATING THE EXCITATION AND METALLICITY OF UGC 9215

We now take a brief look at the excitation and metallicity of UGC 9215, using the emission lines derived in Section 4.1.2 using pPXF. We examine several metallicity indicators, following the empirical indicators used in De Vis (2016). These are the N2 and O3N2 indicators of Pettini et al. (2004), the R<sub>23</sub> indicator of Leonid S. Pilyugin et al. (2005), and the PG16R and PG16S indicators of L. S. Pilyugin et al. (2016). We also evaluate the ionisation parameter, P, from Leonid S. Pilyugin et al. (2005).

The calculated excitation parameter and metallicity indicators for UGC 9215 are shown in Figure 4.17. The excitation parameter map shows areas of ionisation in the spiral arms and parts of the bulge; the lower bulge in particular has two areas of high ionisation which matches the region that possessed spectral features consistent with a starburst in Section 4.3. The maps of the N2 and O3N2 indicators are very similar, and show sensitivity to the excitation parameter. There appears to be a systematic offset between these two indicators, with the N2 indicator being higher by approximately  $0.12 + \log(\text{O}/\text{H})$  than O3N2. The R<sub>23</sub> indicator shows a high sensitivity to the excitation parameter, with very low values of  $12 + \log(\text{O}/\text{H})$  when compared to the same regions in the other metallicity maps. The PG16 indicators both show a relatively smooth gradient across the KOALA field of view, and both show no signs of correlation with the excitation parameter. However, the R and S indicators also show a systematic offset, with the R indicator being approximately  $0.15 12 + \log(\text{O}/\text{H})$  higher than the S indicator. Overall, there is a lack of consistency between the metallicity indicators used here, with both the structure within the maps and the overall values of  $12 + \log(\text{O}/\text{H})$  differing greatly.

We can think back to the paradoxical properties of the BADGRS, and the final paradox, *metal rich but CO poor*. Investigating the CO emission is beyond the scope of this work, however, we have been able to map the spatially resolved metallicity, which was not possible with the single fibre spectra available for this source. However, due to the lack of consistency between the metallicity indicators, further work will also be needed to understand which of these indicators would be best for studying the BADGRS metallicities in detail.

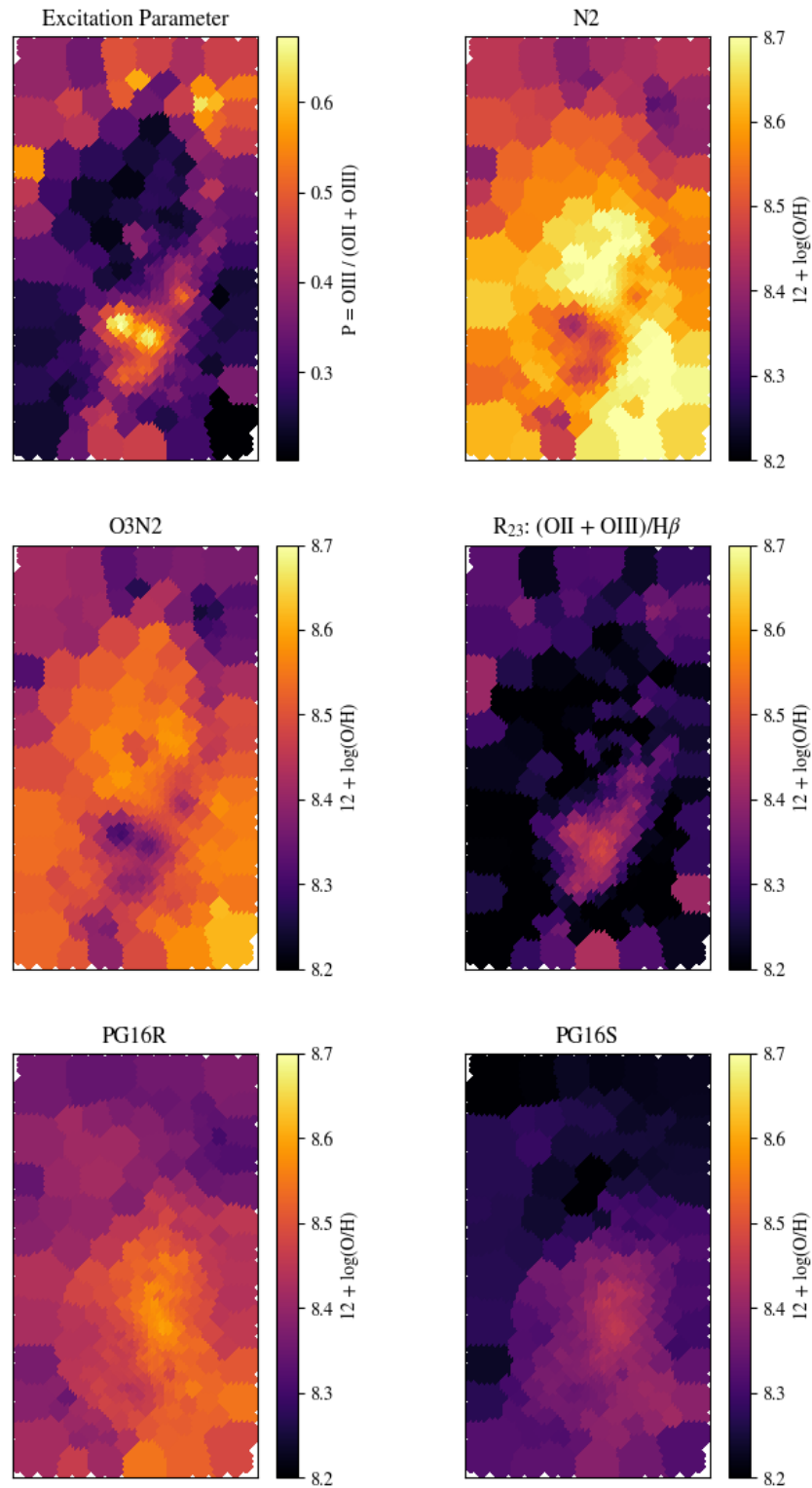


**Figure 4.17.** Maps for a selection of metallicity and excitation indicators for UGC 9215. We show the N2 and O3N2 indicators from Pettini et al. (2004), the parameter P and R<sub>23</sub> indicator from Leonid S. Pilyugin et al. (2005), and the PG16R and PG16S indicators from L. S. Pilyugin et al. (2016). All metallicity indicators are given in terms of  $12 + \log(\text{O}/\text{H})$ .

## 4.5 CONCLUSIONS

In this chapter, we have investigated the properties of one of the main sample of BADGRS, UGC 9215, using the reduced and calibrated KOALA IFU data cube. To obtain a consistent signal to noise across the data cube, we performed Voronoi binning, resulting in 304 spatial bins. The spectra in each of these spatial bins was fit with the software pPXF to obtain emission lines fluxes for the important emission lines within the KOALA wavelength range.

We first use the fitted Balmer emission lines,  $H\alpha$ ,  $H\beta$ ,  $H\gamma$  and  $H\delta$ , to investigate the dust attenuation law of UGC 9215. We apply a model using these fluxes to obtain a value for the slope,  $\delta$ , of the modified Calzetti reddening law of Salim et al. (2018).  $\delta$  was found to be -0.25 for UGC 9215 when all spatial bins were considered together. This is steeper than the Calzetti et al. (2000) starburst attenuation curve, but is still shallow when compared with the results of Salim et al. (2018). A shallow attenuation curve can indicate a clumpy dust geometry, a high fraction of unobscured OB stars and areas that have become transparent to UV emission; this could go some way to explaining the *blue but dusty* and *hot but cold* BADGRS. We also use the Balmer emission lines to calculate a dust mass from the attenuation in UGC 9215, and compare this to a value calculated by De Vis et al. (2017b) using the SED fitting software MAGPHYS da Cunha et al. (2008) on the panchromatic photometry of UGC 9215, scaled for the KOALA field of view. We find a lower dust mass from attenuation than from photometry, which fits well with the hypothesis of a clumpy dust geometry, resulting in areas where light does not interact with the dust in UGC 9215.

We take a brief look at two of the other paradoxes of the BADGRS using the IFU data for UGC 9215; *young but old* and *metal rich but CO poor*. For the former paradox, we study the spectra in the very blue end of the KOALA wavelength range for several different high signal regions in the UGC 9215 data cube, looking at their features to get an idea of their star formation histories. We also look at the weighting of stellar templates from Vazdekis et al. (2010) that make up the best fitting spectrum to the stellar component of these regions. Some regions exhibit clear signs of a current or recent starburst, but there are also indications of older populations of stars. For the latter paradox, we use the emission lines fitted from pPXF to examine the excitation and metallicity of UGC 9215 with indicators from Pettini et al. (2004), Leonid S. Pilyugin et al. (2005), and L. S. Pilyugin et al. (2016). We find a lack of consistency between the chosen metallicity indicators, therefore further work will be needed to understand which indicator is best for studying the BADGRS.

# CHAPTER 5

## CONCLUSIONS

---

---

---

*“[She] had reached [her] goal. [She] had climbed the unclimbable mountain.”*

---

Inheritance, Christopher Paolini

In this Thesis, we obtain integral field spectroscopy of a pilot sample of Blue And Dusty Gas-Rich Sources, or BADGRS, discovered in the first dust-selected survey from the *Herschel* ATLAS. These sources make up more than 50% of the local H-ATLAS volume, have lower average dust temperatures and  $M_{\text{H}_2}/M_d$  ratios, and higher average dust-to-stellar mass ratios when compared to other local galaxies with similar metallicities. The properties of the BADGRS provide a mystery that can be summarised with four paradoxes: *blue but dusty*, they have bright UV emission despite having high dust masses; *hot but cold*, they have lower than average dust temperatures despite their bright UV emission; *young but old*, they have blue colours and high gas fractions, indicating that they are young, whilst also having lots of dust emission and being reasonably metal rich, indications of an older population; *metal rich but CO poor*, they have low amounts of  $\text{H}_2$  with respect to their dust content, despite being reasonably metal rich in their central regions. We attempt with this Thesis to shed light on these paradoxical properties, with particular emphasis on the first.

In Chapter 2, we introduce the pilot sample of BADGRS studied in this Thesis and describe the data obtained for these sources from the KOALA IFU. The four sources that make up the pilot sample of BADGRS are NGC 5584, NGC 5496, UGC 9215 and UGC 9299. These galaxies were chosen in Dunne et al. (2018) to provide a representative sample of BADGRS to study in further detail, on the basis that their stellar mass, gas fraction, morphology and  $FUV - K_S$  colour spans the full range of the parent sample. Integral field spectroscopy of this pilot sample

of BADGRS was obtained using the KOALA IFU on the Anglo-Australian Telescope across two observing runs, which took place over the 28<sup>th</sup> April – 1<sup>st</sup> May 2016 and the 21<sup>st</sup> – 23<sup>rd</sup> May 2017, covering a wavelength range from 3700 Å to 5700 Å in the blue end of the optical, and from 6200 Å to 7200 Å in the red end of the optical. All of the planned observations of the BADGRS pilot sample were completed with a total exposure time of at least 3.33 hours, which was the original target time. Total exposure times were increased if there were poor weather conditions during the observing time. We also obtain integral field spectroscopy for three ancillary targets, NGC 0007, NGC 7361 and NGC 4030, which were observed when the BADGRS were not visible in the sky.

In Chapter 3, we describe the data reduction and calibration process for the KOALA IFU data obtained for the pilot sample of BADGRS and ancillary targets. Some of the steps in the process were carried out using software and scripts provided by the AAO KOALA team, whilst the other steps were created as part of this Thesis. Additional steps in the pipeline were included, and adaptations were made to some of the AAO scripts, to ensure we obtained the highest quality final data products.

In Chapter 4, we analyse the KOALA IFU data of one of the pilot BADGRS, UGC 9215, with their paradoxical properties in mind. To ensure a consistent signal across the field of view for UGC 9215, we apply Voronoi binning to the KOALA data cube, resulting in 304 spatial bins of varying sizes. We run the spectral fitting software pPXF on each spatial bin, and obtain emission line fluxes from OII at approximately 3727 Å down to SII at approximately 6720 Å.

We first investigated the dust attenuation law of UGC 9215. We applied a model using the measurements of the first four Balmer emission lines and the intrinsic Balmer line ratios to constrain the slope,  $\delta$ , of the Salim et al. (2018) modified reddening law for each spatial bin in UGC 9215. We found a poor constraint on  $\delta$  when considered each spatial bin individually, so we applied the model to the KOALA field as a whole, and found a best fitting  $\delta$  value of -0.25. This resulted in an attenuation curve steeper than the starburst curve of Calzetti et al. (2000), but quite shallow when compared to similar galaxies in the sample investigated by Salim et al. (2018). A shallow attenuation curve can indicate a more complex, clumpy dust geometry. It can also indicate, in galaxies that are dusty and forming stars, the presence of a high fraction of unobscured OB stars and regions where the galaxy has become transparent to UV radiation. This finding may indicate that the *blue but dusty* and *hot but cold* BADGRS are just being caught in a stage of their evolution where they have lots of clumpy dust, and regions that are transparent to the UV radiation of the young OB

stars present.

We also estimate a dust mass for UGC 9215 from its attenuation, using the ratios of the observed Balmer emission lines to calculate an optical depth. We then compare this dust mass from attenuation to that calculated by De Vis et al. (2017a) by fitting the SED to the panchromatic photometry of UGC 9215 using the MAGPHYS algorithm (da Cunha et al., 2008). Assuming spherical dust grains of size  $0.1 \mu\text{m}$  and density  $3 \text{g cm}^{-3}$ , we find a dust mass of approximately  $5.9 \log_{10} M_{\odot}$  from the attenuation in UGC 9215, compared with a value of  $6.55 \log_{10} M_{\odot}$  from photometry. The lower value of dust mass from attenuation could strengthen the hypothesis that there is clumpy dust present in UGC 9215, as the attenuation will only detect dust that is interacting with the light being emitted from the stars in the galaxy, whereas the dust mass from photometry is sensitive to thermal emission from all of the dust content. However, these results are subject to significant uncertainties due to unknown dust parameters required in our calculation.

We briefly investigate the stellar populations in UGC 9215. We selected regions of the galaxy in the bulge and spiral arm to study the spectrum in the wavelength range  $3700 \text{ \AA}$  to  $4150 \text{ \AA}$ , comparing the strength of the Balmer absorption lines and  $4000 \text{ \AA}$  break to the study of Rowlands et al. (2018). We find a region in the bulge and a HII region in the spiral arm that exhibit signs of a current or recent starburst, whereas another region in the bulge suggests it may be transitioning to post-starburst or star-forming. We also study the weighting of the templates from Vazdekis et al. (2010) that make up the best fitting stellar spectrum for these regions from pPXF. These suggest that there are older populations of stars present in the starburst regions. Considering the *young but old* paradox, we suggest that perhaps UGC 9215 is going through a current starburst period, but has had previous bouts of star formation, building up the metals in this galaxy. More in depth study of this paradox is needed to fully understand it.

Finally, we use the derived emission line fluxes to examine the excitation and metallicity of UGC 9215. We map the excitation and metallicity using indicators from Pettini et al. (2004), Leonid S. Pilyugin et al. (2005) and L. S. Pilyugin et al. (2016). We find areas of high ionisation in the bulge and spiral arm, consistent with the starburst regions detected in UGC 9215. However, we find a lack of consistency between the metallicity indicators used within this work. Further work will be needed to understand which of these indicators will be best to use for a detailed study of the metallicity within the BADGRS. The IFU data available for the BADGRS as a result of this Thesis can be used alongside studies of the CO from Dunne et al. (2018) to fully understand the *metal rich but CO poor* paradox.

In future, this work should be extended to include the other sources within the pilot sample of BADGRS using the available KOALA data cubes, to see whether they also exhibit shallow attenuation curves. The ancillary targets can be used as a point of comparison, in particular NGC 4030; this source was a part of the HAPLESS and therefore has the same suite of data available for it as the BADGRS, but was not classified as one of the BADGRS. Further study is needed into the latter two paradoxes of the BADGRS, *young but old* and *metal rich but CO poor*. Applying the principal component analysis technique of Rowlands et al. (2018) to all of the spectra available for each of the pilot sample of BADGRS would give a far better understanding of the stellar populations within these sources. The data for these sources from the KOALA IFU can be used alongside planned further studies of the atomic and molecular gas (Dunne et al., 2018) of the pilot sample of BADGRS, and hopefully continue to unravel the mystery these galaxies pose.

# CHAPTER A

## ADDITIONAL OBSERVING INFORMATION

---



---

Table A.1 shows the full observing log for the KOALA IFU data.

**Table A.1.** Log of all observations completed of the standard star LTT3218 and each galaxy target field during the two observing runs, carried out over the 28<sup>th</sup> April – 1<sup>st</sup> May 2016 and 21<sup>st</sup> – 23<sup>rd</sup> May 2017. The date, ID number and exposure time in seconds is given for each observation carried out, along with any notes made on the observing conditions during the exposure.

Target Field	Date	ID	Exposure [s]	Notes
Standard LTT3218	28/04/16	16	120	Clouds moving through
Standard LTT3218	28/04/16	17	120	Mostly fine
Standard LTT3218	29/04/16	27	120	Mostly clear
Standard LTT3218	29/04/16	28	120	Clear
Standard LTT3218	21/05/17	44	120	-
Standard LTT3218	21/05/17	45	120	-
NGC 5584 (TF1)	28/04/16	23	2400	Fine
NGC 5584 (TF1)	28/04/16	25	2400	Fine
NGC 5584 (TF1)	28/04/16	26	2400	Fine
NGC 5584 (TF1)	28/04/16	28	2400	Small, patchy cloud
NGC 5584 (TF1)	28/04/16	29	2400	Small, patchy cloud
NGC 5584 (TF2)	29/04/16	34	1800	Some cloud
NGC 5584 (TF2)	29/04/16	36	1800	Cloudy
NGC 5584 (TF2)	29/04/16	37	1800	Very thick cloud
NGC 5584 (TF2)	29/04/16	38	1800	Slightly clearer
NGC 5584 (TF2)	29/04/16	39	600	Tracking issue, stopped after 600 s

Table A.1 Continued.

Target Field	Date	ID	Exposure [s]	Notes
NGC 5584 (TF2)	30/04/16	18	700	Stopped after 700 s, too much cloud
NGC 5584 (TF2)	30/04/16	19	1800	Mainly clear, cloudy after 1600 s
NGC 5584 (TF2)	30/04/16	20	1800	Partly cloudy
NGC 5584 (TF2)	30/04/16	22	1800	Cloudy for about half the time
NGC 5584 (TF2)	30/04/16	23	1800	Fine
NGC 5584 (TF2)	30/04/16	24	600	Stopped after 600 s, too much cloud
NGC 5584 (TF3)	21/05/17	20	2400	Clear skies
NGC 5584 (TF3)	21/05/17	22	2400	Clear skies
NGC 5584 (TF3)	21/05/17	23	2400	Clear skies
NGC 5584 (TF3)	21/05/17	25	2400	Clear skies
NGC 5584 (TF3)	21/05/17	26	2400	Clear skies
UGC 9299	28/04/16	31	2400	Cloudy, getting thicker
UGC 9299	28/04/16	33	2400	Thick cloud
UGC 9299	28/04/16	34	2400	Slightly less cloud
UGC 9299	28/04/16	36	2400	Low cloud for some time
UGC 9299	28/04/16	37	2400	Low cloud for some time
UGC 9299	01/05/16	21	1800	Fine
UGC 9299	01/05/16	24	1800	Fine
UGC 9299	21/05/17	60	1800	Some cloud
UGC 9299	21/05/17	62	1800	Some cloud
UGC 9299	21/05/17	63	1800	Intermittent cloud, lost guide star
UGC 9299	21/05/17	65	1800	Intermittent cloud
UGC 9299	23/05/17	15	2400	Hazy
UGC 9299	23/05/17	17	2400	Intermittent cloud from 700 s
UGC 9215	01/05/16	26	2400	Some fog blowing past
UGC 9215	01/05/16	28	2400	Some fog blowing past
UGC 9215	01/05/16	30	2400	Some fog blowing past
UGC 9215	22/05/17	30	2400	Clear skies
UGC 9215	22/05/17	32	2400	Clear skies

**Table A.1** Continued.

<b>Target Field</b>	<b>Date</b>	<b>ID</b>	<b>Exposure [s]</b>	<b>Notes</b>
UGC 9215	22/05/17	33	2400	Clear skies
NGC 5496 (TF1)	21/05/17	50	2400	Intermittent cloud
NGC 5496 (TF1)	21/05/17	52	2400	Intermittent cloud
NGC 5496 (TF1)	21/05/17	53	2400	Wispy cloud
NGC 5496 (TF1)	21/05/17	55	2400	Wispy cloud
NGC 5496 (TF1)	21/05/17	56	2400	Some cloud
NGC 5496 (TF2)	23/05/17	21	2400	Intermittent cloud
NGC 5496 (TF2)	23/05/17	23	2400	Intermittent cloud
NGC 5496 (TF2)	23/05/17	24	2400	Clear skies, but not great seeing
NGC 0007	23/05/17	30	2400	Some cloud
NGC 0007	23/05/17	32	2400	Hazy
NGC 4030	28/04/16	21	2400	Fine
NGC 4030	29/04/16	30	2400	Cloudy after 600 s
NGC 4030	29/04/16	31	2400	Some cloud
NGC 7361	21/05/17	71	2400	Wispy cloud
NGC 7361	21/05/17	74	2400	Some cloud towards end of exposure
NGC 7361	22/05/17	38	2400	Clear skies
NGC 7361	22/05/17	40	2400	Clear skies
NGC 7361	22/05/17	41	2400	Wispy cloud
NGC 7361	22/05/17	43	2400	Intermittent cloud, guiding failure



# CHAPTER B

## MORE DETAILS ON DATA REDUCTION CHANGES

---

---

### B.1 INVESTIGATING THE UPTURN IN THE BLUE END OF THE SPECTRA

When going through the data reduction and calibration process, we find an upturn in flux in the blue end of the spectra from KOALA. This is important to fix as this upturn in the spectrum makes it difficult to fit our spectra with the standard templates that are available. This upturn could be caused by issues with the flux calibration, and also could be due to scattered light. We consider each of these possibilities in the following sections.

#### B.1.1 BIASES IN FLUX CALIBRATION CURVES

The first thing we tried to do was improve the quality of our flux calibration curves. The blue flux calibration curves also have a very sharp upturn at the blue end of the spectrum, making them a possible source of the upturn in the galaxy data after flux calibration.

Initially, we used only the brightest fibre in our flux standard observations to obtain the spectrum of the standard star. However, this means that the spectrum obtained from the standard star will be subject to the effects of atmospheric dispersion. Atmospheric dispersion causes the image of the star to be spread out on the sky, with the blue end of the spectrum being shifted further than the red end of the spectrum. With only one fibre being used to create the spectrum for the standard star, we miss some of the blue flux from the star. This means that the spectrum is

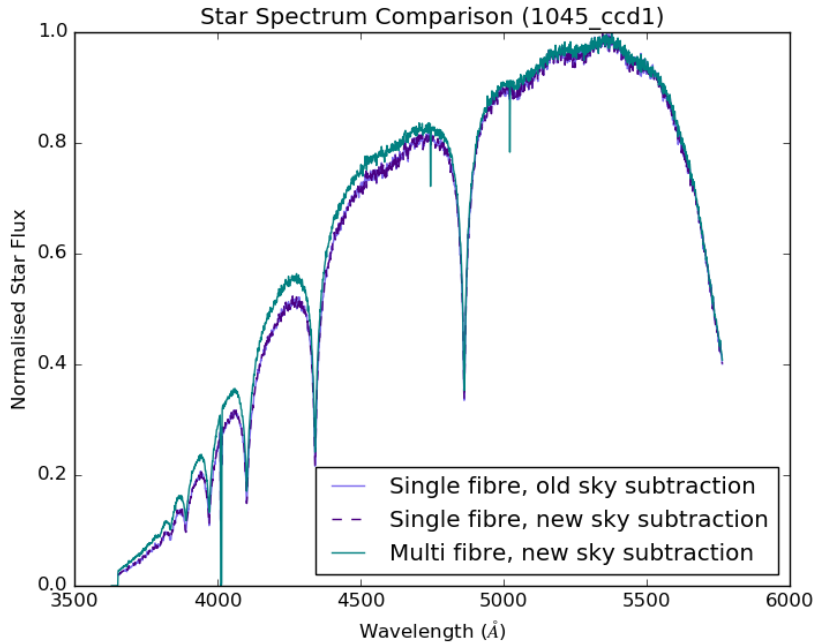


**Figure B.1.** Plots of the spectrum obtained from our KOALA observations of the flux standard LTT3218. The light purple solid line and dark purple dashed line indicate the spectrum of the star obtained using a single fibre and different methods of sky subtraction for the KOALA flux standard observations. The teal solid line indicates the spectrum of the star obtained when using multiple fibres.

lower in the blue end than it should be, and the calibration curve will be increased to compensate for this.

To address this, we instead use multiple fibres that have the largest percentages of stellar flux, and sum their contributions together to obtain the spectrum from the standard star. This ensures we collect all of the dispersed light from the star, and that we correct any artificial upturn introduced because of that. An example of the effect this has on the spectrum is shown in Figure B.1; the spectrum created from multiple fibres has noticeably higher flux in the very blue end than for the cases where single fibres were used to obtain the flux of the star. We find that this goes some way towards improving the upturn in the final data, however, this does not completely solve the problem. The contribution from this alone is not enough to completely remove the upturn in the blue end of the spectrum.

### B.1.2 CHARACTERISING THE SCATTERED LIGHT

As mentioned in Section 3.3, scattered light has been found to be an issue for instruments on the AAT which use the AAOmega spectrograph (Green et

al., 2018). To try and solve any issues caused by scattered light, we attempt to characterise the scattered light in each of our observations, and subsequently remove it. We carried this out using some of the products obtained from the reduction process of 2dFdr. The im.fits files have only had a small part of the reduction process carried out when they are created by 2dFdr; at this point, only bias subtraction using the overscan region in each frame has been applied. The flux of each fibre has not yet been extracted, meaning that it is still spread over several pixels, and there are still gaps present between each fibre and the fibre bundles they are part of. It is these gaps that we are interested in for the purposes of scattered light characterisation. The scattered light is present across the whole frame of each observation, however, light from the observations is only present where a fibre sits. This means that the gaps between fibres should contain the profile of the scattered light with wavelength.

Therefore, to obtain the scattered light profile for each observed frame, we mask out all pixels where the flux from a fibre would be read out onto the CCD. The profiles obtained from each region are then averaged together to obtain the final scattered light profile. This process assumes that the scattered light does not change as you move down the CCD, however we know from looking at the quartz flat in Figure B.8 that this is not the case; the scattered light is more prominent at the top and bottom of the CCD. Therefore, we try several different methods of removing the scattered light from the data.

The first method we use is described above; we average the scattered light profiles together from each of the gaps in the data, to obtain one final scattered light profile. This is dubbed the 1D scattered light removal technique. The data is put through a preliminary simple data reduction process within 2dFdr to obtain the im.fits files that are created from it. These files are then used to obtain the 1D scattered light profiles, which are then subtracted from each row of pixels in the raw data frames. This data is then put back through the final data reduction process in 2dFdr.

We also attempted this 1D scattered light subtraction after the final reduction process had been carried out in 2dFdr. To do this, the scattered light profile is obtained in the same way as above, using the im.fits files created in a preliminary reduction from 2dFdr. The raw data frames are then put through their final data reduction using 2dFdr. We are interested in the reduced files that are returned from this process, as we then want to subtract the scattered light profile from each fibre in those reduced frames. We cannot just subtract the profile on it's own however; when the fluxes of the reduced frames are extracted from the raw frames, the flux is integrated over several pixels to obtain the final fibre flux. The scattered light profile

is present in every row of pixels, so the final fibres end up with several contributions of the scattered light included in their final fluxes. This means we need to multiply the scattered light profile by a factor of 3.33 to get the scattered light profile in the final fibres; this factor is chosen as the approximate number of pixels each fibre occupies on the CCD. We do this comparison to check that there are no issues introduced into this scattered light removal process by the reduction and extraction process within 2dFdr.

The final process we try is a 2D version of the 1D scattered light subtraction. This again uses the im.fits files to obtain the scattered light profiles from the regions in between the fibres on the CCD. We saw from looking at the quartz flats that the scattered light present in the frames is not constant from the top of the CCD to the bottom. So instead of averaging the profiles from the gaps to obtain one final profile, the profiles from the gap regions are used to model the scattered light in between and obtain a 2D scattered light profile for each frame. This 2D profile is then subtracted from the raw frames before they are put through 2dFdr for their final reduction.

We compared these different methods of scattered light subtraction against one another to see which was the most effective at removing the scattered light. The results are shown in Figure B.2. We tested each method with several different object frames for different galaxy fields to see if they improved the quality of the spectra. Figure B.2 shows that all three of the methods have approximately the same effect on the average spectrum taken from the object frames that were tested, when compared to the same spectrum with no scattered light subtraction.

We expected the two methods of 1D scattered light subtraction to be very similar; this confirms the multiplicative factor of 3.33 was roughly correct for the contribution that the scattered light has to the final extracted fibre spectrum. The similar result confirms that there is nothing odd happening to the data during the extraction process of 2dFdr after the scattered light subtraction. However, we expected the 2D scattered light subtraction to be better at removing the scattered light contamination than the 1D methods. To check that the method was doing what we expected, we tested it on a simple case; the quartz flats are the perfect example for this as they are free of any bright emission lines and should show the same spectrum in every fibre, barring any differences in throughput.

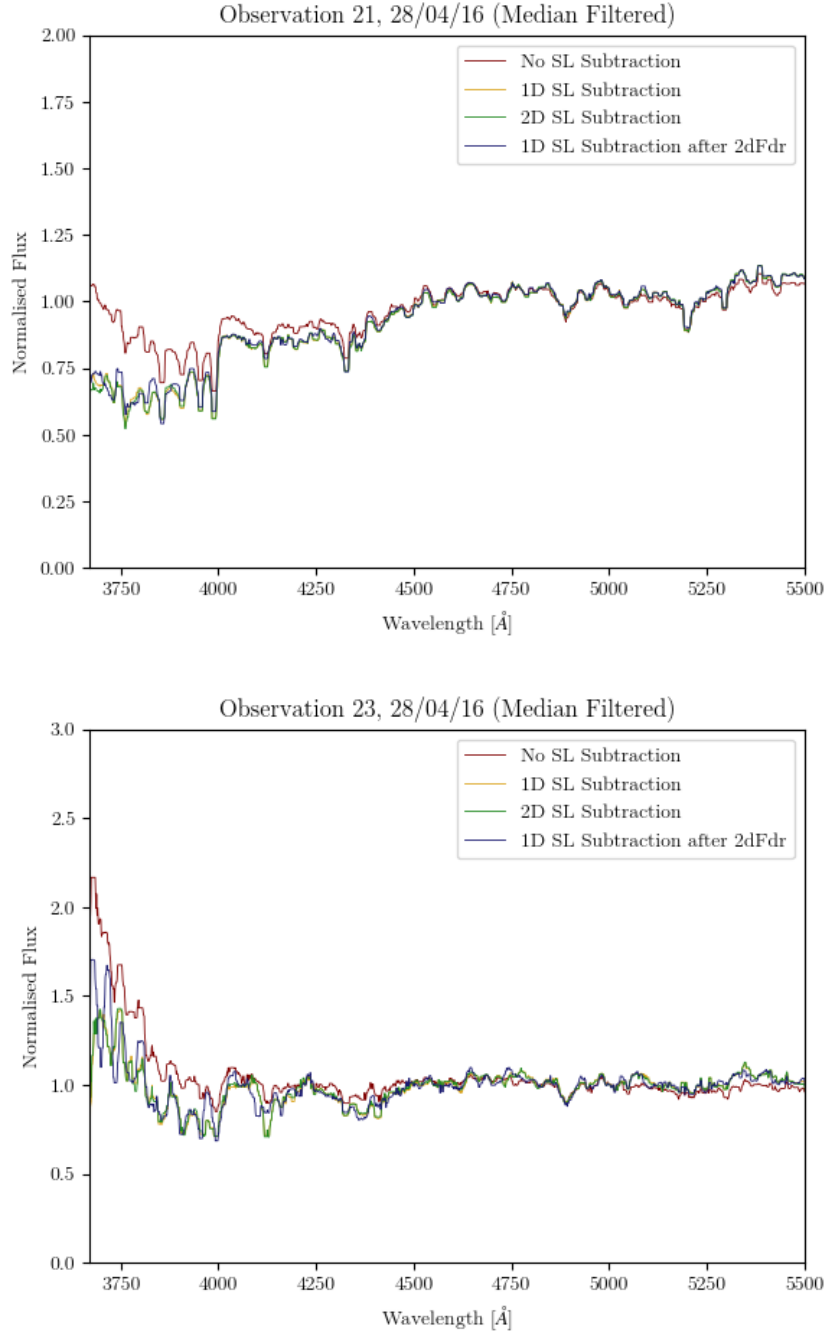


**Figure B.2.** Comparisons of the different methods of scattered light subtraction for two different object frames; the top panel shows an observation of NGC 4030, and the bottom panel shows an observation of NGC 5584. The average, normalised flux of each frame is shown against wavelength. The spectrum with no scattered light subtraction is plotted as the red line, the two methods of 1D scattered light subtraction are plotted as the yellow and blue line, and the 2D scattered light subtraction is plotted as the green line in each plot. A median filter has been applied to each spectrum to clean it up and make the differences caused by the scattered light subtraction clearer.

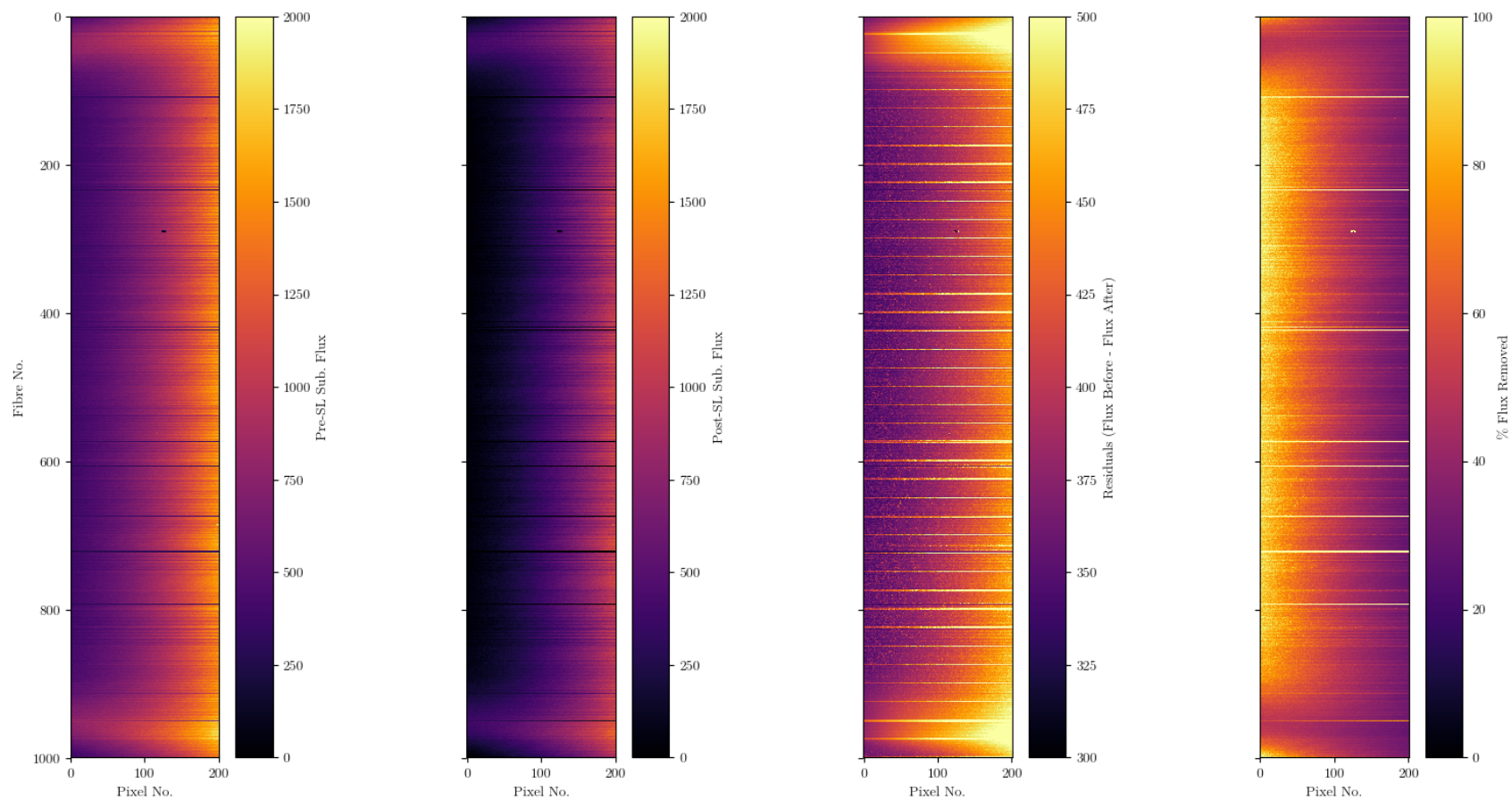


**Figure B.3.** An example of the first 200 pixels of a quartz flat after being put through the 2D scattered light subtraction process. From left to right the panels show; the quartz flat before 2D scattered light subtraction, the quartz flat after 2D scattered light subtraction, the difference between the data before and the data after, and the percentage difference in the data before and after.

If the 2D scattered light subtraction was working correctly for the quartz flats, then we would expect the bright areas in the corners of the CCD to be removed, such that the very blue end of the fibres that sit at the top and bottom of the CCD are brought more in line with the fibres that sit in the middle of the CCD. These bright areas are shown in the far left panel of Figure B.3; the top 100 and bottom 100 fibres show much brighter flux over the first 100 pixels of the CCD than the other fibres do. The same area of the CCD after the 2D scattered light subtraction has been carried out is shown in the next panel along in Figure B.3; the colourbar is kept consistent between the two plots. Overall, there is less flux all the way down the CCD after scattered light subtraction; the same scattered light profile seems to be present in the top and bottom fibres of the CCD. This is also demonstrated in Figure B.4, the top panel shows the average spectrum before 2D scattered light subtraction over the first 200 pixels for the top and bottom 100 fibres, and compares it to the spectrum for the middle 200 fibres. The bottom panel shows the same areas after the scattered light subtraction has been carried out. This confirms that the 2D scattered light is not removing the scattered light the way we would want it to, as the spectra of the top and bottom 100 fibres do not match with those in the middle of the CCD.

The final two panels of Figure B.3 give an insight into what might be happening here. The third panel along shows the difference between the data without any scattered light correction and the data post scattered light subtraction, and the final panel shows this quantity as a percentage of the light present in the initial data. This shows that there is more flux being removed in the areas where there is scattered light, but seemingly only because these areas are brighter; the model of the 2D scattered light is removing the same percentage of light from all of the fibres, without focusing on removing a higher percentage of light from the areas that are most affected by the scattered light. This is not what we want from the 2D scattered light subtraction, so we opt to use one of the 1D scattered light subtraction methods. We use the 1D method which is applied before we put the data through its final reduction process in 2dFdr, as this method means we don't have to assume any factors to scale up the scattered light profile; everything is taken care of during the extraction portion of the process. This is the method we use during the final data reduction and calibration process for our data.

Overall, the scattered light is not removed completely from the data, but the 1D scattered light removal method does improve the upturn in flux in most cases. To completely remove the contribution from the scattered light, a more intensive and complicated removal procedure would be necessary, which is beyond the

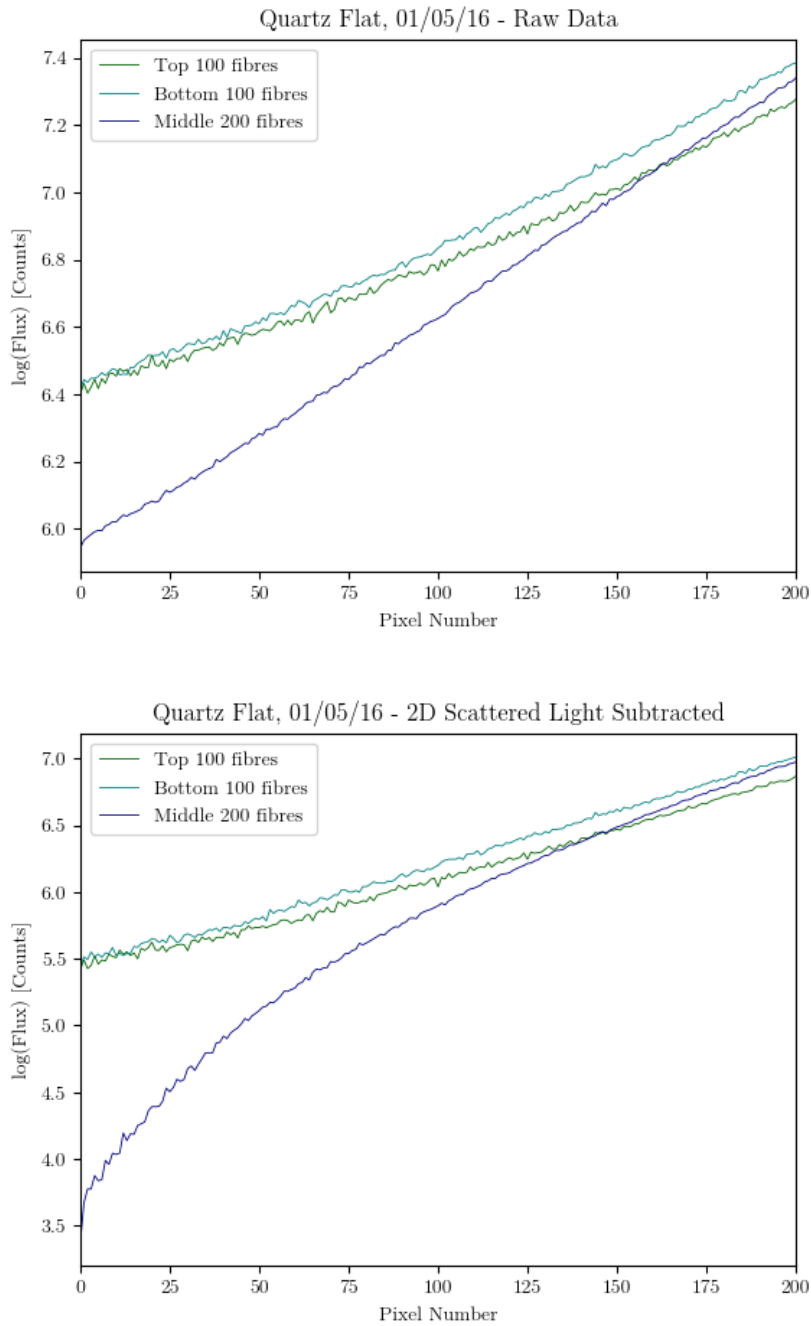


**Figure B.4.** Plots of the flux in the first 200 pixels of the CCD for the top 100 fibres (green line), bottom 100 fibres (light blue line) and the middle 200 fibres (dark blue line). The top panel shows the flux for these regions before the 2D scattered light subtraction has been applied, and the bottom panel shows the same data after the 2D scattered light subtraction has been applied.

scope of the project here. If this upturn still poses a problem when we are trying to fit our data with standard templates, then we will correct for it using polynomials.

## B.2 2DFDR SETTINGS

During our initial investigations of the data reduction process using version 6.28 of 2dFdr (the recommended release version at the time), we tried using the internal version of PyCosmic with a couple of the different extraction methods available in 2dFdr; Gauss and OPTEX. During our testing, we encountered an issue with that version of 2dFdr, where we found that using PyCosmic with OPTEX as the chosen extraction method was unstable and gave unsatisfactory results, regardless of the parameters being used in PyCosmic. We did not encounter the same problems with the Gauss extraction option selected. This is demonstrated in Figure B.5, where the same part of one of our observations is shown after being reduced with both the Gauss and OPTEX extraction methods with PyCosmic turned on within 2dFdr. The frame that was reduced using the Gauss extraction method removes most of the cosmic rays present without any problems, whereas when the OPTEX extraction method is used, it fails to remove cosmic rays completely, or misses them entirely. It also appears to remove flux where there are no cosmic rays at all. It therefore seems that there is a bug present that affects PyCosmic when it is used alongside OPTEX in this version of 2dFdr.

## B.3 GAUSS VERSUS OPTEX EXTRACTION METHODS

We compare the Gauss and OPTEX extraction methods to check that the OPTEX method is functioning as stated, i.e. that it is removing cross-talk, and is therefore worth the extra running time. The first thing we wanted to investigate to check for cross-talk was fitting the stellar profile in both the Gauss and OPTEX extracted cases, and then comparing the residuals to see if the fit varied for the two reduction methods. The assumption was made that if the OPTEX extraction method is doing its job correctly, then the flux we see should be as close to a true representation of the stellar profile as possible, without any extra flux due to cross talk. This should not be the case for the Gauss extracted data, and the fits should not be as good. Therefore, we compare the quality of the fits to one another, particularly in the regions where we expect cross-talk, such as within fibres 430 and 432.

Initially, we tried fitting several different functions to the stellar profile of the OPTEX extracted data to see which one best represented it. The functions we

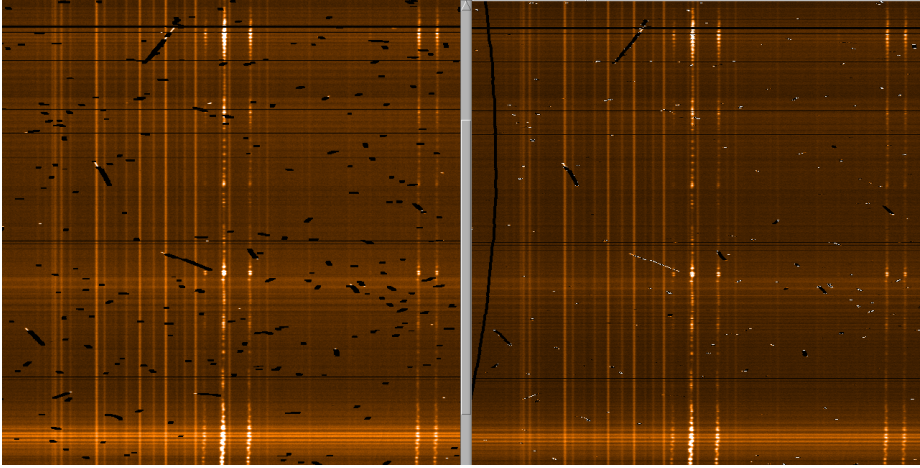


**Figure B.5.** An example of the differences in the behaviour of PyCosmic depending on the extraction method used for part of an object frame from KOALA. On the left is data reduced using the Gauss extraction method alongside PyCosmic within 2dFdr, and on the right is the same data but with the OPTEX extraction used. In the case where OPTEX is used, many cosmic rays are left untouched by the PyCosmic algorithm, and others are not completely removed. There is also an area where a large line of flux has been removed from the top to the bottom of the image when there is no cosmic ray present. These issues are not seen when Gauss is used.

fitted included a single two dimensional Gaussian function, of the form:

$$f(x, y) = a \exp \left( - \left[ \frac{(x - x_o)^2}{2\sigma_x^2} + \frac{(y - y_o)^2}{2\sigma_y^2} \right] \right) + b, \quad (\text{B.1})$$

where  $x_o$  and  $y_o$  are the central positions of the Gaussian function,  $\sigma_x$  and  $\sigma_y$  are the standard deviations in  $x$  and  $y$  respectively, and  $a$  and  $b$  are constants. The next function we fitted was a double two dimensional Gaussian function, of the form:

$$f(x, y) = a \exp \left( - \left[ \frac{(x - x_o)^2}{2\sigma_1^2} + \frac{(y - y_o)^2}{2\sigma_1^2} \right] \right) + b \exp \left( - \left[ \frac{(x - x_o)^2}{2\sigma_2^2} + \frac{(y - y_o)^2}{2\sigma_2^2} \right] \right) + c, \quad (\text{B.2})$$

where  $x_o$  and  $y_o$  are the central positions of the Gaussian function,  $\sigma_1$  and  $\sigma_2$  are the standard deviations of the first and second Gaussian functions respectively, and  $a$ ,  $b$  and  $c$  are constants. The final function we fitted was a Moffat profile, a more complex function often used to fit stellar point spread functions (PSFs), of the form:

$$f(x, y) = A \left( \frac{\beta - 1}{\pi\alpha^2} \right) \left( 1 + \left[ \frac{(x - x_o)^2 + (y - y_o)^2}{\alpha^2} \right] \right)^{-\beta} + B, \quad (\text{B.3})$$

where  $x_o$  and  $y_o$  are the central positions of the Moffat function,  $\beta$  determines the shape of the function and  $\alpha$  determines the scale of the function, and  $A$  and  $B$  are

constants. The best fitting parameters of the functions were found by minimising the sum of the squared residuals between the data and the model. The model fits and their residuals for each function are shown in Figure B.6.

The single 2D Gaussian function (top row, left panel of Figure B.6) does not do a good job of fitting the low level wings of the stellar PSF. The Moffat function (bottom row, left panel of Figure B.6) does a slightly better job at fitting these low level wings. However, the best fitting model to the PSF of the star, with the lowest summed squared residuals of the model fits, is the double 2D Gaussian (middle row, left panel of Figure B.6). Therefore, a double 2D Gaussian function was fit to the Gauss extracted data as well, so that the two extraction methods could be compared directly to each other. The ratio of the residuals from the model fit to the Gauss extracted data to the model fluxes of the OPTEX extracted data was then calculated, and is shown in Figure B.7. This does not clearly show a great difference between the Gauss and OPTEX extracted data.

## B.4 THROUGHPUT CALIBRATION USING QUARTZ FLATS

When comparing the quality of the quartz flats as a method of determining the throughput calibration of the KOALA IFU data, we discovered an issue with the quartz flats that effects their ability to accurately determine the throughputs of each fibre. This is shown in Figure B.8; this is an image of a reduced quartz flat in it's row stacked spectra form, i.e. with each fibre stacked one on top of the other in the image, with the horizontal axis representing wavelength. Most of the regions in the spectra are very uniform, however, at the edges there are bright regions. This is caused by scattered light from the detector; we have found this to be a serious issue for our data (Section 3.3). Indeed, the quartz flats have lower flux in these edge regions and the scattered light contributes a significant contribution to the total flux. These bright regions at the corners of the field affect the brightness of about 250 of the fibres in the field of view of KOALA, meaning that around a quarter of the fibres are brighter than they should be in these observations simply due to scattered light issues, thereby rendering the quartz flats unsuitable for using to determine the throughput calibration.

## B.5 SKY SUBTRACTION

Here we describe the changes we needed to make to perform sky subtraction and to remove sky emission lines. We found that using 2dFdr, we were left

with a number of emission lines in our object spectrum due to incorrect subtraction. We changed one of the settings in the Calib tab of 2dFdr, and enabled wavelength calibration using sky emission lines, which lines up the sky emission lines in object and offset sky frames. We hoped that this would make sure that the sky emission lines were removed correctly. However, we initially found that after we enabled this feature, the removal of sky lines improved for some spectra, but got worse for others. To diagnose the problem, we focused on a small area of the spectrum around a sky emission line when the wavelength calibration option was enabled and disabled at different stages of the reduction process; the result of this investigation is shown in Figure B.9. Through this, we discovered that the wavelength calibration was being applied to any frame with NDF class ‘MFOBJECT’, but not to those frames with NDF class ‘MFSKY’ during the reduction process within 2dFdr. This meant that only our object frames were having the wavelength calibration applied to them, so when we then used the offset sky spectra, classified as ‘MFSKY’, to perform the sky subtraction, the sky emission lines were still offset from one another.

To solve this problem, we made copies of our offset sky frames, and changed the NDF class of the copies to be ‘MFOBJECT’. That way, we still had our original offset skies present as a guide to perform the wavelength calibration, but the changes necessary were then applied to both object and offset sky frames. This change unfortunately does not work for the blue CCD, as there is only one sky emission line present in that wavelength range, and therefore there is not enough information for the calibration to use. An example result for the red CCD can be seen in Figure B.10, which shows the average spectrum for the same object frame before and after these changes were made. The spectrum that results from sky subtraction using these newly classified ‘MFOBJECT’ offset skies is much cleaner, and shows that the wavelength calibration is now being applied correctly. When reducing data using version 6.28 of 2dFdr, wavelength calibration from sky lines is one of the final options selected, with changes in the classification of the offset sky observations to ‘MFOBJECT’ being applied.

This was the method used to ensure the sky emission lines were removed correctly whilst we were using version 6.28 of 2dFdr. However, due to another issue with the data (Chapter 3), we had to switch to using the more recent version 6.88 of 2dFdr. Updates made recently to the functionality of the wavelength calibrate from sky lines option have caused a bug in the 2dFdr code, which is preventing this option from working. To solve this problem, we added a cross-correlation step to our sky subtraction code.

### B.5.1 SKY SUBTRACTION ON MOONLIT NIGHTS

During testing of our data reduction and calibration process, we discovered an issue with our sky subtraction for some of our observing nights. When performing our sky subtraction, some of the object observations were coming out of this process with barely any flux, or even negative flux. This was particularly noticeable for the data from the 28<sup>th</sup> April 2016. This prompted us to investigate the flux of our individual offset sky observations for all of the observing nights. The results of this are shown in Figure B.11.

We discovered that the brightness of the offset skies was increasing as the night went on during the 28<sup>th</sup> April 2016. This was due to the rising of the moon early on that night. Dark sky time was requested during the observing proposals to the AAT, but it is not always possible to obtain this for every observing run, and unfortunately the moon was still full enough during this night that it caused issues with the data. This was also found to be an issue for the latter part of the night on the 21<sup>st</sup> May 2017, where, after moonrise, there is a sharp increase in the flux of the final offset sky that was taken. However, this affected a far smaller portion of the data than the moonlight on the 28<sup>th</sup> April 2016.

Due to this increase in flux, we were unable to use the same sky subtraction technique for the moonlit nights. The creation of a master sky requires the offset sky flux to be consistent throughout the night for an accurate median sky to be created. For both of the nights affected by moonlight, this was obviously not the case. This can be clearly seen in Figure B.12 for the objects and offset skies from the 28<sup>th</sup> April 2016. In both cases where there was contamination from moonlight, the brightness of the sky rises approximately linearly with time. Therefore, to remove the correct amount of sky flux during the sky subtraction for each object frame, we interpolate between the observed offset skies to obtain the sky flux at the time each object observation was taken, according to the following equation:

$$S(t_{Obs}) = \frac{S(t_1)(t_2 - t_{Obs}) + S(t_2)(t_{Obs} - t_1)}{(t_2 - t_1)} \quad (\text{B.4})$$

where  $S(t_{Obs})$  is the sky flux at the time a particular object observation was taken,  $S(t_1)$  and  $S(t_2)$  are the fluxes of offset skies taken before and after the object observation respectively, and  $t_{Obs}$ ,  $t_1$  and  $t_2$  are the times the object observation, sky before the object observation and sky after the object observation were taken respectively.

An example of the interpolation is shown in Figure B.13. Some of our galaxy fields had observations that were affected by moonlight and some that were

not, and could therefore be sky subtracted in the normal way; when the resulting spectra for those fields were compared against one another, we find good agreement between the spectra that were sky subtracted using different methods. Due to this agreement, we feel confident that this interpolation is working correctly, and use this to solve the problem of moonlight in our final reduction and calibration process.

## B.6 FLUX CALIBRATION

To perform the flux calibration, we first need to extract the spectrum of the standard star LTT3218 from our KOALA observations as shown in Figure B.14. When creating flux calibration curves of the standard star, we see a lot of spectral features present in the spectrum of the star. We remove these remaining features to obtain a smooth calibration curve by applying a median filter to each calibration curve. An example is shown in Figure B.15, before and after the median filter is applied.

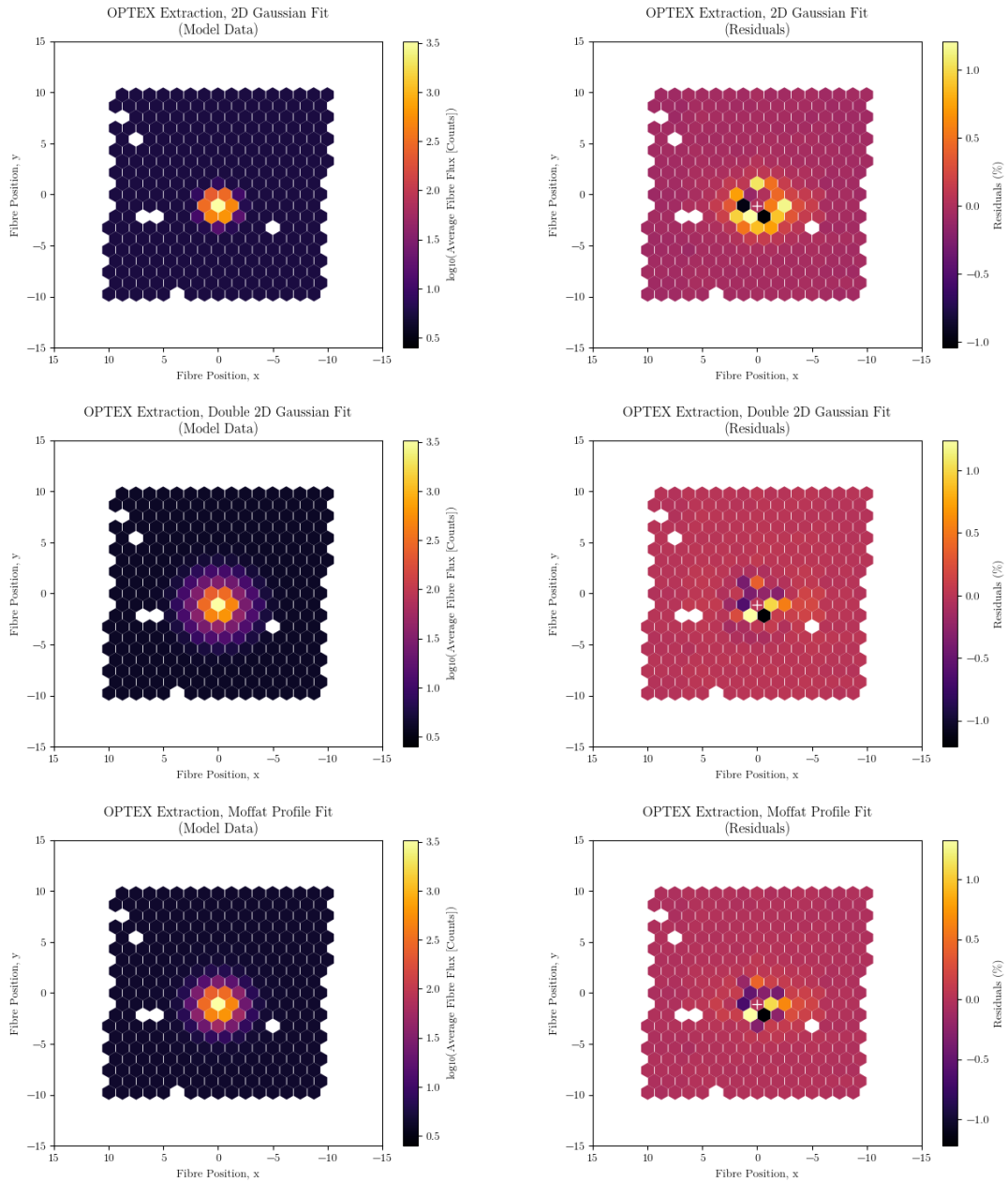


**Figure B.6.** Top row: Results from the 2D Gaussian function fit to the OPTEX extracted flux standard data. The left panel shows the model fluxes from the fitting routine and the right panel shows the residuals between the model fluxes and the OPTEX extracted data. Middle row: Results from the double 2D Gaussian function fit to the OPTEX extracted flux standard data. The left panel shows the model fluxes from the fitting routine and the right panel shows the residuals between the model fluxes and the OPTEX extracted data. Bottom row: Results from the Moffat function fit to the OPTEX extracted flux standard data. The left panel shows the model fluxes from the fitting routine and the right panel shows the residuals between the model fluxes and the OPTEX extracted data.

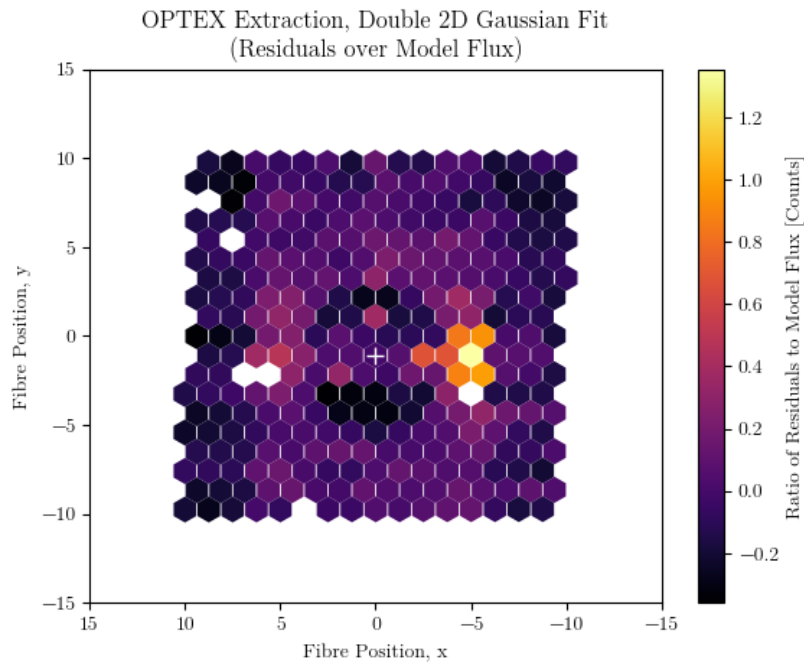


**Figure B.7.** Ratio of the residuals of the double 2D Gaussian model fit to the Gauss extracted data to the model fit to the OPTEX extracted data.

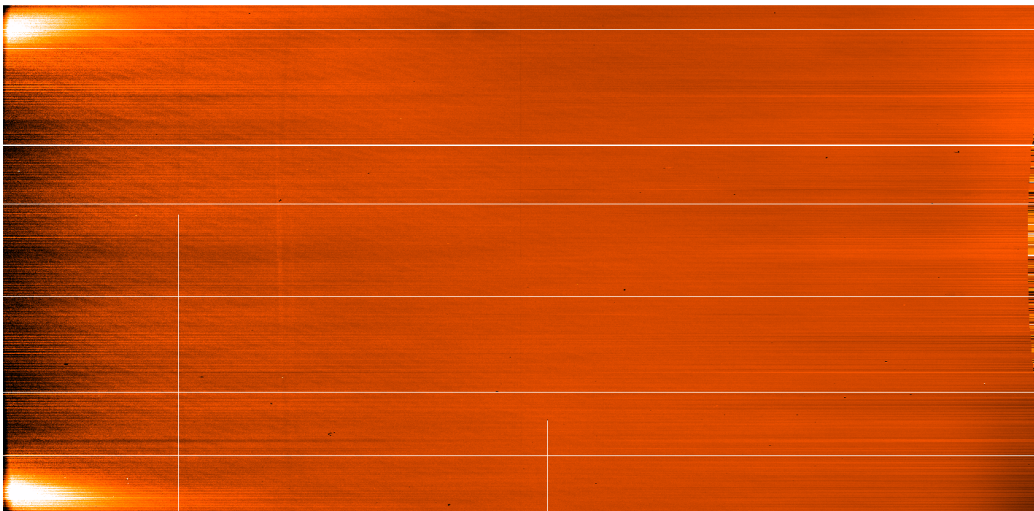


**Figure B.8.** An example of a quartz flat in its row stacked spectra form, with wavelength along the horizontal axis and fibre number on the vertical axis. There is clear contamination from scattered light in the top and bottom left of this observation.

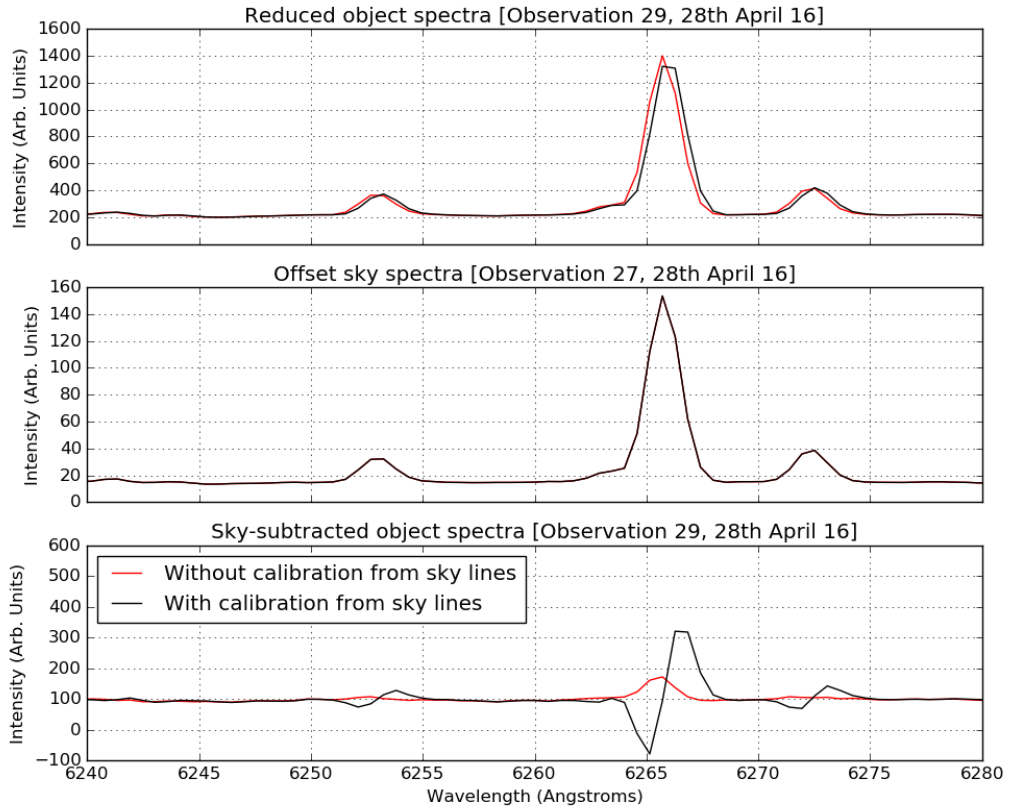


**Figure B.9.** Investigation into the functionality of the wavelength calibrate from sky lines option withing 2dFdr. The top panel shows a section of a reduced object spectrum, the middle panel a reduced offset sky spectrum, and the bottom panel the resulting spectrum when the offset sky spectrum is used to sky subtract the object spectrum in the top panel. All spectra focus on the same wavelength range, where there are several sky emission lines present. The black and red lines in each panel indicate whether the spectra were reduced with or without the wavelength calibrate from sky lines option enabled.

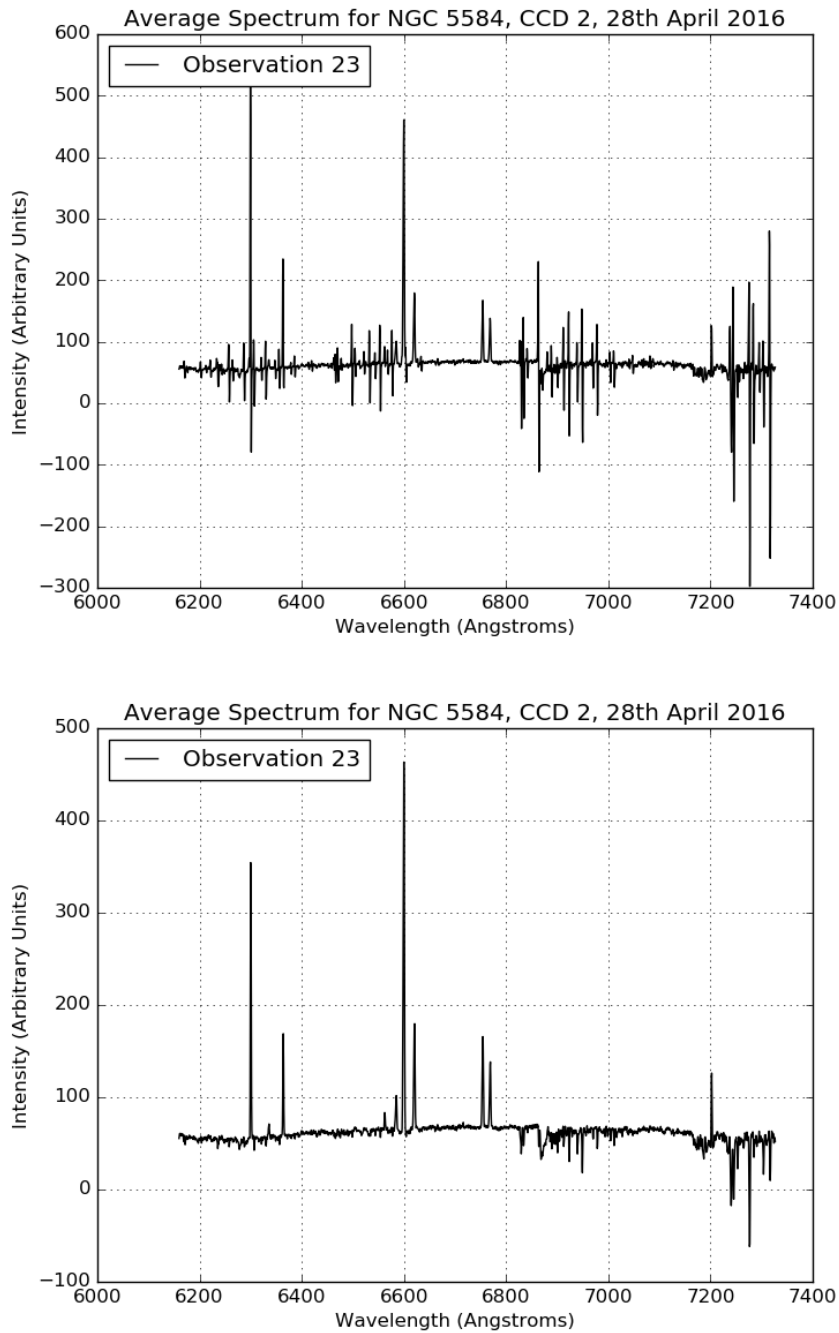


**Figure B.10.** Examples of the average sky-subtracted spectrum of an observation of NGC 5584, taken on 28<sup>th</sup> April 2016, with the wavelength calibration function being applied correctly and incorrectly. The top panel shows the resulting spectrum with incorrect wavelength calibration, and the bottom panel shows the resulting spectrum with correctly applied wavelength calibration.

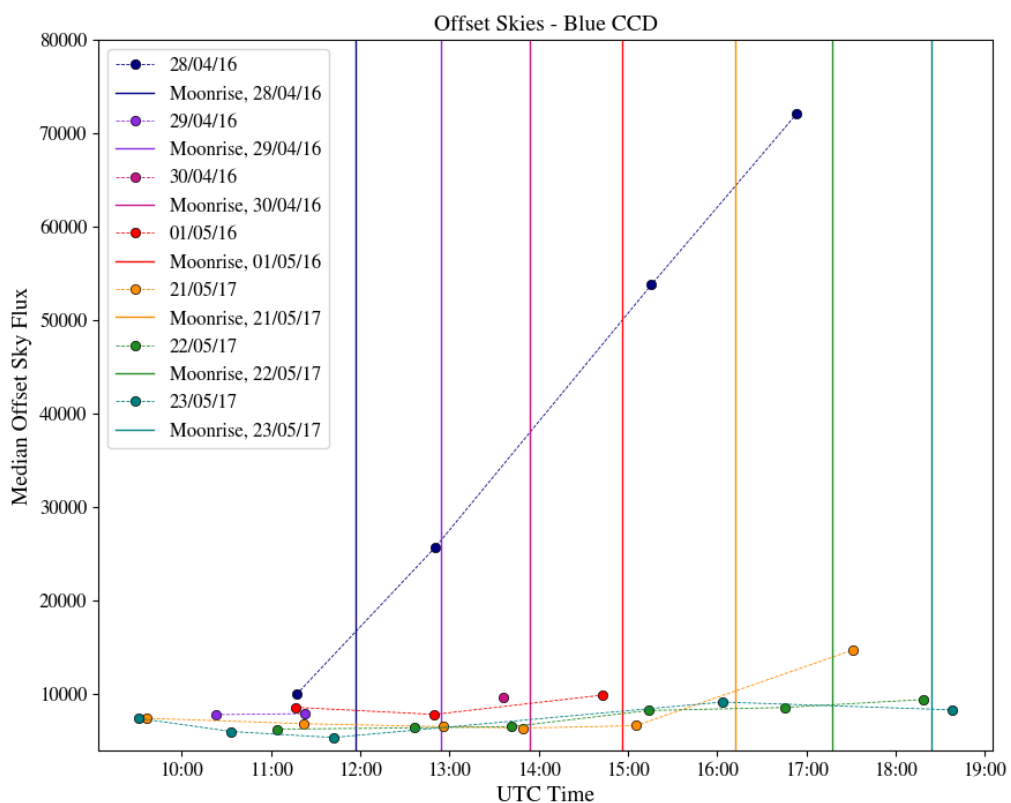


**Figure B.11.** Plot of the median offset sky flux with time for each observing night. The brightness of the offset skies for each night are shown as different coloured circles connected by dashed lines in various colours. The time of moonrise for that each night is shown as a vertical line of the same colour as the circles of the offset skies.

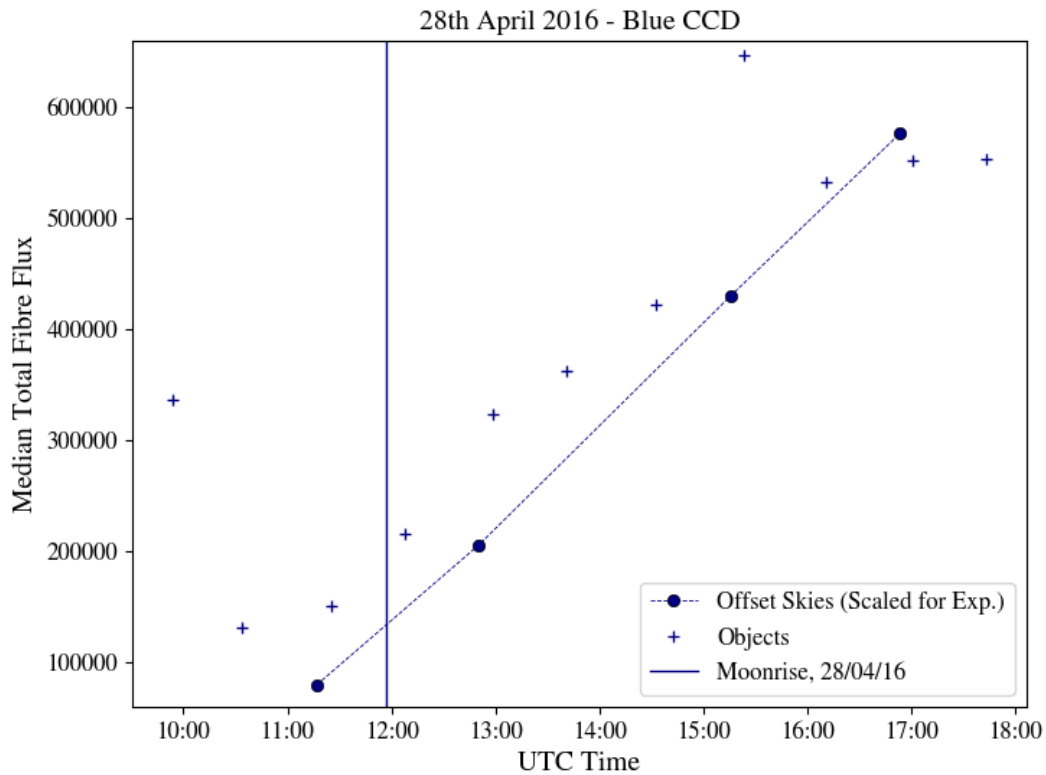


**Figure B.12.** Plot of the median fibre flux with time for the object and offset sky observations taken on the 28<sup>th</sup> April 2016. Object observations are plotted as crosses, and offset sky observations as circles connected by the dashed line. The time of moonrise on that night is indicated with the solid vertical line.

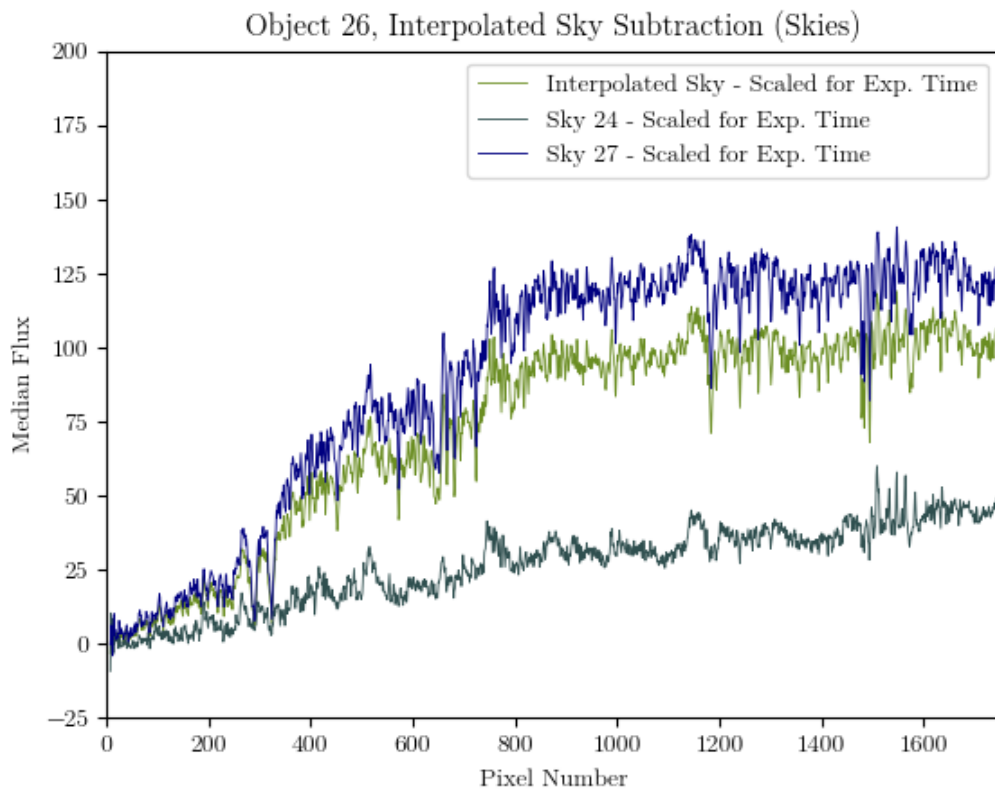


**Figure B.13.** Example spectra of NGC 5584, taken on the 28<sup>th</sup> April 2016 to demonstrate that the interpolation between the two closest sky observations works. The spectrum ‘Sky 24’ was taken before the source observation and ‘Sky 27’ was taken after (blue and dark green respectively). Using Equation B.4 we interpolate to determine the sky spectrum at the source - which lies between them (light green).

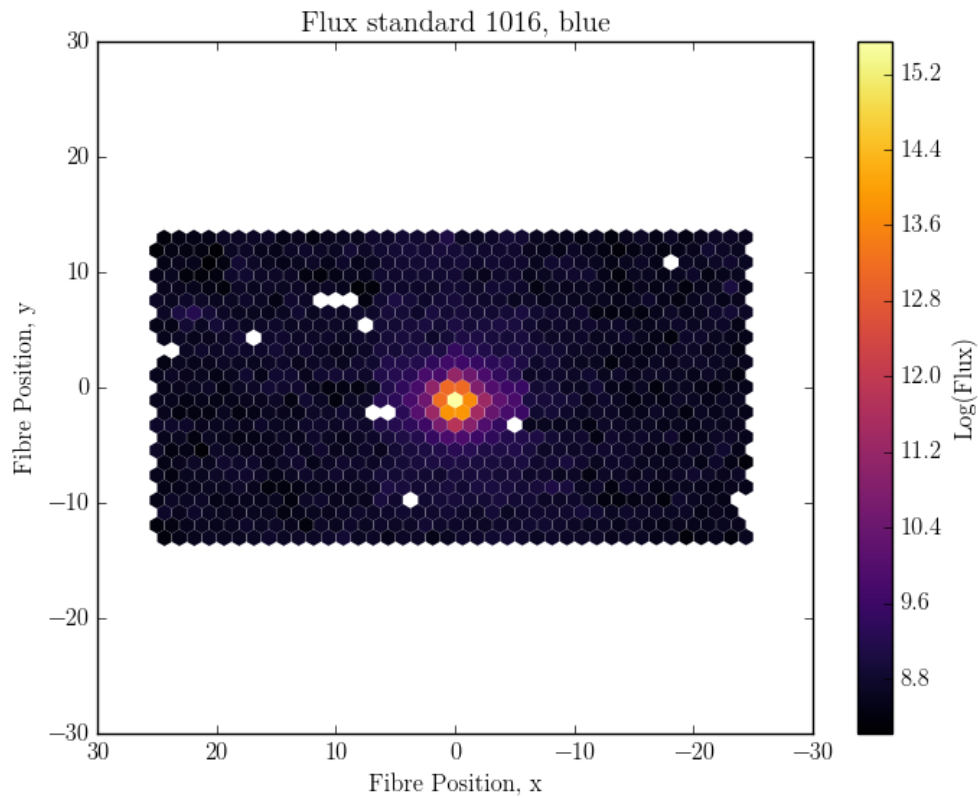


**Figure B.14.** Fibre intensity map for one of the flux standard observations taken on the 28<sup>th</sup> April 2016 using the blue CCD of the standard star LTT3218. Regions of bright flux emission are limited to a small area around the star, which is observed in the centre of the field of view.

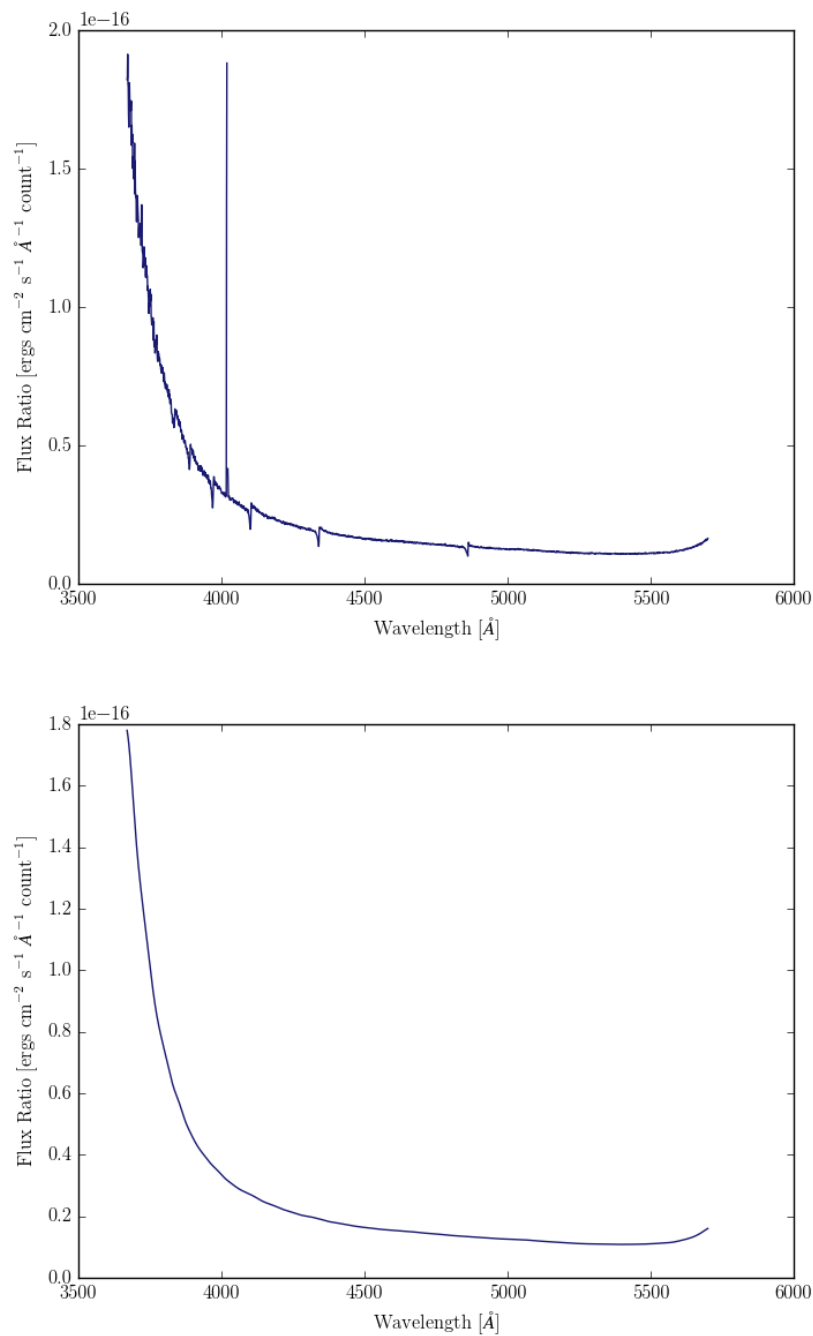


**Figure B.15.** An example of the difference between the smoothed and unsmoothed calibration curve for one of the standard star observations obtained during our observing runs with KOALA. The top panel shows the flux ratio before the median filter is applied, and the bottom panel shows the result after the median filter has been applied and the curve has been smoothed.



# BIBLIOGRAPHY

---

---

- AAO Software Team (May 1, 2015). “2dfdr: Data Reduction Software”. In: *Astrophysics Source Code Library*, ascl:1505.015. URL: <http://adsabs.harvard.edu/abs/2015ascl.soft05015A> (visited on 05/15/2021).
- Allen, J. T., S. M. Croom, I. S. Konstantopoulos, J. J. Bryant, R. Sharp, et al. (Jan. 1, 2015). “The SAMI Galaxy Survey: Early Data Release”. In: *Monthly Notices of the Royal Astronomical Society* 446, pp. 1567–1583. ISSN: 0035-8711. DOI: [10.1093/mnras/stu2057](https://doi.org/10.1093/mnras/stu2057). URL: <http://adsabs.harvard.edu/abs/2015MNRAS.446.1567A> (visited on 05/13/2021).
- Bacon, R., J. Vernet, E. Borisova, N. Bouché, J. Brinchmann, et al. (Sept. 1, 2014). “MUSE Commissioning”. In: *The Messenger* 157, pp. 13–16. ISSN: 0722-6691. URL: <http://adsabs.harvard.edu/abs/2014Msng.157...13B> (visited on 05/16/2021).
- Bacon, Roland, Svend Bauer, Petra Böhm, Didier Boudon, Sylvie Brau-Nogue, et al. (June 1, 2006). “Probing Unexplored Territories with MUSE: A Second-Generation Instrument for the VLT”. In: *The Messenger* 124. ISSN: 0722-6691. URL: <http://adsabs.harvard.edu/abs/2006Msng.124...5B> (visited on 05/13/2021).
- Bacon, Roland, Simon Conseil, David Mary, Jarle Brinchmann, Martin Shepherd, et al. (Dec. 1, 2017). “The MUSE Hubble Ultra Deep Field Survey. I. Survey Description, Data Reduction, and Source Detection”. In: *Astronomy and Astrophysics* 608, A1. ISSN: 0004-6361. DOI: [10.1051/0004-6361/201730833](https://doi.org/10.1051/0004-6361/201730833). URL: <http://adsabs.harvard.edu/abs/2017A%26A...608A...1B> (visited on 05/16/2021).
- Baillard, A., E. Bertin, V. de Lapparent, P. Fouqué, S. Arnouts, et al. (Aug. 1, 2011). “The FIGI Catalogue of 4458 Nearby Galaxies with Detailed Morphology”. In: *Astronomy and Astrophysics* 532, A74. ISSN: 0004-6361. DOI: [10.1051/0004-6361/201016423](https://doi.org/10.1051/0004-6361/201016423). URL: <http://adsabs.harvard.edu/abs/2011A%26A...532A..74B> (visited on 12/22/2020).

- Baldry, I. K., S. P. Driver, J. Loveday, E. N. Taylor, L. S. Kelvin, et al. (Mar. 1, 2012). “Galaxy And Mass Assembly (GAMA): The Galaxy Stellar Mass Function at  $z < 0.06$ ”. In: *Monthly Notices of the Royal Astronomical Society* 421, pp. 621–634. ISSN: 0035-8711. DOI: [10.1111/j.1365-2966.2012.20340.x](https://doi.org/10.1111/j.1365-2966.2012.20340.x). URL: <http://adsabs.harvard.edu/abs/2012MNRAS.421..621B> (visited on 12/22/2020).
- Bolatto, Alberto D., Mark Wolfire, and Adam K. Leroy (Aug. 1, 2013). “The CO-to-H<sub>2</sub> Conversion Factor”. In: *Annual Review of Astronomy and Astrophysics* 51, pp. 207–268. ISSN: 0066-4146. DOI: [10.1146/annurev-astro-082812-140944](https://doi.org/10.1146/annurev-astro-082812-140944). URL: <http://adsabs.harvard.edu/abs/2013ARA%26A..51..207B> (visited on 12/22/2020).
- Bundy, Kevin, Matthew A. Bershady, David R. Law, Renbin Yan, Niv Drory, et al. (Jan. 1, 2015). “Overview of the SDSS-IV MaNGA Survey: Mapping Nearby Galaxies at Apache Point Observatory”. In: *The Astrophysical Journal* 798, p. 7. ISSN: 0004-637X. DOI: [10.1088/0004-637X/798/1/7](https://doi.org/10.1088/0004-637X/798/1/7). URL: <http://adsabs.harvard.edu/abs/2015ApJ...798....7B> (visited on 05/16/2021).
- Buta, Ronald J., Kartik Sheth, E. Athanassoula, A. Bosma, Johan H. Knapen, et al. (Apr. 1, 2015). “A Classical Morphological Analysis of Galaxies in the Spitzer Survey of Stellar Structure in Galaxies (S4G)”. In: *The Astrophysical Journal Supplement Series* 217, p. 32. ISSN: 0067-0049. DOI: [10.1088/0067-0049/217/2/32](https://doi.org/10.1088/0067-0049/217/2/32). URL: <http://adsabs.harvard.edu/abs/2015ApJS..217...32B> (visited on 12/22/2020).
- Calzetti, Daniela, Lee Armus, Ralph C. Bohlin, Anne L. Kinney, Jan Koornneef, et al. (Apr. 1, 2000). “The Dust Content and Opacity of Actively Star-Forming Galaxies”. In: *The Astrophysical Journal* 533, pp. 682–695. ISSN: 0004-637X. DOI: [10.1086/308692](https://doi.org/10.1086/308692). URL: <http://adsabs.harvard.edu/abs/2000ApJ...533..682C> (visited on 01/20/2021).
- Calzetti, Daniela, Andrew J. Battisti, Irene Shivaie, Matteo Messa, Michele Cignoni, et al. (Mar. 1, 2021). “Revisiting Attenuation Curves: The Case of NGC 3351”. In: *arXiv e-prints* 2103, arXiv:2103.12117. URL: <http://adsabs.harvard.edu/abs/2021arXiv210312117C> (visited on 04/30/2021).
- Calzetti, Daniela, Anne L. Kinney, and Thaisa Storchi-Bergmann (July 1, 1994). “Dust Extinction of the Stellar Continua in Starburst Galaxies: The Ultraviolet and Optical Extinction Law”. In: *The Astrophysical Journal* 429, pp. 582–601. ISSN: 0004-637X. DOI: [10.1086/174346](https://doi.org/10.1086/174346). URL: <http://adsabs.harvard.edu/abs/1994ApJ...429..582C> (visited on 04/30/2021).
- Cappellari, Michele (Apr. 1, 2017). “Improving the Full Spectrum Fitting Method: Accurate Convolution with Gauss-Hermite Functions”. In: *Monthly Notices of*

- the Royal Astronomical Society* 466, pp. 798–811. ISSN: 0035-8711. DOI: [10.1093/mnras/stw3020](https://doi.org/10.1093/mnras/stw3020). URL: <http://adsabs.harvard.edu/abs/2017MNRAS.466..798C> (visited on 01/14/2021).
- Cappellari, Michele and Yannick Copin (June 1, 2003). “Adaptive Spatial Binning of Integral-Field Spectroscopic Data Using Voronoi Tessellations”. In: *Monthly Notices of the Royal Astronomical Society* 342, pp. 345–354. ISSN: 0035-8711. DOI: [10.1046/j.1365-8711.2003.06541.x](https://doi.org/10.1046/j.1365-8711.2003.06541.x). URL: <http://adsabs.harvard.edu/abs/2003MNRAS.342..345C> (visited on 01/13/2021).
- Cappellari, Michele and Eric Emsellem (Feb. 1, 2004). “Parametric Recovery of Line-of-Sight Velocity Distributions from Absorption-Line Spectra of Galaxies via Penalized Likelihood”. In: *Publications of the Astronomical Society of the Pacific* 116, pp. 138–147. ISSN: 0004-6280. DOI: [10.1086/381875](https://doi.org/10.1086/381875). URL: <http://adsabs.harvard.edu/abs/2004PASP..116..138C> (visited on 01/14/2021).
- Cardelli, Jason A., Geoffrey C. Clayton, and John S. Mathis (Oct. 1, 1989). “The Relationship between Infrared, Optical, and Ultraviolet Extinction”. In: *The Astrophysical Journal* 345, pp. 245–256. ISSN: 0004-637X. DOI: [10.1086/167900](https://doi.org/10.1086/167900). URL: <http://adsabs.harvard.edu/abs/1989ApJ...345..245C> (visited on 05/06/2021).
- Charlot, Stéphane and S. Michael Fall (Aug. 1, 2000). “A Simple Model for the Absorption of Starlight by Dust in Galaxies”. In: *The Astrophysical Journal* 539, pp. 718–731. ISSN: 0004-637X. DOI: [10.1086/309250](https://doi.org/10.1086/309250). URL: <http://adsabs.harvard.edu/abs/2000ApJ...539..718C> (visited on 05/20/2021).
- Chevallard, J., S. Charlot, B. Wandelt, and V. Wild (July 1, 2013). “Insights into the Content and Spatial Distribution of Dust from the Integrated Spectral Properties of Galaxies”. In: *Monthly Notices of the Royal Astronomical Society* 432, pp. 2061–2091. ISSN: 0035-8711. DOI: [10.1093/mnras/stt523](https://doi.org/10.1093/mnras/stt523). URL: <http://adsabs.harvard.edu/abs/2013MNRAS.432.2061C> (visited on 05/20/2021).
- Clark, C. J. R., L. Dunne, H. L. Gomez, S. Maddox, P. De Vis, et al. (Sept. 1, 2015). “Herschel-ATLAS: The Surprising Diversity of Dust-Selected Galaxies in the Local Submillimetre Universe”. In: *Monthly Notices of the Royal Astronomical Society* 452, pp. 397–430. ISSN: 0035-8711. DOI: [10.1093/mnras/stv1276](https://doi.org/10.1093/mnras/stv1276). URL: <http://adsabs.harvard.edu/abs/2015MNRAS.452..397C> (visited on 12/22/2020).
- Colless, Matthew, Gavin Dalton, Steve Maddox, Will Sutherland, Peder Norberg, et al. (Dec. 1, 2001). “The 2dF Galaxy Redshift Survey: Spectra and Redshifts”. In: *Monthly Notices of the Royal Astronomical Society* 328, pp. 1039–1063.

- ISSN: 0035-8711. DOI: [10.1046/j.1365-8711.2001.04902.x](https://doi.org/10.1046/j.1365-8711.2001.04902.x). URL: <http://adsabs.harvard.edu/abs/2001MNRAS.328.1039C> (visited on 12/22/2020).
- Colless, Matthew, Bruce A. Peterson, Carole Jackson, John A. Peacock, Shaun Cole, et al. (June 1, 2003). “The 2dF Galaxy Redshift Survey: Final Data Release”. In: *arXiv Astrophysics e-prints*, arXiv:astro-ph/0306581. URL: <http://adsabs.harvard.edu/abs/2003astro.ph..6581C> (visited on 12/22/2020).
- Croom, Scott M., Jon S. Lawrence, Joss Bland-Hawthorn, Julia J. Bryant, Lisa Fogarty, et al. (Mar. 1, 2012). “The Sydney-AAO Multi-Object Integral Field Spectrograph”. In: *Monthly Notices of the Royal Astronomical Society* 421, pp. 872–893. ISSN: 0035-8711. DOI: [10.1111/j.1365-2966.2011.20365.x](https://doi.org/10.1111/j.1365-2966.2011.20365.x). URL: <http://adsabs.harvard.edu/abs/2012MNRAS.421..872C> (visited on 05/13/2021).
- Da Cunha, Elisabete, Stéphane Charlot, and David Elbaz (Aug. 1, 2008). “A Simple Model to Interpret the Ultraviolet, Optical and Infrared Emission from Galaxies”. In: *Monthly Notices of the Royal Astronomical Society* 388, pp. 1595–1617. ISSN: 0035-8711. DOI: [10.1111/j.1365-2966.2008.13535.x](https://doi.org/10.1111/j.1365-2966.2008.13535.x). URL: <http://adsabs.harvard.edu/abs/2008MNRAS.388.1595D> (visited on 12/22/2020).
- Dale, D. A., G. Aniano, C. W. Engelbracht, J. L. Hinz, O. Krause, et al. (Jan. 1, 2012). “Herschel Far-Infrared and Submillimeter Photometry for the KINGFISH Sample of Nearby Galaxies”. In: *The Astrophysical Journal* 745, p. 95. ISSN: 0004-637X. DOI: [10.1088/0004-637X/745/1/95](https://doi.org/10.1088/0004-637X/745/1/95). URL: <http://adsabs.harvard.edu/abs/2012ApJ...745...95D> (visited on 12/22/2020).
- De Vis, P. (2016). “Dust and Gas in Local Galaxies in the Equatorial H-ATLAS Fields”. PhD Thesis. University of Canterbury & Ghent University.
- De Vis, P., L. Dunne, S. Maddox, H. L. Gomez, C. J. R. Clark, et al. (Feb. 1, 2017a). “Herschel -ATLAS: Revealing Dust Build-up and Decline across Gas, Dust and Stellar Mass Selected Samples - I. Scaling Relations”. In: *Monthly Notices of the Royal Astronomical Society* 464, pp. 4680–4705. ISSN: 0035-8711. DOI: [10.1093/mnras/stw2501](https://doi.org/10.1093/mnras/stw2501). URL: <http://adsabs.harvard.edu/abs/2017MNRAS.464.4680D> (visited on 12/22/2020).
- De Vis, P., H. L. Gomez, S. P. Schofield, S. Maddox, L. Dunne, et al. (Oct. 1, 2017b). “Using Dust, Gas and Stellar Mass-Selected Samples to Probe Dust Sources and Sinks in Low-Metallicity Galaxies”. In: *Monthly Notices of the Royal Astronomical Society* 471, pp. 1743–1765. ISSN: 0035-8711. DOI: [10.1093/mnras/stx981](https://doi.org/10.1093/mnras/stx981). URL: <http://adsabs.harvard.edu/abs/2017MNRAS.471.1743D> (visited on 12/22/2020).

- Dole, H., G. Lagache, J.-L. Puget, K. I. Caputi, N. Fernández-Conde, et al. (May 1, 2006). “The Cosmic Infrared Background Resolved by Spitzer. Contributions of Mid-Infrared Galaxies to the Far-Infrared Background”. In: *Astronomy and Astrophysics* 451, pp. 417–429. ISSN: 0004-6361. DOI: [10.1051/0004-6361:20054446](https://doi.org/10.1051/0004-6361/20054446). URL: <http://adsabs.harvard.edu/abs/2006A%26A...451..417D> (visited on 12/22/2020).
- Draine, B. T. and Aigen Li (Mar. 1, 2007). “Infrared Emission from Interstellar Dust. IV. The Silicate-Graphite-PAH Model in the Post-Spitzer Era”. In: *The Astrophysical Journal* 657, pp. 810–837. ISSN: 0004-637X. DOI: [10.1086/511055](https://doi.org/10.1086/511055). URL: <http://adsabs.harvard.edu/abs/2007ApJ...657..810D> (visited on 05/28/2021).
- Driver, Simon P., Peder Norberg, Ivan K. Baldry, Steven P. Bamford, Andrew M. Hopkins, et al. (Oct. 1, 2009). “GAMA: Towards a Physical Understanding of Galaxy Formation”. In: *Astronomy and Geophysics* 50, pp. 5.12–5.19. ISSN: 1366-8781. DOI: [10.1111/j.1468-4004.2009.50512.x](https://doi.org/10.1111/j.1468-4004.2009.50512.x). URL: <http://adsabs.harvard.edu/abs/2009A%26G...50e..12D> (visited on 12/22/2020).
- Dunne, L., Z. Zhang, P. De Vis, C. J. R. Clark, I. Oteo, et al. (Sept. 1, 2018). “The Unusual ISM in Blue and Dusty Gas-Rich Galaxies (BADGRS)”. In: *Monthly Notices of the Royal Astronomical Society* 479, pp. 1221–1239. ISSN: 0035-8711. DOI: [10.1093/mnras/sty1465](https://doi.org/10.1093/mnras/sty1465). URL: <http://adsabs.harvard.edu/abs/2018MNRAS.479.1221D> (visited on 12/22/2020).
- Eales, S., L. Dunne, D. Clements, A. Cooray, G. De Zotti, et al. (May 1, 2010). “The Herschel ATLAS”. In: *Publications of the Astronomical Society of the Pacific* 122, p. 499. ISSN: 0004-6280. DOI: [10.1086/653086](https://doi.org/10.1086/653086). URL: <http://adsabs.harvard.edu/abs/2010PASP..122..499E> (visited on 12/22/2020).
- Eales, Stephen, Simon Lilly, Walter Gear, Loretta Dunne, J. Richard Bond, et al. (Apr. 1, 1999). “The Canada-UK Deep Submillimeter Survey: First Submillimeter Images, the Source Counts, and Resolution of the Background”. In: *The Astrophysical Journal* 515, pp. 518–524. ISSN: 0004-637X. DOI: [10.1086/307069](https://doi.org/10.1086/307069). URL: <http://adsabs.harvard.edu/abs/1999ApJ...515..518E> (visited on 12/22/2020).
- Edge, A., W. Sutherland, K. Kuijken, S. Driver, R. McMahon, et al. (Dec. 1, 2013). “The VISTA Kilo-Degree Infrared Galaxy (VIKING) Survey: Bridging the Gap between Low and High Redshift”. In: *The Messenger* 154, pp. 32–34. ISSN: 0722-6691. URL: <http://adsabs.harvard.edu/abs/2013Msngr.154...32E> (visited on 12/22/2020).

- Fanelli, Michael N., Robert W. O’Connell, and Trinh X. Thuan (Nov. 1, 1988). “Spectral Synthesis in the Ultraviolet. II - Stellar Populations and Star Formation in Blue Compact Galaxies”. In: *The Astrophysical Journal* 334, pp. 665–687. ISSN: 0004-637X. DOI: [10.1086/166869](https://doi.org/10.1086/166869). URL: <http://adsabs.harvard.edu/abs/1988ApJ...334..665F> (visited on 05/20/2021).
- Ferrara, Andrea, Simone Bianchi, Andrea Cimatti, and Carlo Giovanardi (Aug. 1, 1999). “An Atlas of Monte Carlo Models of Dust Extinction in Galaxies for Cosmological Applications”. In: *The Astrophysical Journal Supplement Series* 123, pp. 437–445. ISSN: 0067-0049. DOI: [10.1086/313244](https://doi.org/10.1086/313244). URL: <http://adsabs.harvard.edu/abs/1999ApJS..123..437F> (visited on 05/20/2021).
- Fitzpatrick, E. (1989). “Interstellar Extinction in External Galaxies”. In: 135, p. 37. URL: <http://adsabs.harvard.edu/abs/1989IAUS..135...37F> (visited on 05/07/2021).
- Fitzpatrick, Edward L. (Jan. 1, 1999). “Correcting for the Effects of Interstellar Extinction”. In: *Publications of the Astronomical Society of the Pacific* 111, pp. 63–75. ISSN: 0004-6280. DOI: [10.1086/316293](https://doi.org/10.1086/316293). URL: <http://adsabs.harvard.edu/abs/1999PASP..111...63F> (visited on 05/06/2021).
- Fitzpatrick, Edward L. and Derck Massa (May 1, 1988). “An Analysis of the Shapes of Ultraviolet Extinction Curves. II - The Far-UV Extinction”. In: *The Astrophysical Journal* 328, pp. 734–746. ISSN: 0004-637X. DOI: [10.1086/166332](https://doi.org/10.1086/166332). URL: <http://adsabs.harvard.edu/abs/1988ApJ...328..734F> (visited on 05/07/2021).
- Glover, S. C. O. and M.-M. Mac Low (Mar. 1, 2011). “On the Relationship between Molecular Hydrogen and Carbon Monoxide Abundances in Molecular Clouds”. In: *Monthly Notices of the Royal Astronomical Society* 412, pp. 337–350. ISSN: 0035-8711. DOI: [10.1111/j.1365-2966.2010.17907.x](https://doi.org/10.1111/j.1365-2966.2010.17907.x). URL: <http://adsabs.harvard.edu/abs/2011MNRAS.412..337G> (visited on 12/22/2020).
- Gordon, Karl D., Daniela Calzetti, and Adolf N. Witt (Oct. 1, 1997). “Dust in Starburst Galaxies”. In: *The Astrophysical Journal* 487, pp. 625–635. ISSN: 0004-637X. DOI: [10.1086/304654](https://doi.org/10.1086/304654). URL: <http://adsabs.harvard.edu/abs/1997ApJ...487..625G> (visited on 05/20/2021).
- Green, Andrew W., Scott M. Croom, Nicholas Scott, Luca Cortese, Anne M. Medling, et al. (Mar. 1, 2018). “The SAMI Galaxy Survey: Data Release One with Emission-Line Physics Value-Added Products”. In: *Monthly Notices of the Royal Astronomical Society* 475, pp. 716–734. ISSN: 0035-8711. DOI: [10.1093/mnras/stx3135](https://doi.org/10.1093/mnras/stx3135). URL: <http://adsabs.harvard.edu/abs/2018MNRAS.475..716G> (visited on 12/22/2020).

- Griffin, M. J., A. Abergel, A. Abreu, P. A. R. Ade, P. André, et al. (July 1, 2010). “The Herschel-SPIRE Instrument and Its in-Flight Performance”. In: *Astronomy and Astrophysics* 518, p. L3. ISSN: 0004-6361. DOI: [10.1051/0004-6361/201014519](https://doi.org/10.1051/0004-6361/201014519). URL: <http://adsabs.harvard.edu/abs/2010A%26A...518L...3G> (visited on 12/22/2020).
- Groves, Brent, Jarle Brinchmann, and Carl Jakob Walcher (Jan. 1, 2012). “The Balmer Decrement of Sloan Digital Sky Survey Galaxies”. In: *Monthly Notices of the Royal Astronomical Society* 419, pp. 1402–1412. ISSN: 0035-8711. DOI: [10.1111/j.1365-2966.2011.19796.x](https://doi.org/10.1111/j.1365-2966.2011.19796.x). URL: <http://adsabs.harvard.edu/abs/2012MNRAS.419.1402G> (visited on 01/21/2021).
- Herschel Astrophysical Terahertz Large Area Survey Cutouts* (2021). URL: [https://irsa.ipac.caltech.edu/data/Herschel/H-ATLAS/index\\_cutouts.html](https://irsa.ipac.caltech.edu/data/Herschel/H-ATLAS/index_cutouts.html) (visited on 05/29/2021).
- Ho, I.-Ting, Lisa J. Kewley, Michael A. Dopita, Anne M. Medling, J. T. Allen, et al. (Nov. 1, 2014). “The SAMI Galaxy Survey: Shocks and Outflows in a Normal Star-Forming Galaxy”. In: *Monthly Notices of the Royal Astronomical Society* 444, pp. 3894–3910. ISSN: 0035-8711. DOI: [10.1093/mnras/stu1653](https://doi.org/10.1093/mnras/stu1653). URL: <http://adsabs.harvard.edu/abs/2014MNRAS.444.3894H> (visited on 12/22/2020).
- Holland, W. S., E. I. Robson, W. K. Gear, C. R. Cunningham, J. F. Lightfoot, et al. (Mar. 1, 1999). “SCUBA: A Common-User Submillimetre Camera Operating on the James Clerk Maxwell Telescope”. In: *Monthly Notices of the Royal Astronomical Society* 303, pp. 659–672. ISSN: 0035-8711. DOI: [10.1046/j.1365-8711.1999.02111.x](https://doi.org/10.1046/j.1365-8711.1999.02111.x). URL: <http://adsabs.harvard.edu/abs/1999MNRAS.303..659H> (visited on 12/22/2020).
- Husemann, B., S. Kamann, C. Sandin, S. F. Sánchez, R. García-Benito, et al. (Oct. 1, 2012). “PyCosmic: Detecting Cosmics in CALIFA and Other Fiber-Fed Integral-Field Spectroscopy Datasets”. In: *Astrophysics Source Code Library*, ascl:1210.027. URL: <http://adsabs.harvard.edu/abs/2012ascl.soft10027H> (visited on 12/22/2020).
- Inoue, Akio K. (May 1, 2005). “Attenuation Law of Normal Disc Galaxies with Clumpy Distributions of Stars and Dust”. In: *Monthly Notices of the Royal Astronomical Society* 359, pp. 171–182. ISSN: 0035-8711. DOI: [10.1111/j.1365-2966.2005.08890.x](https://doi.org/10.1111/j.1365-2966.2005.08890.x). URL: <http://adsabs.harvard.edu/abs/2005MNRAS.359..171I> (visited on 05/20/2021).

- Kelz, Andreas, Marc A. W. Verheijen, Martin M. Roth, Svend M. Bauer, Thomas Becker, et al. (Jan. 1, 2006). “PMAS: The Potsdam Multi-Aperture Spectrophotometer. II. The Wide Integral Field Unit PPak”. In: *Publications of the Astronomical Society of the Pacific* 118, pp. 129–145. ISSN: 0004-6280. DOI: [10.1086/497455](https://doi.org/10.1086/497455). URL: <http://adsabs.harvard.edu/abs/2006PASP..118..129K> (visited on 05/13/2021).
- Kessler, M. F., J. A. Steinz, M. E. Anderegg, J. Clavel, G. Drechsel, et al. (Nov. 1, 1996). “The Infrared Space Observatory (ISO) Mission.” In: *Astronomy and Astrophysics* 315, pp. L27–L31. ISSN: 0004-6361. URL: <http://adsabs.harvard.edu/abs/1996A%26A...315L..27K> (visited on 12/22/2020).
- Kewley, Lisa J., Michael A. Dopita, Claus Leitherer, Romeel Davé, Tiantian Yuan, et al. (Sept. 1, 2013). “Theoretical Evolution of Optical Strong Lines across Cosmic Time”. In: *The Astrophysical Journal* 774, p. 100. ISSN: 0004-637X. DOI: [10.1088/0004-637X/774/2/100](https://doi.org/10.1088/0004-637X/774/2/100). URL: <http://adsabs.harvard.edu/abs/2013ApJ...774..100K> (visited on 12/22/2020).
- Kim, Sang-Hee and P. G. Martin (Aug. 1, 1994a). “The Size Distribution of Interstellar Dust Particles as Determined from Polarization: Infinite Cylinders”. In: *The Astrophysical Journal* 431, pp. 783–796. ISSN: 0004-637X. DOI: [10.1086/174529](https://doi.org/10.1086/174529). URL: <http://adsabs.harvard.edu/abs/1994ApJ...431..783K> (visited on 05/18/2021).
- Kim, Sang-Hee, P. G. Martin, and Paul D. Hendry (Feb. 1, 1994b). “The Size Distribution of Interstellar Dust Particles as Determined from Extinction”. In: *The Astrophysical Journal* 422, pp. 164–175. ISSN: 0004-637X. DOI: [10.1086/173714](https://doi.org/10.1086/173714). URL: <http://adsabs.harvard.edu/abs/1994ApJ...422..164K> (visited on 05/18/2021).
- Koribalski, B. S., L. Staveley-Smith, V. A. Kilborn, S. D. Ryder, R. C. Kraan-Korteweg, et al. (July 1, 2004). “The 1000 Brightest HIPASS Galaxies: HI Properties”. In: *The Astronomical Journal* 128, pp. 16–46. ISSN: 0004-6256. DOI: [10.1086/421744](https://doi.org/10.1086/421744). URL: <http://adsabs.harvard.edu/abs/2004AJ...128...16K> (visited on 12/22/2020).
- Law, David R., Renbin Yan, Matthew A. Bershady, Kevin Bundy, Brian Cherinka, et al. (July 1, 2015). “Observing Strategy for the SDSS-IV/MaNGA IFU Galaxy Survey”. In: *The Astronomical Journal* 150, p. 19. ISSN: 0004-6256. DOI: [10.1088/0004-6256/150/1/19](https://doi.org/10.1088/0004-6256/150/1/19). URL: <http://adsabs.harvard.edu/abs/2015AJ....150...19L> (visited on 05/13/2021).

- Lawrence, A., S. J. Warren, O. Almaini, A. C. Edge, N. C. Hambly, et al. (Aug. 1, 2007). “The UKIRT Infrared Deep Sky Survey (UKIDSS)”. In: *Monthly Notices of the Royal Astronomical Society* 379, pp. 1599–1617. ISSN: 0035-8711. DOI: [10.1111/j.1365-2966.2007.12040.x](https://doi.org/10.1111/j.1365-2966.2007.12040.x). URL: <http://adsabs.harvard.edu/abs/2007MNRAS.379.1599L> (visited on 12/22/2020).
- Leroy, Adam K., Alberto Bolatto, Karl Gordon, Karin Sandstrom, Pierre Gratier, et al. (Aug. 1, 2011). “The CO-to-H<sub>2</sub> Conversion Factor from Infrared Dust Emission across the Local Group”. In: *The Astrophysical Journal* 737, p. 12. ISSN: 0004-637X. DOI: [10.1088/0004-637X/737/1/12](https://doi.org/10.1088/0004-637X/737/1/12). URL: <http://adsabs.harvard.edu/abs/2011ApJ...737...12L> (visited on 12/22/2020).
- Mauch, Tom, Hans-Rainer Klöckner, Steve Rawlings, Matt Jarvis, Martin J. Hardcastle, et al. (Oct. 1, 2013). “A 325-MHz GMRT Survey of the Herschel-ATLAS/GAMA Fields”. In: *Monthly Notices of the Royal Astronomical Society* 435, pp. 650–662. ISSN: 0035-8711. DOI: [10.1093/mnras/stt1323](https://doi.org/10.1093/mnras/stt1323). URL: <http://adsabs.harvard.edu/abs/2013MNRAS.435..650M> (visited on 12/22/2020).
- Meyer, M. J., M. A. Zwaan, R. L. Webster, L. Staveley-Smith, E. Ryan-Weber, et al. (June 1, 2004). “The HIPASS Catalogue - I. Data Presentation”. In: *Monthly Notices of the Royal Astronomical Society* 350, pp. 1195–1209. ISSN: 0035-8711. DOI: [10.1111/j.1365-2966.2004.07710.x](https://doi.org/10.1111/j.1365-2966.2004.07710.x). URL: <http://adsabs.harvard.edu/abs/2004MNRAS.350.1195M> (visited on 12/22/2020).
- Millard, Jenifer S., Benedikt Diemer, Stephen A. Eales, Haley L. Gomez, Rosemary Beeston, et al. (Jan. 2021). “IllustrisTNG and S2COSMOS: Possible Conflicts in the Evolution of Neutral Gas and Dust”. In: *Monthly Notices of the Royal Astronomical Society* 500.1, pp. 871–888. ISSN: 0035-8711. DOI: [10.1093/mnras/staa3207](https://doi.org/10.1093/mnras/staa3207). URL: <https://ui.adsabs.harvard.edu/abs/2021MNRAS.500..871M/abstract> (visited on 12/22/2020).
- Moehler, S., A. Modigliani, W. Freudling, N. Giammichele, A. Gianninas, et al. (Dec. 1, 2014). “Flux Calibration of Medium Resolution Spectra from 300 Nm to 2500 Nm — Model Reference Spectra and Telluric Correction”. In: *The Messenger* 158, pp. 16–20. ISSN: 0722-6691. URL: <http://adsabs.harvard.edu/abs/2014Msngr.158...16M> (visited on 12/22/2020).
- Mortier, A. M. J., S. Serjeant, J. S. Dunlop, S. E. Scott, P. Ade, et al. (Oct. 1, 2005). “The SCUBA Half-Degree Extragalactic Survey - I. Survey Motivation, Design and Data Processing”. In: *Monthly Notices of the Royal Astronomical Society* 363, pp. 563–580. ISSN: 0035-8711. DOI: [10.1111/j.1365-2966.2005.09460.x](https://doi.org/10.1111/j.1365-2966.2005.09460.x).

- x. URL: <http://adsabs.harvard.edu/abs/2005MNRAS.363..563M> (visited on 12/22/2020).
- Narayanan, Desika, Charlie Conroy, Romeel Davé, Benjamin D. Johnson, and Gergö Popping (Dec. 1, 2018). “A Theory for the Variation of Dust Attenuation Laws in Galaxies”. In: *The Astrophysical Journal* 869, p. 70. ISSN: 0004-637X. DOI: [10.3847/1538-4357/aaed25](https://doi.org/10.3847/1538-4357/aaed25). URL: <http://adsabs.harvard.edu/abs/2018ApJ...869...70N> (visited on 05/20/2021).
- Natale, Giovanni, Cristina C. Popescu, Richard. J. Tuffs, Victor P. Debattista, Jörg Fischera, et al. (May 1, 2015). “Predicting the Stellar and Non-Equilibrium Dust Emission Spectra of High-Resolution Simulated Galaxies with DART-RAY”. In: *Monthly Notices of the Royal Astronomical Society* 449, pp. 243–267. ISSN: 0035-8711. DOI: [10.1093/mnras/stv286](https://doi.org/10.1093/mnras/stv286). URL: <http://adsabs.harvard.edu/abs/2015MNRAS.449..243N> (visited on 05/20/2021).
- Neugebauer, G., H. J. Habing, R. van Duinen, H. H. Aumann, B. Baud, et al. (Mar. 1, 1984). “The Infrared Astronomical Satellite (IRAS) Mission”. In: *The Astrophysical Journal Letters* 278, pp. L1–L6. ISSN: 0004-637X. DOI: [10.1086/184209](https://doi.org/10.1086/184209). URL: <http://adsabs.harvard.edu/abs/1984ApJ...278L...1N> (visited on 12/22/2020).
- Noll, S., D. Burgarella, E. Giovannoli, V. Buat, D. Marcillac, et al. (Dec. 1, 2009). “Analysis of Galaxy Spectral Energy Distributions from Far-UV to Far-IR with CIGALE: Studying a SINGS Test Sample”. In: *Astronomy and Astrophysics* 507, pp. 1793–1813. ISSN: 0004-6361. DOI: [10.1051/0004-6361/200912497](https://doi.org/10.1051/0004-6361/200912497). URL: <http://adsabs.harvard.edu/abs/2009A%26A...507.1793N> (visited on 01/20/2021).
- Optical Spectra Overview — SDSS* (2020). URL: <https://www.sdss.org/dr15/spectro/> (visited on 12/22/2020).
- Papadopoulos, Padelis P., Paul P. van der Werf, E. M. Xilouris, K. G. Isaak, Yu Gao, et al. (Nov. 1, 2012). “The Molecular Gas in Luminous Infrared Galaxies - I. CO Lines, Extreme Physical Conditions and Their Drivers”. In: *Monthly Notices of the Royal Astronomical Society* 426, pp. 2601–2629. ISSN: 0035-8711. DOI: [10.1111/j.1365-2966.2012.21001.x](https://doi.org/10.1111/j.1365-2966.2012.21001.x). URL: <http://adsabs.harvard.edu/abs/2012MNRAS.426.2601P> (visited on 12/22/2020).
- Pei, Yichuan C. (Aug. 1, 1992). “Interstellar Dust from the Milky Way to the Magellanic Clouds”. In: *The Astrophysical Journal* 395, pp. 130–139. ISSN: 0004-637X. DOI: [10.1086/171637](https://doi.org/10.1086/171637). URL: <http://adsabs.harvard.edu/abs/1992ApJ...395..130P> (visited on 05/06/2021).

- Pettini, Max and Bernard E. J. Pagel (Mar. 1, 2004). “[OIII]/[NII] as an Abundance Indicator at High Redshift”. In: *Monthly Notices of the Royal Astronomical Society* 348, pp. L59–L63. ISSN: 0035-8711. DOI: [10.1111/j.1365-2966.2004.07591.x](https://doi.org/10.1111/j.1365-2966.2004.07591.x). URL: <http://adsabs.harvard.edu/abs/2004MNRAS.348L..59P> (visited on 05/30/2021).
- Pilbratt, G. L., J. R. Riedinger, T. Passvogel, G. Crone, D. Doyle, et al. (July 1, 2010). “Herschel Space Observatory. An ESA Facility for Far-Infrared and Submillimetre Astronomy”. In: *Astronomy and Astrophysics* 518, p. L1. ISSN: 0004-6361. DOI: [10.1051/0004-6361/201014759](https://doi.org/10.1051/0004-6361/201014759). URL: <http://adsabs.harvard.edu/abs/2010A%26A...518L...1P> (visited on 12/22/2020).
- Pilyugin, L. S. and E. K. Grebel (Apr. 1, 2016). “New Calibrations for Abundance Determinations in H II Regions”. In: *Monthly Notices of the Royal Astronomical Society* 457, pp. 3678–3692. ISSN: 0035-8711. DOI: [10.1093/mnras/stw238](https://doi.org/10.1093/mnras/stw238). URL: <http://adsabs.harvard.edu/abs/2016MNRAS.457.3678P> (visited on 12/22/2020).
- Pilyugin, Leonid S. and Trinh X. Thuan (Sept. 1, 2005). “Oxygen Abundance Determination in H II Regions: The Strong Line Intensities-Abundance Calibration Revisited”. In: *The Astrophysical Journal* 631, pp. 231–243. ISSN: 0004-637X. DOI: [10.1086/432408](https://doi.org/10.1086/432408). URL: <http://adsabs.harvard.edu/abs/2005ApJ...631..231P> (visited on 05/30/2021).
- Poglitsch, A., C. Waelkens, N. Geis, H. Feuchtgruber, B. Vandenbussche, et al. (July 1, 2010). “The Photodetector Array Camera and Spectrometer (PACS) on the Herschel Space Observatory”. In: *Astronomy and Astrophysics* 518, p. L2. ISSN: 0004-6361. DOI: [10.1051/0004-6361/201014535](https://doi.org/10.1051/0004-6361/201014535). URL: <http://adsabs.harvard.edu/abs/2010A%26A...518L...2P> (visited on 12/22/2020).
- Rémy-Ruyer, A., S. C. Madden, F. Galliano, S. Hony, M. Sauvage, et al. (Sept. 1, 2013). “Revealing the Cold Dust in Low-Metallicity Environments. I. Photometry Analysis of the Dwarf Galaxy Survey with Herschel”. In: *Astronomy and Astrophysics* 557, A95. ISSN: 0004-6361. DOI: [10.1051/0004-6361/201321602](https://doi.org/10.1051/0004-6361/201321602). URL: <http://adsabs.harvard.edu/abs/2013A%26A...557A..95R> (visited on 12/22/2020).
- Rousselot, P., C. Lidman, J.-G. Cuby, G. Moreels, and G. Monnet (Feb. 1, 2000). “Night-Sky Spectral Atlas of OH Emission Lines in the near-Infrared”. In: *Astronomy and Astrophysics* 354, pp. 1134–1150. ISSN: 0004-6361. URL: <http://adsabs.harvard.edu/abs/2000A%26A...354.1134R> (visited on 03/10/2021).

- Rowlands, K., T. Heckman, V. Wild, N. L. Zakamska, V. Rodriguez-Gomez, et al. (Oct. 1, 2018). “SDSS-IV MaNGA: Spatially Resolved Star Formation Histories and the Connection to Galaxy Physical Properties”. In: *Monthly Notices of the Royal Astronomical Society* 480, pp. 2544–2561. ISSN: 0035-8711. DOI: [10.1093/mnras/sty1916](https://doi.org/10.1093/mnras/sty1916). URL: <http://adsabs.harvard.edu/abs/2018MNRAS.480.2544R> (visited on 05/29/2021).
- Ryś, Agnieszka, Jesús Falcón-Barroso, and Glenn van de Ven (Feb. 1, 2013). “Virgo Cluster and Field Dwarf Ellipticals in 3D - I. On the Variety of Stellar Kinematic and Line-Strength Properties”. In: *Monthly Notices of the Royal Astronomical Society* 428, pp. 2980–2994. ISSN: 0035-8711. DOI: [10.1093/mnras/sts245](https://doi.org/10.1093/mnras/sts245). URL: <http://adsabs.harvard.edu/abs/2013MNRAS.428.2980R> (visited on 12/22/2020).
- Salim, Samir, Médéric Boquien, and Janice C. Lee (May 1, 2018). “Dust Attenuation Curves in the Local Universe: Demographics and New Laws for Star-Forming Galaxies and High-Redshift Analogs”. In: *The Astrophysical Journal* 859, p. 11. ISSN: 0004-637X. DOI: [10.3847/1538-4357/aabf3c](https://doi.org/10.3847/1538-4357/aabf3c). URL: <http://adsabs.harvard.edu/abs/2018ApJ...859...11S> (visited on 01/20/2021).
- Salim, Samir and Desika Narayanan (Aug. 1, 2020). “The Dust Attenuation Law in Galaxies”. In: *Annual Review of Astronomy and Astrophysics* 58, pp. 529–575. ISSN: 0066-4146. DOI: [10.1146/annurev-astro-032620-021933](https://doi.org/10.1146/annurev-astro-032620-021933). URL: <http://adsabs.harvard.edu/abs/2020ARA%26A...58..529S> (visited on 04/30/2021).
- Sánchez, S. F., R. C. Kennicutt, A. Gil de Paz, G. van de Ven, J. M. Vílchez, et al. (Feb. 1, 2012). “CALIFA, the Calar Alto Legacy Integral Field Area Survey. I. Survey Presentation”. In: *Astronomy and Astrophysics* 538, A8. ISSN: 0004-6361. DOI: [10.1051/0004-6361/201117353](https://doi.org/10.1051/0004-6361/201117353). URL: <http://adsabs.harvard.edu/abs/2012A%26A...538A...8S> (visited on 05/13/2021).
- Scoville, N., K. Sheth, H. Aussel, P. Vanden Bout, P. Capak, et al. (Apr. 1, 2016). “ISM Masses and the Star Formation Law at  $Z = 1$  to 6: ALMA Observations of Dust Continuum in 145 Galaxies in the COSMOS Survey Field”. In: *The Astrophysical Journal* 820, p. 83. ISSN: 0004-637X. DOI: [10.3847/0004-637X/820/2/83](https://doi.org/10.3847/0004-637X/820/2/83). URL: <http://adsabs.harvard.edu/abs/2016ApJ...820...83S> (visited on 12/22/2020).
- Seon, Kwang-Il and Bruce T. Draine (Dec. 1, 2016). “Radiative Transfer Model of Dust Attenuation Curves in Clumpy, Galactic Environments”. In: *The Astrophysical Journal* 833, p. 201. ISSN: 0004-637X. DOI: [10.3847/1538-4357/](https://doi.org/10.3847/1538-4357/)

- 833/2/201. URL: <http://adsabs.harvard.edu/abs/2016ApJ...833..201S> (visited on 05/20/2021).
- Sharp, R., J. T. Allen, L. M. R. Fogarty, S. M. Croom, L. Cortese, et al. (Jan. 1, 2015). “The SAMI Galaxy Survey: Cubism and Covariance, Putting Round Pegs into Square Holes”. In: *Monthly Notices of the Royal Astronomical Society* 446, pp. 1551–1566. ISSN: 0035-8711. DOI: [10.1093/mnras/stu2055](https://doi.org/10.1093/mnras/stu2055). URL: <http://adsabs.harvard.edu/abs/2015MNRAS.446.1551S> (visited on 12/22/2020).
- Soifer, B. T., G. Neugebauer, and J. R. Houck (1987). “The IRAS View of the Extragalactic Sky”. In: *Annual Review of Astronomy and Astrophysics* 25, pp. 187–230. ISSN: 0066-4146. DOI: [10.1146/annurev.aa.25.090187.001155](https://doi.org/10.1146/annurev.aa.25.090187.001155). URL: <http://adsabs.harvard.edu/abs/1987ARA%26A..25..187S> (visited on 12/22/2020).
- Storey, P. J. and D. G. Hummer (Jan. 1, 1995). “Recombination Line Intensities for Hydrogenic Ions-IV. Total Recombination Coefficients and Machine-Readable Tables for Z=1 to 8”. In: *Monthly Notices of the Royal Astronomical Society* 272, pp. 41–48. ISSN: 0035-8711. DOI: [10.1093/mnras/272.1.41](https://doi.org/10.1093/mnras/272.1.41). URL: <http://adsabs.harvard.edu/abs/1995MNRAS.272...41S> (visited on 01/21/2021).
- Stoughton, Chris, Robert H. Lupton, Mariangela Bernardi, Michael R. Blanton, Scott Burles, et al. (Jan. 1, 2002). “Sloan Digital Sky Survey: Early Data Release”. In: *The Astronomical Journal* 123, pp. 485–548. ISSN: 0004-6256. DOI: [10.1086/324741](https://doi.org/10.1086/324741). URL: <http://adsabs.harvard.edu/abs/2002AJ....123..485S> (visited on 12/22/2020).
- Tacconi, L. J., R. Genzel, A. Saintonge, F. Combes, S. García-Burillo, et al. (Feb. 1, 2018). “PHIBSS: Unified Scaling Relations of Gas Depletion Time and Molecular Gas Fractions”. In: *The Astrophysical Journal* 853, p. 179. ISSN: 0004-637X. DOI: [10.3847/1538-4357/aaa4b4](https://doi.org/10.3847/1538-4357/aaa4b4). URL: <http://adsabs.harvard.edu/abs/2018ApJ...853..179T> (visited on 12/22/2020).
- Theureau, G., L. Bottinelli, N. Coudreau-Durand, L. Gouguenheim, N. Hallet, et al. (June 1, 1998). “Kinematics of the Local Universe. VII. New 21-Cm Line Measurements of 2112 Galaxies”. In: *Astronomy and Astrophysics Supplement Series* 130, pp. 333–339. ISSN: 0365-0138. DOI: [10.1051/aas:1998416](https://doi.org/10.1051/aas:1998416). URL: <http://adsabs.harvard.edu/abs/1998A%26AS..130..333T> (visited on 12/22/2020).
- Trayford, James W., Claudia del P. Lagos, Aaron S. G. Robotham, and Danail Obreschkow (Jan. 1, 2020). “Fade to Grey: Systematic Variation of Galaxy Attenuation Curves with Galaxy Properties in the EAGLE Simulations”. In: *Monthly Notices of the Royal Astronomical Society* 491, pp. 3937–3951. ISSN:

- 0035-8711. DOI: [10.1093/mnras/stz3234](https://doi.org/10.1093/mnras/stz3234). URL: <http://adsabs.harvard.edu/abs/2020MNRAS.491.3937T> (visited on 05/20/2021).
- Tuffs, Richard (2008). “Galex-Gama Near-Ir Observations of ~100K Galaxies”. In: *GALEX Proposal*, p. 48. URL: <http://adsabs.harvard.edu/abs/2008galx.prop...48T> (visited on 12/22/2020).
- Tully, R. Brent, Hélène M. Courtois, and Jenny G. Sorce (Aug. 1, 2016). “Cosmicflows-3”. In: *The Astronomical Journal* 152, p. 50. ISSN: 0004-6256. DOI: [10.3847/0004-6256/152/2/50](https://doi.org/10.3847/0004-6256/152/2/50). URL: <http://adsabs.harvard.edu/abs/2016AJ...152...50T> (visited on 12/22/2020).
- Van de Sande, Jesse, Joss Bland-Hawthorn, Lisa M. R. Fogarty, Luca Cortese, Francesco d’Eugenio, et al. (Jan. 1, 2017). “The SAMI Galaxy Survey: Revisiting Galaxy Classification through High-Order Stellar Kinematics”. In: *The Astrophysical Journal* 835, p. 104. ISSN: 0004-637X. DOI: [10.3847/1538-4357/835/1/104](https://doi.org/10.3847/1538-4357/835/1/104). URL: <http://adsabs.harvard.edu/abs/2017ApJ...835..104V> (visited on 12/22/2020).
- Vazdekis, A., P. Sánchez-Blázquez, J. Falcón-Barroso, A. J. Cenarro, M. A. Beasley, et al. (June 1, 2010). “Evolutionary Stellar Population Synthesis with MILES - I. The Base Models and a New Line Index System”. In: *Monthly Notices of the Royal Astronomical Society* 404, pp. 1639–1671. ISSN: 0035-8711. DOI: [10.1111/j.1365-2966.2010.16407.x](https://doi.org/10.1111/j.1365-2966.2010.16407.x). URL: <http://adsabs.harvard.edu/abs/2010MNRAS.404.1639V> (visited on 01/14/2021).
- Walborn, Nolan R. and Edward L. Fitzpatrick (Apr. 1, 1990). “Contemporary Optical Spectral Classification of the OB Stars - A Digital Atlas”. In: *Publications of the Astronomical Society of the Pacific* 102, pp. 379–411. ISSN: 0004-6280. DOI: [10.1086/132646](https://doi.org/10.1086/132646). URL: <http://adsabs.harvard.edu/abs/1990PASP..102..379W> (visited on 06/01/2021).
- Werner, M. W., T. L. Roellig, F. J. Low, G. H. Rieke, M. Rieke, et al. (Sept. 1, 2004). “The Spitzer Space Telescope Mission”. In: *The Astrophysical Journal Supplement Series* 154, pp. 1–9. ISSN: 0067-0049. DOI: [10.1086/422992](https://doi.org/10.1086/422992). URL: <http://adsabs.harvard.edu/abs/2004ApJS...154...1W> (visited on 12/22/2020).
- Whittet, Doug CB (2002). *Dust in the Galactic Environment*. CRC press.
- Wild, Vivienne, Stéphane Charlot, Jarle Brinchmann, Timothy Heckman, Oliver Vince, et al. (Nov. 1, 2011). “Empirical Determination of the Shape of Dust Attenuation Curves in Star-Forming Galaxies”. In: *Monthly Notices of the Royal Astronomical Society* 417, pp. 1760–1786. ISSN: 0035-8711. DOI: [10.1111/j.1365-2966.2011.19811.x](https://doi.org/10.1111/j.1365-2966.2011.19811.x).

- [1111/j.1365-2966.2011.19367.x](http://adsabs.harvard.edu/abs/2011MNRAS.417.1760W). URL: <http://adsabs.harvard.edu/abs/2011MNRAS.417.1760W> (visited on 05/20/2021).
- Wild, Vivienne, Guinevere Kauffmann, Tim Heckman, Stéphane Charlot, Gerard Lemson, et al. (Oct. 1, 2007). “Bursty Stellar Populations and Obscured Active Galactic Nuclei in Galaxy Bulges”. In: *Monthly Notices of the Royal Astronomical Society* 381, pp. 543–572. ISSN: 0035-8711. DOI: [10.1111/j.1365-2966.2007.12256.x](https://doi.org/10.1111/j.1365-2966.2007.12256.x). URL: <http://adsabs.harvard.edu/abs/2007MNRAS.381..543W> (visited on 05/31/2021).
- Witt, Adolf N. and Karl D. Gordon (June 1, 1996). “Multiple Scattering in Clumpy Media. I. Escape of Stellar Radiation from a Clumpy Scattering Environment”. In: *The Astrophysical Journal* 463, p. 681. ISSN: 0004-637X. DOI: [10.1086/177282](https://doi.org/10.1086/177282). URL: <http://adsabs.harvard.edu/abs/1996ApJ...463..681W> (visited on 05/20/2021).
- (Jan. 1, 2000). “Multiple Scattering in Clumpy Media. II. Galactic Environments”. In: *The Astrophysical Journal* 528, pp. 799–816. ISSN: 0004-637X. DOI: [10.1086/308197](https://doi.org/10.1086/308197). URL: <http://adsabs.harvard.edu/abs/2000ApJ...528..799W> (visited on 05/20/2021).
- Wolfire, Mark G., David Hollenbach, and Christopher F. McKee (June 1, 2010). “The Dark Molecular Gas”. In: *The Astrophysical Journal* 716, pp. 1191–1207. ISSN: 0004-637X. DOI: [10.1088/0004-637X/716/2/1191](https://doi.org/10.1088/0004-637X/716/2/1191). URL: <http://adsabs.harvard.edu/abs/2010ApJ...716.1191W> (visited on 12/22/2020).